CZECH TECHNICAL UNIVERSITY IN PRAGUE
Faculty of Mechanical Engineering

NUMERICAL SIMULATION OF INCOMPRESSIBLE FLOWS

in Environmental and Biomedical Applications

author : Tomáš Bodnár

Contents

Chapter I

Introduction

I.1 Motivation of the Work

In the waste majority of textbooks on fluid dynamics, the incompressible fluid is defined using assumptions of constant density (and viscosity) of the fluid. The side-effect of such over-simplified definition is that the resulting mathematical model, known as the system of *incompressible Navier-Stokes equations*, only describes a very narrow, specific subclass of incompressible flows which have constant density and simple rheological behavior characterized by constant viscosity.

Many of the flows of practical interest do not satisfy these elementary assumptions. This is e.g the case of complex flows in *Environmental* and *Biomedical* applications that are addressed further in this work. Hereafter will be given few basic examples of situations where the constant density and viscosity assumptions have to be relaxed to properly describe the physical phenomena that is being investigated.

Variable density

This phenomena could be best demonstrated by a simple analysis of continuity equation, that represents a mathematical formulation of mass conservation principle. In the flow described by velocity field $v(x, t)$ and density field $\rho(x, t)$ these quantities are[1] governed by the continuity equation:

$$\frac{\partial \rho}{\partial t} + \mathrm{div}(\rho v) = 0 \quad .\tag{I.1}$$

Using the product rule of differentiation, the equation (I.1) can be rewritten into the form:

$$\frac{\partial \rho}{\partial t} + v \cdot \mathrm{grad}\rho = -\rho \, \mathrm{div}v \quad .\tag{I.2}$$

This equation could be understood as an advection equation for density with a source term on the right-hand side. This source represents the effects of local changes of volume of considered flow parcels. The equation (I.2) thus states that because of the conservation of mass, the changes of the volume of a fluid parcel have to be compensated by corresponding variation in its density. In this context the *isochoric* (volume preserving) motion can thus be described by a kinematic condition imposed on the velocity field, $\mathrm{div}v = 0$. This *divergence-free* constraint represents what most people understand under the term "incompressibility".

---

[1]in the absence of sources and sinks of mass

Assuming now only the class of divergence-free flows, the mass conservation principle represented by the equation (I.2) splits into two independent requirements:

$$\underbrace{\frac{\partial \rho}{\partial t} + \boldsymbol{v} \cdot \text{grad}\rho}_{=0} = \underbrace{-\rho \, \text{div}\boldsymbol{v}}_{=0} \; . \tag{I.3}$$

This could roughly be explained as splitting of mass conservation into two simultaneous requirements on the conservation of volume and density.

1. Conservation of volume

$$\text{div}\boldsymbol{v} = 0 \tag{I.4}$$

2. Conservation of density

$$\frac{\partial \rho}{\partial t} + \boldsymbol{v} \cdot \text{grad}\rho = 0 \tag{I.5}$$

The equation (I.5) is an advection equation for density. Therefore in general there is no reason, why the density should be considered as a constant. The density is in this case just a scalar quantity advected by the flow and thus it depends on initial and boundary conditions whether it will be constant or not. It is clear that if a constant density field is used as an initial condition with boundary conditions fixed at the same value, than the equation (I.5) is automatically satisfied. In this special case the density will remain constant in space and time. However this is just a very special case. In general, the incompressible flows are allowed to have variable density.

There are many physical phenomena involving incompressible flows with variable density. As an example of such flow, could serve e.g. a river inflow into the sea. The fresh river water enters the see, where the water is salty and thus have higher density than the fresh water. There is no doubt that the flow is incompressible in this case, however it is also evident that the local density (and viscosity) depends on the water salinity (i.e. the local salt concentration).

In a little bit broader sense, the variable density incompressible flow concept could also be used to describe physical situations, where the incompressibility (divergence-free) constraint is satisfied only approximately. A typical example of such situation is the case when the density depends on temperature (i.e. thermal dilatation of fluid is allowed). In the case the temperature based variations in density are allowed, the temperature (or equivalent density) equation should be solved simultaneously with the equations of motion, because the temperature influences (via density) the main flow. A typical example of a model based on this kind of arguments is the *Boussinesq approximation*. It can be successfully applied e.g. to problems involving thermal convection of fluids in the atmosphere or ocean [2].

This second kind of situations, when the divergence-free constrain is only satisfied approximately, represents an area of mathematical modeling, where specific models are developed and used for specific applications. In general one could believe that everything can be simulated by the most general model (e.g. the compressible Navier-Stokes-Fourier equations). However in many cases of practical interest it is not possible (or extremely difficult) to use the the full compressible model due to the significant mathematical, numerical and computational problems arising in the case of nearly incompressible (low-Mach number) flows. Thus it is a common practice to use in these situations models based on incompressibility assumption. This

---

[2]More details on these models will be given in the Chapter E

includes e.g. the mixing of incompressible fluids, some models of free-surface flows, convection of thermally dilatating fluids, and also simulations of fluid flows in weakly-compressible regime.

Variable viscosity

This introductory section only aims to give some motivation and examples of situations where the variable viscosity plays an important role[3]. There are basically two main reasons why the viscosity should be assumed variable in specific cases. The first reason originates directly in the *physics* of fluids. This includes the situations where the viscosity variation is experimentally measurable depending e.g. on the type of the fluid actually studied, on the temperature, concentration of some chemicals or on time. There is a whole branch of fluid mechanics, dealing with the rheology of fluids, which addresses the viscosity (and other rheological parameters) variability from the physical point of view. This leads to existence of many different viscosity constitutive relations applicable in specific situations for various fluids and flow situations.

In the second group of situations, where the variable viscosity assumption is often applied, the viscosity variation is used as a *mathematical modeling* tool in order to take into account some more complex physical phenomena, that results into effects analogical to those of (physically) variable viscosity. An example of this approach is the eddy viscosity concept often used in various models applied to turbulent flow simulations.

The boundary between these two groups of reasons for the use of variable viscosity is not always quite clear. For example the microstructure of certain liquids (such as e.g. polymeric liquids or blood) determines its macroscopic behavior. Thus also the *apparent viscosity* of these fluids strongly depends (in space and time) on the actual microstructure of the fluid. The continuum models used in fluid mechanics usually can not include directly the description of this microstructure and thus a suitable viscosity constitutive relation can be used as a bulk parameter to encounter for the local changes in the microstructure of liquid. So in fact the unresolved micro-physics is hidden in the macroscopic viscosity constitutive law. A very similar situation arises e.g. in the turbulence modeling. In Large Eddy Simulations for example the smallest scale motion is filtered out and included in the model by the means of the so called *eddy viscosity*. So again, the unresolved micro-physics is hidden in the bulk parameters of the flow. Similar approach is used with Reynolds averaging of flow where the analogy of turbulent and molecular diffusion is used to define the *turbulent viscosity*. This is the main principle of many algebraic and one and two-equational models of turbulence (such as e.g. $k - \epsilon$ or $k - \omega$).

These above examples demonstrate why the mathematical modeling and numerical solution of incompressible flows represents a challenging problem for theoretical and applied researchers. This work presents a short overview of few of the numerical methods useable in complex incompressible flows simulations. The applicability of these methods is demonstrated by solving problems arising in environmental and biomedical applications.

---

[3]Some more complex rheological models will be introduced later, in the Chapter B.

I.2   Objectives of the Work

The aim of this work is to present several numerical methods that have been successfully applied to simulation of various complex incompressible flows.
     The following steps are taken to achieve the objectives of the present work:

> **I.** *Presentation of numerical schemes*
>   The models and numerical methods will be shortly described to be later used in specific applications.
>
> **II.** *Application to environmental problems*
>   Some of the models used in environmental aerodynamics and hydraulics will be introduced.
>
> **III.** *Application to biomedical problems*
>   Short introduction to rheology and its application in solving biomedical fluid mechanics problems will be given.

I.3   Structure of the Work

The work is conceived as a collection of papers. These are sorted into two main blocks dealing with either *environmental* or *biomedical* applications. These specialized parts are preceded by a common introduction that contains the description of *numerical methods* that have been used. According to the above points the presented text can be divided into three main parts.
     Chapter N–Numerical Methods for Incompressible Flows   *(25 pages)*
The introduction to this chapter contains brief description of the classical incompressible Navier-Stokes system of equations. The main difficulties related to its numerical solution are revealed. This introduction is followed by an overview of numerical methods that have been later used in the environmental and biomedical applications mentioned in chapters E and B. List of relevant references is given to document where are these numerical methods coming from and where they have been used.
     Chapter E–Environmental Applications   *(5 pages + 4 papers)*
This chapter starts with a summary of the most notable characteristic properties of environmental flows that make their simulation so challenging. Special attention is paid to models describing turbulent, variable-density and stratified flows. This theoretical summary is followed by selected papers demonstrating the use of these models and their numerical solution.
     Chapter B–Biomedical Applications   *(5 pages + 4 papers)*
The specificity of biomedical applications is mainly related to the non-Newtonian rheological behavior of the considered fluids. This issue will be addressed with special focus on blood flows, including shear-thinning, viscoelastic and biochemical models of blood. Again, this brief introduction is followed by selected papers demonstrating the use of these models and their numerical solution.

Chapter N

Numerical Methods for Incompressible Flows

Contents

Introduction

The incompressible model can formally be obtained as a limit case of the full compressible Navier-Stokes-Fourier system for *Mach number* going to zero. The mathematically rigorous derivation of this (and some other) singular limits can be found e.g. in the recent book [N.15]. As a result of such limiting process (including all the simplifying assumptions), the energy

equation becomes decoupled from the equations of motion, pressure changes its role from thermodynamical quantity to some kind of kinematic forcing and incompressibility constraint is expressed in terms of divergence-free velocity field. Here we will only mention some of the final stages of the formal derivation of the incompressible model.

N.1   Mathematical Model

The model is based on balance of mass and linear momentum, and is complemented by suitable constitutive laws for stress tensor.

N.1.1   Balance Laws

1. *Balance of mass*
   For the flow described by velocity field $\boldsymbol{v}(\boldsymbol{x}, t)$ and density field $\rho(\boldsymbol{x}, t)$ in the absence of sources/sinks of mass, the mass conservation principle could be written as

$$\frac{\partial \rho}{\partial t} + \operatorname{div}(\rho \boldsymbol{v}) = 0 \quad . \tag{N.1}$$

   This equation (as well as its other variants) is often referred to as the *continuity equation*.

2. *Balance of (linear) momentum*
   The inertial tendency of fluid can be expressed by the well known *Newton's second law*, which follows from the principle of conservation of momentum.

$$\frac{\partial \rho \boldsymbol{v}}{\partial t} + \operatorname{div}(\rho \boldsymbol{v} \otimes \boldsymbol{v}) = \operatorname{div}\mathsf{S} + \rho \boldsymbol{f} \quad . \tag{N.2}$$

   Here the $\boldsymbol{f}(\boldsymbol{x}, t)$ stands for volume forces and S for stress tensor. The constitutive law, relating the stress tensor to other flow variables, depends mainly on the considered fluid and it will be discussed in the Section N.1.2.

N.1.2   Stress Tensor

Using the Stokes law the stress tensor S could be split into normal and viscous (i.e. spherical and deviatoric) parts as $\mathsf{S} = \mathsf{T} - p\mathsf{I}$, where T stands for the viscous stress tensor, while the normal stress contribution is represented by pressure $p(\boldsymbol{x}, t)$ (I being the identity tensor).

There is wide range of constitutive relations available for the definition of the stress tensor in various fluids. One of the most widely used is the one of *Newtonian fluid*:

$$\mathsf{T} = \mu \left(\boldsymbol{\nabla} \boldsymbol{v} + \boldsymbol{\nabla} \boldsymbol{v}^T - \frac{2}{3} \operatorname{div}\boldsymbol{v} \, \mathsf{I} \right) + \eta \operatorname{div}\boldsymbol{v} \, \mathsf{I} \quad , \tag{N.3}$$

In the relation (N.3) μ denotes the dynamic viscosity and η is used for bulk viscosity coefficient. It is good to note at this place that due to the angular momentum conservation and application of frame invariance principle, the stress tensor is symmetric and also depends just on the symmetric part of the velocity gradient. An easy observation also shows, that in the case of incompressible (i.e. divergence-free) flows, the relation (N.3) degenerates into

$$\mathsf{T} = \mu \left(\boldsymbol{\nabla} \boldsymbol{v} + \boldsymbol{\nabla} \boldsymbol{v}^T \right) = 2\mu \mathsf{D} \quad , \tag{N.4}$$

where D denotes the symmetric part of the velocity gradient defined as $\mathsf{D} = (\boldsymbol{\nabla} \boldsymbol{v} + \boldsymbol{\nabla} \boldsymbol{v}^T)/2$.

N.1.3 Non-Homogeneous Incompressible Model

The motion equations describing the flow of incompressible fluid can be written in the following general form: [1]:

$$\frac{\partial \rho}{\partial t} + \operatorname{div}(\rho \boldsymbol{v}) = 0 \tag{N.5}$$

$$\frac{\partial \rho \boldsymbol{v}}{\partial t} + \operatorname{div}(\rho \boldsymbol{v} \otimes \boldsymbol{v}) = \operatorname{div}\mathsf{S} + \rho \boldsymbol{f} \tag{N.6}$$

These equations together with the incompressibility constraint $\operatorname{div}\boldsymbol{v} = 0$ and the constitutive relation for Newtonian incompressible fluid $\mathsf{S} = -p\,\mathsf{I} + 2\mu\mathsf{D}$ and gravity force (acting along the z coordinate axis) expressed as $\boldsymbol{f} = (0, 0, g)$ lead (exactly) to the following set of governing equations for unknowns $\boldsymbol{v}$, p and ρ:

$$\frac{\partial u}{\partial x} + \frac{\partial v}{\partial y} + \frac{\partial w}{\partial z} = 0 \tag{N.7}$$

$$\frac{\partial \rho}{\partial t} + \frac{\partial(\rho u)}{\partial x} + \frac{\partial(\rho v)}{\partial y} + \frac{\partial(\rho w)}{\partial z} = 0 \tag{N.8}$$

$$\frac{\partial(\rho u)}{\partial t} + \frac{\partial(\rho u^2)}{\partial x} + \frac{\partial(\rho uv)}{\partial y} + \frac{\partial(\rho uw)}{\partial z} = -\frac{\partial p}{\partial x} + \mu\Delta u \tag{N.9}$$

$$\frac{\partial(\rho v)}{\partial t} + \frac{\partial(\rho uv)}{\partial x} + \frac{\partial(\rho v^2)}{\partial y} + \frac{\partial(\rho vw)}{\partial z} = -\frac{\partial p}{\partial y} + \mu\Delta v \tag{N.10}$$

$$\frac{\partial(\rho w)}{\partial t} + \frac{\partial(\rho uw)}{\partial x} + \frac{\partial(\rho vw)}{\partial y} + \frac{\partial(\rho w^2)}{\partial z} = -\frac{\partial p}{\partial z} + \mu\Delta w + \rho g \tag{N.11}$$

The conservation of mass is represented by the continuity equation

$$\frac{\partial \rho}{\partial t} + \operatorname{div}(\rho \boldsymbol{v}) = 0 \tag{N.12}$$

Using the product rule of differentiation this could be rewritten as:

$$\frac{\partial \rho}{\partial t} + \boldsymbol{v} \cdot \operatorname{grad}\rho = -\rho \operatorname{div}\boldsymbol{v} . \tag{N.13}$$

For incompressible flows satisfying the divergence-free constraint $\operatorname{div}\boldsymbol{v} = 0$ the right-hand side of equation (N.13) vanishes and thus the continuity equation reduces to:

$$\frac{\partial \rho}{\partial t} + \boldsymbol{v} \cdot \operatorname{grad}\rho = 0 . \tag{N.14}$$

This equation can be used together with the chain rule of differentiation to rewrite the left-hand side of the momentum balance (N.2):

$$\frac{\partial \rho \boldsymbol{v}}{\partial t} + \operatorname{div}(\rho \boldsymbol{v} \otimes \boldsymbol{v}) = \tag{N.15}$$

$$= \boldsymbol{v}\frac{\partial \rho}{\partial t} + \rho\frac{\partial \boldsymbol{v}}{\partial t} + \rho \operatorname{div}(\boldsymbol{v} \otimes \boldsymbol{v}) + \boldsymbol{v}\,(\boldsymbol{v} \cdot \operatorname{grad}\rho) = \tag{N.16}$$

$$= \rho\left(\frac{\partial \boldsymbol{v}}{\partial t} + \operatorname{div}(\boldsymbol{v} \otimes \boldsymbol{v})\right) + \boldsymbol{v}\underbrace{\left(\frac{\partial \rho}{\partial t} + \boldsymbol{v} \cdot \operatorname{grad}\rho\right)}_{=0} \tag{N.17}$$

---

[1]Here we assume that the energy equation is decoupled from the equations of motion and the consequences of this simplification could be neglected. This e.g. means that heat production due to the mechanical energy dissipation is neglected. So is the possible density change related to temperature variations.

Using the above described manipulation, the governing system (N.7)-(N.11) could alternatively be rewritten as:

$$\frac{\partial u}{\partial x} + \frac{\partial v}{\partial y} + \frac{\partial w}{\partial z} = 0 \tag{N.18}$$

$$\frac{\partial \rho}{\partial t} + \frac{\partial(\rho u)}{\partial x} + \frac{\partial(\rho v)}{\partial y} + \frac{\partial(\rho w)}{\partial z} = 0 \tag{N.19}$$

$$\rho\left(\frac{\partial u}{\partial t} + \frac{\partial(u^2)}{\partial x} + \frac{\partial(uv)}{\partial y} + \frac{\partial(uw)}{\partial z}\right) = -\frac{\partial p}{\partial x} + \mu\Delta u \tag{N.20}$$

$$\rho\left(\frac{\partial v}{\partial t} + \frac{\partial(uv)}{\partial x} + \frac{\partial(v^2)}{\partial y} + \frac{\partial(vw)}{\partial z}\right) = -\frac{\partial p}{\partial y} + \mu\Delta v \tag{N.21}$$

$$\rho\left(\frac{\partial w}{\partial t} + \frac{\partial(uw)}{\partial x} + \frac{\partial(vw)}{\partial y} + \frac{\partial(w^2)}{\partial z}\right) = -\frac{\partial p}{\partial z} + \mu\Delta w + \rho g \tag{N.22}$$

Here we have kept the continuity equation in its full original form, however it is also possible to replace the equation (N.19) by the simplified version (N.14).

The governing systems (N.18)-(N.22), resp. (N.7)-(N.11), represent the full incompressible (Newtonian) variable density model[2]. This model is sometimes called the *non-homogeneous (incompressible) Navier-Stokes equations*.

N.1.4   Constant Density Incompressible Model

The constant density assumption further simplifies the above described full model (N.18)-(N.22). It can now be written as:

$$\frac{\partial u}{\partial x} + \frac{\partial v}{\partial y} + \frac{\partial w}{\partial z} = 0 \tag{N.23}$$

$$\frac{\partial u}{\partial t} + \frac{\partial(u^2)}{\partial x} + \frac{\partial(uv)}{\partial y} + \frac{\partial(uw)}{\partial z} = -\frac{\partial P}{\partial x} + \nu\Delta u \tag{N.24}$$

$$\frac{\partial v}{\partial t} + \frac{\partial(uv)}{\partial x} + \frac{\partial(v^2)}{\partial y} + \frac{\partial(vw)}{\partial z} = -\frac{\partial P}{\partial y} + \nu\Delta v \tag{N.25}$$

$$\frac{\partial w}{\partial t} + \frac{\partial(uw)}{\partial x} + \frac{\partial(vw)}{\partial y} + \frac{\partial(w^2)}{\partial z} = -\frac{\partial P}{\partial z} + \nu\Delta w + g \tag{N.26}$$

where the original pressure p is rescaled by density to give $P = p/\rho$ and the *dynamical viscosity* μ is converted to *kinematical viscosity* $\nu = \mu/\rho$. The equation (N.19) resp. (N.14) has disappeared, because it is automatically satisfied when the density ρ does not depends on space and time. The system can be written in compact notation:

$$\operatorname{div}\boldsymbol{v} = 0 \tag{N.27}$$

$$\frac{\partial \boldsymbol{v}}{\partial t} + \operatorname{div}(\boldsymbol{v} \otimes \boldsymbol{v}) = -\boldsymbol{\nabla}P + \nu\boldsymbol{\Delta}\boldsymbol{v} + \boldsymbol{f} \tag{N.28}$$

This system is called (homogeneous, incompressible) *Navier-Stokes equations.* The momentum equations (N.28) are written in so called *conservative* (or divergence) form, which is often recasted to the *non-conservative* (convective) form:

$$\frac{\partial \boldsymbol{v}}{\partial t} + (\boldsymbol{v} \cdot \boldsymbol{\nabla})\boldsymbol{v} = -\boldsymbol{\nabla}P + \nu\boldsymbol{\Delta}\boldsymbol{v} + \boldsymbol{f}. \tag{N.29}$$

---

[2]Only the gravity force was considered as an example of many possible volume forces (e.g. Coriolis).

It is good to remind here that the above system (N.28) assumes Newtonian fluids only, where $\mathbf{T} = 2\mu\mathbf{D}$. For non-Newtonian (as well as for many turbulent) fluids models, the right-hand side of momentum equations should be kept in a more general form:

$$\frac{\partial \boldsymbol{v}}{\partial t} + \mathrm{div}(\boldsymbol{v} \otimes \boldsymbol{v}) = -\boldsymbol{\nabla}P + \mathrm{div}\mathbf{T} + \boldsymbol{f} \qquad \text{(N.30)}$$

allowing for other constitutive relations for the stress tensor $\mathbf{T}$.

Observations & Remarks

For low Mach number flows the transition from full compressible model to the incompressible one has some advantages but also drawbacks. The main advantage is that most of the computational difficulties found in low-Mach flow simulations disappear. Also there are fewer variables (and thus equations) in the classical incompressible model, so the simulations can be more efficient. On the other hand, the drawback of the incompressible model can be that due to the limit passage of Mach number $Ma \longrightarrow 0$ (i.e. the speed of sound $c \longrightarrow \infty$), the character of the original equations has changed. The continuity equation, which was originally a hyperbolic type evolution equation, degenerated into an elliptic type equation, which can be interpreted as kinematic constraint imposed on velocity field. Also pressure has lost its original thermodynamical character and became a kind of Lagrange multiplier to enforce the incompressibility (i.e. the divergence-free constraint).

This change is also the cornerstone of most of the numerical challenges related to numerical solution of incompressible flows. The major issue is how to compute the pressure. Typically, if the momentum equations are used to obtain velocity components, the only equation remaining to compute pressure is the degenerated continuity equation $\mathrm{div}\boldsymbol{v} = 0$, that does not even explicitly contains the pressure. To overcome this pressure-velocity coupling problems, several algorithms have been developed. Here we only shortly mention one of them that has been used in the numerical simulations presented within this work.

N.2 Artificial Compressibility Method

The *artificial compressibility* method was originally developed by A. Chorin in the late sixties (see [N.13]) as a simple and robust alternative to the already known, but in certain situations quite fragile and expensive projection and fractional step methods. This method is also closely related to the well known *Uzawa algorithm* that is widely used in finite-elements based methods [N.17].

The basic idea behind the artificial compressibility is quite simple. It relies on the relaxation of the incompressibility constraint, that is manifested by infinite speed of sound. By the re-introduction of a finite (pseudo-) speed of sound into the continuity equation, an algorithm can be constructed to compute pressure and enforce the divergence-free constraint. The continuity equation is modified by adding the (pseudo-) time-derivative of pressure properly scaled by the artificial speed of sound[3] $\mathfrak{c}$ as follows:

$$\frac{1}{\mathfrak{c}^2}\frac{\partial p}{\partial t} + \mathrm{div}\ \boldsymbol{v} = 0. \qquad \text{(N.31)}$$

---

[3]This artificial speed of sound has to be properly chosen with respect to the stability of the method, it should not however influence the final, fully converged result.

It is easy to see that this non-physical modification of the continuity equation disappears as soon as the solution reaches its steady, divergence-free state. This is why this method is often used together with *time-marching approach* to solve *steady* incompressible flows problems. The main advantage of this method is that it is simple and robust. It does not requires the solution of Poisson type equations as many other methods. On the other hand, this method is mainly suitable for steady flow simulations, while for unsteady flows it has to be further extended by a dual time-stepping technique, to enhance its accuracy in time.

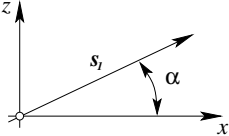## N.3   Semi-Implicit Finite-Difference Scheme

The main reasons behind the choice of this method were simplicity (finite-difference discretization) and robustness (semi-implicit approach). The method was first tested in [N.9] for a simplified boundary layer approximation. It was later extended for the complete incompressible (Reynolds-Averaged) Navier-Stokes equations including the pollution dispersion model. The detailed analysis as well as many numerical results were summarized in the author's PhD thesis [N.1]. Hereafter just the basic concepts of this method are summarized.

The system of governing equations (N.32),(N.33) is written in non-conservative form, taking into account the non-constant *turbulent viscosity K*.
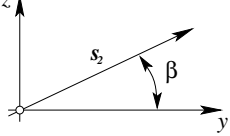
$$u_x + v_y + w_z = 0 \tag{N.32}$$

$$V_t + uV_x + vV_y + wV_z = \underbrace{-\frac{\nabla p}{\rho} + [KV_x]_x + [KV_y]_y + [KV_z]_z}_{=RHS} \tag{N.33}$$

This system (of Reynolds-Averaged Navier-Stokes) equations has been discretized on a non-orthogonal, structured, boundary (i.e. terrain in this case), following mesh. Because of the mesh non-orthogonality it was necessary to transform the equations from the $x - y - z$ coordinates to the mesh-wise directional local coordinate system $s_1 - s_2 - z$:

$$\frac{\partial}{\partial x} = \frac{1}{\cos \alpha}\left(\frac{\partial}{\partial s_1} - \frac{\partial}{\partial z}\sin\alpha\right) \qquad \frac{\partial}{\partial y} = \frac{1}{\cos \beta}\left(\frac{\partial}{\partial s_2} - \frac{\partial}{\partial z}\sin\beta\right) \qquad \delta_s = \frac{1}{2}(\overleftarrow{\delta_s} + \overrightarrow{\delta_s})$$

$$\overleftarrow{\delta_s} = \frac{V_i - V_{i-1}}{\Delta s^-}$$

$$\overrightarrow{\delta_s} = \frac{V_{i+1} - V_i}{\Delta s^+}$$

Figure N.1: Local coordinate transformation

The symbol δ_s denotes the central difference with respect to the direction s. Similarly the $\overrightarrow{\delta_s}, \overleftarrow{\delta_s}$ denote the forward and backward differences.

After the above described transformation the continuity equation (N.32) takes the form:

$$\frac{u_{s_1}}{\cos\alpha} + \frac{v_{s_2}}{\cos\beta} + w_z - u_z\tan\alpha - v_z\tan\beta = 0 \quad , \tag{N.34}$$

while the momentum equations will be transformed to: [4]

$$V_t + \tilde{u}V_{s_1} + \tilde{v}V_{s_2} + \tilde{w}V_z = \widetilde{RHS} \quad . \tag{N.35}$$

The modified coefficients are defined as follows:

$$\tilde{u} = \frac{u}{\cos\alpha} \qquad \tilde{v} = \frac{v}{\cos\beta} \qquad \tilde{w} = w - u\tan\alpha - v\tan\beta$$

The right-hand side is transformed in a similar way. The left-hand side of momentum equations is discretized[5] at time levels n and $n+1$ in the following way:

$$
\begin{aligned}
V_t \quad &\sim \quad \overrightarrow{\delta_t}\mathsf{V}_{i,j,k}^n \\
\tilde{u}V_{s_1} \quad &\sim \quad \frac{1}{2}\left(\tilde{u}_{i+1/2}^n \overrightarrow{\delta_{s_1}}\mathsf{V}_{i,j,k}^n + \tilde{u}_{i-1/2}^n \overleftarrow{\delta_{s_1}}\mathsf{V}_{i,j,k}^{n+1} \right) \\
\tilde{v}V_{s_2} \quad &\sim \quad \frac{1}{2}\left\{ \frac{1}{2}\left(\tilde{v}_{j+1/2}^n \overrightarrow{\delta_{s_2}}\mathsf{V}_{i,j,k} + \tilde{v}_{j-1/2}^n \overleftarrow{\delta_{s_2}}\mathsf{V}_{i,j,k} \right)^n + \right. \\
&\qquad\qquad \left. + \frac{1}{2}\left(\tilde{v}_{j+1/2}^n \overrightarrow{\delta_{s_2}}\mathsf{V}_{i,j,k} + \tilde{v}_{j-1/2}^n \overleftarrow{\delta_{s_2}}\mathsf{V}_{i,j,k} \right)^{n+1} \right\} \\
\tilde{w}V_z \quad &\sim \quad \frac{1}{2}\left\{ \frac{1}{2}\left(\tilde{w}_{k+1/2}^n \overrightarrow{\delta_z}\mathsf{V}_{i,j,k} + \tilde{w}_{k-1/2}^n \overleftarrow{\delta_z}\mathsf{V}_{i,j,k} \right)^n + \right. \\
&\qquad\qquad \left. + \frac{1}{2}\left(\tilde{w}_{k+1/2}^n \overrightarrow{\delta_z}\mathsf{V}_{i,j,k} + \tilde{w}_{k-1/2}^n \overleftarrow{\delta_z}\mathsf{V}_{i,j,k} \right)^{n+1} \right\}
\end{aligned}
$$

The coefficients $\tilde{u}, \tilde{v}, \tilde{w}$ are fixed at the time-level n in order to linearize locally the system to obtain Oseen-like iterative solver. The combination of different asymmetric space discretization at time levels n and $n+1$ allows us to construct finally the numerical scheme that is centered and second order in both space and time. The dissipative terms on right-hand side are approximated in the same manner. Using this discretization, the system of linear algebraic equations in each column of grid-points is obtained:

$$a_1 \mathsf{V}_{i,j+1,k}^{n+1} + a_2 \mathsf{V}_{i,j,k}^{n+1} + a_3 \mathsf{V}_{i,j-1,k}^{n+1} + a_4 \mathsf{V}_{i,j,k+1}^{n+1} + a_5 \mathsf{V}_{i,j,k-1}^{n+1} = \overline{RHS} \tag{N.36}$$

This system is solved iteratively in vertical plane $i = const$. So the five-diagonal system is converted into the three-diagonal.

$$a_5 \mathsf{V}_{i,j,k-1}^{\eta+1} + a_2 \mathsf{V}_{i,j,k}^{\eta+1} + a_4 \mathsf{V}_{i,j,k+1}^{\eta+1} = \overline{RHS} - a_1 \mathsf{V}_{i,j+1,k}^{\eta} - a_3 \mathsf{V}_{i,j-1,k}^{\eta+1} \tag{N.37}$$

The η denotes here the iterative index. Usually after $3-5$ iterations the values of $\mathsf{V} = (u,v,w)^T$ are known with sufficient accuracy. Exactly the same solution scheme can also be used for the scalar transport equations

> *This method has been used in the papers shown in the Sections E.1–E.2 as well as in many other publications, solving the atmospheric boundary layer flows problems. These are listed in the author's full bibliography in the Appendix A, page 205.*

---

[4]The $\widetilde{RHS}$ and $\overline{RHS}$ are the modified right-hand sides
[5]in the Crank-Nicolson style

N.4 Explicit Finite-Volume Scheme

This scheme was chosen because it ensures conservativity and robustness even on highly distorted grids. The choice of simple central fluxes was mainly driven by the requirement of low numerical diffusion of the method and easy predictability of results.

The whole formulation is based on the principle of semi-discretization, where the time- and space- discretizations are separated. In this section only the finite-volume spatial discretization step is briefly summarized. For suitable time-discretizations (that have been used alongside with this method) see the Section N.6.

The governing system of equations is a conservative formulation of Navier-Stokes equations[6] (N.27)–(N.28) written here in a vector form.

$$\tilde{R}\mathsf{W}_t + \mathsf{F}_x + \mathsf{G}_y + \mathsf{H}_z = \mathsf{R}_x + \mathsf{S}_y + \mathsf{T}_z + \mathsf{f}_\mathsf{w} \tag{N.38}$$

Where $\mathsf{W} = col(p, u, v, w)$ is the vector of unknowns, inviscid flux vectors are defined as $\mathsf{F} = col(u, u^2 + p, uv, uw)$, $\mathsf{G} = col(v, uv, v^2 + p, vw)$, $col\mathsf{H} = (w, uw, vw, w^2 + p)$. The viscous fluxes $\mathsf{R} = col(0, Ku_x, Kv_x, Kw_x)$, $\mathsf{S} = col(0, Ku_y, Kv_y, Kw_y)$, $\mathsf{T} = col(0, Ku_z, Kv_z, Kw_z)$. The vector of volume forces is denoted by f_w. The symbol $\tilde{R} = diag(0, 1, 1, 1)$ denotes a diagonal matrix that is in our model modified for the use of artificial compressibility by replacing R by $\tilde{R} = diag(1/\mathfrak{c}^2, 1, 1, 1)$. In this case $\mathfrak{c}$ is the pseudo speed of sound[7]

Using this notation, the spatial finite-volume semi-discretization in the cell D can be written in the following form:

$$\frac{\partial \mathsf{W}}{\partial t} = \frac{-1}{|D|} \oint_{\partial D} \Big[(\mathsf{F} - \mathsf{R}), (\mathsf{G} - \mathsf{S}), (\mathsf{H} - \mathsf{T}) \Big] \cdot \hat{\boldsymbol{\nu}} \, dS \;\; + \frac{1}{|D|} \int_D \mathsf{f}_\mathsf{w} \tag{N.39}$$

Here D denotes the computational cell, $\hat{\boldsymbol{\nu}}$ is the outer unit normal vector of the cell boundary, dS is the surface element of this boundary. Equation (N.39) can be rewritten in operator form:

$$\frac{\partial \mathsf{W}}{\partial t} = -\mathcal{L}(\mathsf{W}) \tag{N.40}$$

Here $\mathcal{L}$ stands for the finite-volume discretization operator. This operator is still exact at this stage and it must be properly discretized to allow for numerical solution. For clarity we write here the space discretization operator definition:

$$\mathcal{L}\mathsf{W} = \frac{1}{|D|} \left\{ \underbrace{\oint_{\partial D} [\mathsf{F}, \mathsf{G}, \mathsf{H}] \cdot \hat{\boldsymbol{\nu}} \, dS}_{\text{inviscid flux}} - \underbrace{\oint_{\partial D} [\mathsf{R}, \mathsf{S}, \mathsf{T}] \cdot \hat{\boldsymbol{\nu}} \, dS}_{\text{viscous flux}} + \underbrace{\int_D \tilde{\mathsf{f}}_\mathsf{w} \, dV}_{\text{external force}} \right\} \tag{N.41}$$

The computational mesh is structured, consisting of hexahedral primary control volumes. To evaluate the viscous fluxes also dual finite volumes are needed. These have octahedral shape and are centered around the corresponding primary cell faces. See the figure N.2 for the schematic view of such configuration.

---

[6] possibly with some generalizations for turbulent and non-Newtonian flows

[7] In the following text we use for simplicity $\mathfrak{c} = 1$ and therefore the matrices R and $\tilde{R}$ no more appear in expressions.
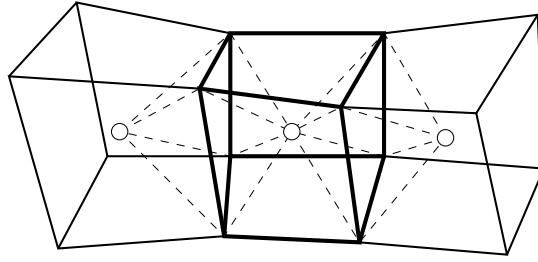
Figure N.2: Finite-volume grid in 3D

The inviscid flux integral can be approximated using centered cell fluxes, e.g. the value of the flux F on the cell face with index $\ell = 1$ is computed as the average of cell-centered values from both sides of this face:

$$\mathsf{F}_1^n = \frac{1}{2}[\mathsf{F}(\mathsf{W}_{i,j,k}^n) + \mathsf{F}(\mathsf{W}_{i+1,j,k}^n)] \tag{N.42}$$

The contribution of inviscid fluxes is finally summed up over the cell faces $\ell = 1, \ldots, 6$. In this way we can write the inviscid flux approximation:

$$\oint_{\partial D} \mathsf{F}\nu^x \, dy \, dz \approx \sum_{\ell=1}^{6} \mathsf{F}_\ell \nu_\ell^x S_\ell \tag{N.43}$$

The discretization of viscous fluxes is a little bit more complicated since the vectors $\mathsf{R}, \mathsf{S}, \mathsf{T}$ were defined using the derivatives of velocity components and these derivatives need to be approximated at cell faces. This can be done using the dual finite-volume grid that is centered around the corresponding faces (see Figure N.2).

The evaluation of the velocity gradient components is then replaced by the evaluation of the surface integral over the dual volume boundary. Finally, this surface integral is approximated by a discrete sum over the dual cell faces (with indices $m = 1, \ldots, 8$). For example trying to evaluate the first component of the viscous flux R_1 (i.e. approximate u_x) at the cell face $l = 1$ we must proceed in the following way:

$$u_x \approx \oint_{\partial \tilde{D}} u \, \nu^x \, dy \, dz \approx \sum_{m=1}^{8} u_m \nu_m^x S_m \tag{N.44}$$

The outer normal of the dual cell faces should be properly approximated $\nu^x \approx \nu_m^x$. The values of velocity components in the middle nodes of these faces are taken as an average of the values in the corresponding vertices.

The problem is now in the semi-discrete form:

$$\frac{d\mathsf{W}_{ijk}}{dt} = -\tilde{\mathcal{L}}\,\mathsf{W}_{i,j,k} \tag{N.45}$$

This system of ordinary differential equations, for time-evolution of cell averaged quantities, can be solved e.g. by some of the Runge-Kutta multistage methods shown in the Section N.6.

This method has been used e.g. in the papers solving the free-surface [N.10] or turbulent variable density flows in [N.7, N.5]. Blood flow and coagulation problems were solved using this method e.g. in [N.11], [N.12] or in the chapter [N.4] in [N.8]. Some of the biomedical applications of this method are shown in the Sections B.1–B.4. Further examples of the use of this method can be found in some works listed in the author's full bibliography in the Appendix A, page 205.

N.5　Compact Finite-Difference Scheme

This type of discretization[8] was chosen because it offers high resolution while retaining well defined dispersion/diffusion characteristics. This is quite rare among the modern high resolution methods that often employ complicated non-linear reconstruction and stabilization techniques. The family of compact (in the sense of narrow computational stencil) schemes in its current form was introduced in [N.24] and is successfully used e.g. in computational aeroacoustics (see e.g. [N.16], [N.30]). Its superior resolution and low numerical diffusion/dispersion makes it suitable for capturing various wave phenomena, including those in stratified flows (as it is shown in the Section E.3).

　　The basic concept of the compact finite-difference schemes naturally extends and generalizes the construction of the classical (sometimes called explicit) finite difference approximations. In the classical approach the central approximation of first derivative $\phi'(x)$ of a (sufficiently smooth) function $\phi(x)$ can be obtained as a (symmetric) linear combination of neighboring grid values ϕ_i (resp. their divided differences).

$$\phi'_i \approx \alpha_1 \frac{\phi_{i+1} - \phi_{i-1}}{2h} + \alpha_2 \frac{\phi_{i+2} - \phi_{i-2}}{4h} + \ldots + \alpha_\ell \frac{\phi_{i+\ell} - \phi_{i-\ell}}{2\ell h} \tag{N.46}$$

The coefficients α_m; $m = 0, \ldots, \ell$ are obtained by matching the above expression to Taylor expansion of $\phi(x_i \pm mh)$. So the classical central finite-difference approximations take the following form.

$$\phi'_i \approx \sum_{m=1}^{m=\ell} \alpha_m \frac{\phi_{i+m} - \phi_{i-m}}{2mh} \tag{N.47}$$

In vector (matrix) form the process of obtaining approximation of derivatives could be written as follows:

$$\mathsf{I}\,\vec{\phi}' = \mathbf{D}_\alpha \vec{\phi} \tag{N.48}$$

Here I is the identity matrix and $\mathbf{D}_\alpha$ is the anti-symmetric $(2\ell + 1)$-diagonal matrix of coefficients α_m. The identity matrix on the left-hand side means that to obtain the approximation of derivatives we don't have to solve any linear system, and the derivatives are obtained by explicit calculation. In general, the classical finite-difference approximation of the order p requires a computational stencil of the width ph which contains $p + 1$ grid points.

　　The compact approximations can reduce the computational stencil (needed for given order of accuracy) and in some cases also improve the resolution of the method. The main idea of compact finite differencing is quite simple. Instead of looking for an (explicit) formula approximating the value of ϕ'_i, we will rather approximate a (symmetric) linear combination of neighboring derivatives $(\ldots, \phi'_{i-1}, \phi'_i, \phi'_{i+1}, \ldots)$.

$$a_q \phi'_{i-q} + \ldots + a_2 \phi'_{i-2} + a_1 \phi'_{i-1} + \phi'_i + a_1 \phi'_{i+1} + a_2 \phi'_{i+2} + \ldots + a_q \phi'_{i+q} \approx \tag{N.49}$$

$$\approx \alpha_1 \frac{\phi_{i+1} - \phi_{i-1}}{2h} + \alpha_2 \frac{\phi_{i+2} - \phi_{i-2}}{4h} + \ldots + \alpha_\ell \frac{\phi_{i+\ell} - \phi_{i-\ell}}{2\ell h} \tag{N.50}$$

The approximation (N.49) could be understood as an implicit relation between the function values ϕ_i and the approximate derivatives ϕ'_i. This approach generalizes the classical finite-differencing, which now becomes just a special case of the compact approach.

---

[8]The principle of semi-discretization is used to first discretize the governing equations in space and then to solve the resulting system of ODE's. This section only contains the information about the space-discretization step. For time-integration methods see Section N.6.

Using the compact differencing, the approximation formula becomes more complicated.

$$\phi_i' + \sum_{n=1}^{n=q} a_n(\phi_{i-n}' + \phi_{i+n}') \approx \sum_{m=1}^{m=\ell} \alpha_m \frac{\phi_{i+m} - \phi_{i-m}}{2mh} \tag{N.51}$$

In vector (matrix) form the process of obtaining approximation of derivatives could be written as follows:

$$\mathbf{D}_a \vec{\phi}' = \mathbf{D}_\alpha \vec{\phi} \tag{N.52}$$

This contrasts with the classical differencing where an explicit formula $\mathbf{I}\,\vec{\phi}' = \mathbf{D}_\alpha \vec{\phi}$ is obtained. The matrix $\mathbf{D}_a$ on the left-hand side is the symmetric $(2q + 1)$-diagonal matrix of coefficients a_n. Similarly the $\mathbf{D}_\alpha$ is the anti-symmetric $(2\ell + 1)$-diagonal matrix of coefficients α_m. In the non-trivial case of $q > 0$ the matrix $\mathbf{D}_a$ can not be easily inverted. Thus in order to obtain the approximate derivatives $\vec{\phi}'$ we have to solve a system of linear algebraic equations (with $(2q + 1)$-diagonal matrix).

Now let's concentrate on compact schemes with at maximum penta-diagonal system of equations and seven-point discretization stencil. These could be written in the form

$$a_2\phi_{i-2}' + a_1\phi_{i-1}' + \phi_i' + a_1\phi_{i+1}' + a_2\phi_{i+2}' = \alpha_1 \frac{\phi_{i+1} - \phi_{i-1}}{2h} + \alpha_2 \frac{\phi_{i+2} - \phi_{i-2}}{4h} + \alpha_3 \frac{\phi_{i+3} - \phi_{i-3}}{6h} \tag{N.53}$$

To get the approximation formula of desired order, it is necessary to match the general formula with Taylor series expansions. The first non-matching coefficient determines the leading order of the truncation error. The following conditions on the coefficients should be satisfied to attain the required order of accuracy.

Second order	$\alpha_1 + \alpha_2 + \alpha_3 = 1 + 2a_1 + 2a_2$
Fourth order	$\alpha_1 + 2^2\alpha_2 + 3^2\alpha_3 = 2\frac{3!}{2!}\left(a_1 + 2^2 a_2\right)$
Sixth order	$\alpha_1 + 2^4\alpha_2 + 3^4\alpha_3 = 2\frac{5!}{4!}\left(a_1 + 2^4 a_2\right)$
Eighth order	$\alpha_1 + 2^6\alpha_2 + 3^6\alpha_3 = 2\frac{7!}{6!}\left(a_1 + 2^6 a_2\right)$
Tenth order	$\alpha_1 + 2^8\alpha_2 + 3^8\alpha_3 = 2\frac{9!}{8!}\left(a_1 + 2^8 a_2\right)$

Table N.1: Order conditions for the compact approximations

It is obvious that for the approximations of the order lower than ten, there are more unknown parameters than equations from the which these parameters can be computed. This means that the coefficients for the lower order schemes are not unique. This offers a possibility to choose a-priori some of the coefficients (usually to make the solution easier). For example we may get schemes with tri-diagonal matrix (for $a_2 = 0$) and also classical (explicit) difference schemes if both $a_2 = 0$ and $a_1 = 0$. In the same way the discretization stencil width can be reduced by choosing e.g. $\alpha_3 = 0$. This is shown in the table N.2, where the coefficients of the compact finite difference schemes with tridiagonal matrix, having up to seven point stencil, are summarized.

Scheme	a_1	a_2	α_1	α_2	α_3	Diagonals	Points	Order
A	a	0	$\frac{2}{3}(a+2)$	$\frac{1}{3}(4a-1)$	0	3	5	4
B	$a=\frac{1}{3}$	0	$\frac{14}{9}$	$\frac{1}{9}$	0	3	5	6
C	$a=\frac{1}{4}$	0	$\frac{3}{2}$	0	0	3	3	4
D	a	0	$\frac{2}{3}(a+2)$	$\frac{1}{3}(4a-1)$	b	3	7	4
E	a	0	$\frac{1}{6}(a+9)$	$\frac{1}{15}(32a-9)$	$\frac{1}{10}(-3a+1)$	3	7	6
F	$a=\frac{3}{8}$	0	$\frac{25}{16}$	$\frac{1}{5}$	$-\frac{1}{80}$	3	7	8

Table N.2: Parameters for tri-diagonal schemes

The scheme denoted by *A* in the table N.2 was constructed using the constraint for the tri-diagonality of the resulting system of equation and therefore the coefficient a_2 was set to zero. Moreover the requirement of reduced computational stencil (up to five points) leads to the setting $\alpha_3 = 0$. Without further constraints, this setup leads to one-parametric family of schemes of the type *A*. Various specific choices of the free parameter a may further lead to either increase of the order of accuracy of the scheme (as for $a = 1/3$ leading to, highest in this class, 6th order of accuracy).

> *This method has been used in the papers shown in the Section E.3-E.4 and in publications [N.3] and [N.6] solving stratified environmental flows. Some more publications where this scheme was used are listed in the author's full bibliography in the Appendix A, page 205.*

N.6   Runge-Kutta Time-Integration Methods

As it was already mentioned in the previous sections, the concept of semi-discretization of evolutionary PDE's, allows to transform problems involving both space- and time- derivatives into problems containing only the derivatives with respect to time. A typical example of such approach could be the discretization of hyperbolic conservation laws. Written in one space dimension, the conservation of scalar quantity w can be expressed in differential form as[9]:

$$w_t + f(w)_x = 0 . \tag{N.54}$$

Assuming now that the equation (N.54) was discretized in space, e.g. using one of the suitable FV or FD discretizations (e.g those described in Section N.4 and N.5), it is transformed into the system of ODE's of the form:

$$\mathsf{W}_t = \widetilde{\mathcal{L}}(t, \mathsf{W}(t)) , \tag{N.55}$$

where $\mathsf{W} = \mathsf{W}(t)$ is the vector of discretized variable, i.e. $[\mathsf{W}(t)]_i = \mathsf{W}_i(t) = w(x_i, t)$, and $\widetilde{\mathcal{L}}$ is a discrete version of the differentiation in space operator $\mathcal{L} = -f(w(t, x_i))_x$.

The system (N.55) describes the evolution in time of the discrete grid values of unknown function w. In order to solve the initial value problem based on this system of ODE's, virtually any of the methods originally developed for ODE's could be used.

---

[9]The subscripts are used to denote partial derivatives.

N.6.1 Classical Runge-Kutta (RK) Methods

A general Runge-Kutta method for the solution of the system (N.55) can be written in the following form:[10]

$$
\mathsf{W}^{(r)} \;=\; \mathsf{W}^n + \Delta t \sum_{p=1}^{s} a_{rp} \widetilde{\mathcal{L}}(t_n + c_p \Delta t, \mathsf{W}^{(p)}) \qquad r = 1, \ldots, s \tag{N.56}
$$

$$
\mathsf{W}^{n+1} \;=\; \mathsf{W}^n + \Delta t \sum_{r=1}^{s} b_r \widetilde{\mathcal{L}}(t_n + c_r \Delta t, \mathsf{W}^{(r)})
$$

Here the coefficients c_p indicate the positions, within the step, of the stage values, the coefficient a_{rp} (forming an $s \times s$ matrix $\boldsymbol{A}$) are showing the dependence of the stages on the derivatives found at other stages, and the values b_r represent the weights of the stage derivatives in the final step quadrature. It is a common practice to represent a Runge-Kutta method of the form (N.56) by a partitioned tableau of its coefficients (sometimes called *Butcher-array* or table):

$$
\begin{array}{c|c}
\boldsymbol{c} & \boldsymbol{A} \\
\hline
 & \boldsymbol{b}^T
\end{array}
\;=\;
\begin{array}{c|ccc}
c_1 & a_{11} & \cdots & a_{1s} \\
\vdots & \vdots & & \vdots \\
c_s & a_{s1} & \cdots & a_{ss} \\
\hline
 & b_1 & \cdots & b_s
\end{array}
\tag{N.57}
$$

In this work we only focus on some of the explicit methods suitable for time-integration of semi-discretized evolutionary PDE's. Within the class of explicit RK methods, there are some them, that are widely considered as "classical". Let's mention few of them for illustration. First of all, it's good to mention that the *Euler* method

$$
\mathsf{W}^{n+1} = \mathsf{W}^n + \Delta t \widetilde{\mathcal{L}}(t_n, \mathsf{W}^n) , \tag{N.58}
$$

could be written in the form (N.56), resp. (N.57)[11]:

$$
\begin{aligned}
\mathsf{W}^{(1)} &= \mathsf{W}^n \\
\mathsf{W}^{n+1} &= \mathsf{W}^n + \Delta t \widetilde{\mathcal{L}}(t_n, \mathsf{W}^{(1)})
\end{aligned}
\qquad \text{resp.} \qquad
\begin{array}{c|c}
0 & 0 \\
\hline
 & 1
\end{array}
$$

Higher order RK methods can be constructed and used. The Butcher arrays for two of the classical methods of third and fourth order are

$$
\begin{array}{c|ccc}
0 & & & \\
\frac{1}{3} & \frac{1}{3} & & \\
\frac{2}{3} & 0 & \frac{2}{3} & \\
\hline
 & \frac{1}{4} & 0 & \frac{3}{4}
\end{array}
\tag{N.59}
$$

$$
\begin{array}{c|cccc}
0 & & & & \\
\frac{1}{2} & \frac{1}{2} & & & \\
\frac{1}{2} & 0 & \frac{1}{2} & & \\
1 & 0 & 0 & 1 & \\
\hline
 & \frac{1}{6} & \frac{1}{3} & \frac{1}{3} & \frac{1}{6}
\end{array}
\tag{N.60}
$$

The above third-order method (N.59) is usually called the *Heun's* method, while the fourth order method (N.60) is referred to as *the* method of *Runge-Kutta*.

The above methods have been constructed to attain the maximal possible order of accuracy (for given number of stages). In some cases however it is more useful to relax the accuracy order constraints to gain some other desirable properties. Some of the most relevant (for the papers presented in this work) cases are discussed in following sections.

---

[10] See e.g. [N.21]

[11] The zero elements on diagonal of $\boldsymbol{A}$ and above are dropped for simplicity.

N.6.2   Low-Storage RK Methods

Taking a closer look at the above classical examples of Runge-Kutta methods we may observe that the amount of memory needed to calculate the value of W^{n+1} differs significantly for these methods. For example in the fourth order, four stage method (N.60), it is necessary to remember all the values of $\widetilde{\mathcal{L}}(t_n + c_r \Delta t, W^{(r)})$ for $r = 1, \ldots, 4$. This is because the weight coefficients b_r appearing in the integration formula (N.56) are all non-zero.

Such behavior might be acceptable for the solution of single ODE's or even for small systems of ODE's. However in the case of solution of very large systems of ODE's, appearing as a result of the semidiscretization of multidimensional PDE's, the memory consumption of time-integration method may become a serious issue.

For low-storage algorithms we will require that the stage values of $\widetilde{\mathcal{L}}$ are always only used once, only at the next stage evaluation, and then could be forgotten/replaced. Such behavior is quite desirable especially for RK methods with higher number of stages. The Butcher tableau for such method has a form:

$$
\begin{array}{c|ccccc}
0 & & & & & \\
c_2 & a_{21} & & & & \\
\vdots & 0 & \ddots & & & \\
c_r & 0 & \cdots & a_{r,r-1} & & \\
\vdots & 0 & \cdots & & \ddots & \\
c_s & 0 & \cdots & 0 & a_{s,s-1} & \\
\hline
 & 0 & \cdots & 0 & 0 & b_s
\end{array}
\tag{N.61}
$$

This already simple form of the Butcher array could further be reduced using the natural consistency requirements valid for all of the above RK methods, namely the $\sum_{p=1}^{s} a_{rp} = c_r$ and $\sum_{r=1}^{s} b_r = 1$. The class of explicit s-stage low-storage RK methods introduced here could be written in the simplified form:

$$
\begin{aligned}
W^{(0)} &= W^n \\
W^{(r)} &= W^{(0)} + \alpha_{(r)} \Delta t \widetilde{\mathcal{L}}(W^{(r-1)}) \qquad r = 1, \ldots, s \\
W^{n+1} &= W^{(s)}
\end{aligned}
\tag{N.62}
$$

It is clear that such a method is fully determined by the choice of the coefficients $\alpha_{(r)}$. The methods we have used in our simulations were three- resp. four-stage variants with coefficients $\alpha_{(1)} = 1/2$, $\alpha_{(2)} = 1/2$, $\alpha_{(3)} = 1$ resp. $\alpha_{(1)} = 1/4$, $\alpha_{(2)} = 1/3$, $\alpha_{(3)} = 1/2$, $\alpha_{(3)} = 1$. The order of accuracy m of these methods is slightly lower than the number of stages s, i.e. $m = s - 1$, which is compensated by larger stability region of these RK methods. When, for example, these methods are applied to advection equation, the maximum allowable CFL number is equal to 2, resp. to $2\sqrt{2}$ for the above three- resp. four-stage schemes.

This method has been used together with the above described finite-volume space discretization e.g. in the paper [N.10] and in other publications, solving the free-surface and internal turbulent flows problems. These publications are listed in the author's full bibliography in the Appendix A, page 205.

N.6.3 Advection-Diffusion Optimized RK Methods

From the definition of the multistage Runge-Kutta methods is obvious, that these methods require multiple evaluations of the operator $\widetilde{\mathcal{L}}$ within a single time-step. In the case discussed here, $\widetilde{\mathcal{L}}$ is a space discretization operator which is based on the original PDE's and the selected discretization method. The construction of this operator is often quite complicated and its evaluation might be computationally expensive. Thus the amount of computational work increases rapidly with the number of stages of the applied RK method. This disadvantage is usually compensated by the higher accuracy or higher stability of multistage methods.

In specific cases however, it is possible to reduce the amount of necessary computational work per RK stage and improve the stability of the method at the same time. The approach presented here (following the original references [N.23],[N.22]) is designed for the numerical solution of advection-diffusion equations. The main idea behind this specific modification of RK methods is that the discrete advection-diffusion operator $\widetilde{\mathcal{L}}$ could be split into the advection and the diffusion part, and instead of evaluating the full operator $\widetilde{\mathcal{L}}(W^{(r)})$ at each stage of RK method, only a part of $\widetilde{\mathcal{L}}$ is updated at each stage (e.g. the advection part for advection dominated problems), while the value of the remaining (diffusion) part of $\widetilde{\mathcal{L}}$ is kept frozen from previous RK stage.

$$
\begin{aligned}
W^{(0)} &= W^n \\
W^{(r+1)} &= W^{(0)} - \alpha_{(r)}\Delta t\left(\mathcal{Q}^{(r-1)} + \mathcal{D}^{(r-1)}\right) \qquad r = 1,\ldots,s
\end{aligned}
\tag{N.63}
$$

$$
W^{n+1} = W^{(s)}
\tag{N.64}
$$

Here the space discretization operator at stage (r) is split as follows:

$$
\widetilde{\mathcal{L}}W^{(r)} = \mathcal{Q}^{(r)} + \mathcal{D}^{(r)} \, .
\tag{N.65}
$$

The inviscid (advection) flux $\mathcal{Q}$ is evaluated in usual way at each stage

$$
\mathcal{Q}^{(r)} = \mathcal{Q}W^{(r)} \, .
\tag{N.66}
$$

The viscous (diffusive) flux $\mathcal{D}$ uses a blended value of from the previous stage and the actual stage according to the following rule:

$$
\mathcal{D}^{(r)} = \beta_{(r)}\mathcal{D}W^{(r)} + (1 - \beta_{(r)})\mathcal{D}^{(r-1)} \qquad \text{with} \qquad \mathcal{D}^{(0)} = \mathcal{D}W^n
\tag{N.67}
$$

The coefficients $\alpha_{(r)}$ and $\beta_{(r)}$ are chosen to guarantee large enough stability region for the Runge-Kutta method. The following set of coefficients was used for this study:

$$
\begin{aligned}
\alpha_{(1)} &= 1/3 & \beta_{(1)} &= 1 \\
\alpha_{(2)} &= 4/15 & \beta_{(2)} &= 1/2 \\
\alpha_{(3)} &= 5/9 & \beta_{(3)} &= 0 \\
\alpha_{(4)} &= 1 & \beta_{(4)} &= 0
\end{aligned}
$$

It is easy to see that for this four-stage method only two evaluations of dissipative terms are needed which saves significant amount of calculations while retaining the advantage of large stability region of the method. Further admissible sets of coefficients together with comment on the increase of the efficiency and robustness could be found in the original papers [N.23] and [N.22] and the references therein.

This method has been used together with the above described finite-volume space discretization e.g. in the papers [N.7, N.5] dealing with variable density turbulent flows or in biomedical applications shown in Sections B.1-B.4. Remaining publications employing this method are listed in the author's full bibliography in the Appendix A, page 205.

N.6.4 Strong Stability Preserving (SSP) RK Methods

The need of specific non-oscillatory time-discretizations arose for the first time in the late 80's, when the high resolution spatial discretizations were introduced. These new Total Variation Diminishing (TVD) and Essentially Non-Oscillatory (ENO) schemes, among others, have been used in conjunction with various time-discretizations to solve evolutionary PDE's. It has been found quite soon, that even in the case that a non-oscillatory space-discretization was used, the numerical solution might still be spoiled by non-physical oscillations. These spurious artifacts were introduced at the time-integration step by an inappropriate choice of time-discretization.

The early stages of the research in this field could be tracked down to the works [N.25] and [N.26], where the idea of high order TVD time-discretizations has been developed for the class of multistep schemes. About ten years later, similar approach was applied in the framework of multistage Runge-Kutta schemes in [N.19], where the class of TVD Runge-Kutta schemes has been developed and analyzed in detail. A little bit later, in [N.20], the theoretical background of the Total Variation Diminishing (TVD) Runge-Kutta methods has been revised and generalized to cover a new, broader class of so called Strong Stability Preserving (SSP) Runge-Kutta schemes. Since then, the SSP RK methods have been further developed and optimized e.g. in [N.28] and [N.18].

The strong stability concept is based on the following definition (see e.g. [N.28]):

Definition N.1 *The sequence* $\{W^n\}$ *is called strongly stable in a certain norm* $\| \cdot \|$, *iff in the same norm* $\|W^{n+1}\| \leq \|W^n\|$ *holds for all* $n \geq 0$.

Assuming that sequence $\{W^n\}$ generated by the (forward) Euler method (N.58) is strongly stable, for given PDE and applied space discretization, the time-integration method itself is called strongly stable. Problem is that the classical Euler method is only first order accurate. Higher order methods, having the strong stability preserving property, could e.g. be constructed as Runge-Kutta multistage methods.

The family of explicit SSP Runge-Kutta schemes is usually written in the form introduced in [N.26][12] :

$$
\begin{aligned}
W^{(0)} &= W^n \\
W^{(r)} &= \sum_{p=0}^{r-1} \left(\alpha_{rp} W^{(p)} + \beta_{rp} \Delta t \widetilde{\mathcal{L}}(W^{(p)}) \right) \qquad r = 1, \ldots, s \\
W^{n+1} &= W^{(s)}
\end{aligned}
\tag{N.68}
$$

It is not difficult to see that in the case the coefficients β_{rp} are positive, the method (N.68) is nothing but a convex combination of Euler stages with fractional time-steps of the length $\frac{\beta_{rp}}{\alpha_{rp}} \Delta t$. Here we just shortly present some of the optimal, in the sense of accuracy versus stability, SSP

---

[12]It is possible to show, that the above SSP-RK methods could be rewritten from the Shu-Osher form (N.68) to the more conventional Butcher form (N.56), resp. (N.57). The coefficients of some of these methods given in both, Shu-Osher and Butcher formalism, are presented e.g. in [N.28].

RK methods originally studied in [N.28]. The coefficients of second order SSP-RK methods are shown in the table N.3, wherethe SSP(s,o) denotes the Runge-Kutta method which consists of s stages and has order of accuracy o.

Method	α_{rp}				β_{rp}				CFL
SSP(2,2)	1				1				1
	$\frac{1}{2}$	$\frac{1}{2}$			0	$\frac{1}{2}$			
SSP(3,2)	1				$\frac{1}{2}$				2
	0	1			0	$\frac{1}{2}$			
	$\frac{1}{3}$	0	$\frac{2}{3}$		0	0	$\frac{1}{3}$		
SSP(4,2)	1				$\frac{1}{3}$				3
	0	1			0	$\frac{1}{3}$			
	0	0	1		0	0	$\frac{1}{3}$		
	$\frac{1}{4}$	0	0	$\frac{3}{4}$	0	0	0	$\frac{1}{4}$	

Table N.3: Second order SSP-RK methods

This method has been used together with the compact FD discretization in the papers shown in the Sections E.3-E.4 and in publications [N.3] and [N.6] solving stratified environmental flows. Some more publications where this scheme was used are listed in the author's full bibliography in the Appendix A, page 205.

N.7 Numerical Stabilization Techniques

All the schemes presented in this work are based on central space-discretization. This means they have low numerical diffusion which causes their oscillatory behavior in presence of high solution gradients. Throughout this work this approach was chosen to be able to split the numerical discretization and its stabilization into separate steps which offers more flexibility in constructing problem-specific numerical methods. The following sections review the methods that have been used to stabilize the numerical solution and make it free of non-physical oscillations.

N.7.1 Artificial Viscosity

Numerical discretizations in general contain some amount of imbedded numerical diffusion and/or dispersion. This is due to the corresponding character of the leading order terms of the discretization error. This can be shown by analyzing the modified equations of these numerical methods[13]. The numerical methods that are based on discretizations with low numerical diffusivity (as the central schemes used in this work) tend to be highly oscillatory and unstable. One of the oldest and simplest ways, how to stabilize these numerical methods is the addition of *artificial viscosity* terms. These terms are added explicitly and are emulating the effects of

---

[13]See e.g. the PhD thesis [N.1].

physical diffusivity by enhancing the insufficient numerical diffusivity of the scheme. In order to retain the resolution properties of the original method, the numerical viscosity terms should be kept as small as possible just to damp the non-physical oscillations and to diminish with the grid refinement.

As an example of such artificial viscosity the following artificial dissipation of second and fourth order is shown.

$$
\begin{aligned}
\mathrm{D V}_i^n &= \mathrm{D}^2 \mathrm{V}_i^n + \mathrm{D}^4 \mathrm{V}_i^n \\
\mathrm{D}^2 \mathrm{V}_i^n &= \tilde{\epsilon}_2 \Delta x^3 \frac{\partial}{\partial x} |\mathrm{V}_x| \mathrm{V}_x = \tilde{\epsilon}_2 \Delta x^2 (\epsilon_{i+1/2} \mathrm{V}_x - \epsilon_{i-1/2} \mathrm{V}_x) \\
\epsilon_{i+1/2} &= \begin{cases} |\mathrm{V}_{i+1} - \mathrm{V}_i| & \text{for } |\mathrm{V}_{i+1} - \mathrm{V}_i| < \frac{K}{10} \\ \frac{K}{10} & \text{for } |\mathrm{V}_{i+1} - \mathrm{V}_k| \geq \frac{K}{10} \end{cases} \\
\mathrm{D}^4 \mathrm{V}_i^n &= \tilde{\epsilon}_4 \Delta x^4 \mathrm{V}_{xxxx} = \tilde{\epsilon}_4 \left(\mathrm{V}_{i-2}^n - 4\mathrm{V}_{i-1}^n + 6\mathrm{V}_i^n - 4\mathrm{V}_{i+1}^n + \mathrm{V}_{i+2}^n \right)
\end{aligned}
$$

The $K = \nu + \nu_t$ is coefficient of turbulent diffusion. The coefficients $\tilde{\epsilon}_2, \tilde{\epsilon}_4 \in \mathbb{R}$ are constants of order Δx^2 respectively Δx^4.

The fourth order viscosity was used to smooth the highest (spatial) frequency oscillations, while the second order is applied close to high solution gradients. It is good to note that the second order viscosity coefficients increase with the solution gradient, but are bounded from above by the physical (in this case turbulent) diffusivity. This helps to reduce the unwanted effects of these artificial terms which may spoil the solution of the original problem.

> *This method has been used mainly together with the semi-implicit finite-difference scheme in the papers shown in the Sections E.1–E.2 as well as in many other publications, solving the atmospheric boundary layer flows problems. These are listed in the author's full bibliography in the Appendix A, page 205.*

N.7.2 Pressure Stabilization

Even if the artificial viscosity concept works well most of the time, in some cases however it may affect the velocity field too strongly and interfere with the physical viscosity. Therefore some other stabilization techniques have to be found that will help to stabilize the solution without the unwanted effects on the velocity field.

One of such methods could be the pressure stabilization introduced in [N.29]. This pressure stabilization method that consists in adding a pressure dissipation term (Laplacian) on the right-hand side of the modified continuity equation (N.31). This term takes the form:

$$
Q_{i,j,k} = \frac{1}{|D_{i,j,k}|} \sum_{\ell=1}^{2N} \frac{p_\ell - p_{i,j,k}}{b_\ell} S_\ell. \tag{N.69}
$$

Here ℓ denotes the control volume cell face index, p_ℓ is the pressure in the corresponding neighboring cell and S_ℓ is the cell face area. The value b_ℓ has the dimension of velocity and represents the maximal convective velocity in the domain and local diffusive velocity.

$$
b_\ell = \max(\sqrt{u^2 + v^2 + w^2}) + \frac{2\nu}{L_\ell} \tag{N.70}
$$

Symbol L_ℓ corresponds to a distance between the current and the neighboring cell centers. It is possible to show that on the uniform cartesian mesh with cells of size δx this term is given by:

$$Q = \frac{\delta x}{2b} \Delta p \qquad (N.71)$$

This stabilization method has some advantages over the classical artificial diffusion applied to the velocity components. The artificial effects induced by the pressure dissipation term only indirectly affect the velocity field and thus they do not interfere that much with the physical viscous effects. Moreover, this stabilization term contains only second derivatives of the pressure and will vanish if pressure is a linear function of space coordinates (like e.g. in the Poiseuille flow or within a boundary layer).

> *This method has been used together with the finite-volume scheme in the papers shown in the Sections E.1 and B.1–B.3 as well as in other publications, solving the free-surface and blood flow problems. These are listed in the author's full bibliography in the Appendix A, page 205.*

N.7.3 Non-Linear TVD Filtering

As it was already discussed above, the numerical solution obtained using certain schemes suffers from non-physical oscillations. This is why many specialized, non-oscillatory discretizations have been developed and successfully used (ENO, TVD, ...). The drawback of the use of such non-oscillatory discretizations is that they are often computationally expensive and hard to implement into already existing codes.

One of the alternative ways of obtaining oscillation-free solution, lies in the post-processing of the resulting data, rather than in modification of the discretization algorithm itself. This idea comes from the area of signal (image, acoustic, etc.) processing. It has been found that the algorithms used for the signal de-noising can successfully be applied to remove the numerical point-to-point oscillations that often appear in the numerical solution of physical problems.

The filter presented here follows the paper [N.14], where a family of discrete filters has been proposed and studied. The general idea of this filtering algorithm can be written as follows:

i) *Localize* - The oscillations appear as the local minima/maxima of the solution. Thus the filtering will only be applied to the points of local extrema. Non-extremal points will remain unchanged.

ii) *Measure* - The amplitude of an oscillation could be estimated e.g. as a fraction of backward/forward difference.

iii) *Remove* - As the value in the actual point is reduced/increased to remove the oscillatory maxima/minima, the neighboring value(s) should also be modified to retain the overall conservativity of the algorithm.

One of the simplest versions of such algorithm can be summarized as follows. Let's have a set of grid values ϕ_i, for $i = 0, \ldots, N$, which approximate the scalar function values $\phi(x_i)$ at regularly spaced grid points x_i. For each of the grid points in the range $i = 1, \ldots, N-1$ do the following:

i) To localize the oscillation, compute the backward and forward differences of ϕ, i.e. $(\delta_-\phi)_i = \phi_i - \phi_{i-1}$ and $(\delta_+\phi)_i = \phi_{i+1} - \phi_i$. If $(\delta_-\phi)_i \cdot (\delta_+\phi)_i < 0$, then there is a local extrema in x_i, that needs to be adjusted.

ii) Estimate the amplitude of the oscillation at point x_i as $osc = \min\{(\delta\phi)_{min}, \ 0.5(\delta\phi)_{max}\}$, where $(\delta\phi)_{min} = \min\{|(\delta_-\phi)_i|, \ |(\delta_+\phi)_i|\}$ and $(\delta\phi)_{max} = \max\{|(\delta_-\phi)_i|, \ |(\delta_+\phi)_i|\}$.

iii) Adjust the local extrema by subtracting/adding the value $\delta\phi = \text{sign}((\delta_+\phi)_i) \cdot osc$ to the ϕ_i, i.e set $\phi_i = \phi_i + \delta\phi$. It means if $(\delta_+\phi)_i < 0$ (local maxima) set $\phi_i = \phi_i - osc$, or $\phi_i = \phi_i + osc$ when $(\delta_-\phi)_i > 0$ (local minima). To preserve the conservativity of the method, redistribute the subtracted/added value osc, to the neighboring point(s). E.g. adjust the value ϕ_{i-1} or ϕ_{i+1}, depending on which of them is further from ϕ_i. I.e. if $|(\delta_-\phi)_i| > |(\delta_+\phi)_i|$ set $\phi_{i-1} = \phi_{i-1} - \delta\phi$, or $\phi_{i+1} = \phi_{i+1} - \delta\phi$, if $|(\delta_-\phi)_i| < |(\delta_+\phi)_i|$.

The procedure should be repeated until the stopping criterion (TV bound, number of filter passes, ...) is satisfied. This filter, originally proposed in [N.14], was further extended and studied in detail in [N.27]. The above algorithm could be fine-tuned by the appropriate choice of relaxation parameter ω, by the which the correction value $\delta\phi$ can be multiplied.

The effect of the filter could be seen from the following figure N.7.3 (page 26) showing the solution of 1D advection equation with stepwise initial data.

(a) Lax-Wendroff without filter

(b) Lax-Wendroff with filter ($n_f = 2, \omega = 1.3$)

(c) Lax-Friedrichs

(d) Upwind
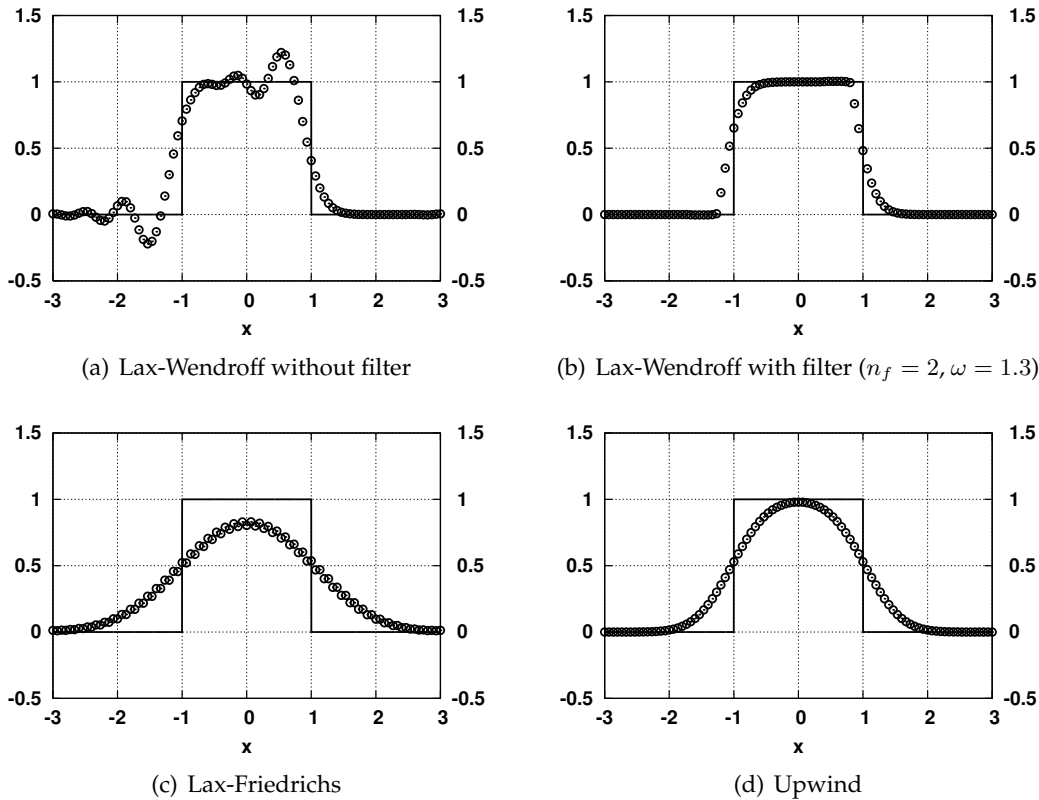
Figure N.3: Comparison of the filtered Lax-Wendroff scheme with some other classical numerical schemes CFL=0.5. (∘ numerical solution, —exact solution).

This method has been studied in detail in [N.2]. It was used in the papers shown in the Sections B.1 and B.4. Some more publications where this technique was used are listed in the author's full bibliography in the Appendix A, page 205.

N.7.4 Compact Filters

The main idea of filtering comes from the area of signal processing, where so called low-pass filters are used to suppress high frequencies in various signals. The amplitudes of high frequency modes are reduced, while low-frequencies remain unchanged. The filtering is in some sense very close to the classical artificial viscosity approach used for the stabilization of the numerical solution of hyperbolic PDEs. The filtering however is a little bit more general concept because it can also be used for other than hyperbolic problems.

An important subclass of low-pass filters is formed by the compact filters. Specific compact approximation functions are constructed in a similar fashion as the compact finite-difference schemes described in the Section N.5. This approach was proposed in [N.24] and applied and analyzed in [N.16] and [N.30]. According to [N.24] a typical compact filter could be written in the following form:

$$b_2 \hat{\phi}_{i-2} + b_1 \hat{\phi}_{i-1} + \hat{\phi}_i + b_1 \hat{\phi}_{i+1} + b_2 \hat{\phi}_{i+2} = \tag{N.72}$$

$$= \beta_0 \phi_i + \beta_1 \frac{\phi_{i+1} + \phi_{i-1}}{2} + \beta_2 \frac{\phi_{i+2} + \phi_{i-2}}{2} + \beta_3 \frac{\phi_{i+3} + \phi_{i-3}}{2} \ .$$

The symmetric linear combination of the filtered grid values $\hat{\phi}_i$ is expressed as a weighted sum of averages of the non-filtered values ϕ_i over stencils of different width. In the above example five-diagonal system of equations needs to be solved to obtain the filtered values $\hat{\phi}$. The choice of coefficients b_j and β_j defines a specific filter in terms of its order of approximation, stencil width and number of non-empty diagonals in the corresponding system of equations.

In the context of the compact finite-difference schemes introduced in the table N.2 it is natural to focus the attention on the compact filters leading to the solution of tri-diagonal system of equations. This family of filters could be written in the following simple form:

$$b \hat{\phi}_{i-1} + \hat{\phi}_i + b \hat{\phi}_{i+1} = \sum_{n=0}^{N} \frac{\beta_n}{2} (\phi_{i-n} + \phi_{i+n}) \ . \tag{N.73}$$

The coefficients β_i can be chosen to obtain filters of various orders. The single remaining parameter b takes the values $-0.5 \leqq b \leqq 0.5$. From the table N.4, summarizing the coefficients of compact filters, follows that the filter of order P can be obtained using the stencil of the width $2Ph$, i.e. using $2P+1$ points. The effect of a certain filter could be characterized by its *transfer*

Filter	β_0	β_1	β_2	β_3	β_4	β_5
F2	$\frac{1+2b}{2}$	$\frac{1+2b}{2}$	0	0	0	0
F4	$\frac{5+6b}{8}$	$\frac{1+2b}{2}$	$\frac{2b-1}{8}$	0	0	0
F6	$\frac{11+10b}{16}$	$\frac{15+34b}{32}$	$\frac{3(2b-1)}{16}$	$\frac{1-2b}{32}$	0	0
F8	$\frac{93+70b}{128}$	$\frac{7+18b}{16}$	$\frac{7(2b-1)}{32}$	$\frac{1-2b}{16}$	$\frac{2b-1}{128}$	0
F10	$\frac{193+126b}{256}$	$\frac{105+302b}{256}$	$\frac{15(2b-1)}{64}$	$\frac{45(1-2b)}{512}$	$\frac{5(2b-1)}{256}$	$\frac{1-2b}{512}$

Table N.4: Coefficients of the tri-diagonal family of compact filters.

function[14]. When both the original and filtered "signal" is represented in Fourier space by its

---

[14]Sometimes called spectral function or spectral response (see e.g. [N.30] for more details)

wave number and corresponding amplitude, the value of transfer function $T(w)$ is obtained as the ratio of the amplitudes of filtered and non-filtered signal for a given wave number w. According to [N.24] the transfer function of the tri-diagonal compact filter family is given by

$$T(w) = \frac{\sum_{n=0}^{N} \beta_n \cos(nw)}{1 + 2b \cos(w)} \tag{N.74}$$

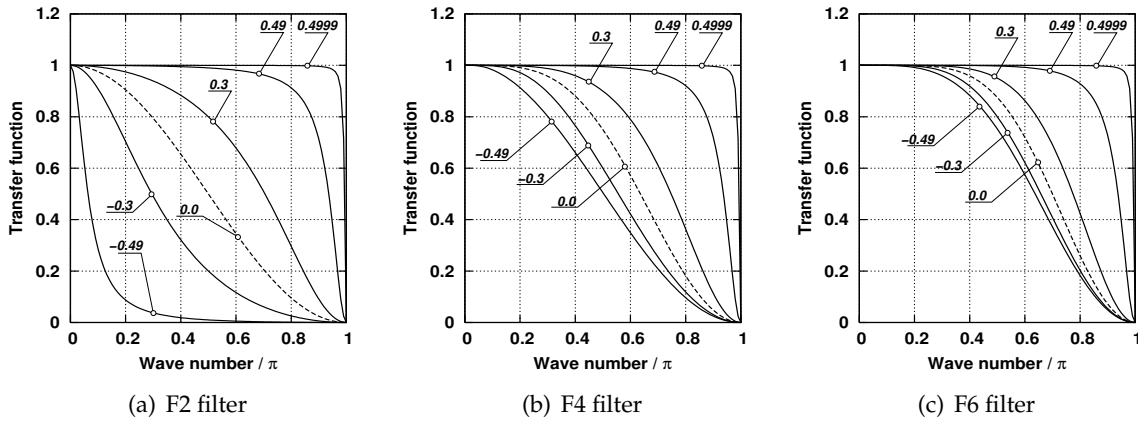The shape of the transfer functions for different filters and values of the coefficient b are shown in the figure N.4.

(a) F2 filter   (b) F4 filter   (c) F6 filter

Figure N.4: Transfer functions of different compact filters.

From the above figures it is evident that the damping effect of all the filters is stronger with lower values of parameter b. Reduction of the parameter b forces also lower frequencies being damped. The opposite effect is achieved by choosing the parameter b close to 0.5, when only the highest wave number (corresponding to grid frequency, point-to-point oscillations) components are damped. In the limit case of $b = 0.5$ the filter relation (N.73) reduces to identity, i.e. $\hat{\phi} = \phi$, and no damping occurs at all.

> *This method has been used in the paper shown in the Sections E.3-E.4 and in publications [N.3] and [N.6] solving stratified environmental flows. Some more publications where this scheme was used are listed in the author's full bibliography in the Appendix A, page 205.*

References - N

[N.1] BODNÁR, T. *Numerical Simulation of Flows and Pollution Dispersion in Atmospheric Boundary Layer*. PhD thesis, Czech Technical University in Prague, 2003.

[N.2] BODNÁR, T. On the use of non-linear TVD filters in finite-volume simulations. In *Algoritmy 2012 Proceedings of Contributed Papers and Posters*. (Bratislava, 2012), Slovak University of Technology, Faculty of Civil Engineering, pp. 190–199.

[N.3] BODNÁR, T., AND BENEŠ, L. On some high resolution schemes for stably stratified fluid flows. In *Finite Volumes for Complex Applications VI, Problems & Perspectives* (2011), vol. 4 of *Springer Proceedings in Mathematics*, Springer Verlag, pp. 145–153.

[N.4] BODNÁR, T., FASANO, A., AND SEQUEIRA, A. *Fluid-Structure Interaction and Biomedical Applications*. Birkhäuser Basel, 2014, ch. Mathematical Models for Blood Coagulation.

[N.5] BODNÁR, T., AND FRAUNIÉ, P. Numerical study of stratification effects on local wind flow and pollution dispersion. In *Topical Problems of Fluid Mechanics 2015* (Prague, 2015), Institute of Thermomechanics CAS, pp. 11–16.

[N.6] BODNÁR, T., FRAUNIÉ, P., AND KOZEL, K. Numerical simulations of stably stratified fluid flow using compact finite–difference schemes. In *ICNAAM 2010 International Conference on Numerical Analysis and Applied Mathematics* (2010), vol. 1281 of *AIP Conference Proceedings*, American Institute of Physics, pp. 103–106.

[N.7] BODNÁR, T., FRAUNIÉ, P., AND KOZEL, K. Simulation of the start-up of a turbulent free convection driven by wall heating and cooling. In *Topical Problems of Fluid Mechanics 2014* (Prague, 2014), Institute of Thermomechanics AS CR, pp. 21–24.

[N.8] BODNÁR, T., GALDI, G., AND Š. NEČASOVÁ, Eds. *Fluid-Structure Interaction and Biomedical Applications*, vol. XII. of *Advances in Mathematical Fluid Mechanics*. Birkhäuser Basel, 2014.

[N.9] BODNÁR, T., KOZEL, K., FRAUNIÉ, P., AND JAŇOUR, Z. Numerical simulation of flow and pollution dispersion in 3D atmospheric boundary layer. *Computing and Visualization in Science 3*, 1–2 (2000), 3–8.

[N.10] BODNÁR, T., AND PŘÍHODA, J. Numerical simulation of turbulent free-surface flow in curved channel. *Journal of Flow, Turbulence and Combustion 76*, 4 (June 2006), 429–442.

[N.11] BODNÁR, T., AND SEQUEIRA, A. Numerical simulation of the coagulation dynamics of blood. *Computational and Mathematical Methods in Medicine 9*, 2 (2008), 83–104.

[N.12] BODNÁR, T., AND SEQUEIRA, A. On the implementation of a non-linear viscoelastic model into coupled blood flow-biochemistry model. In *SIMULTECH 2013 - Proceedings of the 3rd International Conference on Simulation and Modeling Methodologies, Technologies and Applications* (2013), pp. 652–657.

[N.13] CHORIN, A. A numerical method for solving incompressible viscous flows problems. *Journal of Computational Physics 2*, 1 (1967), 12–26.

[N.14] ENGQUIST, B., LÖTSTEDT, P., AND SJÖGREEN, B. Nonlinear filters for efficient shock computation. *Mathematics of Computation 52*, 186 (1989), 509–537.

[N.15] FEIREISL, E., AND NOVOTNÝ, A. *Singular Limits in Thermodynamics of Viscous Fluids*. Advances in Mathematical Fluid Mechanics. Birkhäuser, 2009.

[N.16] GAITONDE, D. V., SHANG, J. S., AND YOUNG, J. L. Practical aspects of higher-order numerical schemes for wave propagation phenomena. *International Journal for Numerical Methods in Engineering 45* (1999), 1849–1869.

[N.17] GLOWINSKI, R. *Handbook of Numerical Analysis : Numerical Methods for Fluids (Part 3)*. Elsevier, 2003.

[N.18] GOTTLIEB, S. On high order strong stability preserving runge-kutta and multi step time discretizations. *Journal of Scientific Computing 25*, 1 (2005), 105–128.

[N.19] GOTTLIEB, S., AND SHU, C. W. Total variation diminishing runge-kutta schemes. *Mathematics of Computation 67*, 221 (1998), 73–85.

[N.20] GOTTLIEB, S., SHU, C. W., AND TADMOR, E. Strong stability-preserving high-order time discretization methods. *SIAM Review 43*, 1 (2001), 89–112.

[N.21] HUNDSDORFER, W., AND VERWER, J. G. *Numerical Solution of Time-Dependent Advection-Diffusion-Reaction Equations*. Springer Verlag, 2003.

[N.22] JAMESON, A. Time dependent calculations using multigrid, with applications to unsteady flows past airfoils and wings. In *AIAA 10th Computational Fluid Dynamics Conference, Honolulu* (June 1991). AIAA Paper 91-1596.

[N.23] JAMESON, A., SCHMIDT, W., AND TURKEL, E. Numerical solutions of the Euler equations by finite volume methods using Runge-Kutta time-stepping schemes. In *AIAA 14th Fluid and Plasma Dynamic Conference, Palo Alto* (June 1981). AIAA paper 81-1259.

[N.24] LELE, S. K. Compact finite difference schemes with spectral-like resolution. *Journal of Computational Physics 103* (1992), 16–42.

[N.25] SHU, C. W. Total-variation-diminishing time discretizations. *SIAM Journal of Scientific & Statistical and Computing 9* (1988), 1073–1084.

[N.26] SHU, C. W., AND OSHER, S. Efficient implementation of essentially non-oscillatory shock-capturing schemes. *Journal of Computational Physics 77* (1988), 439–471.

[N.27] SHYY, W., CHEN, M.-H., MITTAL, R., AND UDAYKUMAR, H. On the suppression of numerical oscillations using a non-linear filter. *Journal of Computational Physics 102* (1992), 49–62.

[N.28] SPITERI, R. J., AND RUUTH, S. J. A new class of optimal high-order strong-stability-preserving time discretization methods. *SIAM Journal on Numerical Analysis 40*, 2 (2002), 469–491.

[N.29] VIERENDEELS, J., RIEMSLAGH, K., AND DICK, E. A multigrid semi-implicit line-method for viscous incompressible and low-Mach-number flows on high aspect ratio grids. *Journal of Computational Physics 154* (1999), 310–344.

[N.30] VISBAL, M., AND GAITONDE, D. On the use of higher-order finite-difference schemes on curvilinear and deforming meshes. *Journal of Computational Physics 181* (2002), 155–185.

Chapter E

Environmental Applications

Contents

  The specific characteristics of the environmental applications included in this part of the work are related to their rather complex geometry and mainly to the effects of *turbulence* and *variable density*. The main aim of this introductory section is to present at one place an overview of models generalizing the standard incompressible model derived in the section N.1. These generalized models have further been used in the papers shown in the Sections E.1-E.4.

Models of Turbulence

Turbulence modeling in environmental flows is very complex and difficult task. The models used in this work are based on Reynolds-Averaged Navier-Stokes equations and Boussinesq assumption on the approximation of turbulent fluxes. The resulting system of incompressible Reynolds-Averaged Navier-Stokes equations (with constant density) can be written in the following way[1]:

$$\mathrm{div}\boldsymbol{v} = 0 \tag{E.1}$$

$$\frac{\partial \boldsymbol{v}}{\partial t} + \mathrm{div}(\boldsymbol{v} \otimes \boldsymbol{v}) = -\boldsymbol{\nabla}P + \mathrm{div}(2K\mathbf{D}) + \boldsymbol{f} \tag{E.2}$$

It means that the model looks formally the same as the original Navier-Stokes system (N.27), (N.30), however the variables changed their role from instantaneous to time-averaged quantities. Due to Boussinesq assumption, the molecular (constant) viscosity is replaced by a (non-constant) *turbulent diffusion coefficient* $K = \nu + \nu_T$ where the additional turbulent viscosity ν_T has to be determined using suitable turbulence parametrization.

---

[1]The tensor $\mathbf{D}$ is the strain-rate tensor i.e. the symmetric part of the velocity gradient tensor. See the Chapter B for details.

The following two models have been used in this work.

Algebraic mixing length model

This model was chosen because of its simplicity and adaptation to atmospheric flows including stratification.

According to idea of Prandtl[2] it can be assumed that a fluid parcel is an entity that moves at the distance (*mixing length*) ℓ keeping its original momentum. So the mixing length is in some way analogous to the mean free path in the description of molecular diffusion. This analogy leads to a simple expression for the turbulent (kinematic) viscosity ν_T

$$\nu_T = \ell^2 \left\| \boldsymbol{\nabla v} \right\| \tag{E.3}$$

For Atmospheric Boundary Layer (ABL), it can be assumed that the horizontal velocity gradients are negligible in comparison to the vertical ones. Moreover it's often supposed that the vertical velocity component tends to zero and also its gradients are negligible. The basic mixing length model (originally proposed by Prandtl) was modified for boundary layer flows by Blackadar (1962) and generalized for stability effects by Estoque and Bhumralkar (1969). For the flow in thermally stratified boundary layer the following stability function $\mathcal{G}$ can be used:

$$\nu_T = \ell^2 \left[\left(\frac{\partial \bar{u}}{\partial z} \right)^2 + \left(\frac{\partial \bar{v}}{\partial z} \right)^2 \right]^{1/2} \mathcal{G} \tag{E.4}$$

Where the function $\mathcal{G}$ is given by :

$$\begin{aligned} \mathcal{G} &= (1 + \beta\, Ri)^{-2} \qquad \text{for } Ri > 0 \\ \mathcal{G} &= (1 - \beta\, Ri)^{2} \qquad \text{for } Ri \leq 0 \end{aligned} \tag{E.5}$$

where β is a constant (≈ 3) and Ri stands for (gradient) Richardson number.

In this way the problem of turbulent closure was reduced to the problem of finding some suitable formula for the mixing length ℓ. The general expression for ℓ, given by von Kármán is:

$$\ell = \frac{-\varkappa\, \partial |\boldsymbol{v}|/\partial z}{\partial^2 |\boldsymbol{v}|/\partial z^2} \tag{E.6}$$

Here the parameter $\varkappa = 0.36 - 0.41$ is *von Kármán's constant*. The simplest assumption that can be made on ℓ (inside the boundary layer) is that the mixing length is equal zero on the wall and grows linearly with the distance from the surface.

$$\ell = \varkappa z \tag{E.7}$$

This simple linear dependency can give good results in the proximity of wall. At larger distances it is usually replaced by some suitable asymptotic value ℓ_∞. This free-stream mixing length is the tuning parameter that can either be evaluated by experimental fitting or estimated according to some empirical formula.

The above approach was reported e.g. in [E.1] or [E.10] detailed description can be found in author's PhD thesis [E.2].

This method has been used in the papers shown in the Sections E.1–E.2 as well as in many other publications, solving the atmospheric boundary layer flows problems. These are listed in the author's full bibliography in the Appendix A, page 205.

---

[2]See e.g. the classical book [E.12]

Hellsten's modification of Menter's SST $k - \omega$ model

This two-equation model was chosen as a step up from the elementary algebraic turbulence model that only accounts for local velocity gradients. The aim was to better handle the turbulence history in the flow, including large flow curvature and massive recirculation.

The main idea of this model is an attempt to locally use the better from the classical $k - \epsilon$ and the $k - \omega$ models, depending on the flow regime. The experience shows, that the $k - \omega$ model usually performs best close to the wall, while the $k - \epsilon$ model performs better away from the wall. Thus, following the construction of the original $k - \omega$ model of Wilcox, Menter [E.11] created the Shear Stress Transport (SST) $k - \omega$ model using the fact, that both $k - \epsilon$ and $k - \omega$ models can be formulated in the same way (just with different coefficients in the governing equations) and then an automatic blending function can be used to smoothly switch between the two models, depending on local flow conditions. The turbulent viscosity $\mu_T = \rho\nu_T$ can be computed from

$$\mu_T = \frac{\rho\,k}{\omega} \tag{E.8}$$

The turbulent kinetic energy k and specific rate of its dissipation ω can be determined by solving the following set of transport equations:

$$\rho\frac{\partial k}{\partial t} + \rho\sum_{j=1}^{3} v_j\frac{\partial k}{\partial x_j} = P - \beta^*\rho k\omega + \sum_{j=1}^{3}\frac{\partial}{\partial x_j}\left[\left(\mu + \frac{\mu_T}{\sigma_k}\right)\frac{\partial k}{\partial x_j}\right] \tag{E.9}$$

$$\rho\frac{\partial\omega}{\partial t} + \rho\sum_{j=1}^{3} v_j\frac{\partial\omega}{\partial x_j} = \frac{\gamma\rho}{\mu_T}P - F_4\beta\rho\omega^2 + \sum_{j=1}^{3}\frac{\partial}{\partial x_j}\left[\left(\mu + \frac{\mu_T}{\sigma_\omega}\right)\frac{\partial\omega}{\partial x_j}\right] + 2\rho\frac{1-F_1}{\sigma_{\omega 2}\omega}\sum_{j=1}^{3}\frac{\partial k}{\partial x_j}\frac{\partial\omega}{\partial x_j}$$

The coefficients appearing in these equations are described e.g. in [E.8] or [E.9].

Further modification of this model for high streamline curvature was provided by Hellsten in 1998 (see [E.9]). This modification suggests that the centrifugal force can act in a way similar to gravity in stratified flows and thus a correction term is added to the Menter's original SST $k-\omega$ model to account for this effect. The values of function F_4 are in this modification computed using:

$$F_4 = \frac{1}{1 + C_{rc}Ri} \qquad \text{where} \qquad C_{rc} \approx 3.6 \tag{E.10}$$

where the Richardson number analog Ri is defined by:

$$Ri = \frac{|\Omega_{ij}|}{|S_{ij}|}\left(\frac{|\Omega_{ij}|}{|S_{ij}|} - 1\right) \quad \text{where} \quad S_{ij} = \frac{1}{2}\left(\frac{\partial v_i}{\partial x_j} + \frac{\partial v_j}{\partial x_i}\right) \quad \text{and} \quad \Omega_{ij} = \frac{1}{2}\left(\frac{\partial v_i}{\partial x_j} - \frac{\partial v_j}{\partial x_i}\right). \tag{E.11}$$

This model has been used in the paper [E.8] and [E.7]. An extension for buoyant flows was described and used in [E.6]. Other publications, solving the turbulent free-surface or stratified flows problems, using this model are listed in the author's full bibliography in the Appendix A, page 205.

Variable Density Models

Variable density is one of the typical features of environmental flows. The causes of these density variations can however be very different from case to case. It can be e.g. the mixing of

fluids with different densities (like the river to sea inflow), thermally driven convection (like the thermal convection in atmosphere) or fluid density affected by the local concentration of contaminants (e.g. salinity driven currents in the ocean). Typically a slightly different model is used for each such phenomena, however all of them come from the basic non-homogeneous incompressible model derived in the Section N.1. Only the few variations of this model will be shown here, that were used in the full-length papers listed further in this chapter.

Surface capturing method for free-surface flows

The liquid/gas (water/air) interfaces are quite common in environmental flows. One of the possible approaches how to handle situations involving such two-phase flows is to treat both these phases as a single liquid with variable material properties (density and viscosity). In this way, the whole problem can be solved as a single-component, but non-homogeneous fluid problem. The interface between the two (typically immiscible) fluids is not a-priori known during the simulations. It can however be obtained at any moment as one of the isosurfaces of (e.g.) density. The governing system of equations can be the following:

$$\operatorname{div}\boldsymbol{v} \;=\; 0 \tag{E.12}$$

$$\frac{\partial \rho}{\partial t} + \boldsymbol{v} \cdot \boldsymbol{\nabla}\rho \;=\; 0 \tag{E.13}$$

$$\frac{\partial \boldsymbol{v}}{\partial t} + \operatorname{div}(\boldsymbol{v} \otimes \boldsymbol{v}) \;=\; -\frac{\boldsymbol{\nabla}p}{\rho} + \frac{1}{\rho}\operatorname{div}\Big[2\mu(\rho)\mathbf{D}\Big] + \boldsymbol{g} \tag{E.14}$$

The viscosity μ is no longer a constant, but depends on the local density $\rho(x,y,z,t)$ which serves as a phase indicator. This means that the viscosity of fluid can take either the values of μ_G for gas or μ_L for liquid, depending if the local density is equal to ρ_G or ρ_L. The free-surface shape can then be tracked down as the isosurface of density $\rho_S = (\rho_G + \rho_L)/2$.

This generic formulation represents a basis for the Volume Of Fluid (VOF) method and can further be refined. The density ρ in this case is a function that has discontinuity at the liquid/gas interface. This jump can cause numerical difficulties. The spatio-temporal evolution of density is governed by the advection equation (E.13). This e.g. means, that in steady case $\boldsymbol{v} \perp \boldsymbol{\nabla}\rho$, i.e. the density does not changes along a streamline. This directly leads to an idea to use some other function, instead of density, as the phase indicator. Typically such a function can have a character of the (signed) distance from the surface. In such case the function $r(x,y,z,t)$ will be smooth, with values that will e.g. be negative in the gas, while positive in the liquid. The evolution of the indicator quantity r will be driven by the same advection equation as the density. The free-surface is in this case represented by the isosurfaces $r = 0$, while the actual density $\rho(r)$ and viscosity $\mu(r)$ can be determined depending on the sign of r.

The advantage of this kind of model is its simplicity, with very straightforward possibility of the extension for turbulent flows. The disadvantage might be its sensitivity to numerical discretization and more difficult implementation of surface tension.

This model has been applied in the papers [E.8] and [E.7] as well as in other publications, solving the turbulent free-surface flows problems. These are listed in the author's full bibliography in the Appendix A, page 205.

Boussinesq approximation

This simplification is made, in situations when there exist an important background density and pressure field to which the actual flow only adds a perturbation. This is typically the case of flows that can be seen as a perturbation of hydrostatic state. In such a case the pressure and density fields in the model (N.18)-(N.22) can be decomposed as $\rho = \rho_0 + \rho'$ and $p = p_0 + p'$, where the background fields are given and linked together by the hydrostatic balance $\boldsymbol{\nabla} p_0 = \rho_0 \boldsymbol{g}$. In this way, the (usually time-independent) hydrostatic fields can be subtracted from equations:

$$\operatorname{div} \boldsymbol{v} \;=\; 0 \tag{E.15}$$

$$\frac{\partial \rho'}{\partial t} + \boldsymbol{v} \cdot \boldsymbol{\nabla} \rho' \;=\; -\boldsymbol{v} \cdot \boldsymbol{\nabla} \rho_0 \tag{E.16}$$

$$\frac{\partial \boldsymbol{v}}{\partial t} + \operatorname{div}(\boldsymbol{v} \otimes \boldsymbol{v}) \;=\; \frac{1}{\rho_0 + \rho'}\left[-\boldsymbol{\nabla} p' + \operatorname{div}\!\left(2\mu \mathbf{D}\right) + \rho' \boldsymbol{g}\right] \tag{E.17}$$

This system is still complete and equivalent to (N.18)-(N.22). The simplification in the Boussinesq approximation is to neglect the density perturbation ρ' in the scaling factor $(\rho_0 + \rho')$, but to keep it in the buoyancy term $\rho' \boldsymbol{g}$. So the full density $(\rho_0 + \rho')$ is replaced either by the background density field ρ_0 or even in some cases by a constant (mean) density $\bar{\rho}$. This model is typically used in flows, where the gravity acts along the vertical axis and thus the background fields $\rho_0(z)$ and $p_0(z)$ are horizontally homogeneous. Moreover if the flow is shallow, the $(\rho_0 + \rho')$ can easily be replaced by $\bar{\rho}$ to give:

$$\frac{\partial \rho'}{\partial t} + \boldsymbol{v} \cdot \boldsymbol{\nabla} \rho' \;=\; -w \frac{\partial \rho_0}{\partial z} \tag{E.18}$$

$$\frac{\partial \boldsymbol{v}}{\partial t} + \operatorname{div}(\boldsymbol{v} \otimes \boldsymbol{v}) \;=\; -\boldsymbol{\nabla} P' + \nu \Delta \boldsymbol{v} + \frac{\rho'}{\bar{\rho}} \boldsymbol{g} \tag{E.19}$$

The above described model is often, just with minor modifications, also used for the simulation of thermal convection. In that case, the density variation is a consequence of thermal dilatation of the fluid. Therefore, strictly speaking, the flow is no-more divergence-free (fluid parcels are changing their volume) and thus another approximations have to be made to be able to use the system (E.15)-(E.17). The transport equation for density perturbation (E.18) is then replaced by the following advection-diffusion equation for *potential temperature* perturbation:

$$\frac{\partial \Theta'}{\partial t} + \boldsymbol{v} \cdot \boldsymbol{\nabla} \Theta' = -w \frac{\partial \Theta_0}{\partial z} + K_\Theta \Delta \Theta' \tag{E.20}$$

Here again $\Theta = \Theta_0(z) + \Theta'(x, y, z, t)$ and K_Θ is the thermal diffusivity. It is good to note that this equation has been obtained from the conservation of energy, rather than its density based counterpart that comes from mass conservation[3]. The buoyancy term $\rho'/\bar{\rho}$ in (E.19) is similarly replaced by $\Theta'/\bar{\Theta}$.

The Boussinesq approximation is popular because it can easily be implemented into existing (constant density) codes, just by adding one more transport equation and the buoyancy term into the homogeneous Navier-Stokes system. From the computational point of view however, it does not brings any advantage over the full system.

> *This model was used in the paper shown in the Section E.3-E.4 and in publications [E.3] and [E.5] solving stratified environmental flows. Some more publications where this model was used are listed in the author's full bibliography in the Appendix A, page 205.*

---

[3]For details see author's PhD thesis [E.2].

References - E

[E.1] ATKINSON, B. Introduction to the fluid mechanics of meso-scale flow fields. In *Diffusion and Transport of Pollutants in Atmospheric Mesoscale Flow Fields*, A. Gyr and F.-S. Rys, Eds., vol. 1 of *ERCOFTAC series*. Kluwer Academic Publishers, 1995, ch. I., pp. 1–22.

[E.2] BODNÁR, T. *Numerical Simulation of Flows and Pollution Dispersion in Atmospheric Boundary Layer*. PhD thesis, Czech Technical University in Prague, 2003.

[E.3] BODNÁR, T., AND BENEŠ, L. On some high resolution schemes for stably stratified fluid flows. In *Finite Volumes for Complex Applications VI, Problems & Perspectives* (2011), vol. 4 of *Springer Proceedings in Mathematics*, Springer Verlag, pp. 145–153.

[E.4] BODNÁR, T., BENEŠ, L., FRAUNIÉ, P., AND KOZEL, K. Application of compact finite-difference schemes to simulations of stably stratified fluid flows. *Applied Mathematics and Computation 219*, 7 (2012), 3336–3353.

[E.5] BODNÁR, T., FRAUNIÉ, P., AND KOZEL, K. Numerical simulations of stably stratified fluid flow using compact finite–difference schemes. In *ICNAAM 2010 International Conference on Numerical Analysis and Applied Mathematics* (2010), vol. 1281 of *AIP Conference Proceedings*, American Institute of Physics, pp. 103–106.

[E.6] BODNÁR, T., FRAUNIÉ, P., AND KOZEL, K. Simulation of the start-up of a turbulent free convection driven by wall heating and cooling. In *Topical Problems of Fluid Mechanics 2014* (Prague, 2014), Institute of Thermomechanics AS CR, pp. 21–24.

[E.7] BODNÁR, T., AND KOZEL, K. Numerical simulation of free-surface flow in a channel with ribbed bottom. In *Proceedings of the conference Fluid Dynamics 2007* (2007), pp. 1–13.

[E.8] BODNÁR, T., AND SEQUEIRA, A. Shear-thinning effects of blood flow past a formed clot. *WSEAS Transactions on Fluid Mechanics 1*, 3 (2006), 207–214.

[E.9] HELLSTEN, A. Some improvements in Menter's $k - \omega$ sst turbulence model. Tech. rep., American Institute of Aeronautics and Astronautics, 1998. AIAA-98-2554.

[E.10] MASON, P. J., AND KING, J. C. Measurements and predictions of flow and turbulence over an isolated hill of moderate slope. *Quarterly Journal of the Royal Meteorological Society 111* (1985), 617–640.

[E.11] MENTER, F. Improved two-equation $k - \omega$ turbulence models for aerodynamic flows. Technical Memorandum NASA-TM-103975, NASA, 1992.

[E.12] PRANDTL, L. The mechanics of viscous fluids. In *Aerodynamic Theory*, W. F. Durand, Ed., vol. III. Julius Springer, 1935, ch. G., pp. 35–208.

E.1 On a Numerical Study of Atmospheric 2D and 3D Flows over a Complex Topography with Forest Including Pollution Dispersion

SLÁDEK I., BODNÁR T., KOZEL K.
In: Journal of Wind Engineering and Industrial Aerodynamics. 2007, vol. 95, no. 9-11, p. 1424-1444. ISSN 0167-6105.

This paper contains an overview of numerical results obtained for several cases of atmospheric boundary layer flows. The comparison of 2D flow over sinusoidal hills with the results found in literature was quite satisfactory, given the very simple algebraic model of turbulence. Another comparison was performed for a forest canopy model in a simplified geometry. The comparison showed only small differences between the numerical results obtained using the two reported numerical methods. The final part shows a 3D example of the forest canopy simulation in a complex terrain.

In this paper T. Bodnár performed the numerical simulations using the *Model-2* solved by semi-implicit finite-difference scheme. The remaining finite-volume simulations were provided by Ivo Sládek using his own code.

On a numerical study of atmospheric 2D and 3D—flows over a complex topography with forest including pollution dispersion

I. Sládek[a,*], T. Bodnár[b,1], K. Kozel[a,2]

[a]*Institute of Technical Mathematics, Czech Technical University in Prague, Czech Republic*
[b]*Institute of Thermo-mechanics, Czech Academy of Sciences, Prague, Czech Republic*

Abstract

The paper presents a mathematical and numerical investigation of the atmospheric boundary layer (ABL) flow over a complex terrain. Two mathematical models described in details are based upon: (1) full RANS equations written in the conservative form and (2) modification of the RANS equations by Boussinesq approximation re-casted in the non-conservative form. Both models are formulated for an incompressible flow under the indifferent atmospheric stratification together with a simple algebraic turbulence model and a stationary boundary conditions. A pollution dispersion of passive pollutant has been considered as well. Both models have been applied to a real case atmospheric problem: an investigation of the influence of a forest stand on the flow over a complex topography given by a surface coal field located in the North Bohemia. A non-homogeneous forest stand is simulated by a special model based on a source term added to the momentum equations. A forest free area is supposed to be covered by a low vegetation and its influence is simulated by a surface roughness parameter.
© 2007 Published by Elsevier Ltd.

Keywords: Atmospheric boundary layer; Turbulence modelling; Numerical analysis; Pollution dispersion

*Corresponding author.

E-mail addresses: sladek@marian.fsik.cvut.cz (I. Sládek), bodnar@marian.fsik.cvut.cz (T. Bodnár), kozelk@fsik.cvut.cz (K. Kozel).

[1]Present address: Dolejškova 5, ZIP 182 00, Prague 8, Czech Republic.
[2]Present address: U12101, Faculty of Mechanical Engineering, Karlovo náměstí 13, ZIP 121 35, Prague 2, Czech Republic.

Nomenclature

$\vert^n$	superscript related to time level
$\vert''$	superscript related to perturbation
$\vert_{1,2,3}$	subscripts related to x, y, z-axis directions resp.
$\vert_{i,j,k}$	subscripts related to reference directions
$\vert_{t,x,y,z}$	subscripts related to derivative in time and in space resp.
$\vert_0$	subscript related to mean value
$\vert_l$	subscript related to the lth face of control volume
$\vert_\infty$	subscript related to free-stream
α_i	Runge–Kutta coefficients
β	artificial sound speed
$\delta, \overset{\rightarrow}{\delta}, \overset{\leftarrow}{\delta}$	central, forward, backward difference operators resp.
κ	von Karman constant
v, v_T	kinematic laminar viscosity, turbulent viscosity resp.
ϱ	density
σ_C	turbulent Prandtl number for concentration
ε	artificial diffusion coefficients
Δt	time step
$\Delta x, \Delta y, \Delta z$	stream-wise, span-wise, wall-normal space increments resp.
Θ	potential temperature
Ω	computational domain
Ω_{ijk}	control volume
a	leaf area density of vegetation
C_D	specific aerodynamic drag coefficient of forest
l	mixing length
p	pressure
r	forest drag coefficient
t	time
u, v, w	stream-wise, span-wise, wall-normal velocity components resp.
z_0	surface roughness
C	concentration of passive pollutant
H, h	height of hill, forest block
K, K_C	turbulent diffusion coefficients
$\mathbf{L}, \mathbf{B}, \mathbf{D}$	space difference operators
$\overset{\rightarrow}{\Delta} S^{(l)}$	surface vector to lth face of control volume
$\vec{f}$	volume force
$\vec{F}, \vec{G}, \vec{H}$	inviscid fluxes
$\vec{R}, \vec{S}, \vec{T}$	viscous fluxes

1. Introduction

The paper deals with a problem of flow and pollution dispersion in the atmospheric boundary layer (ABL). The ABL can be defined as the lowest part of the earth's

atmosphere. Its thickness depends on various conditions and ranges from several hundreds of meters to approximately 2 km. The ABL is significantly influenced by the surface over which the wind flows, its orography and roughness, by the free stream wind and also by the vertical temperature gradient which is associated with the atmospheric thermal stratification.

The ABL has a very close relation to a human activity and a prediction of wind field over complex terrain plays an important role in many engineering applications such as an evaluation of environmental impact by pollutant dispersion, a sitting of wind mills or airports, etc. Because of difficulties and a high cost of experiments associated with the ABL investigation, a reliable mathematical models together with a suitable numerical methods are desired. Remark, a typical horizontal length scale in our flow problems ranges from hundreds of meters to several kilometers (Castro and Apsley, 1997; Bodnár et al., 2003; Sládek, 2005).

2. Mathematical models

The flow is assumed to be steady, viscous, incompressible, turbulent and neutrally stratified.

2.1. Description of Model-1

The governing equations of the first model can be re-casted in the conservative, dimensional and vector form

$$\vec{F}_x + \vec{G}_y + \vec{H}_z = (K \cdot \vec{R})_x + (K \cdot \vec{S})_y + (K \cdot \vec{T})_z. \tag{1}$$

The artificial compressibility method is used for the numerical analysis

$$\vec{W}_t + \vec{F}_x + \vec{G}_y + \vec{H}_z = (K \cdot \vec{R})_x + (K \cdot \vec{S})_y + (K \cdot \vec{T})_z, \tag{2}$$

where $\vec{F} = (u, u^2 + p/\varrho, uv, uw, uC)^{\mathrm{T}}$, $\vec{G} = (v, vu, v^2 + p/\varrho, vw, vC)^{\mathrm{T}}$, $\vec{H} = (w, wu, wv, w^2 + p/\varrho, wC)^{\mathrm{T}}$ represent the physical inviscid fluxes and $\vec{R} = (0, u_x, v_x, w_x, (K_C/K)C_x)^{\mathrm{T}}$, $\vec{S} = (0, u_y, v_y, w_y, (K_C/K)C_y)^{\mathrm{T}}$ and $\vec{T} = (0, u_z, v_z, w_z, (K_C/K)C_z)^{\mathrm{T}}$ denote the viscous fluxes, $\vec{W} = (p/\beta^2, u, v, w, C)^{\mathrm{T}}$ abbreviates the vector of unknown variables, namely the pressure, the three velocity components and the concentration of passive pollutant, respectively, β refers to the artificial sound speed, $\varrho = \text{const}$ is density and finally K, K_C represent the diffusion coefficients, see Eq. (28).

System (2) is solved in the computational domain Ω under a stationary boundary conditions for $t \to \infty$ (t is an artificial time) to obtain the expected steady-state solution for all the unknown variables involved in the vector $\vec{W}$.

2.2. Numerical method for Model-1

A structured non-orthogonal grids made of hexahedral control cells are used for all computations. The finite volume method of cell-centered type together with a multi-stage explicit Runge–Kutta time integration scheme have been applied to solve (2) (Sládek et al.,

2004; Sládek, 2005). Integration of (2) over each control cell Ω_{ijk} gives

$$\int_{\Omega_{ijk}} \vec{W}_t \, \mathrm{d}V = \int_{\Omega_{ijk}} [(\vec{F} - K \cdot \vec{R})_x + (\vec{G} - K \cdot \vec{S})_y + (\vec{H} - K \cdot \vec{T})_z] \, \mathrm{d}V. \tag{3}$$

This identity can be rewritten using the Divergence theorem and the "Mean value" theorem

$$\vec{W}_t|_{ijk} = -\frac{1}{\mu_{ijk}} \oint_{\partial\Omega_{ijk}} [(\vec{F} - K \cdot \vec{R}) \, \mathrm{d}S_1 + (\vec{G} - K \cdot \vec{S}) \, \mathrm{d}S_2 + (\vec{H} - K \cdot \vec{T}) \, \mathrm{d}S_3], \tag{4}$$

where $\vec{W}_t|_{ijk}$ is the mean value of $\vec{W}$ over the cell Ω_{ijk} and $\mu_{ijk} = \int_{\Omega_{ijk}} \mathrm{d}V$ denotes the volume of the control cell. After space discretization of (4), we come up with a set of semi-discrete system of ordinary differential equations for each Ω_{ijk}

$$\vec{W}_t|_{ijk}(t) = \mathbf{L}\vec{W}_{ijk}(t), \tag{5}$$

where $\mathbf{L}\vec{W}_{ijk}$ denotes the operator approximating the right-hand side of (4) which has the following form:

$$\begin{aligned}
\mathbf{L}\vec{W}_{ijk} = & -\frac{1}{\mu_{ijk}} \sum_{l=1}^{6} [(\tilde{\vec{F}}_l - K_l \cdot \tilde{\vec{R}}_l) \Delta S_1^l \\
& + (\tilde{\vec{G}}_l - K_l \cdot \tilde{\vec{S}}_l) \Delta S_2^l + (\tilde{\vec{H}}_l - K_l \cdot \tilde{\vec{T}}_l) \Delta S_3^l].
\end{aligned} \tag{6}$$

All the symbols in Eq. (6) denoted with subscript or superscript l refer to the lth cell face of Ω_{ijk} and $(\Delta S_1^l, \Delta S_2^l, \Delta S_3^l)$ represents the lth outer normal vector.

The inviscid numerical fluxes $\tilde{\vec{F}}_l, \tilde{\vec{G}}_l, \tilde{\vec{H}}_l$ through the lth face of Ω_{ijk} are computed as an average from the mean value over cell Ω_{ijk} and the mean value over the neighbor cell sharing the lth face with cell Ω_{ijk}, thus we get

$$\tilde{\vec{F}}_l = \tfrac{1}{2}(\vec{F}|_{\Omega_{ijk}} + \vec{F}|_{l\text{th neighbor of } \Omega_{ijk}}),$$

$$\tilde{\vec{G}}_l = \tfrac{1}{2}(\vec{G}|_{\Omega_{ijk}} + \vec{G}|_{l\text{th neighbor of } \Omega_{ijk}}),$$

$$\tilde{\vec{H}}_l = \tfrac{1}{2}(\vec{H}|_{\Omega_{ijk}} + \vec{H}|_{l\text{th neighbor of } \Omega_{ijk}}), \quad l = 1, \dots, 6. \tag{7}$$

On the other hand, to compute the viscous fluxes at the lth face of cell Ω_{ijk}, one has to know the derivatives of the velocity components at all six faces of each hexahedral control cell. The derivatives are evaluated using the dual control volumes of the octahedral shape denoted by $\bar{\Omega}_{ijk}^{(l)}$, see Fig. 1. An example of the x-derivative computation of the u-velocity component at the lth face of the hexahedral computational cell Ω_{ijk} then reads

$$u_x|_{ijk}^{(l)} = \int_{\bar{\Omega}_{ijk}^{(l)}} u_x(x, y, z, t) \, \mathrm{d}\bar{V} = \int_{\partial\bar{\Omega}_{ijk}^{(l)}} u \, \mathrm{d}\bar{S}_1 \approx \sum_{q=1}^{8} \tilde{u}_q^{(l)} \Delta \bar{S}_1^{(l,q)}, \tag{8}$$

where the index q goes through all faces of the dual octahedral control volume $\bar{\Omega}_{ijk}^{(l)}$ and $\Delta \bar{S}_1^{(l,q)}$ abbreviates the first component of the qth outer normal vector related to the qth face of the dual cell.
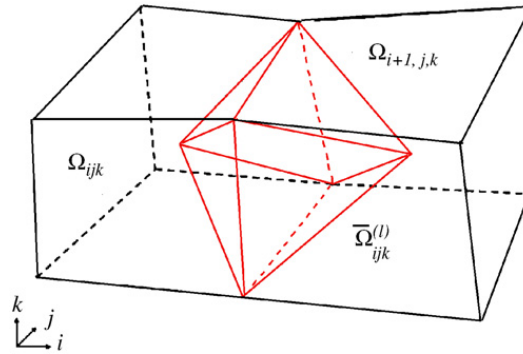
Fig. 1. A dual control volume.

Finally, the (3)-stage explicit Runge–Kutta time integration scheme is applied to system (5) of ODEs

$$\vec{W}_{ijk}^{(0)} = \vec{W}_{ijk}^{n},$$

$$\vec{W}_{ijk}^{(m+1)} = \vec{W}_{ijk}^{(0)} - \alpha_1 \cdot \Delta t \cdot \mathbf{B} \vec{W}_{ijk}^{(m)},$$

$$\vec{W}_{ijk}^{(n+1)} = \vec{W}_{ijk}^{(3)}, \quad m = 0, \dots, 2, \tag{9}$$

where $\alpha_1 = \alpha_2 = \frac{1}{2}$, $\alpha_3 = 1$ and it is second order accurate both in time and space on an orthogonal grids. The operator $\mathbf{B} \vec{W}_{ijk}^{(m)}$ defines a steady residual in the mth time level for each control cell Ω_{ijk} and it can be written as

$$\mathbf{B} \vec{W}_{ijk}^{(m)} = \mathbf{L} \vec{W}_{ijk}^{(m)} + \mathbf{D} \vec{W}_{ijk}^{(0)}, \tag{10}$$

where $\mathbf{L} \vec{W}_{ijk}$ corresponds to the operator resulting from the space discretization of system (4) and the second term $\mathbf{D} \vec{W}_{ijk}$ abbreviates the artificial viscosity contribution either of fourth order (for the pressure-velocity flow-field) or second order (for the concentration field)

$$\mathbf{D} \vec{W}_{ijk} = -\varepsilon_x^{(4)} \Delta x^4 \vec{W}_{xxxx}|_{ijk} - \varepsilon_y^{(4)} \Delta y^4 \vec{W}_{yyyy}|_{ijk} - \varepsilon_z^{(4)} \Delta z^4 \vec{W}_{zzzz}|_{ijk}$$
$$+ \varepsilon_x^{(2)} \Delta x^2 \vec{W}_{xx}|_{ijk} + \varepsilon_y^{(2)} \Delta y^2 \vec{W}_{yy}|_{ijk} + \varepsilon_z^{(2)} \Delta z^2 \vec{W}_{zz}|_{ijk}, \tag{11}$$

where $\varepsilon^{(4)}, \varepsilon^{(2)}$ denote constant coefficients to be tuned empirically and all the derivatives are substituted by central differences as it is shown hereafter for a 1D case for sake of simplicity

$$\mathbf{D} \vec{W}_i = -\varepsilon_x^{(4)} [\vec{W}_{i-2} - 4\vec{W}_{i-1} + 6\vec{W}_i - 4\vec{W}_{i+1} + \vec{W}_{i+2}]$$
$$+ \varepsilon_y^{(2)} [\vec{W}_{i-1} - 2\vec{W}_i + \vec{W}_{i+1}]. \tag{12}$$

This term removes a high frequency oscillations and wiggles generated in the computed flow-field near a sharp corners in geometry or in the vicinity of a large gradients. If not smoothed, the oscillations, resulting mainly due to the central type of differencing, may completely destroy the numerical solution. Remark also, the artificial viscosity term does not change the order of the applied numerical scheme.

Due to the explicit numerical formulation the stability limit criterion valid for a regular orthogonal meshes is applied as well

$$\Delta t \leqslant \min_{\Omega_{ijk}} \frac{\mathrm{CFL}}{\varrho_A/\Delta x + \varrho_B/\Delta y + \varrho_C/\Delta z + 2 \cdot K(1/\Delta x^2 + 1/\Delta y^2 + 1/\Delta z^2)} \tag{13}$$

where $\varrho_A, \varrho_B, \varrho_C$ refer to the spectral radii of the inviscid Jacobi's matrices and $\mathrm{CFL} = 2$ (Sládek et al., 2004; Sládek, 2005).

2.3. Description of Model-2

Hereafter, the full RANS equations are modified by the so-called Boussinesq approximation according to which the mean turbulent quantities appearing in the RANS are decomposed into the background "synoptic-scale" field denoted by subscript $_0$ and the topography induced "meso-scale" perturbation denoted by $''$. This decomposition is applied to the density $\rho = \rho_0 + \rho''$, the pressure $p = p_0 + p''$ and also the potential temperature $\Theta = \Theta_0 + \Theta''$ (Bodnár, 2004).

Under the assumption of a neutral stratification, a constant density ϱ_0 and neglected Coriolis force, a general governing equations can be simplified and transformed in the non-conservative and dimensional form

$$u_x + v_y + w_z = 0, \tag{14}$$

$$\vec{V}_t + u\vec{V}_x + v\vec{V}_y + w\vec{V}_z = -\frac{\nabla p''}{\rho_0} + ([K\vec{V}_x]_x + [K\vec{V}_y]_y + [K\vec{V}_z]_z), \tag{15}$$

$$C_t + uC_x + vC_y + wC_z = ([K_C C_x]_x + [K_C C_y]_y + [K_C C_z]_z), \tag{16}$$

where $\vec{V} = (u, v, w)^{\mathrm{T}}$ stands for the velocity vector and meaning of the other symbols is the same as in the Model-1, see Section 2.1.

2.4. Numerical method for Model-2

Unless the first numerical method described in Section 2.2 which uses the finite volume approach combined with central differencing and the explicit time integration, the numerical treatment of the governing system (14)–(16) yields the finite difference strategy applied together with a semi-implicit time integration resulting in an asymmetric numerical scheme (Bodnár et al., 2000, 2001; Bodnár, 2004).

Due to a mesh non-orthogonality one needs to transform the equations from the x–y–z coordinate system to the mesh-wise directional local coordinate system s_1–s_2–z using the following relations:

$$\frac{\partial}{\partial x} = \frac{1}{\cos\alpha}\left(\frac{\partial}{\partial s_1} - \frac{\partial}{\partial z}\sin\alpha\right), \quad \frac{\partial}{\partial y} = \frac{1}{\cos\beta}\left(\frac{\partial}{\partial s_2} - \frac{\partial}{\partial z}\sin\beta\right). \tag{17}$$

Now, let us define the following difference operators to simplify notation of discretized equations. The symbol δ_s denotes central difference with respect to direction s and

similarly the $\vec{\delta}_s, \overleftarrow{\delta}_s$ denote forward and backward differences

$$\overleftarrow{\delta}_s = \frac{\vec{V}_i - \vec{V}_{i-1}}{\Delta s^-}, \quad \vec{\delta}_s = \frac{\vec{V}_{i+1} - \vec{V}_i}{\Delta s^+}, \quad \delta_s = \frac{1}{2}(\overleftarrow{\delta}_s + \vec{\delta}_s). \tag{18}$$

Let us also denote the right-hand side of (15) by symbol RHS. Using the local coordinate transformations (17), the continuity equation (14) takes the form

$$\frac{u_{s_1}}{\cos \alpha} + \frac{v_{s_2}}{\cos \beta} + w_z - u_z \tan \alpha - v_z \tan \beta = 0 \tag{19}$$

and the equations of motion (15) then read

$$\vec{V}_t + \tilde{u}\vec{V}_{s_1} + \tilde{v}\vec{V}_{s_2} + \tilde{w}\vec{V}_z = \widetilde{\text{RHS}}, \tag{20}$$

where the modified coefficients read

$$\tilde{u} = \frac{u}{\cos \alpha}, \quad \tilde{v} = \frac{v}{\cos \beta}, \quad \tilde{w} = w - u \tan \alpha - v \tan \beta. \tag{21}$$

The right-hand side RHS is transformed in a similar way to $\widetilde{\text{RHS}}$. Now, the left-hand side of momentum equation (15) is discretized as follows:

$$\vec{V}_t \sim \vec{\delta}_t \vec{V}^n_{i,j,k}, \quad \tilde{u}\vec{V}_{s_1} \sim \frac{1}{2}(\tilde{u}^n_{i+1/2} \vec{\delta}_{s_1} \vec{V}^n_{i,j,k} + \tilde{u}^n_{i-1/2} \overleftarrow{\delta}_{s_1} \vec{V}^{n+1}_{i,j,k}), \tag{22}$$

$$\tilde{v}\vec{V}_{s_2} \sim \frac{1}{2}\{\frac{1}{2}(\tilde{v}^n_{j+1/2} \vec{\delta}_{s_2} \vec{V}_{i,j,k} + \tilde{v}^n_{j-1/2} \overleftarrow{\delta}_{s_2} \vec{V}_{i,j,k})^n$$
$$+ \frac{1}{2}(\tilde{v}^n_{j+1/2} \vec{\delta}_{s_2} \vec{V}_{i,j,k} + \tilde{v}^n_{j-1/2} \overleftarrow{\delta}_{s_2} \vec{V}_{i,j,k})^{n+1}\}, \tag{23}$$

$$\tilde{w}\vec{V}_z \sim \frac{1}{2}\{\frac{1}{2}(\tilde{w}^n_{k+1/2} \vec{\delta}_z \vec{V}_{i,j,k} + \tilde{w}^n_{k-1/2} \overleftarrow{\delta}_z \vec{V}_{i,j,k})^n$$
$$+ \frac{1}{2}(\tilde{w}^n_{k+1/2} \vec{\delta}_z \vec{V}_{i,j,k} + \tilde{w}^n_{k-1/2} \overleftarrow{\delta}_z \vec{V}_{i,j,k})^{n+1}\}. \tag{24}$$

A combination of different asymmetric space discretization at time levels n and $n+1$ allows us to construct finally the numerical scheme that is centered and second order in both space and time for steady cases. The diffusion terms on the right-hand side of (15) are approximated in the same manner by central differences and denoted by $\overline{\text{RHS}}$, hence one obtains the system of linear algebraic equations:

$$a_1 \vec{V}^{n+1}_{i,j+1,k} + a_2 \vec{V}^{n+1}_{i,j,k} + a_3 \vec{V}^{n+1}_{i,j-1,k} + a_4 \vec{V}^{n+1}_{i,j,k+1} + a_5 \vec{V}^{n+1}_{i,j,k-1} = \overline{\text{RHS}}. \tag{25}$$

This system is solved iteratively in the vertical plane $i = $ const. So, the five-diagonal system is converted into the three-diagonal one:

$$a_5 \vec{V}^{\eta+1}_{i,j,k-1} + a_2 \vec{V}^{\eta+1}_{i,j,k} + a_4 \vec{V}^{\eta+1}_{i,j,k+1} = \overline{\text{RHS}} - a_1 \vec{V}^{\eta}_{i,j+1,k} - a_3 \vec{V}^{\eta+1}_{i,j-1,k}, \tag{26}$$

where the η denotes the iterative index. Usually after 3–5 iterations we know the values of $\vec{V} = (u, v, w)^T$ with a sufficient accuracy. Exactly the same solution scheme can also be applied to the scalar transport equation (16).

For a steady problems the artificial compressibility method can be used and in such a case the pressure is updated from the modified continuity equation

$$p''_t = -(u_x + v_y + w_z). \tag{27}$$

Also here the above described semi-implicit discretization is used to keep the consistency with the momentum equations solver. Then we skip to $(n + 1)$th time level and repeat the cycle.

In order to improve the convergence of this method for a large Reynolds numbers, the artificial viscosity terms of fourth or second order is added and the form is similar as in the first numerical method for Model-1, see Section 2.2.

3. Turbulence modelling

A simple algebraic turbulence model is applied for both the Model-1 (2) and the Model-2 (14)–(16) of governing equations in order to close the problem. The diffusion coefficients K, K_C can be expressed in the dimensional case as

$$K = v + v_T, \quad K_C = v + \frac{v_T}{\sigma_C} \quad \text{where } v_T = l^2 \sqrt{\left(\frac{\partial u}{\partial z}\right)^2 + \left(\frac{\partial v}{\partial z}\right)^2}, \tag{28}$$

where v_T is the turbulent viscosity, v is the laminar viscosity, $\sigma_C = 0.74$ abbreviates the turbulent Prandtl number. Parameter l refers to the Blackadar's mixing length computed by

$$l = \frac{\kappa(z + z_0)}{1 + \kappa((z + z_0)/l_\infty)}, \quad l_\infty = \frac{27|V_\infty|10^{-5}}{\lambda}, \tag{29}$$

where κ is the von Karman constant, λ denotes the Coriolis parameter, z_0 is the surface roughness parameter, l_∞ represents the mixing length for $z \to \infty$ and $|V_\infty|$ abbreviates the geostrophic free-stream wind velocity (Sládek et al., 2003; Beneš et al., 2004).

4. Boundary conditions

Both models, the Model-1 (2) and the Model-2 (14)–(16), use the following boundary conditions on a boundary $\partial\Omega$ of the computational domain Ω

- Inlet: $u = $ power-law$\sim z^\alpha$, $v = w = C = 0$.
- Outlet: Homogeneous Neumann conditions $u_x = v_x = w_x = C_x = 0$.
- Wall: The no-slip condition for the velocity components and $\partial C/\partial n = 0$.
- Top face: $u = U_\infty$, $v = 0$, $\partial w/\partial z = \partial C/\partial z = 0$ where U_∞ denotes the free-stream wind velocity.
- Side faces: Periodic conditions or homogeneous Neumann conditions $u_y = v_y = w_y = C_y = 0$.

5. Validation study

5.1. Validation of Model-1

This model has been validated through the ERCOFTAC's test-case of fully developed channel water-flow over a 2D polynomial-shaped hill mounted on a flat plate (Almeida et al., 1992; Davroux et al., 1995). The Almeida's experimental and the ERCOFTAC's

reference $k-\varepsilon$ numerical data have been used. The mean centerline velocity is $U_0 = 2.147\,\text{m/s}$ and the hill height is $H = 28\,\text{mm}$ (16% hill) leading to the Reynolds number 6×10^4. The computed stream-wise velocity profiles match the experimental and reference $k-\varepsilon$ profiles with acceptable overall agreement since simple algebraic turbulence model is applied and the wall layer is not finely resolved. A fairly large recirculation zone develops having the length 4.4H in the experiment and 4.3H in simulation, see Figs. 2 and 3.

5.2. Validation of Model-2

According to the data published in Kim et al. (1997) we have chosen a 2D-domain with two different sinusoidal single-hill terrain profiles which are shown in Figs. 4–6. A boundary layer type of air-flow has been studied, characterized by the free-stream velocity $U_\infty = 7\,\text{m/s}$ and boundary layer thickness of $0.25\,\text{m}$ at distance of $4\,\text{m}$ from the beginning of the wind tunnel test section $(6 \times 1.2 \times 1.2\,\text{m})$. The corresponding Reynolds number is 1.17×10^5.

The notation we use here to distinguish between hills with different slopes and heights is the same as in Kim et al. (1997). It means the SxHy stands for the hill with maximum slope $0.x$ and height $y\,\text{cm}$. Our results show relatively good agreement with observation in the case of separated flow over a group of S5-hills. The shape of recirculation zone we have obtained is slightly different than that computed by Kim. However, matching between experimental results and our predictions can be judged as acceptable when taking into account the simplicity of the applied algebraic turbulence model (28).
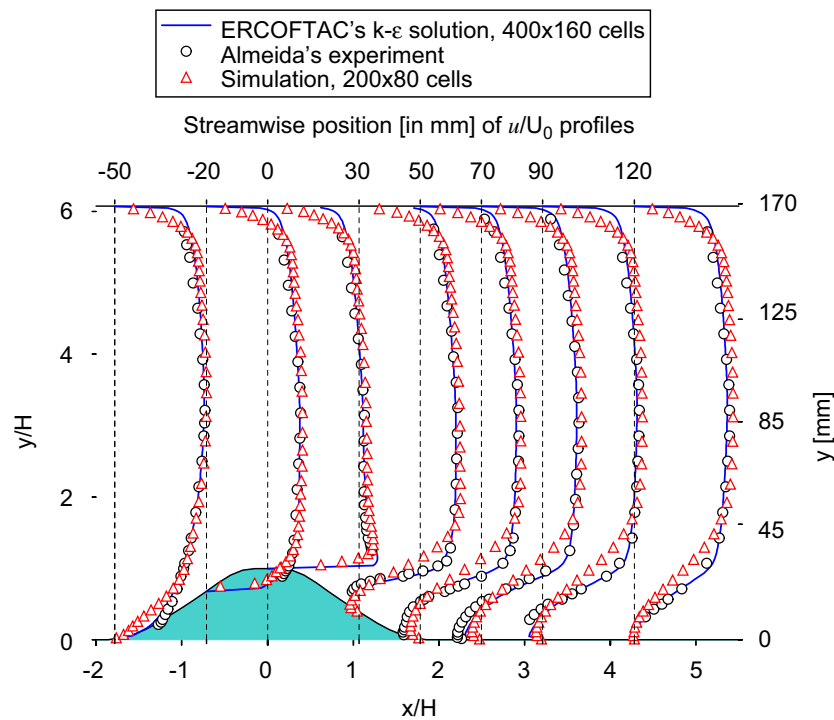
Fig. 2. Stream-wise velocity component.
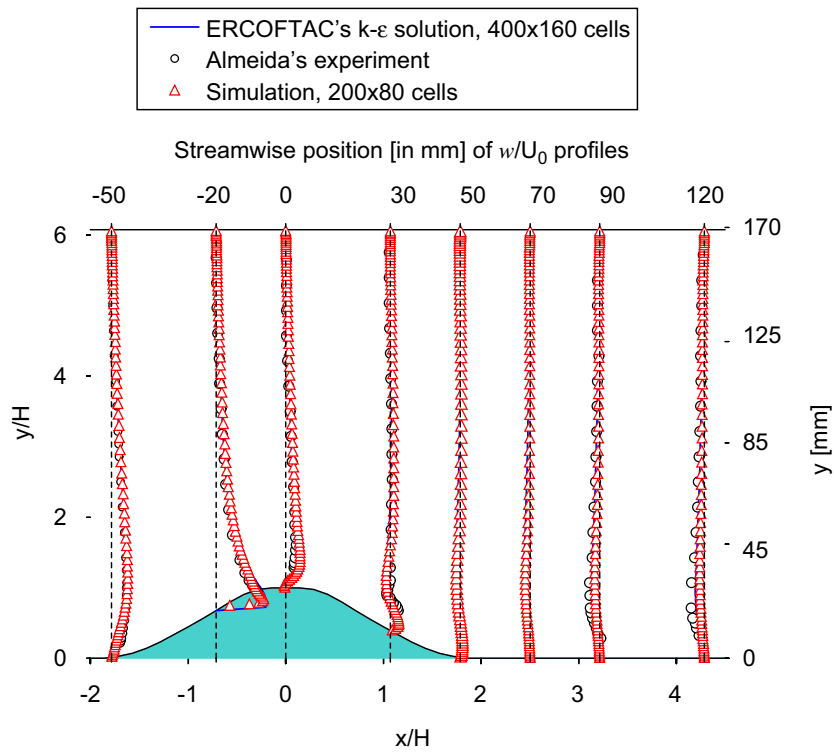
Fig. 3. Wall-normal velocity component.
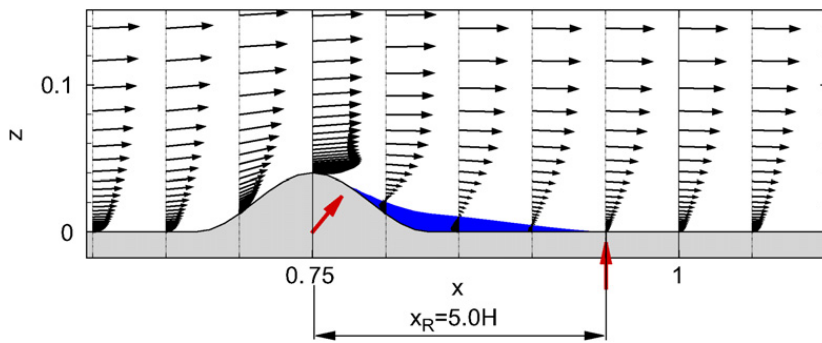
Fig. 4. Flow over S5H4 hill.
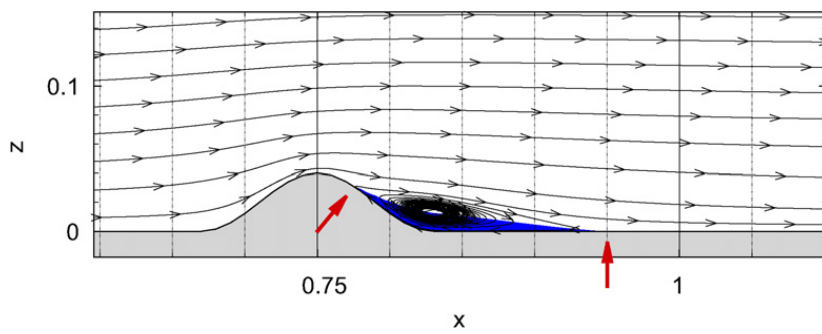
Fig. 5. Separation and re-attachment points marked by arrows, S5H4 hill.
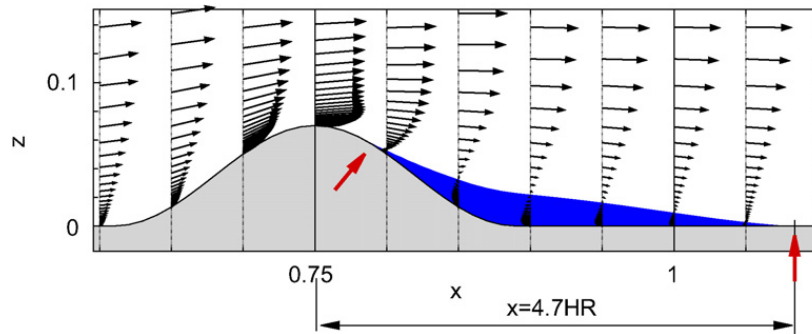
Fig. 6. Flow over S5H7 hill.
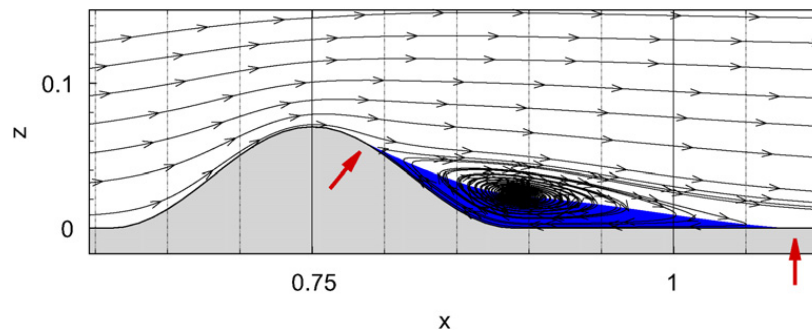
Fig. 7. Separation and re-attachment points marked by arrows, S5H7 hill.

Table 1
Re-attachment point position, the reference data by Kim et al. (1997)

Hill	Experiment	Low-re model	Our model
S5H4	5.25 ± 0.50	4.55	5.0
S5H7	4.30 ± 0.30	4.42	4.7

A single parameter that can be easily compared in these cases is the position of a re-attachment point. This is marked in Figs. 5 and 7 as a distance from the hill crest expressed in the terms of multiples of hill height H. The corresponding reference experimental values for comparison are summarized in Table 1.

6. Forest modelling

In order to simulate a flow over a forest stand, a suitable model must be defined. The vector of the outer forces caused by the presence of such a forest or any higher vegetation obstacle has the following form (Wilson and Flesch, 1999);

$$\vec{f} = (-c_{D}au|V|, -c_{D}av|V|, -c_{D}aw|V|)^{T}, \tag{30}$$

where c_{D} represents the specific aerodynamic drag coefficient, a denotes the leaf area density of the vegetation defined as the surface area of the plant material per unit volume
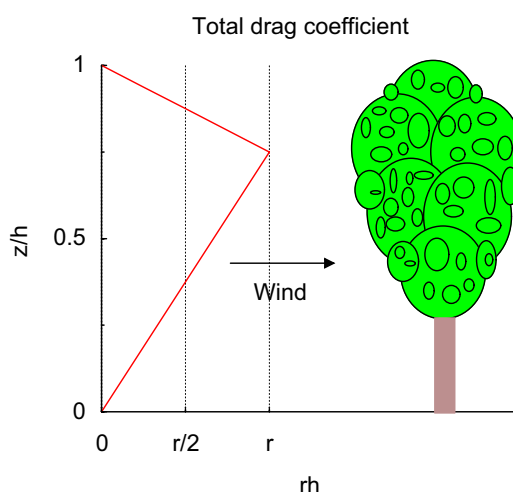
Fig. 8. A typical distribution of r_h drag.

$[m^2\,m^{-3}]$ and finally $|V|$ abbreviates the local velocity magnitude. Let us denote $r_h = c_D \cdot a$ meaning the "total" drag coefficient. The course of r_h with respect to the height z is given by the following expressions, see also Fig. 8:

$$r_h = r\frac{z/h}{0.75} \quad \text{for } \frac{z}{h} \leqslant 0.75 \text{ or}$$

$$r_h = r\frac{1 - z/h}{1 - 0.75} \quad \text{for } 0.75 < \frac{z}{h} \leqslant 1, \tag{31}$$

where the drag coefficient r must be specified a priori. The term (30) has to be added to the three momentum equations on their right-hand sides in both systems: the Model-1 (2) and the Model-2 (14)–(16).

7. Application of Model-1 and Model-2

The real-case problem is related to the flow over a surface coal field located in the North Bohemia. This field is supposed to be partially covered by a high forest stand. Hence, one of the main goal of this numerical study is to estimate the influence of such a forest block (as a vegetation natural obstacle) on the atmospheric flow over a complex topography and its impact on a pollution dispersion as well.

At first, a series of a 2D-simulations over a simplified topography have been performed without pollution dispersion using both the Model-1 (2) and the Model-2 (14)–(16). Mainly, the influence of the forest height h and the forest drag r have been tested and the results compared in between, see Section 7.1. At second, the Model-1 (2) has been applied to a real-case 3D flow problem including a pollution dispersion, see Section 7.2.

7.1. Some 2D-tests of forest model

All the simulations have been performed on a 2D structured non-orthogonal grids. The computational domain is 1000 m long and 300 m high and is discretized by 1000 × 40 cells
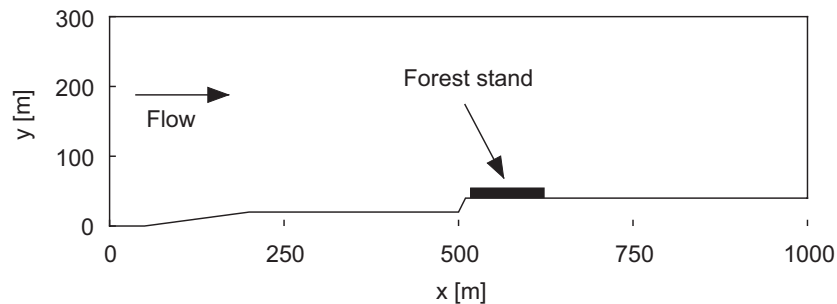
Fig. 9. 2D-computational domain.

or nodes exponentially distributed in the vertical direction with minimal increment about 1 m at the wall.

The other parameters are: the mean free stream velocity $U_\infty = 10$ m/s, the characteristic wall-normal domain dimension $L = 300$ m and the corresponding Reynolds number 2×10^8, the roughness parameter $z_0 = 0.1$ m and the power law exponent $\frac{2}{9}$ are used to reconstruct the inlet velocity profile. No other volume forces are supposed and the indifferent stratification of ABL is assumed. A sketch of a 2D-computational domain is shown in Fig. 9.

7.1.1. Effect of forest height/drag

The vertically non-homogeneous forest stand is supposed to be 90 m long and it starts 5 m after the sudden step at ground representing the edge of a surface coal field, see Fig. 9. The following studies have been performed:

- The effect of different forest heights of 0, 5, 10, 15 m for the given drag coefficient $r = 0.19$ on the flow, see Figs. 10 and 12.
- The effect of different drag coefficients $r = 0.0, 0.04, 0.19, 0.95$ for the given forest height of 10 m, see Figs. 11 and 13.

The position of the forest stand is displayed as a gray strip or a rectangle in Figs. 10–13 where the scale is in [m/s]. Figs. 10 and 12 show the increasing flow deceleration with the increasing forest height on the lee side of the forest block. However, this tendency is not so evident inside the forest. Figs. 11 and 13 show that the deceleration is monotonously dependent on the drag coefficient both inside and also behind the forest stand. So, we can conclude that both models give the same predictions. The u-profiles obtained from the applied models are shifted since the Model-1 (2) is based on the finite volume method and the Model-2 (14)–(16) yields the finite difference method. Thus, the data are related to the cell centers in the first case while the data are stored in the cell vertices in the latter case.

7.1.2. Results for wall-normal velocity component w

Hereafter, the results from both mathematical models related to distribution of the wall-normal w-velocity component over the computational domain are compared in case of the following two configurations;

- No forest stand.
- Forest stand of height 15 m and having the drag $r = 0.19$.
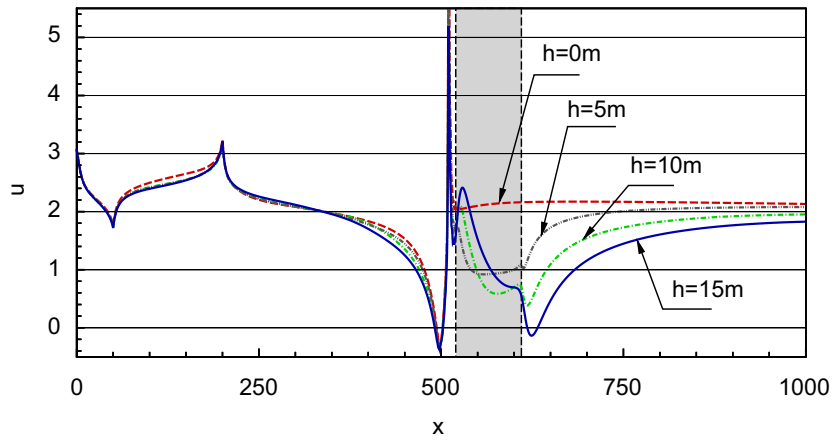
Fig. 10. Near-ground *u*-component, different forest heights, Model-2.
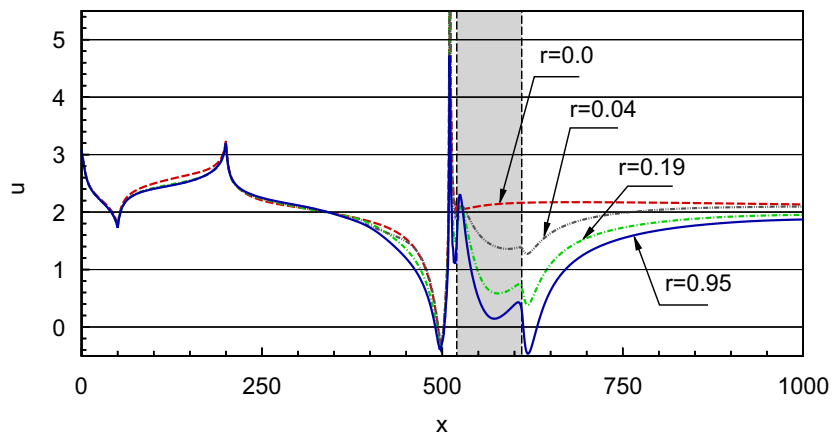
Fig. 11. Near-ground *u*-component, different forest drags, Model-2.
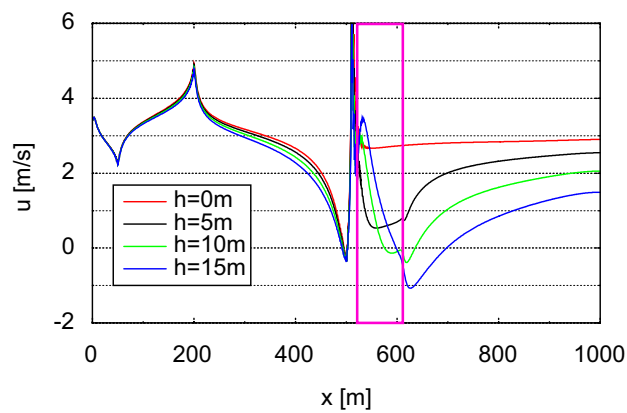
Fig. 12. Near-ground *u*-component, different forest heights, Model-1.
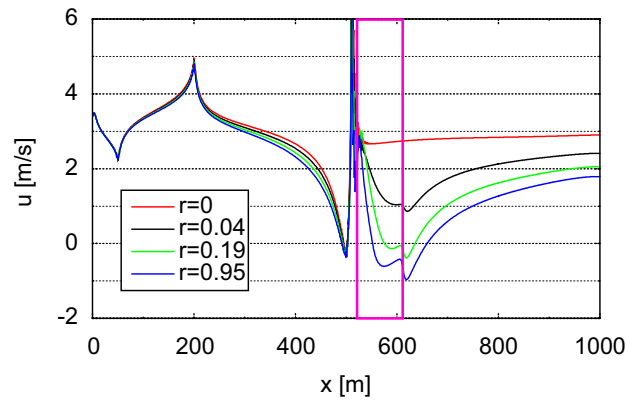
Fig. 13. Near-ground *u*-component, different forest drags, Model-1.
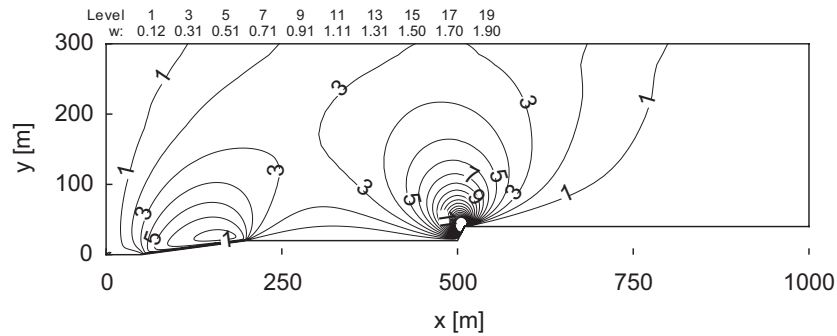
Fig. 14. Forest off, Model-1.
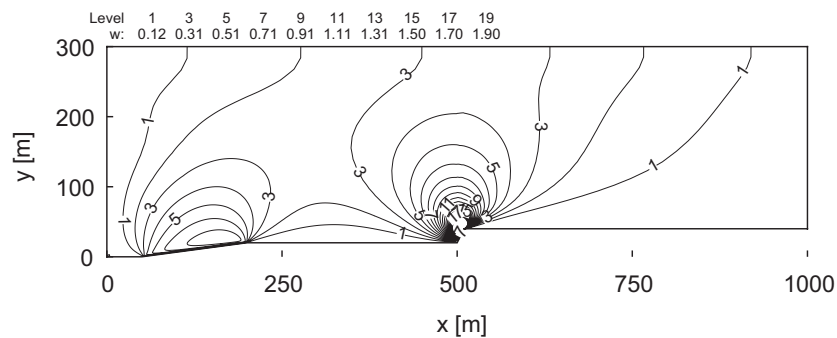
Fig. 15. Forest off, Model-2.

The forest block position is outlined by the white rectangle. See Figs. 14–17 showing the whole computational domain, the scale is in [m/s]. Figs. 18–21 show a detailed view on region behind the sudden topography step the scale is again in [m/s]. A fairly large recirculation zone develops behind the forest block, see Figs. 20 and 21. The predicted length from both mathematical models is comparable.
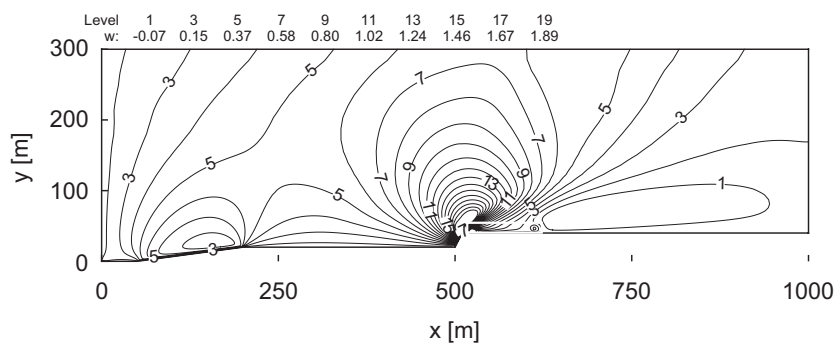
Fig. 16. Forest on, Model-1.
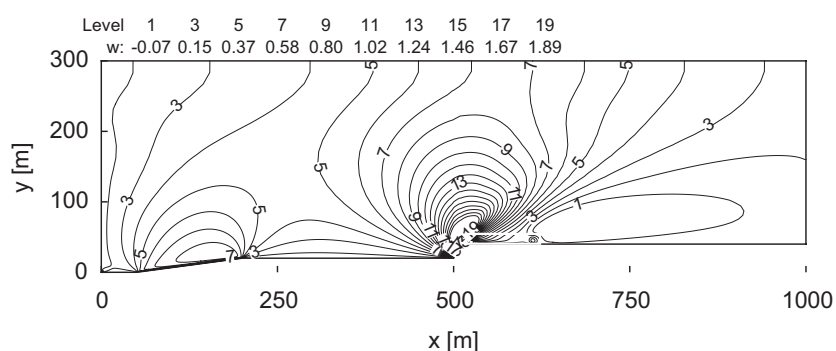
Fig. 17. Forest on, Model-2.
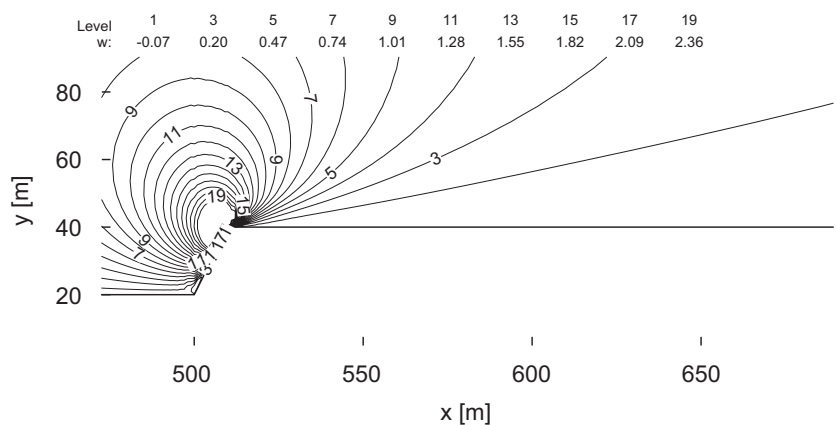
Fig. 18. Forest off, Model-1.

7.2. Real-case 3D-application of Model-1

Hereafter, only the Model-1 (2) has been applied to a problem of flow and pollution dispersion over a complex 3D-surface coal field located in the North Bohemia. Two configurations have been tested and compared

- With no forest blocks.
- With two forest blocks, one located just before and anther one placed just behind the depot.
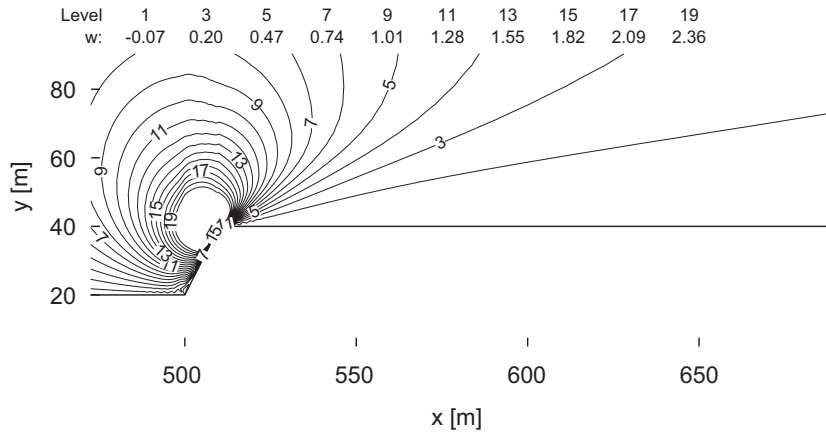
Fig. 19. Forest off, Model-2.
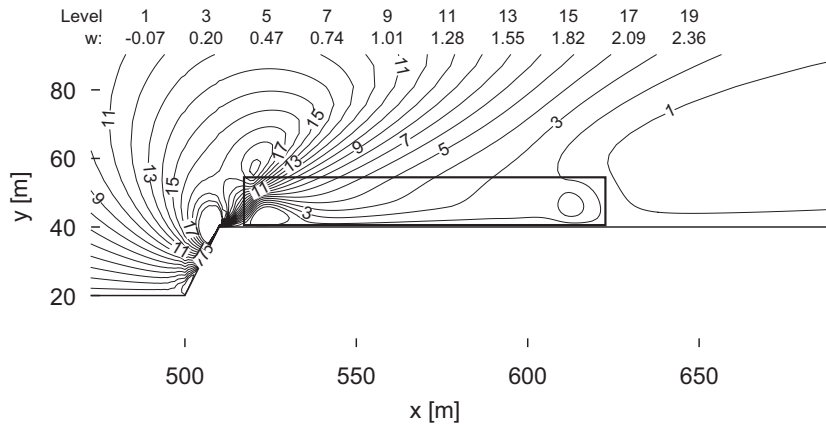
Fig. 20. Forest on, Model-1.
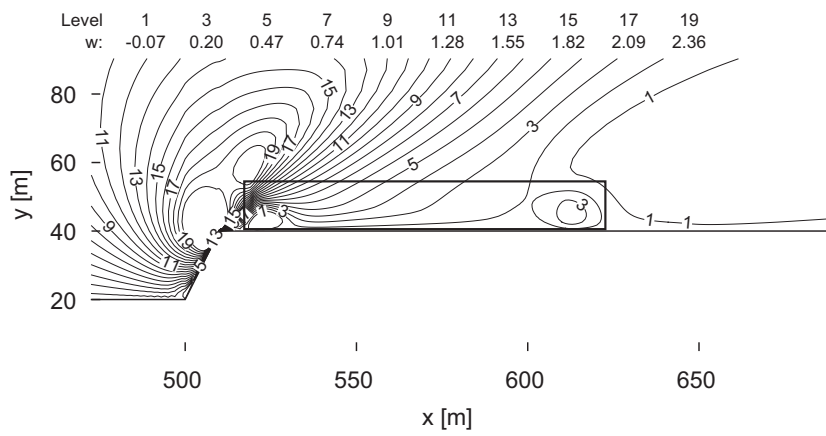
Fig. 21. Forest on, Model-2.

7.2.1. Problem description

The model of a real 3D-relief has been created on the basis of a topographic data obtained by the Brown Coal Research Institute in Most in the Czech Republic. The whole topography has been divided into two parts: a smaller part outlined by the *frame*-2 involved in the big one outlined by the *frame*-1, see Fig. 22. The location of a coal depot is outlined as well as the flow direction. The next parameters for both frames are as follows:

Frame-1: Length 800 m, width 480 m, with horizontal grid resolution of 8 m, gridded with 100 × 60 mesh cells.
Frame-2: Length 400 m, width 240 m, with horizontal grid resolution of 4 m, gridded with 100 × 60 mesh cells as well.

The height of two computational domains based on both frames is the same and equals ~600 m. Notice, both domains are gridded with 40 mesh cells in the vertical direction non-uniformly distributed with a higher density close to a ground. The origin of the coordinate system is located in the center of the coal depot which has the horizontal dimensions 80 × 20 m, see Fig. 22.

Remark, a study concerning the effect of the two forest blocks on the flow-field and also on the pollution dispersion has been performed on the *frame*-2 case only, see Fig. 24 where the blocks are outlined as black rectangles. The two forest blocks are 10 m high with the drag coefficient $r = 0.19$. The purpose of the forest blocks as a natural obstacle is to decrease the amount of the pollutant-dust transported away from the depot.

An important point is that the computational results related to the velocity-field based on the *frame*-1 topography (with horizontally coarser grid) are then interpolated in the *frame*-2 topography case (with finer grid) in order to reconstruct the inlet velocity profile in the second case. This is the reason for the two-frame computational setting of the problem due a high CPU-time cost of 3D-simulations.
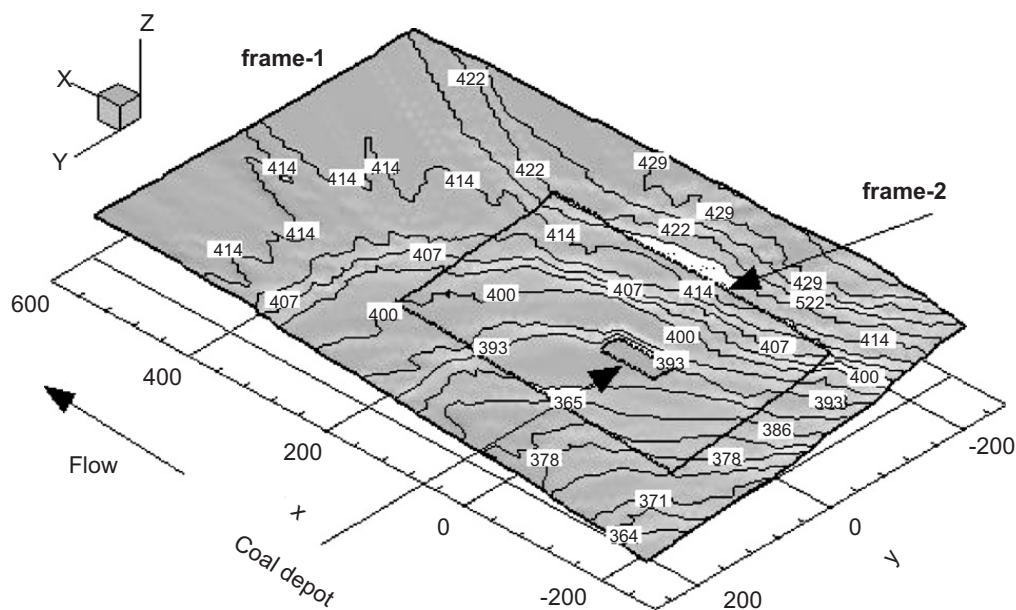
Fig. 22. A topography of 3D-model, altitude labels in [m].

The other parameters are: the mean free stream velocity $U_\infty = 10\,\text{m/s}$, the characteristic wall-normal domain dimension $L = 600\,\text{m}$ leading to the Reynolds number 4×10^8, the roughness parameter $z_0 = 0.1\,\text{m}$ and the power-law exponent $\frac{2}{9}$ is used to reconstruct the inlet velocity profile. No other volume forces are assumed and the intensity of a pollutant-dust emanating from the depot is supposed to be proportional to the local velocity gradient.
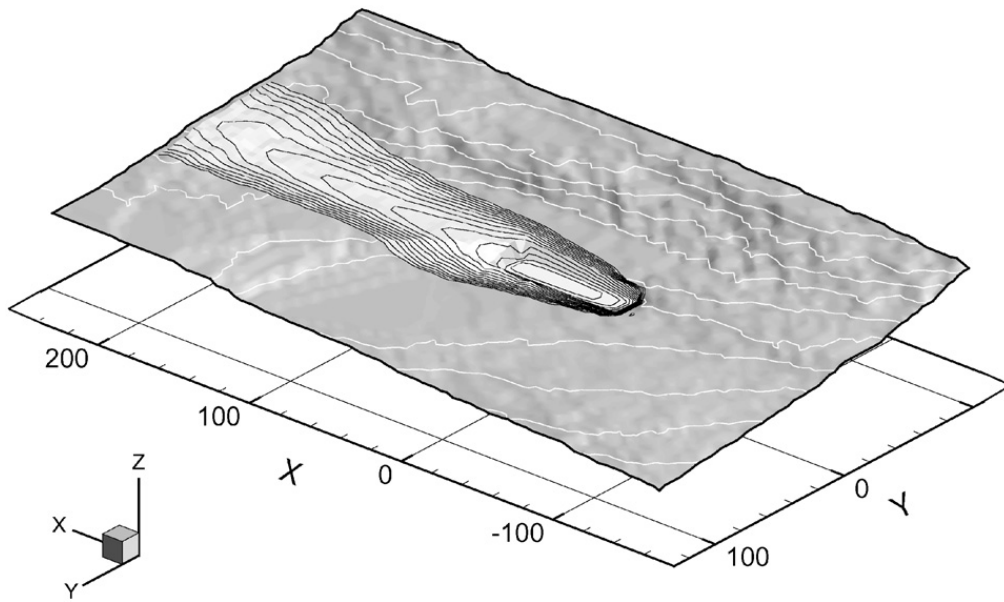

Fig. 23. Pollution dispersion with no forest blocks on frame-2.
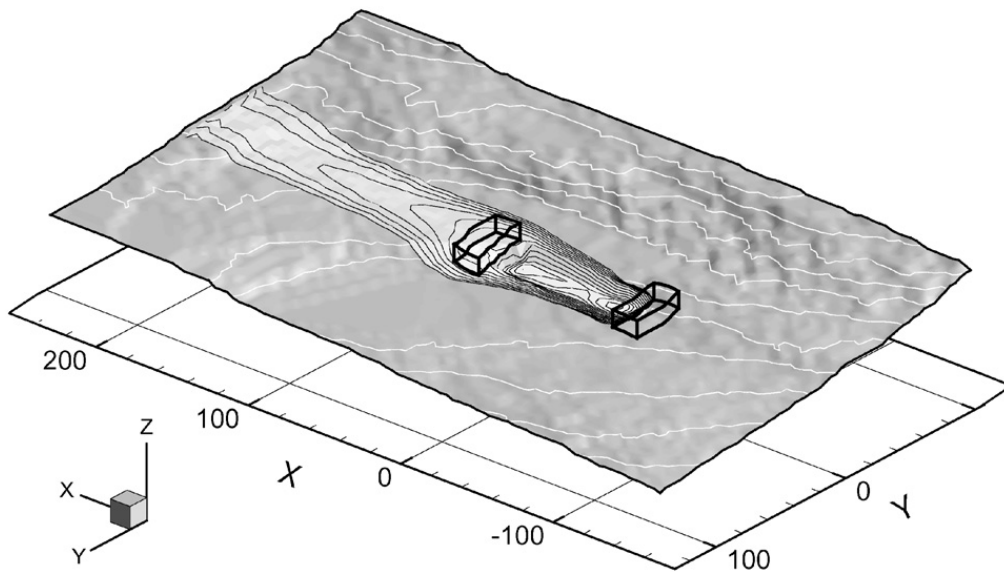
Fig. 24. Pollution dispersion with two forest blocks on frame-2.

7.2.2. Some numerical results

The effect of the two forest blocks on a near-ground pollution dispersion is shown in Figs. 23 and 24 equipped with the geographical altitude white contours and also with the pollutant concentration contours (log-scale) superimposed in the overlay mode. One can clearly see the decreased level of pollutant-dust concentration in the coal depot place and also in the downstream region which is supposed to be inhabited.

8. Conclusion

We have described in details both the Model-1 (2) and the Model-2 (14)–(16). A practical applicability and also a flexibility of the models have been demonstrated through a real-case atmospheric boundary layer 2D and 3D-flow applications. The 3D-case also includes a pollution dispersion of a passive pollutant-dust over a complex surface coal field which is partially covered by a high and porous forest stand influencing the flow-field.

The effect of the forest height/drag has been demonstrated on the basis of results obtained by both mathematical models applied to a 2D-flow simplified problem. I has been found that the codes predict quite a similar results. Moreover, the presence of a forest block significantly decelerates the incoming flow behind the forest and also deviates it from the original direction. The results from the 3D simulations indicate that the level of the pollutant concentration of dust drifted from a surface coal depot, located in between the two forest blocks, is also reduced in the down-stream region from the depot. Thus, a numerical design of the forest blocks represents a very promising methodology for a pollution dispersion control.

Acknowledgments

References

Almeida, G.P., Durao, D.F.G., Heitor, M.V., 1992. Wake flows behind two dimensional model hills. Exp. Thermal Fluid Sci. 7, 87.

Beneš, L., Sládek, I., Jaňour, Z., 2004. On the numerical modelling of 3D—atmospheric boundary layer flow. In: Harmonization within Atmospheric Dispersion Modelling for Regulatory Purposes, vol. 1. Garmisch–Parten Kirchen, Germany, pp. 340–344 ISBN 3-923704-44-5.

Bodnár, T., 2004. Numerical simulation of flows and pollution dispersion in atmospheric boundary layer. PhD thesis, Czech Technical University, Prague.

Bodnár, T., Kozel, K., Frauníé, Ph., Jaňour Z., 2000. Numerical simulation of flow and pollution dispersion in 3D atmospheric boundary layer. Computing and Visualization in Science, vol. 3, number 1–2. Springer, Berlin.

Bodnár, T., Frauníé, P., Kozel, K., Beneš, L., 2001. Numerical modelling of pollution dispersion in complex terrain. In: Air Pollution IX. WIT Press, Southampton, pp. 85–94 ISBN 1-85312-877-5.

Bodnár, T., Beneš, L., Jaňour, Z., Kozel, K., Sládek, I., 2003. On the complex atmospheric flow modelling including pollution dispersion. In: Conference—Wind Effects On Trees, Karlsruhe, pp. 183–188, ISBN 3-00-011922-1.

Castro, I.P., Apsley, D.D., 1997. Flow and dispersion over hills: comparison between numerical predictions and experimental data. J. Wind Eng. Ind. Aerodyn. 67 & 68, 375–386.

Davroux, A., Hoa, C., Laurence, D., 1995. Flow over a 2D hill—reference solutions for k–ε and second moment closure turbulence models, Workshop, Karlsruhe.

Kim, G.H., Lee, M.Ch., Lim, C.H., Kyong, H.N., 1997. An experimental and numerical study on the flow over two-dimensional hills. J. Wind Eng. Ind. Aerodyn. 66 (1), 17–33.

Sládek, I., 2005. Mathematical modelling and numerical solution of some 2D and 3D-cases of atmospheric boundary layer flow. PhD thesis, Czech Technical University, Prague.

Sládek, I., Kozel, K., Jaňour, Z., Gulíková, E., 2004. On the mathematical and numerical investigation of the atmospheric boundary layer flow with pollution dispersion. In: Conference—Urban Wind Engineering and Building Aerodynamics. VKI Brussels, pp. C.9.1–C.9.10 ISBN 2-930389-11-7.

Wilson, J.D., Flesch, T.K., 1999. Wind and remnant tree sway forest cutblocks. III. A windflow model to diagnose spatial variation. Agric. For. Meteorol. (93), 259–282.

E.2   Numerical Simulation of Flow over Barriers in Complex Terrain

BODNÁR T., BENEŠ L., KOZEL K.

In this paper the immersed boundary approach was used to evaluate the possible effect of large obstacles on the flow in atmospheric boundary layer. The immersed boundary method was used to overcome the difficulty of specific grid generation each time a new obstacle is simulated. In this way it was possible to perform all the simulations on the same grid that was only distorted due to the terrain orography. The obstacles were simulated separately. This was important in order to avoid highly distorted or multiblock grids, that would have been hard to handle together with the semi-implicit finite-difference scheme used for this case. The aim of these simulations was to get some idea about the modifications of flow field introduced by the artificial obstacles. This should serve as a guideline for the evaluation of pollution dispersion.

All the simulations presented in this paper were performed by T. Bodnár.

Numerical simulation of flow over barriers in complex terrain

T. Bodnár[2], L. Beneš[1] and K. Kozel[2]

[1] *Faculty of Mechanical Engineering, Czech Technical University - Prague, Czech Republic*
[2] *Institute of Thermomechanics, Academy of Sciences of the Czech Republic*
     Prague, Czech Republic

Summary. — This paper presents some of the results of numerical simulations of flow in the proximity of significant artificial terrain obstacles. The mathematical model is based on Reynolds averaged Navier-Stokes equations for incompressible flows. Turbulent closure of the model is obtained by a simple algebraic turbulence model. The numerical solution is carried out by the semi-implicit finite-difference scheme. The results of simple tests are presented and summarized. Model sensitivity has been studied with respect to the simulated obstacle size and shape.

PACS `92.60.Fm` – Boundary layer structure and processes.

Introduction

This study has been motivated by the request to evaluate the possible effect of downwind obstacles on the deposition of wind drifted coal dust. In the presented part of this project our attention was concentrated on the detailed computation of the flow field characteristics in the vicinity of large terrain obstacles. Special attempt has been made to localize the areas where the flow is decelerating or recirculating. These flow regimes could be critical from the point of view of surface particle deposition.

The problem of flow and pollution dispersion in the vicinity of terrain obstacles was deeply explored in numerous studies in the past. Most papers deal with geometrical set-up based on low smooth hills. One of the classical experimental works is the paper [1] where the wake flows behind 2D polynomial hills are explored. Flow over 2D sinusoidal topography with different hill slopes is studied experimentally in [2] and compared with numerical simulation in [3]. The influence of multiple 2D sinusoidal hills on the flow field is investigated in experimental study [4]. Some comparisons with CFD solutions were presented there. Similar study was presented also in [5]. An experimental investigation of flow and pollution dispersion in the disturbed boundary layer flow over a ridge was

published in papers [6] and [7]. The wind tunnel study of the flow structure and pollution dispersion from point sources in the vicinity of 3D single hill was published in papers [8] and [9]. In these papers series of wind tunnel experiments is described to show the importance of three-dimensionality of the flow- (and concentration-) field. Some further material especially concerning the simulated pollution dispersion can be found in the papers [10-16].

Another large group of studies focuses on the flow over artificial obstacles rather than over smooth hills. The flow over different solid and porous fences was experimentally investigated, *e.g.*, in [17-20] or [21]. The comparison of experimental data with numerical simulations could be found in [22]. The coal dust and sand dispersion in the presence of porous fences was explored, *e.g.*, in [23-26]. The effect of tree-blocks and forest edges on the wind flow and pollution dispersion and deposition was studied, *e.g.*, in [27, 28] or [29].

Most of the above mentioned studies were focused on more or less simple geometry, usually dealing with a flat terrain with single obstacles. The case we need to solve is based on real (and thus complex) orography, where the natural terrain profile dominates the flow. The artificial obstacles placed to the flow in this case only partially modify the flow and concentration patterns. Therefore it is essential for this study to deal with the actual orography corresponding to the true domain of interest.

The complex terrain profile used in this study represents a part of the opencast coal mine where there is placed a coal storage. This storage acts as a source of coal dust which is drifted by the wind. The detailed orography profile was obtained by a combination of data from several geographical resources. In order to get maximum of realistic details a laser scan of the terrain was performed and included into the orography profile. The aim of this study is to give both qualitative and quantitative guidelines for the evaluation of the environmental impact of artificial obstacles placed downwind from the coal storage.

1. – Mathematical model

The flow in atmospheric boundary is turbulent in most simulations. The fluid motion can be thus described by the Reynolds averaged Navier-Stokes equations (RANS). The non-conservative form of the RANS system is represented by the following equations:

$$(1) \qquad u_x + v_y + w_z = 0,$$

$$(2) \qquad V_t + uV_x + vV_y + wV_z = -\frac{\nabla p}{\rho} + [KV_x]_x + [KV_y]_y + [KV_z]_z.$$

Here $V = col(u, v, w)$ is the velocity vector, p is pressure, ρ is density.

The turbulence model is based on the Boussinesq hypothesis on the turbulent diffusion coefficient $K = \nu + \nu_T$ which is expressed as a sum of molecular and eddy viscosity[1]. Finally the following algebraic turbulence model was used to complete the governing

---

[1] The molecular viscosity is usually much smaller than the turbulent one, but it cannot be neglected because it guarantees that the turbulent diffusion coefficient K will remain stricly positive. This is important for the well posedness of the mathematical model and for the stability of the numerical solver.

$$\overleftarrow{\delta_s} = \frac{V_i - V_{i-1}}{\Delta s^-}$$

$$\overrightarrow{\delta_s} = \frac{V_{i+1} - V_i}{\Delta s^+}$$

$$\frac{\partial}{\partial x} = \frac{1}{\cos \alpha} \left(\frac{\partial}{\partial s_1} - \frac{\partial}{\partial z} \sin \alpha \right) \qquad \frac{\partial}{\partial y} = \frac{1}{\cos \beta} \left(\frac{\partial}{\partial s_2} - \frac{\partial}{\partial z} \sin \beta \right)$$

$$\delta_s = \frac{1}{2}(\overleftarrow{\delta_s} + \overrightarrow{\delta_s})$$

Fig. 1. – Local coordinate transformation.

system:

$$(3) \qquad K = \nu + \nu_T, \qquad \text{where} \qquad \nu_T = \ell^2 \left[\left(\frac{\partial u}{\partial z} \right)^2 + \left(\frac{\partial v}{\partial z} \right)^2 \right]^{1/2}.$$

The mixing length ℓ is computed according to the following formula:

$$(4) \qquad \ell = \frac{\varkappa(z + z_0)}{1 + \varkappa \frac{(z+z_0)}{\ell_\infty}}, \qquad \text{where} \qquad \ell_\infty = \frac{27 \, |V_G| \, 10^{-5}}{f_c}.$$

Here $f_c = 1.1 \times 10^{-4}$ ms denotes the Coriolis parameter and V_G is the geostrophic wind velocity at the upper boundary of domain.

2. – Numerical solution

2`1. *Finite-difference discretization.* – To discretize the governing system the non-orthogonal, structured, boundary (*i.e.* terrain), following mesh was constructed. Because of the mesh non-orthogonality it was necessary to transform the equations from the x-y-z coordinates to the mesh-wise directional local coordinate system s_1-s_2-z (see fig. 1).

To simplify the notation of discretized equations the operators of differences are introduced. The symbol δ_s denotes the central difference with respect to the direction $\boldsymbol{s}$. Similarly the $\overrightarrow{\delta_s}$, $\overleftarrow{\delta_s}$ denote the forward and backward differences.

2`2. *Semi-implicit finite-difference scheme.* – The system of governing equations (5), (6) should be transformed into the above-described mesh-wise local coordinate system.

$$(5) \qquad u_x + v_y + w_z = 0,$$

$$(6) \qquad V_t + uV_x + vV_y + wV_z = \underbrace{-\frac{\nabla p}{\rho} + [KV_x]_x + [KV_y]_y + [KV_z]_z}_{=\text{RHS}}.$$

Using the local coordinate transformation, this system could be rewritten so that the continuity equation (5) takes the form

$$(7) \qquad \frac{u_{s_1}}{\cos \alpha} + \frac{v_{s_2}}{\cos \beta} + w_z - u_z \tan \alpha - v_z \tan \beta = 0.$$
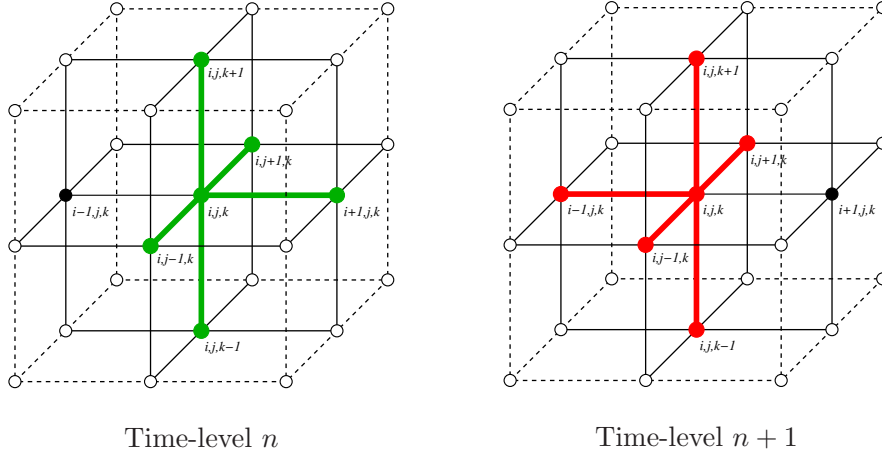
Time-level n · · · · · · · · · · · Time-level $n+1$

Fig. 2. – Computational stencil for semi-implicit FD scheme.

The momentum equations will then be modified to the following form[2]:

$$(8) \qquad V_t + \tilde{u}V_{s_1} + \tilde{v}V_{s_2} + \tilde{w}V_z = \widetilde{RHS}.$$

The modified coefficients are defined as follows:

$$\tilde{u} = \frac{u}{\cos\alpha}\,, \qquad \tilde{v} = \frac{v}{\cos\beta}\,, \qquad \tilde{w} = w - u\tan\alpha - v\tan\beta.$$

The right-hand side is transformed in a similar way. The left-hand side of momentum equations is discretized by the following way:

$$V_t \sim \overrightarrow{\delta_t}\mathsf{V}_{i,j,k}^n,$$

$$\tilde{u}V_{s_1} \sim \frac{1}{2}\left(\tilde{u}_{i+1/2}^n\overrightarrow{\delta_{s_1}}\mathsf{V}_{i,j,k}^n + \tilde{u}_{i-1/2}^n\overleftarrow{\delta_{s_1}}\mathsf{V}_{i,j,k}^{n+1}\right),$$

$$\tilde{v}V_{s_2} \sim \frac{1}{2}\left\{\frac{1}{2}\left(\tilde{v}_{j+1/2}^n\overrightarrow{\delta_{s_2}}\mathsf{V}_{i,j,k} + \tilde{v}_{j-1/2}^n\overleftarrow{\delta_{s_2}}\mathsf{V}_{i,j,k}\right)^n\right.$$

$$\left. + \frac{1}{2}\left(\tilde{v}_{j+1/2}^n\overrightarrow{\delta_{s_2}}\mathsf{V}_{i,j,k} + \tilde{v}_{j-1/2}^n\overleftarrow{\delta_{s_2}}\mathsf{V}_{i,j,k}\right)^{n+1}\right\},$$

$$\tilde{w}V_z \sim \frac{1}{2}\left\{\frac{1}{2}\left(\tilde{w}_{k+1/2}^n\overrightarrow{\delta_z}\mathsf{V}_{i,j,k} + \tilde{w}_{k-1/2}^n\overleftarrow{\delta_z}\mathsf{V}_{i,j,k}\right)^n\right.$$

$$\left. + \frac{1}{2}\left(\tilde{w}_{k+1/2}^n\overrightarrow{\delta_z}\mathsf{V}_{i,j,k} + \tilde{w}_{k-1/2}^n\overleftarrow{\delta_z}\mathsf{V}_{i,j,k}\right)^{n+1}\right\}.$$

The coefficients $\tilde{u}$, $\tilde{v}$, $\tilde{w}$ are fixed at the time-level n in order to linearize locally the system to obtain an Oseen-like iterative solver. The combination of different asymmetric space

---

[2] The $\widetilde{RHS}$ and $\overline{RHS}$ are the modified right-hand sides.

discretization at time levels n and $n+1$ allows us to construct finally the numerical scheme that is centered and second order in both space and time. The computational stencil is different for discretization at time level n and $n+1$ (see fig. 2). The dissipative terms on the right-hand side are approximated in the same manner. Using this discretization, the system of linear algebraic equations in each column of grid-points is obtained:

$$(9) \qquad a_1 \mathsf{V}_{i,j+1,k}^{n+1} + a_2 \mathsf{V}_{i,j,k}^{n+1} + a_3 \mathsf{V}_{i,j-1,k}^{n+1} + a_4 \mathsf{V}_{i,j,k+1}^{n+1} + a_5 \mathsf{V}_{i,j,k-1}^{n+1} = \overline{RHS}.$$

This system is solved iteratively in vertical plane $i = \text{const}$. So the five-diagonal system is converted into the three-diagonal one.

$$(10) \qquad a_5 \mathsf{V}_{i,j,k-1}^{\eta+1} + a_2 \mathsf{V}_{i,j,k}^{\eta+1} + a_4 \mathsf{V}_{i,j,k+1}^{\eta+1} = \overline{RHS} - a_1 \mathsf{V}_{i,j+1,k}^{\eta} - a_3 \mathsf{V}_{i,j-1,k}^{\eta+1}.$$

The η denotes here the iterative index. Usually after 3–5 iterations the values of $\mathsf{V} = (u, v, w)^T$ are known with sufficient accuracy. Exactly the same solution scheme can also be used for the scalar transport equations.

In the steady (or quasi-steady) problems the artificial compressibility method can be used and in such a case the pressure is updated from the modified continuity equation.

$$(11) \qquad\qquad\qquad p_t = -(u_x + v_y + w_z).$$

Also here the above-described semi-implicit discretization is used to keep the consistency with the momentum equations solver.

In order to improve the convergency of this method for high Reynolds numbers, the artificial viscosity terms $\mathsf{DV}_{i,j,k}^n$ are added. Then the solution algorithm skips to the time level $(n+1)$.

2$\cdot$3. *Artificial viscosity.* – The combination of artificial dissipation of second and fourth order is used.

$$\mathsf{DV}_i^n = \mathsf{D}^2 \mathsf{V}_i^n + \mathsf{D}^4 \mathsf{V}_i^n,$$

$$\mathsf{D}^2 \mathsf{V}_i^n = \tilde{\epsilon}_2 \Delta x^3 \frac{\partial}{\partial x} |\mathsf{V}_x| \mathsf{V}_x = \tilde{\epsilon}_2 \Delta x^2 (\epsilon_{i+1/2} \mathsf{V}_x - \epsilon_{i-1/2} \mathsf{V}_x),$$

$$\epsilon_{i+1/2} = \begin{cases} |\mathsf{V}_{i+1} - \mathsf{V}_i| & \text{for} \;\; |\mathsf{V}_{i+1} - \mathsf{V}_i| < \frac{K}{10}\,, \\ \frac{K}{10} & \text{for} \;\; |\mathsf{V}_{i+1} - \mathsf{V}_k| \geq \frac{K}{10}\,, \end{cases}$$

$$\mathsf{D}^4 \mathsf{V}_i^n = \tilde{\epsilon}_4 \Delta x^4 \mathsf{V}_{xxxx} = \tilde{\epsilon}_4 \left(\mathsf{V}_{i-2}^n - 4\mathsf{V}_{i-1}^n + 6\mathsf{V}_i^n - 4\mathsf{V}_{i+1}^n + \mathsf{V}_{i+2}^n \right).$$

The $K = \nu + \nu_t$ is the coefficient of turbulent diffusion. The coefficients $\tilde{\epsilon}_2, \tilde{\epsilon}_4 \in \mathsf{R}$ are constants of order Δx^2, respectively Δx^4.

The details of the numerical discretization could be found, *e.g.*, in [30, 31, 29].

3. – Numerical results

Numerical experiments were performed in a 3D domain of the size $500 \times 250 \times 400$ meters. The bottom boundary represents a complex terrain orography. The contours of terrain elevation are shown in the following figure 3. The height difference between the
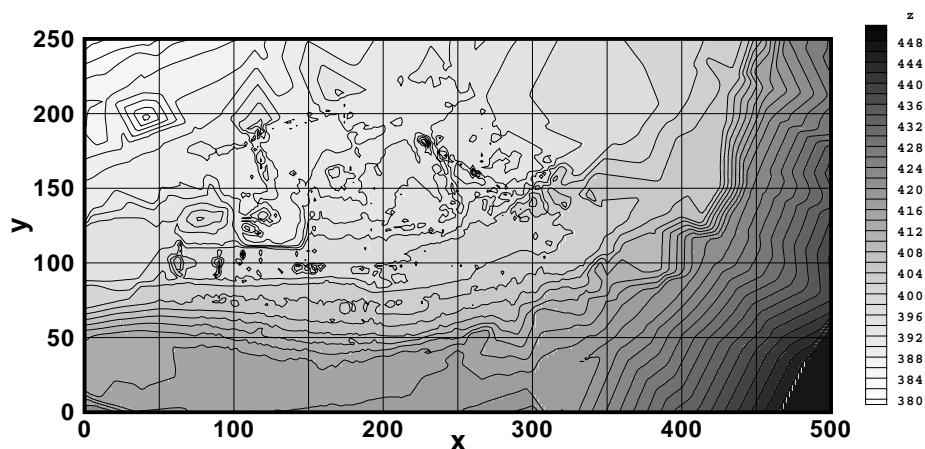
Fig. 3. – Terrain elevation contours.

highest and the lowest point of the terrain profile is about 70 meters. The wind flow in the model domain is forced by the prescribed velocity profile at the inlet ($x = 0$). The maximum velocity 10 m/s is achieved at the upper boundary of the domain.

Figure 4 shows the wind flow streamlines at near-ground level for the basic variant with no obstacles. This variant is used for reference and comparison because it represents the actual state. In order to slow down and deflect the flow we have placed different obstacles downwind from the expected source of pollution. The obstacles differ in their shape and size. The first series of experiments uses an obstacle formed by a block with horizontal size 10×60 meters which is rotated by 45 degrees with respect to mainstream flow direction. The height of the obstacles varies between 3 and 9 meters. The immersed boundary approach was used to simulate this impermeable block.
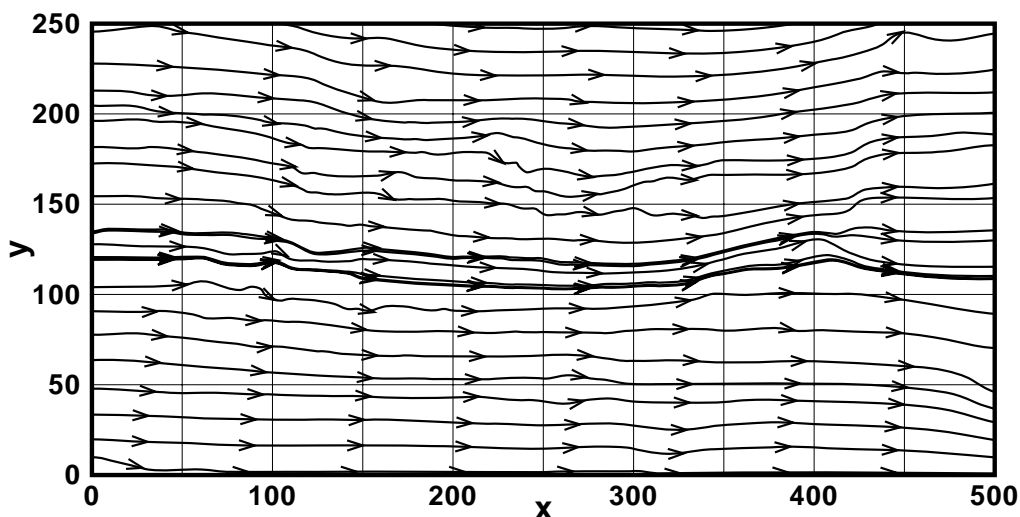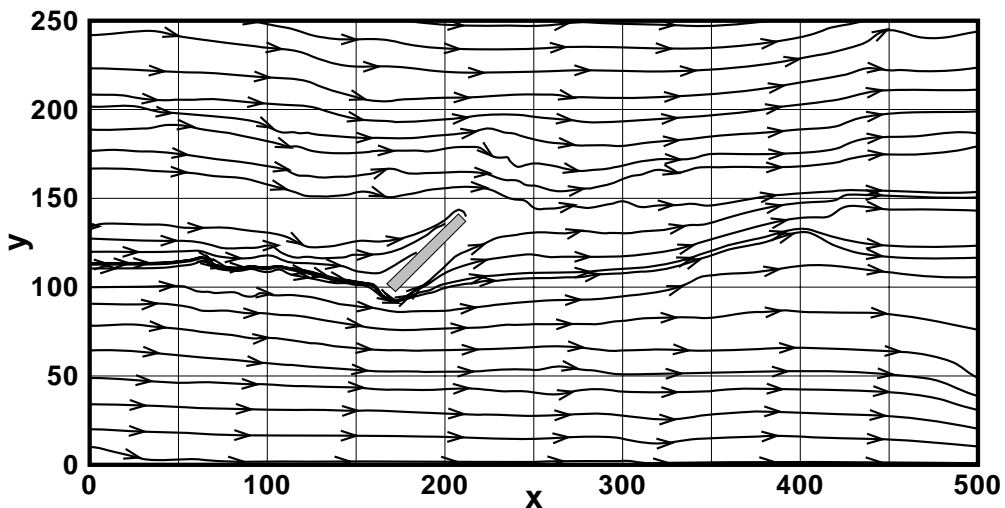

Fig. 4. – Wind flow streamlines at the near-ground level for the case without obstacles.
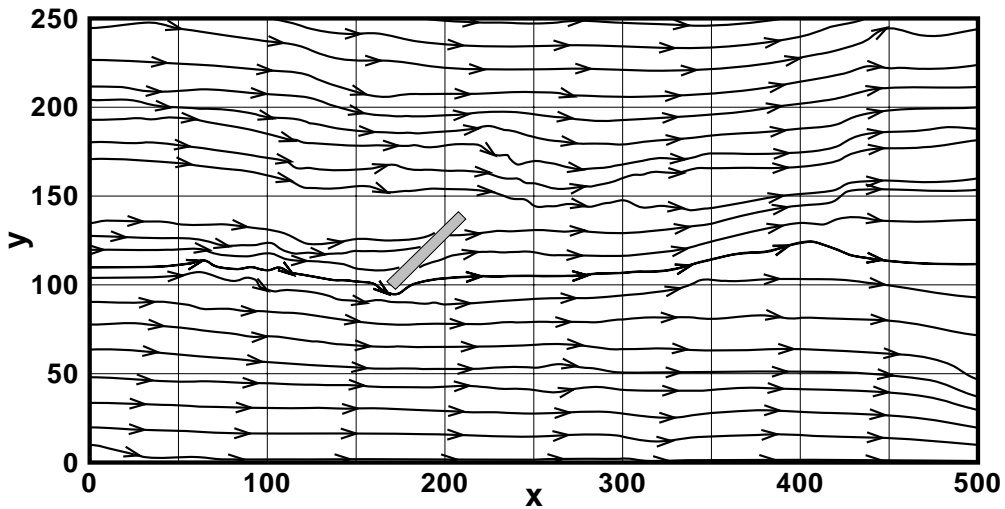
Fig. 5. – Wind flow streamlines at the near-ground level for the case with obstacle of height 3 meters.

In order to evaluate the impact of obstacle height on the flow the simulations were run for the case with single obstacle with height 3, 6 and 9 meters. The streamlines at the near-ground level for these cases are shown in figs. 5, 6 and 7. From the comparison of figs. 5, 6 and 7 it is clearly visible that the increasing height of the obstacle leads to significantly higher flow deviations. For the obstacle height 6 and 9 meters the impact of the artificial obstacle is stronger (at least locally) than the influence of the local orography. However even for the highest obstacle the flow is only disturbed locally and no larger scale flow pattern modification was observed.
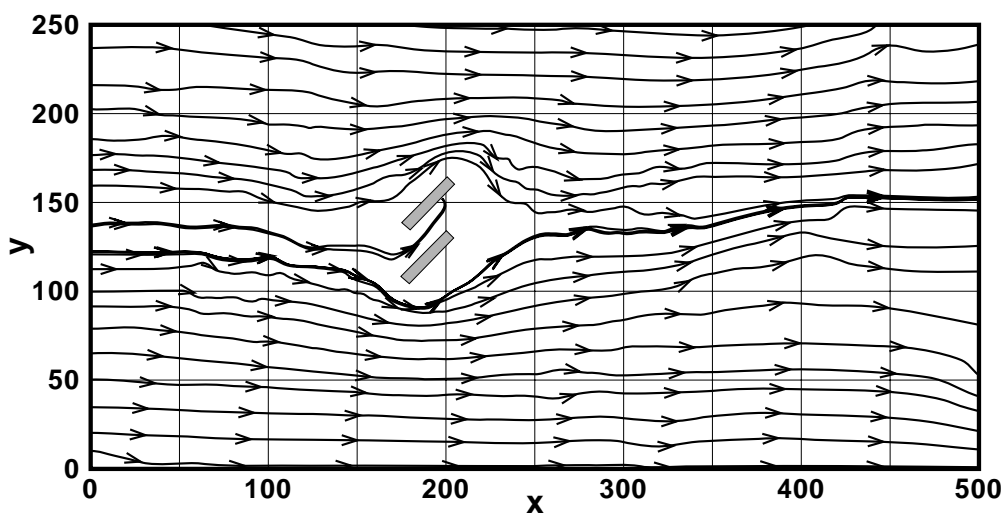

Fig. 6. – Wind flow streamlines at the near-ground level for the case with obstacle of height 6 meters.
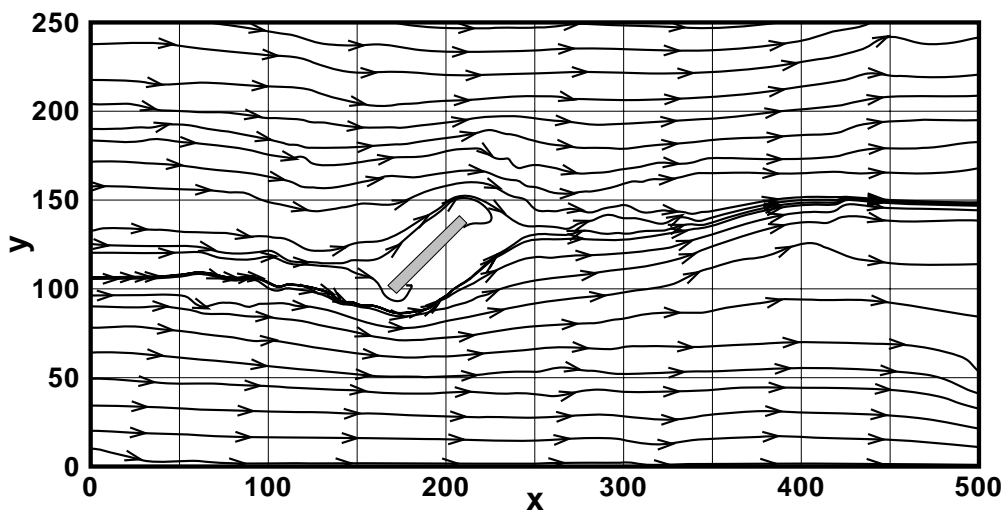
Fig. 7. – Wind flow streamlines at the near-ground level for the case with obstacle of height 9 meters.

From the technological point of view it is not possible to build at the investigated site obstacles higher than 9 meters and also the horizontal size of obstacles is strictly limited. Thus when seeking for obstacles leading to more profound flow modifications it is not possible to increase the obstacles dimensions. Therefore some other configurations of obstacles of similar size were investigated assuming that it is possible to get better results with another obstacle shape rather than larger size.

Two other variants have been tested as an attempt to increase the flow deflection while respecting the technological obstacle size limitations. Instead of one large, two

Fig. 8. – Wind flow streamlines at the near-ground level for the case with two parallel obstacles of height 9 meters.
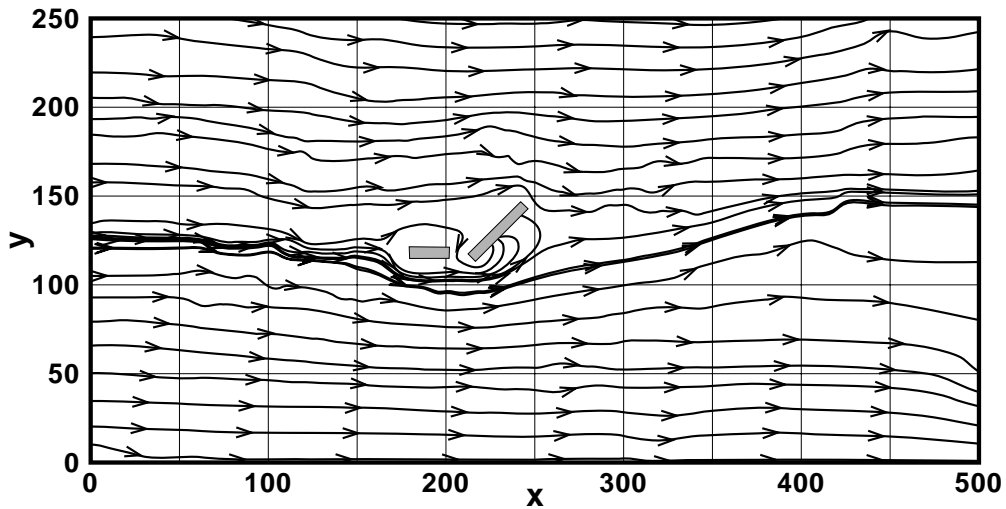
Fig. 9. – Wind flow streamlines at the near-ground level for the case with two obstacles of height 9 meters.

obstacles of smaller size and different configuration have been assumed. In both cases the height of obstacles was 9 meters. The near-ground stramlines are shown in figs. 8 and 9. The simulation results have shown that the obstacles placed in the proximity of the expected pollution source have only local impact on the flow field.

Thus it seems that it is not possible to achieve any larger scale flow deflection and modify the pollutant dispersion trajectories. The only way to influence the downstream airborne dust concentrations is to enhance the particle sedimentation. From this point of view it is evident that the slower the flow is, the more particles will fall out of the
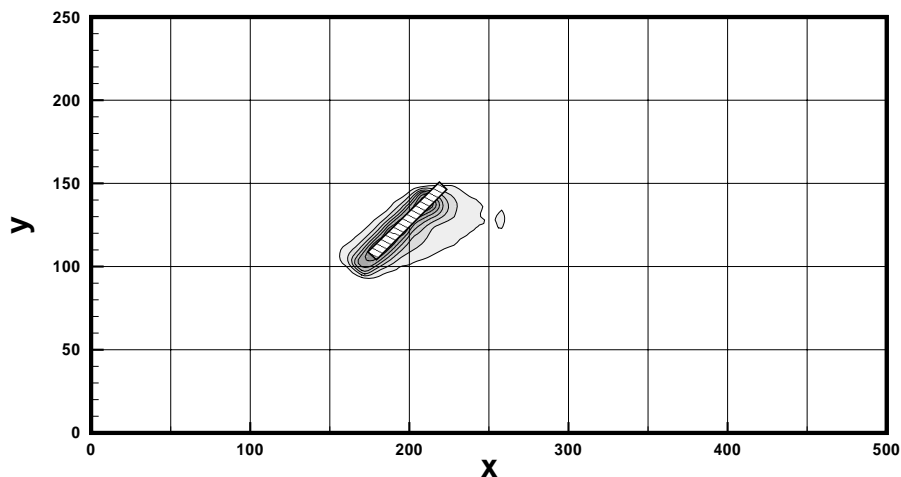
Fig. 10. – Contours of near-ground wind slow-down for the case of obstacle of height 3 meters with respect to the variant with no obstacles.
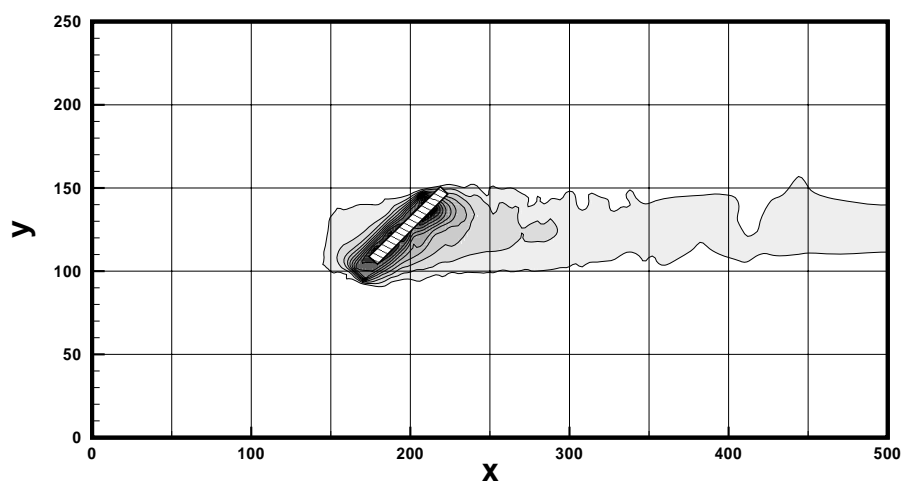
Fig. 11. – Contours of near-ground wind slow-down for the case of obstacle of height 6 meters with respect to the variant with no obstacles.

flow and sediment on the ground. In order to give some hints for evaluation of dust sedimentation, the above mentioned variants of obstacles were evaluated from the point of view of flow speed-up/slow-down at the near-ground level. As the flow slows down, the sedimentation of wind-driven particles becomes more significant and thus to find the regions of decelerated flow is of essential importance. The velocity magnitude fields for all the above-described obstacle configurations were compared with the basic variant without obstacles. This allows us to separate the effect of different obstacles on flow deceleration.
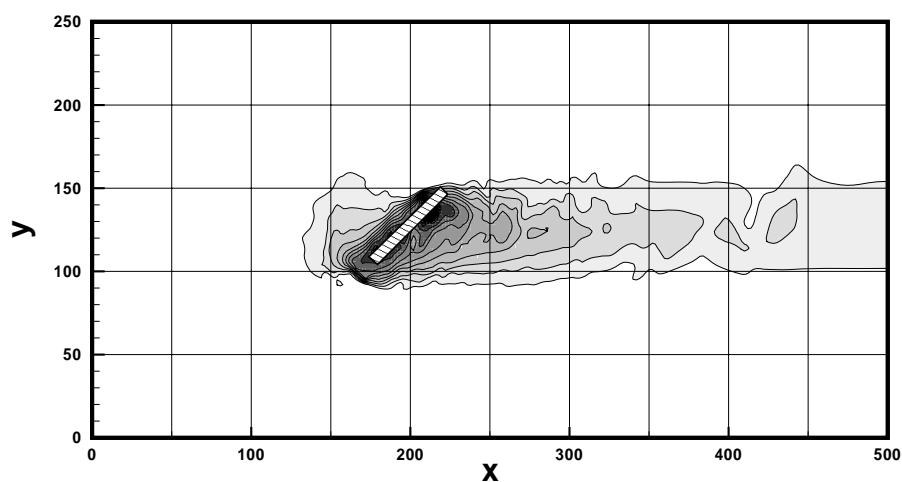
Fig. 12. – Contours of near-ground wind slow-down for the case of obstacle of height 9 meters with respect to the variant with no obstacles.
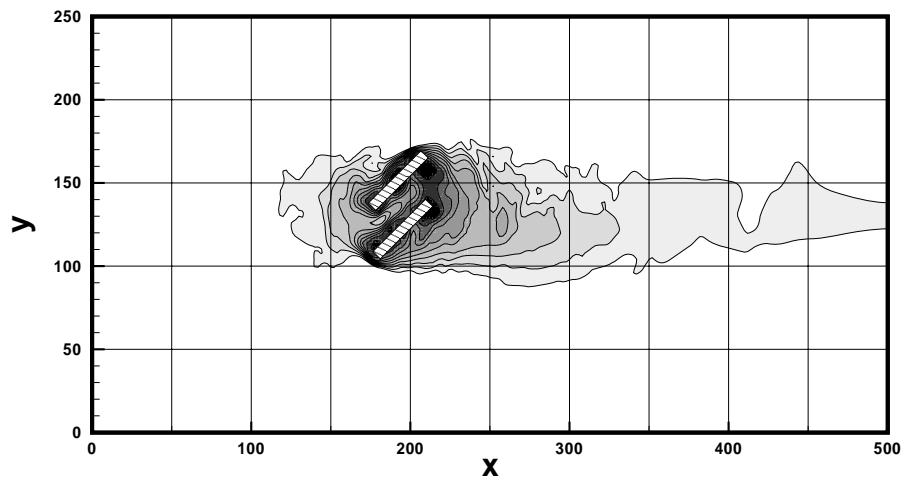
Fig. 13. – Contours of near-ground wind slow-down for the case of two parallel obstacles of height 9 meters with respect to the variant with no obstacles.

Figures 10, 11 and 12 show the case where the obstacle is formed by one single block of height 3, 6 or 9 meters. The contours of the flow deceleration are drawn at the near-ground level where the deposition of wind-drifted particles could occur. The comparison of figs. 10, 11 and 12 again shows the increasing effect of the wind-barriers with their increasing height.

The remaining two variants with two smaller obstacles were compared with the basic case in the same way. The flow deceleration for these cases is drawn in figs. 13 and 14. In order to better understand the effects of different variants of wind-breaking obstacles the detail of both, flow patterns and deceleration contours is drawn for the three most promising variants in figs. 15, 16 and 17. From the comparison of the near-ground wind
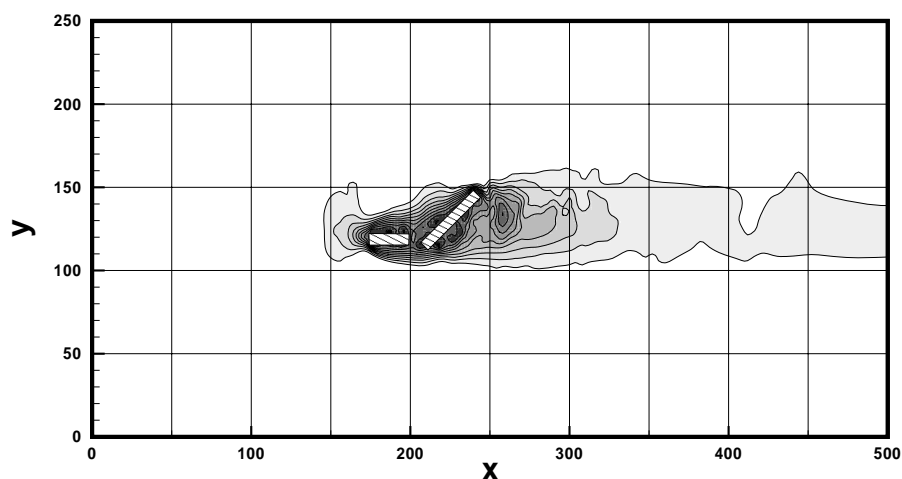

Fig. 14. – Contours of near-ground wind slow-down for the case of two different obstacles of height 9 meters with respect to the variant with no obstacles.
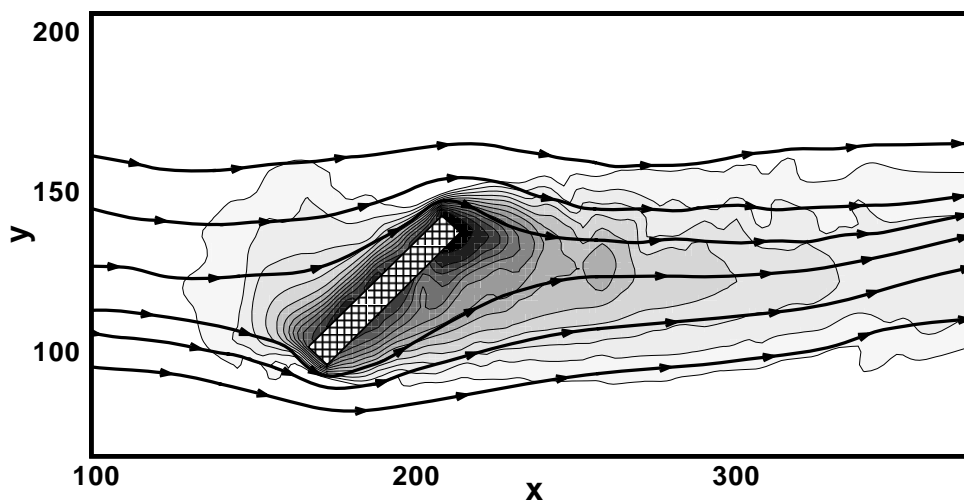
Fig. 15. – Streamlines and contours of wind slow-down at the near-ground level for the case of one large obstacle of height 9 meters with respect to the variant with no obstacles.

slow-down it seems that the variant with two smaller parallel obstacles offers a slightly larger region of flow deceleration and also the local flow deceleration is higher than for the other two variants. Moreover the building area needed for this variant of wind-breakers is a little bit smaller than for the other two cases.
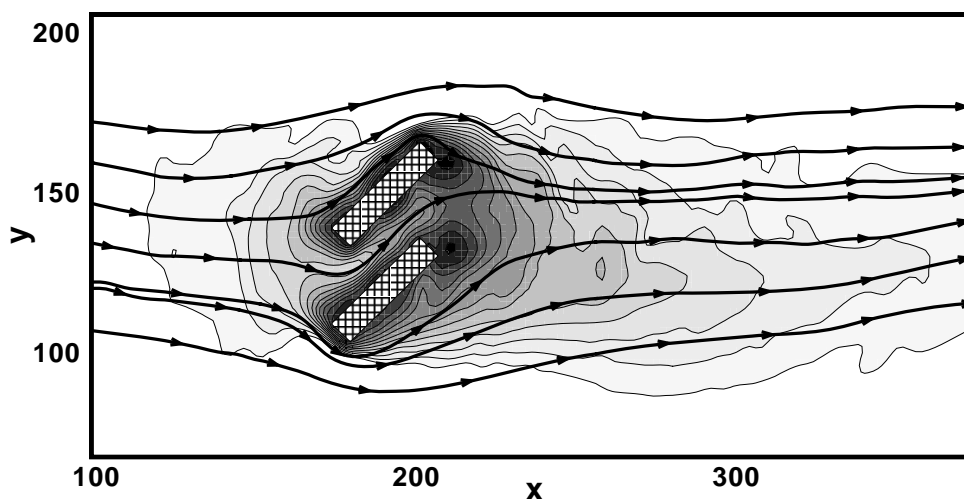

Fig. 16. – Streamlines and contours of wind slow-down at the near-ground level for the case of two parallel obstacles of height 9 meters with respect to the variant with no obstacles.
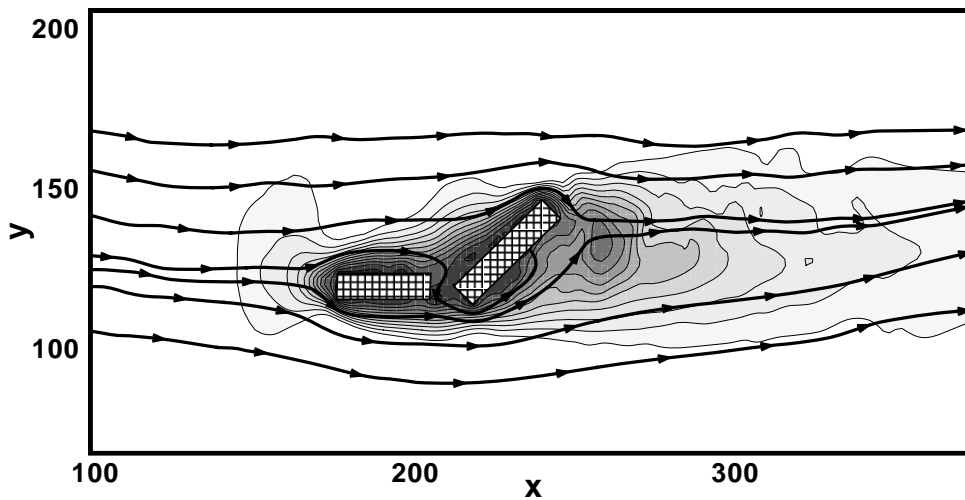
Fig. 17. – Streamlines and contours of wind slow-down at the near-ground level for the case of two different obstacles of height 9 meters with respect to the variant with no obstacles.

4. – Conclusions, remarks

The selected mathematical model is able to properly describe the pollution dispersion problems in complex terrain. Even if more sofisticated models are available for both the flow and the turbulence parametrization, the kind of model used in this study seems to be the right choice for the solution of complex pollution dispersion problems on engineering level.

The numerical method used to solve the set of governing equations has proved sufficient robustness and efficiency for reliable solution of the discussed type of problems. The simple second-order, central in space and time, finite-difference discretization in combination with appropriate artificial viscosity stabilization is very easy to implement and use, so it can be employed without excessive requirements on users and computational resources. The presented numerical simulations have shown that the effect of simulated obstacles has only local impact on the velocity field. This is caused mainly by the complexity of the terrain, where the orography profile involves height changes with scales much larger than the maximum available height of the simulated obstacles. Thus the orography effect is dominant in this case. More detailed study of dust sedimentation should be performed in order to quantify the effects of obstacles on deposition of particles of different sizes. The positive impact of wind-breaking barriers on the deposition of larger particles may be outbalanced by the increase of the turbulent mixing of the smaller particles. Another possible way of the future extension of this study is to assume some of the permeable wind-breaking obstacles, like, *e.g.*, porous fences or forest blocks. This kind of obstacles may be more efficient in dissipating the energy of wind and thus enhancing the sedimentation of airborne particles. The outputs of presented numerical simulations allow very detailed comparison of several variants of wind-barriers. Even simple side-by-side comparison of the above presented figures helps in evaluation of environmental impact and efficiency of the proposed wind-barriers.

* * *

REFERENCES

[1] ALMEIDA G. P., DURÃO D. F. G. and HEITOR M. V., *Exp. Thermal Fluid Sci.*, **7** (1993) 87.
[2] FERREIRA A. D., SILVA M. C. G., VIEGAS D. X. and LOPES A. G., *J. Wind Eng. Ind. Aerodyn.*, **38** (1991) 109.
[3] FERREIRA A. D., LOPES A. M. G., VIEGAS D. X. and SOUSA A. C. M., *J. Wind Eng. Ind. Aerodyn.*, **54/55** (1995) 173.
[4] CARPENTER P. and LOCKE N., *J. Wind Eng. Ind. Aerodyn.*, **83** (1999) 109.
[5] KIM H. G., LEE C. M., LIM H. C. and KYONG N. H., *J. Wind Eng. Ind. Aerodyn.*, **66** (1997) 17.
[6] ARYA S. P. S. and SHIPMAN M. S., *Atmos. Environ.*, **15** (1981) 1173.
[7] ARYA S. P. S., SHIPMAN M. S. and COURTNEY L. Y., *Atmos. Environ.*, **15** (1981) 1185.
[8] SNYDER W. H. and BRITTER R. E., *Atmos. Environ.*, **21** (1987) 735.
[9] CASTRO I. P. and SNYDER W. H., *Atmos. Environ.*, **16** (1982) 1869.
[10] GONG W. and IBBETSON A., *Boundary-Layer Meteorol.*, **49** (1989) 113.
[11] GONG W., *Boundary-Layer Meteorol.*, **54** (1991) 211.
[12] CROOKS G. and RAMSAY S., *Boundary-Layer Meteorol.*, **66** (1993) 155.
[13] ARYA S. P. S., CAPUANO M. E. and FAGEN L. C., *Atmos. Environ.*, **21** (1987) 753.
[14] SNYDER W. H., *Atmos. Environ. A*, **24** (1990) 2071.
[15] CASTRO I. P. and APSLEY D. D., *J. Wind Eng. Ind. Aerodyn.*, **67** & **68** (1997) 375.
[16] CASTRO I. P. and APSLEY D. D., *Atmos. Environ.*, **31** (1997) 839.
[17] LEE S. J. and KIM H. B., *J. Wind Eng. Ind. Aerodyn.*, **80** (1999) 311.
[18] PARK C. W. and LEE S. J., *J. Wind Eng. Ind. Aerodyn.*, **91** (2003) 165.
[19] WANG H. and TAKLE E. S., *Agric. Forest Meteorol.*, **81** (1996) 95.
[20] WILSON J. D. and YEE E., *Agric. Forest Meteorol.*, **115** (2003) 31.
[21] YARAGAL S. C., RAM H. S. G. and MURTHY K. K., *J. Wind Eng. Ind. Aerodyn.*, **66** (1997) 127.
[22] PACKWOOD A. R., *J. Wind Eng. Ind. Aerodyn.*, **88** (2000) 75.
[23] LEE S. J. and PARK C. W., *J. Wind Eng. Ind. Aerodyn.*, **84** (2000) 101.
[24] LEE S. J., PARK K. C. and PARK C. W., *Atmos. Environ.*, **36** (2002) 1453.
[25] ZAGHLOUL N. A., *Atmos. Model. Software*, **12** (1997) 113.
[26] PARK C. W. and LEE S. J., *Atmos. Environ.*, **36** (2002) 2171.
[27] SLÁDEK I., BODNÁR T. and KOZEL K., *J. Wind Eng. Ind. Aerodyn.*, **95** (2007) 9.
[28] OULD-DADA Z., COPPLESTONE D., TOAL M. and SHAW G., *Atmos. Environ.*, **36** (2002) 5595.
[29] BENEŠ L., BODNÁR T., FRAUNIÉ PH. and KOZEL K., *Numerical modelling of pollution dispersion in 3D atmospheric boundary layer*, in SPORTISSE B. (Editor), *Air Pollution Modelling and Simulation* (Springer Verlag) 2002, pp. 69-78.
[30] BODNÁR T., KOZEL K., FRAUNIÉ PH. and JAŇOUR Z., *Comput. Visualization Sci.*, **3** (2000) 3.
[31] BODNÁR T., KOZEL K., FRAUNIÉ PH. and BENEŠ L., *Numerical modelling of pollution dispersion in complex terrain*, in *Air Pollution IX* (WIT Press) 2001, pp. 85-94.

E.3   Application of Compact Finite-Difference Schemes to Simulations of Stably Stratified Fluid Flows

BODNÁR T., BENEŠ L., FRAUNIÉ PH., KOZEL K.

This paper is one of the first where we have presented numerical results from new generation of numerical codes. The compact finite-difference scheme (with compact filters for stabilization) implemented by the author of this work was compared against the AUSM finite-volume scheme. The model solved here was the Boussinesq approximation of stably stratified flow. Despite of the simple test setup, the flow-field is quite complex featuring large wave fields. The tests have shown superior resolution of the family of compact finite-difference schemes for this case. The issues related to numerical damping and grid independence were studied in detail. The tests have helped to validate the numerical methods.

In this paper T. Bodnár performed all the simulations using compact finite-difference scheme. The finite-volume results were provided by Luděk Beneš using his own code.

Contents lists available at SciVerse ScienceDirect

Applied Mathematics and Computation

journal homepage: www.elsevier.com/locate/amc

Application of compact finite-difference schemes to simulations of stably stratified fluid flows

T. Bodnár [a,b,*], L. Beneš [a], Ph. Fraunié [c], K. Kozel [a,b]

[a] *Department of Technical Mathematics, Faculty of Mechanical Engineering, Czech Technical University, Karlovo Náměstí 13, 121 35 Prague 2, Czech Republic*
[b] *Institute of Thermomechanics, Academy of Sciences of Czech Republic, Dolejškova 5, 182 00 Prague 8, Czech Republic*
[c] *Université du Sud Toulon-Var, Laboratoire de Sondages Electromagnétiques de l'Environnement Terrestre, Bâtiment F, BP 132, 83957 La Garde Cedex, France*

ARTICLE INFO

ABSTRACT

This paper presents a comparison of the results of numerical simulations obtained by two different numerical methods for one specific case of stably stratified incompressible flow. The focus in this paper is on the numerical results obtained using some of the compact finite-difference discretizations introduced in the paper [1]. The numerical scheme itself follows the principle of semi-discretisation, with high order compact discretisation in space, while the time integration is carried out by the Strong Stability Preserving Runge–Kutta scheme. Results are compared against the reference solution obtained by the AUSM finite volume method. The test case used to demonstrate the capabilities of selected numerical methods represents the flow of stably stratified fluid over low, smooth, hill-like wall mounted obstacle.

© 2011 Elsevier Inc. All rights reserved.

1. Introduction

The mathematical modelling and numerical simulation of stratified fluid flow presents a challenging problem with many interesting applications. Stably stratified flows form a subclass of variable density flows where the mean flow density gradient points in the direction gravity force. Such a specific configuration results in a buoyancy force that is responsible for very distinct flow behaviour manifested by a presence of large-scale wave patterns in the flow-field.

From the numerical point of view, the simulations of stratified fluid flows are in general more demanding than the solution of similar non-stratified flow cases (see our previous work [2–5] or [6]). There are several arguments supporting this statement. First of all, the governing system describing the variable density fluid flow involves one more equation with respect to classical (constant density) incompressible Navier–Stokes equations. It is the transport equation for the density (or its perturbation), which is coupled to momentum equations by a buoyancy term (see Section 2). As a consequence of this buoyant force the obstacles in flow generate waves that propagate at long distances. These waves need to be properly resolved, without unphysical damping or dispersion. Moreover the appearance of these waves should not be significantly affected by the artificial boundaries of the computational domain. All these aspects of stably stratified fluid flows are addressed in this paper.

The above mentioned characteristic behaviour led us to the idea to use some of the compact finite-difference schemes for the simulation of stratified fluid flows. These schemes have successfully been applied in the field of computational aeroacoustics where they became a standard tool in simulations of wave propagation phenomena. These methods offer a relatively simple way of construction of formally high order discretisations with well defined diffusion and dispersion properties.

---

* Corresponding author at: Department of Technical Mathematics, Faculty of Mechanical Engineering, Czech Technical University, Karlovo Náměstí 13, 121 35 Prague 2, Czech Republic.
  E-mail address: Tomas.Bodnar@fs.cvut.cz (T. Bodnár).

2. Mathematical model

This section describes in detail the development of the simplified mathematical model for variable density incompressible flow. The emphasise is on the explanation of the simplifications made in the model and their justification.

2.1. Full incompressible model

The motion equations describing the flow of incompressible fluid could be written in the following general form [1]:

$$\frac{\partial \rho}{\partial t} + \operatorname{div}(\rho \boldsymbol{u}) = 0, \tag{1}$$

$$\frac{\partial \rho \boldsymbol{u}}{\partial t} + \operatorname{div}(\rho \boldsymbol{u} \otimes \boldsymbol{u}) = \operatorname{div} \mathbb{S} + \rho \boldsymbol{f}. \tag{2}$$

These equations should be complemented by the incompressibility constraint $\operatorname{div} \boldsymbol{u} = 0$ and the rheological constitutive relation for Newtonian incompressible fluid $\mathbb{S} = -p\mathbb{I} + 2\mu\mathbb{D}$ (with $\mathbb{D}$ being the symmetric part of the velocity gradient and $\mathbb{I}$ standing for the identity tensor). Expressing further the gravity force vector as $\boldsymbol{f} = (0,0,g)$, leads (exactly) to the following set of governing equations for unknowns $\boldsymbol{u}$, p and ρ:

$$\frac{\partial u}{\partial x} + \frac{\partial v}{\partial y} + \frac{\partial w}{\partial z} = 0, \tag{3}$$

$$\frac{\partial \rho}{\partial t} + \frac{\partial(\rho u)}{\partial x} + \frac{\partial(\rho v)}{\partial y} + \frac{\partial(\rho w)}{\partial z} = 0, \tag{4}$$

$$\frac{\partial(\rho u)}{\partial t} + \frac{\partial(\rho u^2)}{\partial x} + \frac{\partial(\rho uv)}{\partial y} + \frac{\partial(\rho uw)}{\partial z} = -\frac{\partial p}{\partial x} + \mu \Delta u, \tag{5}$$

$$\frac{\partial(\rho v)}{\partial t} + \frac{\partial(\rho uv)}{\partial x} + \frac{\partial(\rho v^2)}{\partial y} + \frac{\partial(\rho vw)}{\partial z} = -\frac{\partial p}{\partial y} + \mu \Delta v, \tag{6}$$

$$\frac{\partial(\rho w)}{\partial t} + \frac{\partial(\rho uw)}{\partial x} + \frac{\partial(\rho vw)}{\partial y} + \frac{\partial(\rho w^2)}{\partial z} = -\frac{\partial p}{\partial z} + \mu \Delta w + \rho g. \tag{7}$$

The conservation of mass is represented by the continuity Eq. (4) can be written in the vector form

$$\frac{\partial \rho}{\partial t} + \operatorname{div}(\rho \boldsymbol{u}) = 0. \tag{8}$$

Using the chain rule of differentiation this equation can be rewritten as

$$\frac{\partial \rho}{\partial t} + \boldsymbol{u} \cdot \operatorname{grad} \rho = -\rho \operatorname{div} \boldsymbol{u}. \tag{9}$$

For incompressible flows satisfying the divergence-free constraint $\operatorname{div} \boldsymbol{u} = 0$, the right-hand side of Eq. (9) vanishes and thus the continuity equation reduces to transport (advection) equation for density ρ:

$$\frac{\partial \rho}{\partial t} + \boldsymbol{u} \cdot \operatorname{grad} \rho = 0. \tag{10}$$

This equation can be used together with the chain rule of differentiation to rewrite the left-hand side of the momentum balance (2):

$$\frac{\partial \rho \boldsymbol{u}}{\partial t} + \operatorname{div}(\rho \boldsymbol{u} \otimes \boldsymbol{u}) = \boldsymbol{u}\frac{\partial \rho}{\partial t} + \rho\frac{\partial \boldsymbol{u}}{\partial t} + \rho \operatorname{div}(\boldsymbol{u} \otimes \boldsymbol{u}) + \boldsymbol{u}(\boldsymbol{u} \cdot \operatorname{grad} \rho) = \rho\left(\frac{\partial \boldsymbol{u}}{\partial t} + \operatorname{div}(\boldsymbol{u} \otimes \boldsymbol{u})\right) + \boldsymbol{u}\underbrace{\left(\frac{\partial \rho}{\partial t} + \boldsymbol{u} \cdot \operatorname{grad} \rho\right)}_{=0}. \tag{11}$$

Using the above described manipulation, the governing system (3)–(7) could alternatively be rewritten as:

$$\frac{\partial u}{\partial x} + \frac{\partial v}{\partial y} + \frac{\partial w}{\partial z} = 0, \tag{12}$$

$$\frac{\partial \rho}{\partial t} + \frac{\partial(\rho u)}{\partial x} + \frac{\partial(\rho v)}{\partial y} + \frac{\partial(\rho w)}{\partial z} = 0, \tag{13}$$

$$\rho\left(\frac{\partial u}{\partial t} + \frac{\partial(u^2)}{\partial x} + \frac{\partial(uv)}{\partial y} + \frac{\partial(uw)}{\partial z}\right) = -\frac{\partial p}{\partial x} + \mu \Delta u, \tag{14}$$

$$\rho\left(\frac{\partial v}{\partial t} + \frac{\partial(uv)}{\partial x} + \frac{\partial(v^2)}{\partial y} + \frac{\partial(vw)}{\partial z}\right) = -\frac{\partial p}{\partial y} + \mu \Delta v, \tag{15}$$

$$\rho\left(\frac{\partial w}{\partial t} + \frac{\partial(uw)}{\partial x} + \frac{\partial(vw)}{\partial y} + \frac{\partial(w^2)}{\partial z}\right) = -\frac{\partial p}{\partial z} + \mu \Delta w + \rho g. \tag{16}$$

---

[1] Here we assume that the energy equation is decoupled from the equations of motion and the consequences of this simplification could be neglected. This e.g. means that heat production due to the mechanical energy dissipation is neglected.

Here we have kept the continuity equation in its full original form, however it is also possible to replace the Eq. (13) by the simplified (non-conservative) version (10).

The governing systems (12)–(16), resp. (3)–(7), represent the full incompressible variable density model. This model is sometimes called the Non-homogeneous (incompressible) Navier–Stokes equations.

2.2. Boussinesq approximation

Now we will assume that the pressure and density fields are perturbation of hydrostatic equilibrium state, i.e.:

$$\rho(x,y,z,t) = \rho_0(z) + \rho'(x,y,z,t), \tag{17}$$
$$p(x,y,z,t) = p_0(z) + p'(x,y,z,t), \tag{18}$$

where the background density and pressure fields are linked by the hydrostatic relation:

$$\frac{\partial p_0}{\partial z} = \rho_0 g. \tag{19}$$

Using the above decomposition of density where $\rho = \rho_0 + \rho'$, the full continuity equation

$$\frac{\partial \rho}{\partial t} + \mathrm{div}(\rho \boldsymbol{u}) = 0, \tag{20}$$

can be rewritten in the following way:

$$\frac{\partial \rho'}{\partial t} + \mathrm{div}(\rho' \boldsymbol{u}) = -\left(\frac{\partial \rho_0}{\partial t} + \mathrm{div}(\rho_0 \boldsymbol{u})\right). \tag{21}$$

Applying the chain rule on the right-hand side we get:

$$\frac{\partial \rho'}{\partial t} + \mathrm{div}(\rho' \boldsymbol{u}) = -\left(\frac{\partial \rho_0}{\partial t} + \boldsymbol{u} \cdot \mathrm{grad}\ \rho_0 + \rho_0 \mathrm{div}\ \boldsymbol{u}\right). \tag{22}$$

Assuming now that the background density only depends on the vertical coordinate, i.e. $\rho_0 = \rho_0(z)$ and applying the divergence-free constraint, most of the terms on the right-hand side of (22) will disappear:

$$\frac{\partial \rho'}{\partial t} + \frac{\partial(\rho'u)}{\partial x} + \frac{\partial(\rho'v)}{\partial y} + \frac{\partial(\rho'w)}{\partial z} = -\left(\underbrace{\frac{\partial \rho_0}{\partial t}}_{=0} + u\underbrace{\frac{\partial \rho_0}{\partial x}}_{=0} + v\underbrace{\frac{\partial \rho_0}{\partial y}}_{=0} + w\frac{\partial \rho_0}{\partial z} + \rho_0 \underbrace{\mathrm{div}\ \boldsymbol{u}}_{=0}\right). \tag{23}$$

Finally we end-up with the continuity equation rewritten as:

$$\frac{\partial \rho'}{\partial t} + \frac{\partial(\rho'u)}{\partial x} + \frac{\partial(\rho'v)}{\partial y} + \frac{\partial(\rho'w)}{\partial z} = -w\frac{\partial \rho_0}{\partial z}. \tag{24}$$

The Boussinesq approximation of momentum equations is obtained by introducing the above decomposition of density and pressure into the momentum Eqs. ()()()(14)–(16). The density perturbation ρ' is neglected on the left-hand side (in the convective terms) while on the right-hand side it is retained. On the right-hand side the hydrostatic pressure was removed using the hydrostatic relation (19) and the fact that according to (18) the horizontal parts of the background pressure gradient are zero.

$$\frac{\partial u}{\partial x} + \frac{\partial v}{\partial y} + \frac{\partial w}{\partial z} = 0, \tag{25}$$

$$\frac{\partial \rho'}{\partial t} + \frac{\partial(\rho'u)}{\partial x} + \frac{\partial(\rho'v)}{\partial y} + \frac{\partial(\rho'w)}{\partial z} = -w\frac{\partial \rho_0}{\partial z}, \tag{26}$$

$$\frac{\partial u}{\partial t} + \frac{\partial(u^2)}{\partial x} + \frac{\partial(uv)}{\partial y} + \frac{\partial(uw)}{\partial z} = \frac{1}{\rho_0}\left(-\frac{\partial p'}{\partial x} + \mu \Delta u\right), \tag{27}$$

$$\frac{\partial v}{\partial t} + \frac{\partial(uv)}{\partial x} + \frac{\partial(v^2)}{\partial y} + \frac{\partial(vw)}{\partial z} = \frac{1}{\rho_0}\left(-\frac{\partial p'}{\partial y} + \mu \Delta v\right), \tag{28}$$

$$\frac{\partial w}{\partial t} + \frac{\partial(uw)}{\partial x} + \frac{\partial(vw)}{\partial y} + \frac{\partial(w^2)}{\partial z} = \frac{1}{\rho_0}\left(-\frac{\partial p'}{\partial z} + \mu \Delta w + \rho' g\right). \tag{29}$$

This system can equivalently be rewritten using the "complete" density ρ rather than the perturbation ρ'.

$$\frac{\partial u}{\partial x} + \frac{\partial v}{\partial y} + \frac{\partial w}{\partial z} = 0, \tag{30}$$

$$\frac{\partial \rho}{\partial t} + \frac{\partial (\rho u)}{\partial x} + \frac{\partial (\rho v)}{\partial y} + \frac{\partial (\rho w)}{\partial z} = 0, \tag{31}$$

$$\frac{\partial u}{\partial t} + \frac{\partial (u^2)}{\partial x} + \frac{\partial (uv)}{\partial y} + \frac{\partial (uw)}{\partial z} = \frac{1}{\rho_0}\left(-\frac{\partial p'}{\partial x} + \mu \Delta u\right), \tag{32}$$

$$\frac{\partial v}{\partial t} + \frac{\partial (uv)}{\partial x} + \frac{\partial (v^2)}{\partial y} + \frac{\partial (vw)}{\partial z} = \frac{1}{\rho_0}\left(-\frac{\partial p'}{\partial y} + \mu \Delta v\right), \tag{33}$$

$$\frac{\partial w}{\partial t} + \frac{\partial (uw)}{\partial x} + \frac{\partial (vw)}{\partial y} + \frac{\partial (w^2)}{\partial z} = \frac{1}{\rho_0}\left(-\frac{\partial p'}{\partial z} + \mu \Delta w + (\rho - \rho_0)g\right). \tag{34}$$

3. Numerical methods

This section briefly describes the numerical methods used to obtain numerical results presented in the Section 6. The description is mainly focused on the compact schemes. The reference AUSM finite-volume method is only described briefly for completeness.

3.1. Compact finite-difference schemes

Compact finite-difference schemes are presented here in the context of the principle of semi-discretisation. It means that the space-and time-discretisations are carried out in separate steps. First, the space-derivatives are discretised using compact finite-differences and then the resulting system of ODEs is integrated in time (e.g. by a suitable Runge–Kutta multistage scheme in this case). The details of the space-and time-discretisation are discussed below.

3.1.1. Space discretisation

The spatial discretisation used in this work is directly based on the paper [1], where a class of high order compact finite difference schemes was introduced and analysed. Although some more refined compact discretisations have recently been introduced and analysed (e.g. in [7–9] or [10,11]), the original family of simple compact finite-differences introduced in [1] and used in [12,13], will serve us well as a starting point in our investigation of capabilities of compact discretisations [2].

The main idea used to construct this family of schemes is that instead of approximating the spatial derivatives ϕ' of certain quantity ϕ explicitly from the neighbouring values ϕ_i, the (symmetric) linear combination of neighbouring derivatives $(\ldots, \phi'_{i-1}, \phi'_i, \phi'_{i+1}, \ldots)$ is approximated by weighted average of central differences. The simplest compact finite difference schemes use the approximation in the form

$$a\,\phi'_{i-1} + \phi'_i + a\,\phi'_{i+1} = \alpha_1 \frac{\phi_{i+1} - \phi_{i-1}}{2h} + \alpha_2 \frac{\phi_{i+2} - \phi_{i-2}}{4h}. \tag{35}$$

Here $h = x_i - x_{i-1}$ is the spatial step, while a and α_k are the coefficients determining the specific scheme within the family described by (35). It is easy to see that e.g. for $a = 0, \alpha_1 = 1$ and $\alpha_2 = 0$, the explicit second order central discretisation is recovered.

It is evident that the schemes (35) form a subclass of three-diagonal schemes with five-point computational stencil. For the simulations presented here, the following coefficients were used:

$$\alpha_1 = \frac{2}{3}(a + 2) \quad \alpha_2 = \frac{1}{3}(4a - 1). \tag{36}$$

This choice of parameters leads to a one-parametric family of formally fourth order accurate schemes. For $a = 0$ the classical explicit fourth order discretisation is recovered, while for $a = 0.25$ the well known Padé scheme is obtained. As an exception within this family of schemes, a single sixth order method can be obtained for the specific choice of $a = 1/3$.

The above described schemes are based on central discretisation in space with all the well known advantages and also disadvantages of this type of methods. One of the disadvantages of central methods is the appearance of non-physical oscillations in numerical solutions. A very efficient (but still not perfect) algorithm for filtering out these high frequency oscillations was also proposed in [1]. The low-pass filter (for the filtered values $\widehat{\phi}_i$) can be formulated in a form very similar to (35):

$$b\,\widehat{\phi}_{i-1} + \widehat{\phi}_i + b\,\widehat{\phi}_{i+1} = 2\beta_0\phi_i + \beta_1 \frac{\phi_{i+1} + \phi_{i-1}}{2h} + \beta_2 \frac{\phi_{i+2} + \phi_{i-2}}{4h} + \cdots. \tag{37}$$

The filters of different orders can be obtained for various choices of coefficients. Here the sixth order filter with coefficients

$$\beta_0 = \frac{1}{16}(11 + 10b); \quad \beta_1 = \frac{1}{32}(15 + 34b); \quad \beta_2 = \frac{1}{16}(6b - 3); \quad \beta_3 = \frac{1}{32}(1 - 2b), \tag{38}$$

---

[2] We will further follow the terminology used in [1].

Table 1
First order SSP-RK methods coefficients.

Method	α_{rp}			β_{rp}			CFL
SSP(1,1)	1			1			1
SSP(2,1)	1			$\frac{1}{2}$			2
	0	1		0	$\frac{1}{2}$		
	1			$\frac{1}{3}$			
SSP(3,1)	0	1		0	$\frac{1}{3}$		3
	0	0	1	0	0	$\frac{1}{3}$	

Table 2
Second order SSP-RK methods coefficients.

Method	α_{rp}				β_{rp}				CFL
SSP(2,2)	1				1				1
	$\frac{1}{2}$	$\frac{1}{2}$			0	$\frac{1}{2}$			
	1				$\frac{1}{2}$				
SSP(3,2)	0	1			0	$\frac{1}{2}$			2
	$\frac{1}{3}$	0	$\frac{2}{3}$		0	0	$\frac{1}{3}$		
	1				$\frac{1}{3}$				
SSP(4,2)	0	1			0	$\frac{1}{3}$			3
	0	0	1		0	0	$\frac{1}{3}$		
	$\frac{1}{4}$	0	0	$\frac{3}{4}$	0	0	0	$\frac{1}{4}$	

was used. The parameter $-0.5 < b < 0.5$ is used to fine-tune the filter. See Section 6.3 for further details. For other filters from this family see e.g. [12].

More information on the compact space discretisation can be found in [1,12,13] or in more recent works [7–9] or [10,11].

3.1.2. Temporal discretisation

The system of governing partial differential equations was discretised in space using the above described finite-difference technique (represented further by the space discretisation operator $\widetilde{\mathscr{L}}$). This leads to a system of ordinary differential equations (ODE) for time-evolution of grid values of the vector of unknowns W. This concept is called semi-discretisation or the method of lines.

Resulting system of ODEs can be solved by a suitable time-integration method [3]. Even in the case that a non-oscillatory space-discretisation has been used, the numerical solution might still be spoiled by non-physical oscillations. These spurious artifacts can be introduced at the time-integration step by an inappropriate choice of time-discretisation. This is why we have used in this study the so called Strong Stability Preserving (SSP) Runge–Kutta methods.

The family of explicit SSP Runge–Kutta schemes is usually written in the form introduced in [14].

$$
\begin{aligned}
W^{(0)} &= W^n, \\
W^{(r)} &= \sum_{p=0}^{r-1} (\alpha_{rp} W^{(p)} + \beta_{rp} \Delta t \widetilde{\mathscr{L}}(W^{(p)})) \qquad r = 1, \ldots, s, \\
W^{n+1} &= W^{(s)}.
\end{aligned}
\tag{39}
$$

difficult to see that in the case the coefficients β_{rp} are positive, the method (39) is nothing else but a convex combination of Euler stages with fractional time-steps of the length $\frac{\beta_{rp}}{\alpha_{rp}} \Delta t$.

Here we just shortly recall some of the optimal, in the sense of accuracy versus stability, up to the order two SSP RK methods, originally studied in [15]. Hereafter the SSP(s,o) denotes the Runge–Kutta method which consists of s stages and has order of accuracy o (See Table 1).

The method denoted by SSP(1,1) is nothing else but the Euler method, while SSP(2,2) stands for the modified Euler method. The coefficients of some other SSP-RK methods can be found in [15].

The comparison of Tables 1 and 2 shows that the higher order of RK method can only be achieved at the expense of the reduction of the allowable time-step, resp. the CFL number.

The three stage second order SSP(3,2) Runge–Kutta method was used to obtain the results presented here. Other methods have also been tested without visible influence on the final (steady) solution.

---

[3] It should be noted that all the test cases solved in this paper are steady (see Section 4). So even if the model equations and numerical solvers are used in the unsteady form, it is just because the *time-marching technique* is adopted to reach the limit steady solution. This also allows us to use the artificial compressibility method to compute the pressure in both numerical methods.

3.2. AUSM finite-volume scheme

This method has been chosen for comparison with the above described compact finite-difference schemes. It represents a popular choice amongst the modern high resolution finite-volume schemes. This particular scheme was previously used for the simulation of stratified flow and compared successfully with other methods and experiments in [16–18].

3.2.1. Space discretisation

Also for this scheme the artificial compressibility method was used in dual time. The continuity equation is then rewritten in the form (in 2D, x–z plane)

$$\frac{\partial p}{\partial \tau} + \beta^2 \left(\frac{\partial u}{\partial x} + \frac{\partial w}{\partial z} \right) = 0, \tag{40}$$

where τ is artificial time and β denotes the artificial compressibility parameter. The Eqs. (25)–(29) rewritten in the 2D conservative form are

$$PW_t + F(W)_x + G(W)_z = S(W). \tag{41}$$

Here the $W = [\rho, u, v, p]^T$, $F = F^i - vF^v$ and $G = G^i - vG^v$ contain the inviscid fluxes F^i, G^i and viscous fluxes F^v and G^v, S is the source term, and $P = diag(1, 1, 1, 0)$. The fluxes and the source term are

$$F^i(W) = [\rho u, u^2 + p, uw, \beta^2 u]^T, \quad G^i(W) = [\rho w, uw, w^2 + p, \beta^2 w]^T,$$
$$F^v(W) = [0, u_x, w_x, 0]^T, \quad G^v(W) = [0, u_z, w_z, 0]^T, \tag{42}$$
$$S(W) = [-w\partial\rho_0/\partial z, 0, -\rho g, 0]^T.$$

The finite volume AUSM (Advection Upstream Splitting Method) scheme was used for spatial discretisation of the inviscid fluxes:

$$\int_\Omega \left(F^i_x + G^i_z \right) dS = \oint_{\partial\Omega} (F^i n_x + G^i n_z) dl \approx \sum_{k=1}^{4} \left[u_n \begin{pmatrix} \varrho \\ u \\ w \\ \beta^2 \end{pmatrix}_{L/R} + p \begin{pmatrix} 0 \\ n_x \\ n_z \\ 0 \end{pmatrix} \right] \varDelta l_k. \tag{43}$$

where n is the cell face outer normal vector, u_n is the normal velocity vector, and $q_{L/R}$ are the quantities on left/right hand side of the face respectively. The convective part is approximated by the upwind formula,

$$(q)_{L/R} = \begin{cases} (q)_L & \text{if } u_{i+\frac{1}{2}} > 0 \\ (q)_R & \text{otherwise} \end{cases}. \tag{44}$$

Quantities p and ϱ on the cell face are approximated by the central formula from neighbouring cells. Velocities on the cell faces are computed using MUSCL (Monotone Upstream-centred Schemes for Conservation Laws) reconstruction introduced by van Leer [19] with Hemker–Koren limiter. This means that

$$q_R = q_{i+1} - \frac{1}{2}\delta_R \text{ and } q_L = q_i + \frac{1}{2}\delta_L, \tag{45}$$

with the limiter function given by

$$\delta_{L/R} = \frac{a_{L/R} \left(b_{L/R}^2 + 2 \right) + b_{L/R} \left(2a_{L/R}^2 + 1 \right)}{2a_{L/R}^2 + 2b_{L/R}^2 - a_{L/R}b_{L/R} + 3}, \tag{46}$$
$$a_R = q_{i+2} - q_{i+1} \quad a_L = q_{i+1} - q_i \quad b_R = q_{i+1} - q_i \quad b_L = q_i - q_{i-1}.$$

Because the pressure is discretised in a central way, the scheme is stabilised by the pressure diffusion according to [20]. The discrete version of the additional diffusive flux has the following form:

$$F^p_{i+1/2,j} = \begin{pmatrix} 0 \\ 0 \\ 0 \\ \eta \frac{p_{i+1,j} - p_{i,j}}{\omega_x} \end{pmatrix} \quad \omega_x = w_r + \frac{2v}{\varDelta x}, \tag{47}$$

where w_r is reference velocity (in our case the maximum velocity in flow field).

The viscous fluxes are discretised in the central way on a dual mesh. This scheme is formally of the second order of accuracy in space.

3.2.2. Time integration

For the finite-volume AUSM reference model a fully unsteady solver was used. The dual time stepping approach was adopted, so the separate time-discretisations were needed for physical and artificial time. The derivative with respect to the physical time t is discretised by the second order BDF formula,

$$P\frac{3W^{n+1} - 4W^n + W^{n-1}}{2\Delta t} + F_x(W^{n+1}) + G_z(W^{n+1}) = S(W^{n+1}), \tag{48}$$

$$Rez(W^{n+1}) = P\frac{3W^{n+1} - 4W^n + W^{n-1}}{2\Delta t} + F_x(W^{n+1}) + G_z(W^{n+1}) - S(W^{n+1}).$$

Arising system of equations

$$Rez^{n+1}(W) = 0,$$

is solved by artificial compressibility method in the dual (artificial) time τ. The stationary solution of the following system of equations

$$\widetilde{P}W_\tau + PW_t + F(W)_x + G(W)_z = S(W), \tag{49}$$

$$\widetilde{P}W_\tau + Rez(W^{n+1}) = 0, \tag{50}$$

with $\widetilde{P} = diag(1,1,1,1)$ is obtained in each physical time step. This system of ODEs is solved by an explicit 3–stage Runge–Kutta method. The AUSM scheme has been validated in our previous studies. The scheme was successfully used for simulation of the flow around moving ball in 2D and 3D stratified fluid for wide range of Richardson numbers.

4. Computational setup

The whole study is motivated by the investigation of environmental flows, namely the atmospheric boundary layer flows in complex terrain. The computational test case was chosen to be as simple as possible, but retaining some of the features found in real life environmental flows. Nevertheless it should be kept in mind that the flow computed is not atmospheric.[4]

4.1. Computational domain

The 2D computational domain is selected as a part of wall-bounded half space with low smooth cosine-shaped hill (shown in the Fig. 1). The hill height is $h = 1$ m, while the whole domain has dimensions 90×30 m.

4.2. Boundary conditions

Two-dimensional steady case is considered and thus only boundary conditions are given for this 2D case. The time-marching method is used to find the steady solution as a limit of unsteady system solution for $t \to \infty$.

- **Inlet** ... The velocity profile $\boldsymbol{u} = (u(z),0,0)$ is prescribed. The horizontal velocity component u is given by[5] $u(z) = U_0(z/H)^{1/r}$ with $U_0 = 1 m \cdot s^{-1}$ and $r = 40$. Density perturbation ρ' is set to zero, while homogeneous Neumann condition is used for pressure.
- **Outlet** ... Homogeneous Neumann condition is prescribed for all velocity components, as well as for the pressure and density perturbations.
- **Wall** ... No-slip conditions are used on the wall, i.e. the velocity vector is set to $\boldsymbol{u} = (0,0,0)$. Homogeneous Neumann condition is used for pressure and density perturbations.
- **Free stream** ... Homogeneous Neumann condition is used for all quantities including pressure and density perturbations.

The background density field ρ_0 is given by the linear profile $\rho_0(z) = \rho_w + \gamma z$ with $\rho_w = 1.2 \text{ kg} \cdot \text{m}^{-3}$ and $\gamma = -0.01 \text{ kg} \cdot \text{m}^{-4}$. The characteristic Reynolds number is approximately $Re = 1000$ for this test case, based on the maximum inflow velocity $U_0 = 1 m \cdot s^{-1}$, hill height $h = 1 m$ and dynamic viscosity $\mu = 10^{-3} \text{ kg} \cdot \text{m}^{-1} \cdot \text{s}^{-1}$. A range of gravity acceleration g was used to test the behaviour of the model and numerical method for different Brunt-Väisälä frequencies. The values used are $g = -5, -10, -20, -50 \text{ m} \cdot s^{-2}$.

---

[4] E.g. because the viscosity of the fluid is not the one of air and also the used values of gravity acceleration do not correspond to physical value(s) for the Earth.

[5] This inflow condition does not represents the model solution for undisturbed flow. It is an ad-hoc chosen velocity profile specifically suited for the test of numerical methods.
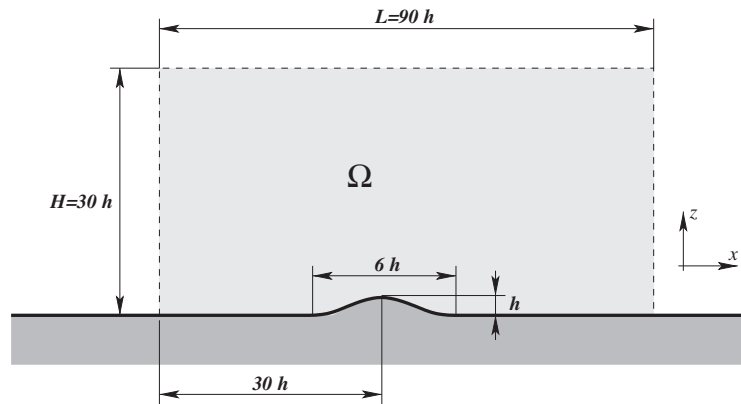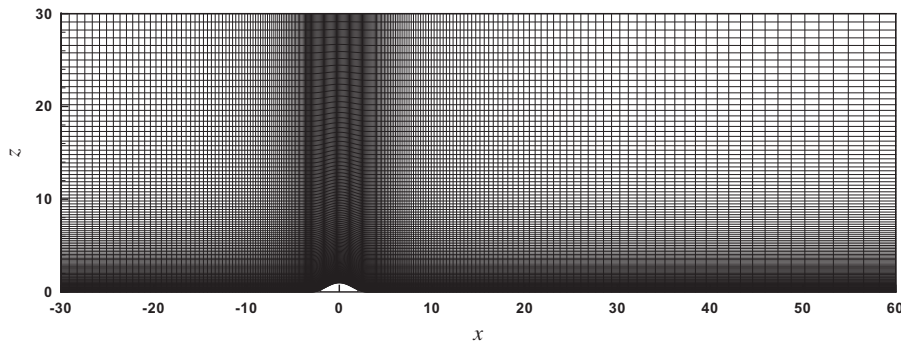
Fig. 1. Computational domain configuration.

Fig. 2. Computational grid structure.

4.3. Computational grid

The numerical simulations were performed on a structured, non-orthogonal wall-fitted grid shown in the Fig. 2. The grid has 233×117 points with the minimum cell size in the near-wall region $\Delta z = 0.03$ m.

5. Relation of the computational setup to environmental flows

The choice of mathematical model and especially the computational setup that we have used were mainly driven by our aim to evaluate the differences in numerical solutions obtained using various numerical methods. Thus the well defined model and simple setup were of primarily importance. The physical interpretation of the whole model setup only plays a secondary role. In this section we only want to show that our setup can easily be "translated" into another one, that is often used in environmental physics.

In our computational setup we have used a single background density profile $\rho_0(z)$ and the stratification was changed by variation of gravity acceleration that we denote for a moment by g_0. Physicists on the other hand usually only work with a single, physical value of gravity acceleration that we denote g_*. Different levels of stratification can only be achieved using various background density profiles $\rho_*(z)$. Based on the similarity of Brunt-Väisälä frequencies in both setups, we can compute an equivalent background density profile for each of the computational cases that we solve in this paper. It can be shown that the computational and physical setups are equivalent (with respect to Brunt-Väisälä frequencies) provided that the following rules hold:

Computational setup. $g_0 = -5, -10, -20, -50 \text{ m} \cdot \text{s}^{-2} \rho_0(z) = \rho_w + \gamma_0 z$, where $\gamma_0 = -0.01 \text{ kg} \cdot \text{m}^{-4}, \rho_w = 1.2 \text{ kg} \cdot \text{m}^{-3}$,

Physical setup $g_* \doteq -10 \text{ m} \cdot \text{s}^{-2} \rho_*(z) = \rho_w \left(\frac{\rho_0(z)}{\rho_w}\right)^{\frac{g_0}{g_*}}$ where $g_0 = -5, -10, -20, -50 \text{m} \cdot \text{s}^{-2}$.

It is necessary to keep in mind that even if we have provided the rules to guarantee the Brunt-Väisälä frequency similarity, the corresponding Reynolds number similarity can not be achieved. In the computational setup, the local Reynolds number profile (that depends on the local background density) is exactly the same in all test cases. For the physical setup however this

profile is different for each of the test cases. Therefore from the numerical point of view we prefer the use of the computational setup, because the various Brunt-Väisälä frequencies can be achieved without affecting the Reynolds number.

6. Numerical results

In this section we present a comparison of numerical results obtained using some of the compact finite-difference schemes and the AUSM finite-volume scheme. The testing of numerical methods was quite extensive and thus it is not possible to show all of the results here. We have chosen the results to be shown in order to demonstrate some of the main features of these numerical methods and to support our findings summarised in the Section 7.

The family of compact schemes summarised in the Section 3.1 offers infinitely many combinations of space discretisations and filters. Moreover even for the schemes and filters of given order there are infinitely many possible choices of parameters a and b. Thus in order to distinguish between these methods we use the notation $CX_{aaa}FY_{bbb}$ for compact scheme of order X with parameter $a = aaa$ combined with the filter of order Y applied with the damping parameter $b = bbb$. For example the following set of results (Fig. 4) was obtained with the fourth order Padé compact scheme (i.e. for $a = 0.25$) combined with the sixth order compact filter with damping parameter $b = 0.45$. Such scheme is further denoted as $C4_{025}F6_{045}$.

6.1. The effects of stratification

The stratification has a severe impact on the flow-field. The inflow is represented by a purely horizontal flow. This is perturbed by a vertical impulse generated by the hill placed in about one third of the length of the computational domain. As a consequence, the gravity waves occur in the flow field. The wavelength of these waves is inversely proportional to the Brunt-Väisälä frequency

$$N = \sqrt{-\frac{g}{\rho}\frac{\partial \rho_0}{\partial z}}. \tag{51}$$

This means that the spatial frequency of gravity waves increases either with the growth of the background density gradient or with the increasing (absolute) value of gravity acceleration g. We have intentionally opted for changing the gravity acceleration rather than the vertical density gradient. The main reason was to avoid the limitations arising from the requirement of positive density and to keep the Reynolds number strictly fixed for all the solved cases. The basic structure of the flow pattern is summarised in the Fig. 3.

The dominant flow feature is clearly the hill generated gravity wave pattern in the proximity of the hill. In agreement with the theory, the wavelength is getting shorter for higher stratification. It is also worth mentioning that the hill induced flow perturbations occupy an extremely large part of the domain. This is in contrast with the classical non-stratified case, where the hill induced flow deviations are localised to the close proximity of the hill and do not significantly affect the flow far away from the hill. This particular difference between the non-stratified and stratified flow is what makes the stratified case much more difficult to solve.

In the simulations presented here the stratification is also responsible for the amplification and propagation of some artifacts related to the choice and implementation of boundary conditions on the artificial boundaries of the computational domain. Most pronounced of these effects is the wave pattern located close to the lower left corner of the domain. This corner effect is neither a numerical instability nor a numerical error. This is a physical effect caused by the choice of inlet velocity profile. If a fully developed profile obtained (by the same method on the same grid) for the flow over a flat plate is prescribed, this corner effect will disappear (or will be negligible). In this corner the prescribed velocity profile (that does not corresponds to a fully developed profile) hits the wall and introduces a small vertical velocity perturbation to the flow. In the non-stratified case this will only locally affect the flow field. In the stratified case however, this perturbation persists and affects the flow in a much larger area. In physically relevant simulations, where often the boundary conditions come from measurements and are not fully compatible with the model equations, such effects can seldom be fully eliminated. We have
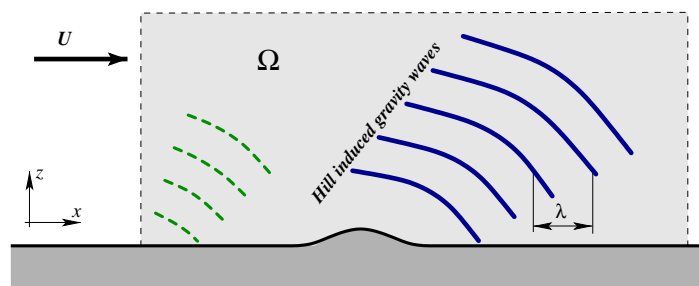

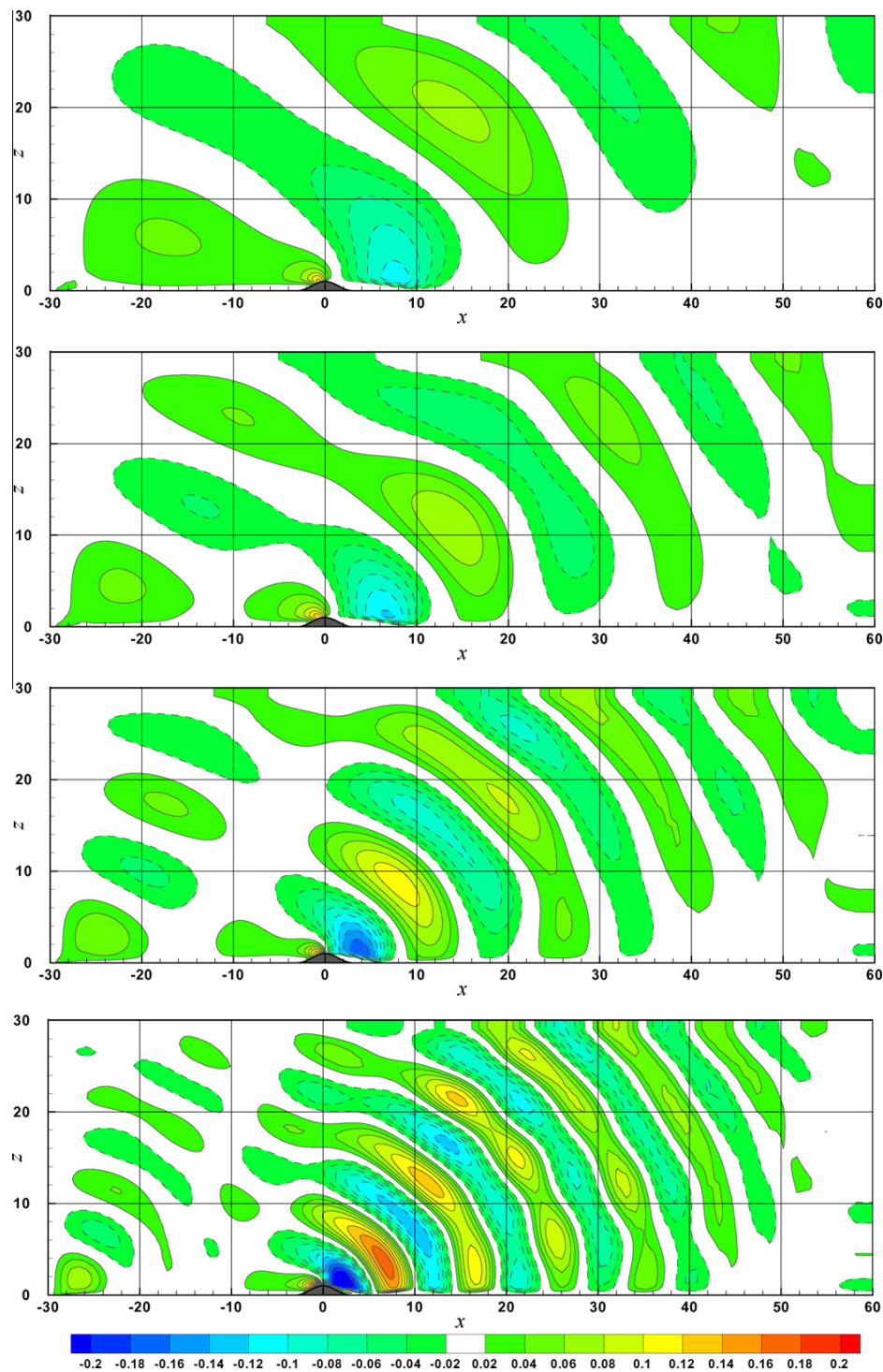**Fig. 3.** Flow structure.

Fig. 4. Vertical velocity contours for different values of stratification (i.e. for different values of gravity acceleration $g = -5, -10, -20, -50 \text{ m} \cdot \text{s}^{-2}$).

intentionally kept this corner effect in our simulations as another flow feature that should be numerically resolved. It is especially interesting because it appears close to the far-field boundary where the grid is rather coarse.

The Fig. 4 shows the vertical velocity contours[6] for four different values of stratification. The visualisation of the flow in terms of the vertical velocity contours has been chosen to emphasise the hill-induced vertical velocity perturbation superposed to the originally purely horizontal background flow. Also the spatial structure of corresponding gravity waves is well documented in these contour figures. The colour scale is kept the same for all the figures in order to be able to evaluate easily both, the frequency and the amplitude of the gravity waves under different conditions. In the contour plots, the near zero contours have been skipped (i.e. replaced by the white colour). The negative contour lines are dashed, while the positive are drawn by solid line.

As mentioned above, the gravity wave pattern generated by the hill can be characterised by the Brunt-Väisälä frequency N or equivalently by a characteristic wavelength $\lambda \propto U_0/N$. This can clearly be seen from the Fig. 5 that shows the graph of the vertical velocity versus the x coordinate on in cut represented by a straight line connecting points $[0;0]$ and $[30;30]$, i.e. on a cut taken at the angle 45 degrees starting from the hill centre.

From the numerical point of view, the most challenging, from the four above shown cases, is the case with highest stratification i.e. with $g = -50 \text{ m} \cdot \text{s}^{-2}$. This is mainly due to the short wavelength of gravity waves that is difficult to resolve on the coarse grid that we (intentionally) use. Further we will focus our attention to this case.

6.2. The influence of discretisation schemes

The influence of space discretisation on results was quite subtle. The major differences are visible in the coarse grid regions. To demonstrate this, the classical second order scheme (i.e. $a = 0, \alpha_1 = 1$ in the approximation formula (35)) was used as a reference. Schemes with $a = 0$ are sometimes called explicit, because this choice results in an explicit formula for the approximation of derivatives instead of solving linear system like in the case of compact schemes. Usually it is recommended to use fourth order damping/filtering with second order schemes, however in order to separate the influence of space discretisation from the effects of stabilisation, the same compact low-pass filter has been used in all cases. The sixth order compact filter with the damping parameter $b = 0.45$ was used for all simulations in this section.

This explicit second order scheme (denoted further as $E2\,F6$) performs quite well in fact (see Fig. 6). This is mainly due to the use of high order filter instead of the application of some classical stabilisation techniques (upwinding, artificial viscosity) which are usually of lower order. This becomes apparent from the comparison with the modern high resolution AUSM finite volume scheme whose results are shown in the Fig. 7.

Both schemes perform very well in the proximity of the hill, where the grid spacing is more than sufficient to resolve the gravity waves. At larger distances, the $E2\,F6$ scheme seems to produce more details with the results being less smoothed. Results closer to the AUSM scheme can be achieved at the expense of the use of stronger damping with the finite-difference discretisation provided e.g. by some lower order filter or in combination with a similar kind of pressure stabilisation as is used with the AUSM scheme.

Another feature shows-up when higher (fourth or sixth) order compact schemes are used instead of the explicit second order formula. Because the grid spacing increases towards the outer boundaries of the computational domain, at some distance the grid resolution becomes insufficient to correctly resolve the short wavelength gravity waves. This is apparent in the above results close to the right, outlet boundary where the waves just fade out without having physical reason for it. Comparing the above low-resolution results with the output higher order method, shown in the Fig. 8, clearly demonstrates the superiority of higher order method that allows on the same grid to better resolve the waves on a coarse grid.

A more detailed comparison of the above methods is possible from the plots of the vertical velocity in different cuts of the computational domain. The first cut, shown in the Fig. 9, is placed horizontally at the height $z = 10$ m.

Another interesting cut, shown in the Fig. 10, goes up-right from the hill centre at the angle of 45 degrees (the same as in the Fig. 4).

In both of the Figs. 9 and 10 the AUSM scheme shows more damping than the other methods, with the compact fourth order scheme having visibly higher resolving power and lower damping in the coarse grid regions.

6.3. The impact of stabilisation techniques

The numerical experiments have shown that the effects of the increasing order of the spatial discretisation are relatively subtle when compared to the influence of different stabilisation methods. The type and amount of damping of non-physical oscillations in the computational field has a strong impact on the convergence rate and the resolution of the numerical method. The compact filters used in this study contain a tuning parameter $b \in (-0.5; 0.5)$ that allows to adjust the cut-off frequency of the low-pass filter. Values of b close to 0.5 result in lower amount of damping, while for the values closer to -0.5 the filtering is stronger and affects also the lower frequencies.

To get a rough idea about the effects of various filters, we may follow the analysis introduced in [1,12] stating that the effect of a certain filter could be characterised by its *transfer function*[7]. When both the original and filtered "signal" is repre-

---

[6] All the figures and results are in SI units, i.e. distances in meters and velocities in meters per second. The contour colour scales are the same for all figures.
[7] Sometimes called spectral function or spectral response (see e.g. [12] for more details)
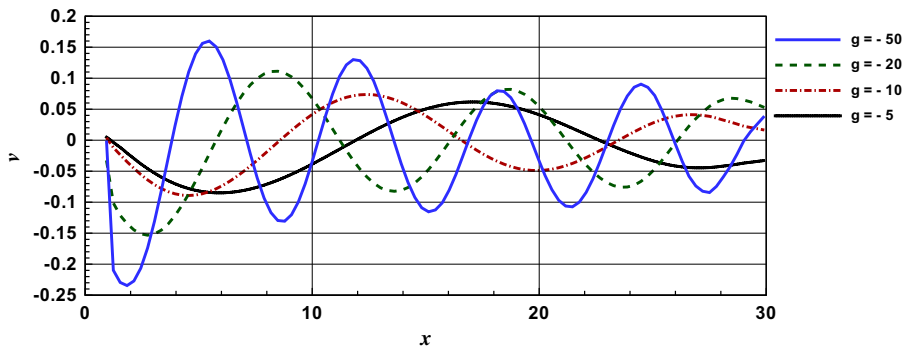
Fig. 5. Vertical velocity plots for different values of stratification.
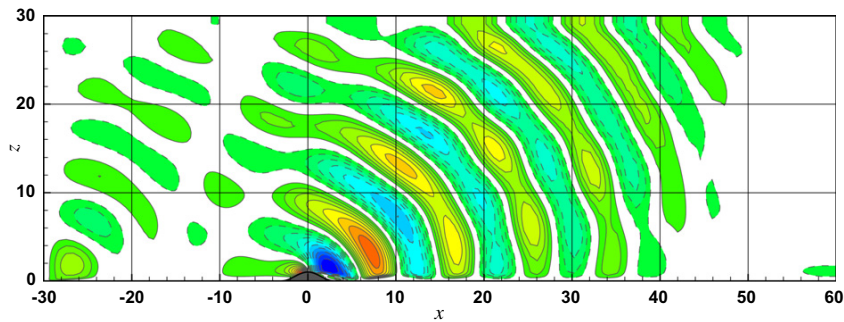

Fig. 6. Explicit second order scheme ($a = 0, \alpha_1 = 1, \alpha_2 = 0$) with compact sixth order filter ($b = 0.45$). Vertical velocity contours.
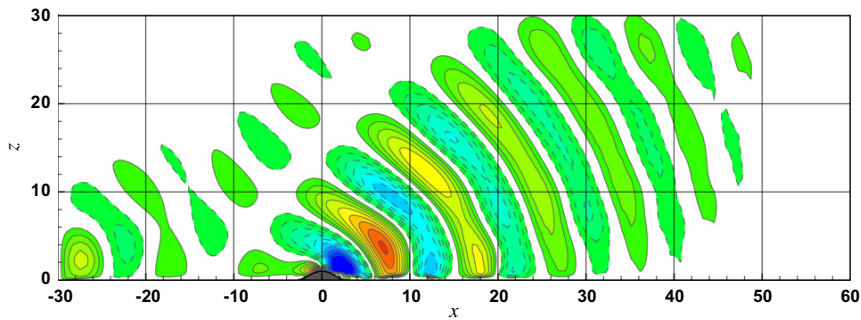

Fig. 7. Finite-volume AUSM scheme with pressure stabilization. Vertical velocity contours.

sented in the Fourier space by its wave number and corresponding amplitude, the value of transfer function $T(w)$ is obtained as the ratio of the amplitudes of filtered and non-filtered signal for a given wave number w. According to [1] the transfer function of the tri-diagonal compact filter of order N is given by

$$T(w) = \frac{\sum_{n=0}^{N} \beta_n \cos(nw)}{1 + 2b \cos(w)}. \tag{52}$$

The shape of the transfer functions for different filters and values of the coefficient b are shown in the Fig. 11.

The above figure only provides rough guidelines for comparison of different filters. A full, mathematically rigorous analysis of the impact of various filters in combination with different spatial and temporal discretisations should be provided in critical cases (See e.g. [8,9]).
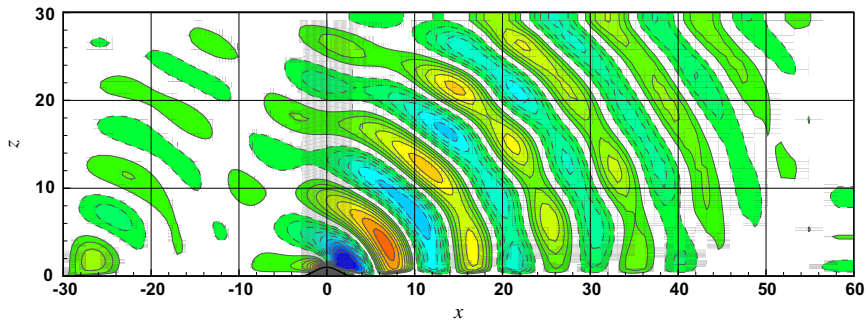
Fig. 8. Compact fourth order scheme $C4_{038}F6_{045}$. Vertical velocity contours.
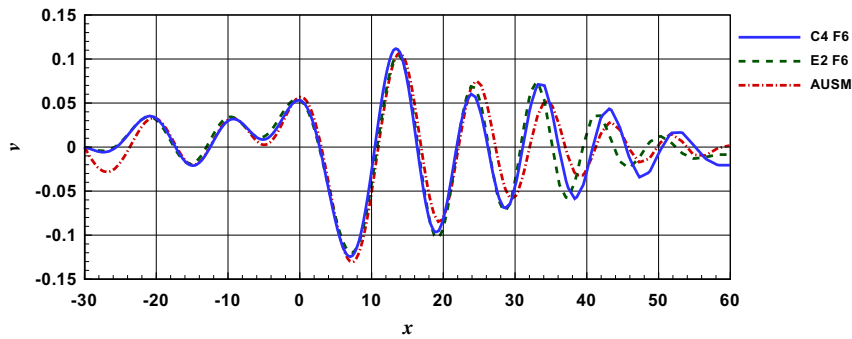

Fig. 9. Vertical velocity plots for different schemes in a cut taken at the height $z = 10$ m.
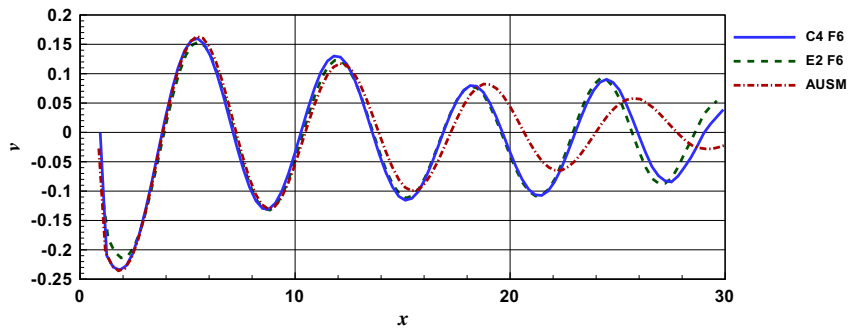

Fig. 10. Vertical velocity plots for different schemes in a cut taken from the hill centre at the angle of 45 degrees.

The Fig. 8 shows the results obtained using the scheme $C4_{038}F6_{045}$, i.e. with the sixth order filter using the damping parameter $b = 0.45$. In order to point out the effect of filtering, two other simulations with alternative values of parameter b were performed. Stronger damping was obtained with $b = 0$ (Fig. 12) and for slightly weaker damping the value $b = 0.48$ was used (Fig. 13).

It is evident that the strong damping has smoothed out the waves in the far-field, while the wave structure (not the amplitude) remains close to the less damped case.

In the case of low damping, the results are still free of point-to-point numerical oscillation, but the wave interferences became more obvious. Further decrease of damping (i.e. $b > 0.48$) results in unsteady or divergent computation.

From the Fig. 11 follows that the high order filters are not able to efficiently damp the low frequency waves in the computational field. This contributes to the high resolving power of the scheme but on the other hand it has also some side effects. The transitional travelling waves present in the computational field during the initial stage of the time-marching process are only weakly damped. Therefore the convergence to steady state can be slow. Second problem comes with the
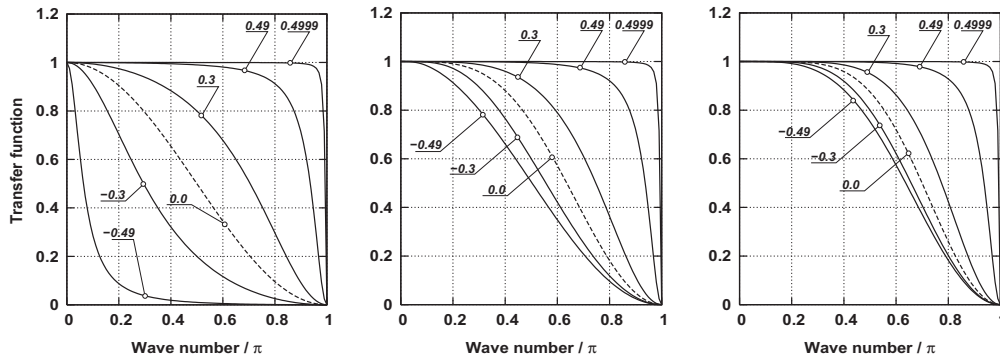
Fig. 11. Transfer functions of compact filters $F2$, $F4$, $F6$ for a range of parameters b.
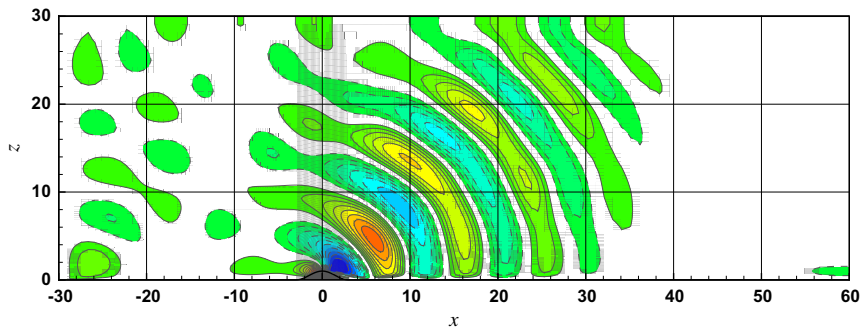

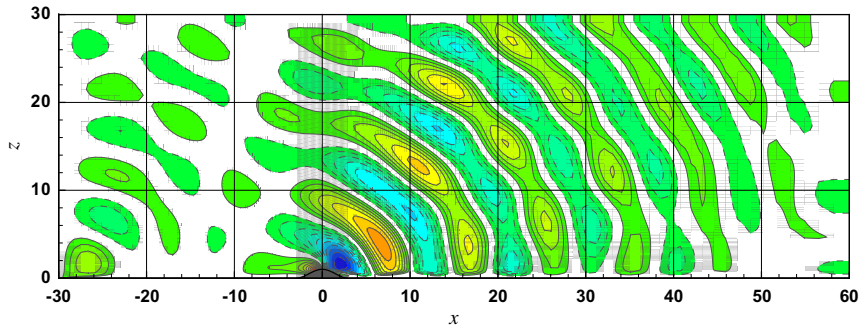**Fig. 12.** Stronger damping. Scheme $C4_{038}F6_{000}$.

Fig. 13. Weaker damping. Scheme $C4_{038}F6_{048}$.

parasitic waves introduced by some boundary conditions (e.g. in the lower left corner in our simulations). These usually unwanted artifacts ere either unresolved or quickly damped by low order methods. With the high resolution scheme/filter these physically irrelevant features remain unaffected and may influence the whole solution. The AUSM method presented in this work used additional pressure stabilisation to face this kind of problem. In the simplest case of equidistant Cartesian grid the pressure stabilisation term can be interpreted as additional Laplacian of pressure on the right hand side of the modified continuity equation. This kind of stabilisation has proved to be very efficient without significantly affecting the resolution of the scheme. Just for curiosity we have tried to apply similar kind of pressure stabilisation together with the high order filter. The following Fig. 14 shows the results of simulation with additional pressure stabilisation. This figure should be directly compared with the last picture in the Fig. 4 or with the Fig. 8, where the same case is shown without the pressure stabilisation.
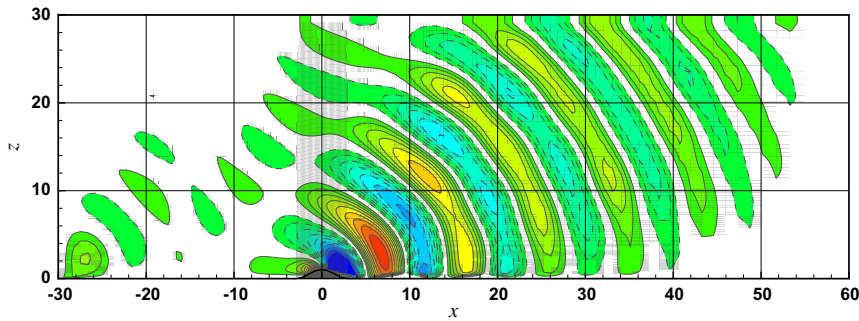
Fig. 14. Additional pressure stabilisation. Scheme $C4_{025}F6_{045}$.

The additional pressure stabilisation helped to speed-up the convergence to steady state and also damped a little bit the waves in the lower left corner of the domain. This has also minimised the wave interferences in the whole computational field. The overall results look much cleaner and smoother without visibly reducing the scheme resolution in the coarse grid areas in the far-field.

6.4. The effect of grid size and resolution

There is no doubt that the grid that we have used in the above presented simulations is in some situations a limiting factor that strongly affects the results of simulations. The grid is relatively small (in the sense of size of computational domain) and also quite coarse in some areas. This choice of grid was made intentionally and we do not claim our results to be physically correct in all the regions of the computational domain. Our goal was to find the limitations of selected numerical methods for given grid.

To quantify the effects of the grid size and spacing, two additional cases are discussed here. First the double-sized grid was used. In the original grid the grid covered the domain defined roughly as as two-dimensional interval $\langle -30; 60 \rangle \times \langle 0; 30 \rangle$. the grid has smallest cells in the proximity of the hill and is smoothly coarsened towards the far-field. The coarsening is limited so that the next cell can only be 3% larger than the actual one. The same rule was used for the double-sized domain defined roughly as $\langle -60; 120 \rangle \times \langle 0; 60 \rangle$. The original grid had 233×117 cells, while on the extended domain there are 384×241 grid cells. Running the computation on this extended domain with very coarse grid in the far-field (and almost identical to the original one in the near-field) gives the results shown in the Fig. 15, where only the detail in the range of the original small domain is shown.

The results look great in this detailed window being free of the boundary induced waves and their consequent interferences with the waves generated by the hill. The global look on the results in the whole domain (Fig. 16) reveals the obvious fact that the very coarse grid spacing in the far-field does not allows for the resolution of any short wavelength gravity waves (either physical or boundary induced) and attributes to the fast damping of all reflected waves.

The insufficient grid resolution of the above used grid in the far-field is demonstrated in the following Fig. 17 showing the results from the double-sized domain with finer grid. In this case the grid coarsening towards the far-field is slower with only 1% cell growth instead of the original 3% limit. In this case the fine, double-sized grid has 508×306 cells.

The finer grid does not allows for efficient damping of the boundary induced waves and their reflections in the far-field using the high order filter only. The Fig. 18 shows the results obtained with the use of additional pressure stabilisation for the same case.
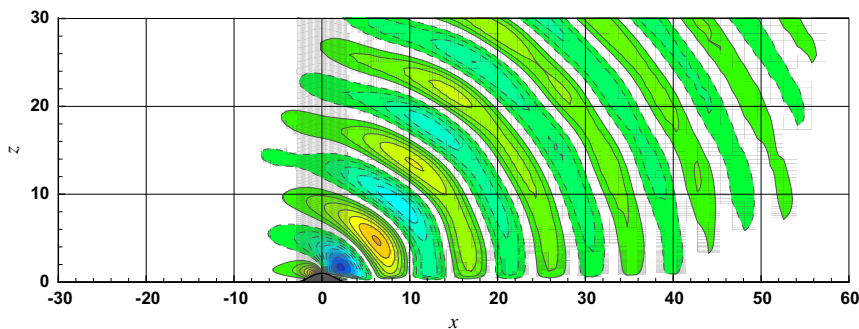

Fig. 15. Detail of the results from double-sized domain with coarse grid. Scheme $C4_{038}F6_{048}$.
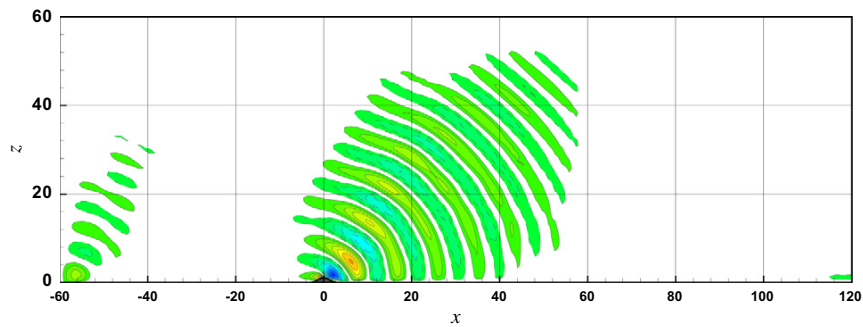
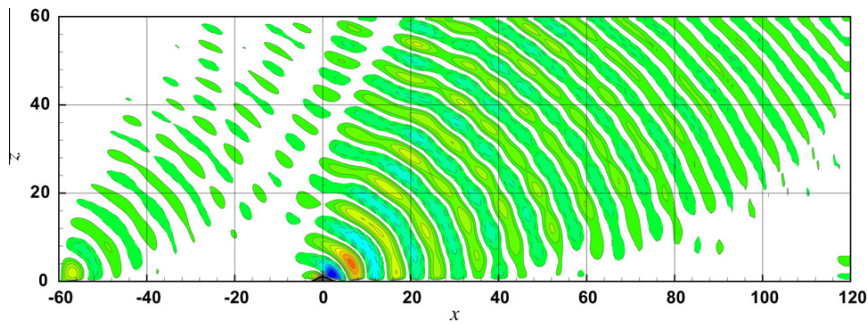**Fig. 16.** Global view of the results from double-sized domain with coarse grid. Scheme $C4_{038}F6_{048}$.

Fig. 17. Results from double-sized domain with fine grid. Scheme $C4_{038}F6_{048}$.
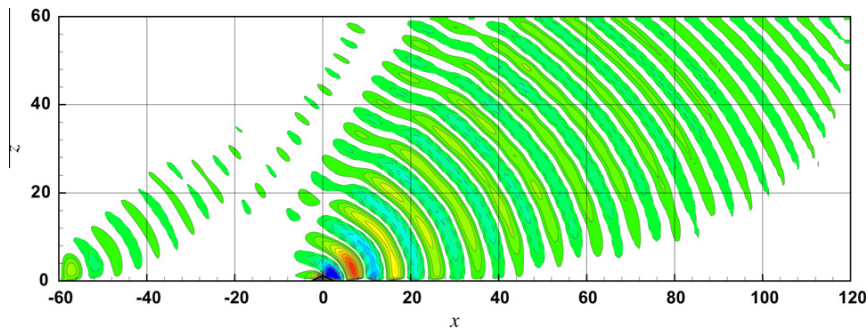

Fig. 18. Results from double-sized domain with fine grid. Scheme $C4_{038}F6_{048}$ with additional pressure stabilisation.

As in the case of smaller domain the pressure stabilisation helps to damp the far-field artifacts and speed-up the convergence without significantly affecting the scheme resolution.

7. Conclusions and final remarks

In this paper we have compared the numerical results obtained using two significantly different numerical methods. We have mainly focused our attention to some simple compact finite-difference schemes introduced in [1] and recalled in the Section 3.1. During the extensive testing of these compact schemes we have found many interesting issues related to their implementation and practical use for the simulation of stably stratified flows. Hereafter a short summary of some of our main findings is presented.

7.1. Discretisation related issues

The above described compact finite-difference discretisation has proved is ability to properly resolve all the flow features of stratified fluid flow. In our simulations the compact schemes have clearly demonstrated its high resolution capabilities, extreme flexibility and robustness. They not only perform well in comparison with standard schemes, but they still have a great potential for further development. When it comes to resolution, the compact schemes are extremely well suited for the simulations high frequency wave phenomena. In our simulations it has shown up that the high order schemes need visibly less grid points per wavelength to correctly resolve the gravity waves.

The use of high order space discretisations has however revealed new problems related to their implementation and efficient use. From this new kind of problems lets point out the issues related to the proper choice and implementation of boundary conditions. In our simulations we have chosen quite steep inlet velocity profile. This choice led to generation of parasitic gravity waves from the lower left corner of computational domain. First of all let's note that this will cause just local problem in the case of non-stratified flow, but with increasing stratification, the affected area will grow in size and importance. These small amplitude waves are well resolved by high order methods and thus may cause more problems and interferences with the hill generated waves in the whole domain. In this aspect, the low order discretisation may help together with coarse grid close to the far-field boundaries,to damp faster the boundary condition related artifacts. The high order discretisation on the other hand helps to resolve all these unwanted phenomena and thus any boundary condition issues will affect the overall results much stronger.

7.2. Stabilisation and damping

The application of high order central in space discretisation requires to use also some kind of high order stabilisation in order to suppress non-physical oscillation appearing in the computational field. In this aspect the simple compact filters that we have used have proved to be extremely efficient and flexible. In contrast to most of the modern high resolution schemes (using e.g. some embedded upwinding or flux limiting), here the choice of stabilisation method is separated from the space discretisation. This gives to the user more flexibility in the choice of type and amount of damping/filtering necessary to stabilise the scheme without excessively affecting the results. In our tests the most efficient damping was usually provided by a filter of two orders higher than the formal order of the chosen space discretisation. This is enough to damp the non-physical (numerical) high frequency oscillations in the computational field. In some cases however it is useful to apply at least temporarily some stronger or lower order stabilisation to speed-up the convergence. This is mainly connected with the need to damp some of the artificial flow phenomena generated by far-field boundary conditions. These unwanted flow features have higher wavelengths than the point-to-point numerical oscillations introduced by space discretisation and thus can not be sufficiently damped by high order filters that only affect the highest frequencies. The temporary application of lower-order damping during the initial part of simulation may speed-up the convergence to steady state by faster damping of the travelling waves in the computational domain. In some cases, this over-damping can be used to partially damp the interferences of physical waves generated by terrain features with those introduced by boundary conditions. In this way you can get better looking results in the far-field, but at the expense of the loss of some resolution of the scheme.

7.3. Grid related issues

As mentioned above, the grid spacing severely affects the results of numerical simulations. While the use of high order space discretisation may help to capture some of the flow features that are usually unresolved by lower order methods on the same grid, the low level of damping that is characteristic for high order methods also brings some new problems to numerical simulations. Some non-physical artifacts introduced by far-field boundary conditions can be unresolved or faster damped by low order methods, while higher order schemes can contribute to the better resolution and longer persistence of these unwanted features in computational field. In some cases, the grid coarsening in the far-field may help to avoid this artificial effects to negatively influence the results in the interior proximity of physically relevant features in the interior of the domain. As the numerical filtering only affects the wavelengths close to the mesh cell size, by appropriate extension of the grid spacing we may intentionally damp also the longer wavelengths close to the far-field boundaries. Of course this means that the numerical results in these coarse-grid regions are not physical anymore and serve only as a buffer region for the smooth transition to the far-field boundary values.

From the physical point of view, there are two limits to be imposed on the grid spacing. The first limit comes from the need to properly resolve the boundary layer in the near-wall region. Here the grid spacing is usually chosen to be inversely proportional to Reynolds number to guarantee some minimal number of grid points in the boundary layer. Another limitation to the grid spacing comes with stratification. In order to properly resolve the terrain induced gravity waves, the grid spacing in the far-field area should not fall below certain threshold defined by the wavelength of these waves. This means that the grid spacing in the physically relevant parts of the computational domain should be limited from above by a certain cell size that is inversely proportional to the Brunt-Väisälä frequency N. The number of grid points needed per resolved wavelength then further depends on the resolving power of the numerical scheme. High order methods in general require less points per wavelength.

7.4. Final remarks

The comparison of numerical results presented in this paper revealed several issues to be further addressed. We have demonstrated that the compact finite-difference schemes that we have used are at least as good in terms of resolution and robustness as the modern AUSM finite-volume scheme. So even if we have only used few of the simplest of the currently available compact finite-difference schemes, it seems that they are able to deliver better resolution than one of the best available finite-volume methods. The simulations have also shown that the use of high resolution methods not only brings more detailed results, it also brings some difficulties. These are mainly connected with some unwanted numerical artifacts being resolved and preserved by the high resolution methods. These non-physical (or better to say numerically introduced) features are usually unresolved or quickly damped by low-order methods.

Our future work should definitely bring more light into the choice and implementation of suitable boundary conditions especially for stratified flow. Another area to be explored is the dispersion and diffusion behaviour of numerical methods with respect to numerical stabilisation in conjunction with high order time-and space-discretisations (see e.g. [7,8] or [9]). Some further more detailed analysis of time-discretisation methods will be necessary for solving also the unsteady problems.

Acknowledgements

References

[1] S.K. Lele, Compact finite difference schemes with spectral-like resolution, Journal of Computational Physics 103 (1992) 16–42.
[2] I. Sládek, T. Bodnár, K. Kozel, On a numerical study of atmospheric 2D and 3D – flows over a complex topography with forest including pollution dispersion, Journal of Wind Engineering and Industrial Aerodynamics 95 (9–11) (2007) 1424–1444.
[3] T. Bodnár, L. Beneš, K. Kozel, Numerical simulation of flow over barriers in complex terrain, Il Nuovo Cimento C 31 (5–6) (2008) 619–632.
[4] L. Beneš, T. Bodnár, P. Fraunié, K. Kozel, Numerical Modelling of Pollution Dispersion in 3D Atmospheric Boundary Layer, in: B. Sportisse (Ed.), Air Pollution Modelling and Simulation, Springer Verlag, 2002, pp. 69–78.
[5] L. Matějíček, Z. Jaňour, L. Beneš, T. Bodnár, E. Gulíková, Spatio - temporal modelling of dust transport over surface mining areas and neighbouring residential zones, Sensors 8 (6) (2008) 3830–3847.
[6] T. Bodnár, K. Kozel, P. Fraunié, Z. Jaňour, Numerical simulation of flow and pollution dispersion in 3D atmospheric boundary layer, Computing and Visualization in Science 3 (1–2) (2000) 3–8.
[7] T.K. Sengupta, S.K. Sircar, A. Dipankar, High accuracy schemes for DNS and acoustics, Journal of Scientific Computing 26 (2) (2006) 151–193.
[8] T.K. Sengupta, Y. Bhumkar, V. Lakshmanan, Design and analysis of a new filter for LES and DES, Computers and Structures 87 (2009) 735–750.
[9] T.K. Sengupta, Y.G. Bhumkar, New explicit two-dimensional higher order filters, Computers & Fluids 39 (2010) 1848–1863.
[10] A. Shah, L. Yuan, A. Khan, Upwind compact finite difference scheme for time-accurate solution of the incompressible Navier–Stokes equations, Applied Mathematics and Computation 215 (2010) 3201–3213.
[11] G. Gürarslan, Numerical modelling of linear and nonlinear diffusion equations by compact finite difference method, Applied Mathematics and Computation 216 (2010) 2472–2478.
[12] M.R. Visbal, D.V. Gaitonde, On the use of higher-order finite-difference schemes on curvilinear and deforming meshes, Journal of Computational Physics 181 (2002) 155–185.
[13] D.V. Gaitonde, J.S. Shang, J.L. Young, Practical aspects of higher-order numerical schemes for wave propagation phenomena, International Journal for Numerical Methods in Engineering 45 (1999) 1849–1869.
[14] C.W. Shu, S. Osher, Efficient implementation of essentially non-oscillatory shock-capturing schemes, Journal of Computational Physics 77 (1988) 439–471.
[15] R.J. Spiteri, S.J. Ruuth, A new class of optimal high-order strong-stability-preserving time discretization methods, SIAM Journal on Numerical Analysis 40 (2) (2002) 469–491.
[16] J. Barth, M. Gabriel, D. Keyes, R. Nieminen, D. Roose, T. Schlick (Eds.), Bail 2008 - Boundary and Interior Layers, Springer, Lecture Notes in Computational Science and Engineering, 2009, Ch. Numerical Simulation of the Towing Tank Problem Using High Order Schemes, pp. 79–94.
[17] L. Beneš, J. Fürst, Numerical simulation of stratified flows past a body, in: ENUMATH 2009, Springer, 2009, p. 8p.
[18] L. Beneš, J. Fürst, Comparison of the two numerical methods for the stratified flow, in: ICFD 2010 10th Conference on Numerical Methods for Fluid Dynamics, Univ. Reading, 2010, p. 6p.
[19] B. van Leer, Towards the ultimate conservative difference scheme, v. a second order sequel to godunov's method, Journal of Computational Physics (31) (1979) 101–136.
[20] E. Dick, J. Vierendeels, Riemslagh, A multigrid semi–implicit line–method for viscous incompressible and low–mach–number flows on high aspects ratio grids, Journal of Computational Physics (154) (1999) 310–341.

E.4   High Resolution Simulation of Three-Dimensional Lee Waves Behind Isolated Hill

BODNÁR T., FRAUNIÉ PH.
Preprint, To be submitted.

This paper presents the newly developed three-dimensional extension of the high-resolution compact finite-difference code, previously used in papers [E.3], [E.4]. Besides of performing the tests of the newly implemented 3D scheme a series of simulations was used to demonstrate the behavior of the Boussinesq model within a range of Reynolds and Froude numbers. Certain issues concerning the boundary conditions were pointed out. This problem will further be addressed in a continuation of this work.

All the numerical simulations presented in this paper were proposed and performed by T. Bodnár.

High Resolution Simulation of Three-Dimensional Lee Waves Behind Isolated Hill

Tomáš Bodnár[1,2] and Philippe Fraunié[2]

[1]*Department of Technical Mathematics, Faculty of Mechanical Engineering, Czech Technical University in Prague, Karlovo Náměstí 13, 121 35 Prague 2, Czech Republic, Tomas.Bodnar@fs.cvut.cz*

[2]*Institute of Mathematics, Czech Academy of Sciences, Žitná 25, 115 67 Prague 1, Czech Republic*

[3]*Mediterranean Institute of Oceanography - MIO, UM 110 USTV - AMU - CNRS/INSU 7294 - IRD 235, Université de Toulon, BP 20132 F-83957 La Garde cedex, France, Philippe.Fraunie@univ-tln.fr*

February 19, 2017

Abstract

The stably stratified fluid flow over smooth hills is one of the essential processes in environmental fluid mechanics. The aim of this paper is to point out some of the key features of this phenomena, both from the physical and mathematical modeling point of view. The three-dimensional laminar flow over a smooth, axisymmetric hill is considered over a range of Froude and Reynolds numbers. The numerical simulations are performed based on the Boussinesq approximation model, solved using a high resolution compact finite difference numerical scheme. The obtained numerical results are discussed with respect to the observed physical phenomenology, taking into account the separate role of varying velocity (Reynolds number) and stratification (Froude number). The encountered mathematical modeling and numerical solvability issues are discussed in detail, pointing out the key role of the computational setup and boundary conditions.

1 Introduction

Stratification is one of the most challenging features of environmental flows. It's a consequence of a gravity force, acting on a fluid with non-constant density, forming a vertically structured density profile. Under typical circumstances, the heavier fluid is close to the bottom, while the lightest is at the top, resulting in a vertically variable density profile, with negative vertical density gradient. This basic fluid stratification is subject to various perturbations, typically introduced by obstacles, over which the fluid flows. In contrast to the classical homogeneous (i.e. non-stratified) case, the flow perturbations in stratified flows become more apparent, by forming a typical internal wave patterns due to the action of buoyancy force.

   The aim of this study is to get a deeper insight into this phenomena by means of numerical experiments. The focus will be on laminar, stably stratified flow over an isolated smooth hill.

1.1 Physical background

The primary motivation for this study comes from atmospheric boundary layer flows over hills. There are three main parameters naturally appearing in the description of this kind of flows.

   1. *Buoyancy frequency*

$$N = \sqrt{\frac{g}{\rho^*}\frac{\partial \rho_0(z)}{\partial z}} \qquad [s^{-1}] \tag{1}$$

   This is the (angular) frequency of oscillations of a fluid parcel that was moved vertically from its equilibrium position. Due to a density difference between the parcel and the surrounding fluid, the buoyancy force tends to return it to equilibrium, which causes oscillations around the equilibrium position. The parameter N is usually referred to as the *Brunt–Väisälä frequency*. Here the key physical parameters are the gravity acceleration g, characteristic density ρ^* and the vertical density gradient[1] $\gamma = \frac{\partial \rho_0}{\partial z}$.

   2. *Reynolds number*

$$Re = \frac{\rho^* U_\infty L_R}{\mu} \tag{2}$$

   This parameter can be interpreted as a characteristic ratio between the inertial and viscous forces in the flow. The physical parameters behind the Reynolds number are the characteristic velocity U_∞, length scale L_R (e.g. the boundary layer thickness or hill height) and the fluid dynamical viscosity μ.

   3. *Froude number*

$$F = \frac{U_\infty}{N L_F} \tag{3}$$

   The interpretation of this parameter depends on the choice of the characteristic length L_F (hill height, its half-length, etc.). It can be understood, for example, as a ratio of buoyancy time-scale $1/N$ over the advection time-scale L_F/U_∞. This is probably the most important parameter characterizing the stratified flow over hills as it combines the effects of hill size with fluid velocity and its stratification.

For the given geometrical configuration and given fluid, there only remain two free parameters characterizing the considered problem. It's the velocity U_∞ of the fluid and its stratification γ, i.e. the parameters Re and N. This is in contrast to several previous experimental and numerical studies, where towing tank experiments were performed under predefined stratification, by only changing the characteristic velocity U_∞. In such a setup, both the Reynolds and Froude numbers, Re and F, vary simultaneously, being proportional to U_∞, while the buoyancy frequency N is kept constant. Thus it's impossible to separate the effects of Re and F. One of the aims of this study is to consider and evaluate the separate effects of these two parameters on the flow field structure.

---

[1]Both g and γ are negative in the chosen coordinate system.

2

1.2   Experimental evidence

The stratified flow over hills was studied in numerous experimental works in the past decades. Probably the most influential study in this field is the paper Hunt and Snyder [15], where *laboratory scale* towing tank experiments are described. The flow over a smooth, rotationally symmetric hill was simulated for various characteristic Froude numbers. The resulting flow field was confronted with field observations as well as with the analytical solutions of some approximate mathematical models. This problem setup was later used as a basis for various experimental and numerical studies (including the one presented in this paper). The three-dimensional wake structure behind a Gaussian shaped hills was studied in Kadri, Bonneton, Chomaz, and Perrier [17]. The towing speed and hill diameter were varied, looking for a change in the resulting wake structure. The papers Castro, Snyder, and Marsh [4] and Castro [3] describe a series of experiments on stratified fluid flow over a sharp, prismatic ridges. Besides the variation in Froude number (due to towing velocity), also the effect of the aspect ratio of the ridge was taken into account. The conical and hemi-spherical hill shapes were used in towing tank experiments presented in Vosper, Castro, Snyder, and Mobbs [43], to study the obstacle shape on flow field and drag under different Froude numbers. In Gyüre and Jánosi [13] quasi-two-dimensional lee-wave formation behind symmetric as well as asymmetric obstacles was studied in another towing tank experiment, looking for typical wavelengths and amplitudes of lee-waves fields. A periodic in space hill (of rectangular, triangular and sinusoidal shape) configuration was used in Sutherland and Aguilar [34] to study the wave generation and boundary layer separation for different configurations and Froude numbers.

It's good to note here, that all the above experiments were performed on scaled-down laboratory sized models, towed in a water tank. Therefore, in fact, the primary way to change the Froude number was to vary the towing velocity.

Another type of laboratory scale experiment is represented by Takahashi, Kato, Murakami, Ooka, Yassin, and Kono [37] considering a wind tunnel (in contrast to the above towing tank experiments) study on the turbulent structure of the airflow around a three-dimensional hill under stable, neutral and unstable stratification. Similar (but 2D) experiments were also described in Ross, Arnold, Vosper, Mobbs, Dixon, and Robins [23].

Some *real scale* atmospheric observations of stratified wind flow over a hill were presented e.g. in Wooldridge, Fox, and Furman [46]. The flow structure over an isolated large hill of moderate slope was described for a range of Froude numbers (both the velocity and stratification have changed). An extension of a dividing streamline concept was tested against the experimental observations in Leo, Thompson, Sabatino, and Fernando [19].

A *combination of analytical solution* of simple mathematical model with experimental investigation is presented e.g. in Davis [5], where a two-dimensional flow over triangular ridge was considered. An overview of simple two- and three-dimensional models is summarized in Smith [27], complemented by an explanation of the physical phenomenology of stratified flows over mountains and experimental demonstration of the most important features. A comparison of linear and nonlinear models for mountain waves are shown in Peltier and Clark [21], comparing the predicted wave-field with satellite observations. Field observation data were compared against the linear model predictions in Weng [45]. Similar, linear theory model comparison with experimental data, this time from towing tank experiment, was published in Thompson, Shipman, and Rottman [38].

1.3   Numerical studies

The mathematical modeling of stratified flows over hills came into play with the simplified models and their analytical or semi-analytical solutions. Typical examples of such works are e.g. the linearized hydrostatic models in Smith [27, 28, 29, 30, 31]. The the structure of lee vortices was analyzed using simplified models in Smolarkiewicz and Rotunno [32] or Rotunno, Grubišić, and Smolarkiewicz [24]. The stratified separated flow around a mountain was solved analytically in Hunt, Vilenski, and Johnson [16].

The fast evolution of computational tools and methods in recent years led to an increasing interest in detailed numerical simulations of stratified flows over hills.

The numerical simulations in Ding, Calhoun, and Street [7] and Ding and Street [6] are based on the towing tank experimental setup introduced in the above mentioned paper [15]. It uses a finite-volume code to solve a Large-Eddy Simulation (LES) extension of Boussinesq equations for the case of a strongly stratified flow over a three-dimensional hill. Similar setup, but in the laminar case was used also in Suzuki and Kuwahara [35], where the Boussinesq equations were solved by a finite difference method using a generalized coordinate system.

The non-homogeneous incompressible Navier-Stokes equations were solved numerically for 3D flow over an isolated hill in Hanazaki [14] and compared with some simplified models predictions. A finite-volume solver on unstructured grids was developed in Szmelter, Zhang, and Smolarkiewicz [36], based on inviscid Boussinesq model. It was used to simulate the flow over an axially symmetric isolated hill of polynomial shape. The effects of Earth's rotation were taken into account in Torres and Castillo [39], where a finite-difference solver was used to simulate the Boussinesq approximation of laminar incompressible Navier-Stokes equations.

The stratified flow separation for various hill heights and Froude numbers was investigated using the inviscid Euler model in Ambaum and Marshall [1]. A two-dimensional numerical simulation of stratified atmospheric flows at low Mach and Froude numbers is presented in Gatti-Bono and Colella [12], where a new anelastic projection algorithm was developed to solve the compressible Euler equations using a finite-volume scheme. Similar problem was recently studied numerically in viscous, compressible, turbulent setup in Sachsperger, Serafina, and Grubišić [25].

A numerical study of stably stratified flows over a two-dimensional hill was presented in [40]. A finite-difference code was used to solve the Boussinesq approximation. This work was later extended in Uchida and Ohya [41] by solving the problem using a 3D code as a quasi 2D case, looking for three-dimensional separation effects and temporal drag evolution. In both cases, the no-slip conditions were only used on the surface of the hill, while the free-slip conditions were used on the other parts of the wall.

Various simplified models were often used, either separately or in a comparison either with more complex models or with the experimental data. In Epifanio and Durran [9] a simplified weakly non-linear semi-analytical model is solved for a free-slip non-rotating flow over a smooth ridge. A shallow-water model was used in Epifanio [8] to study the lee vortices behind an isolated obstacle. A comparison of the Long's hydrostatic solution with a numerically solved non-linear model for a stratified flow over a 2D mountain ridge was presented in Ling and Wang [20]. The influence of the hill height and aspect ratio (spanwise to streamwise size) on the stratified flow field structure was studied in Bauer, Mayr, Vergeiner, and Pichler [2] using the mesoscale code RAMS (Regional Atmospheric Modeling System). A three-dimensional nonhydrostatic ocean model was solved in Ford [10] using a finite-element method for the flow of stratified fluid past an isolated Gaussian seamount.

A comparison of numerical and experimental results for a flow over two-dimensional hills (triangular and sinusoidal ridges) in both neutral and stably stratified turbulent wind flow were published in Ross et al. [23]. The numerical model solved the time-dependent Boussinesq equations in a terrain-following coordinate system and utilized a finite-difference discretization and an explicit time integration scheme[2]. Different turbulence closures were adopted and compared. Similar problem was solved in Wan and Porté-Agel [44] employing a LES turbulence model.

---

[2]The same basic code (BLASIUS model from the U.K. Met Office) was also used in Ross and Vosper [22] for numerical simulations of stably stratified flow through a mountain pass.

2 Mathematical Model

2.1 Full incompressible model

The incompressible fluid flow can be described by velocity field $v(x, t)$ and density field $\rho(x, t)$, that are governed by the balance of mass and linear momentum in the following general form:

$$\frac{\partial \rho}{\partial t} + \operatorname{div}(\rho v) = 0 \tag{4}$$

$$\frac{\partial \rho v}{\partial t} + \operatorname{div}(\rho v \otimes v) = \operatorname{div}\mathbb{S} + \rho f \tag{5}$$

Here the $f(x, t)$ stands for volume forces (only gravity force $f = g = (0, 0, g)$ is assumed further).

The stress tensor $\mathbb{S} = \mathbb{T} - p\mathbb{I}$ (with $\mathbb{I}$ being the identity tensor) can be split into viscous (deviatoric) part $\mathbb{T}$ and normal (spherical) contribution due to pressure $p(x, t)$. The viscous stress tensor in the incompressible *Newtonian fluids* is defined by $\mathbb{T} = \mu \left(\nabla v + \nabla v^T\right) = 2\mu\mathbb{D}$, where $\mathbb{D}$ denotes the symmetric part of the velocity gradient and the coefficient μ is the dynamic viscosity, which is considered to be constant[3] in the present study.

These governing equations for unknowns v, p and ρ are supplemented by the incompressibility constraint $\operatorname{div}v = 0$, that can be understood as a differential formulation of a *conservation of volume* principle. This divergence-free constraint can be used to simplify the above system of equations. The conservation of mass is represented by the continuity equation (4), where the divergence of the product (ρv) this can be expanded as

$$\frac{\partial \rho}{\partial t} + v \cdot \operatorname{grad} \rho = -\rho \operatorname{div} v \tag{6}$$

For incompressible flowsthe right-hand side of equation (6) vanishes and thus the continuity equation reduces to:

$$\frac{\partial \rho}{\partial t} + v \cdot \operatorname{grad} \rho = 0 \tag{7}$$

This is sometimes referred to as the convective (or non-conservative) form of continuity equation. It represents a transport equation for density. This equation can be used to rewrite the left-hand side of the momentum balance (5):

$$\frac{\partial \rho v}{\partial t} + \operatorname{div}(\rho v \otimes v) = \rho \left(\frac{\partial v}{\partial t} + \operatorname{div}(v \otimes v)\right) + v \underbrace{\left(\frac{\partial \rho}{\partial t} + v \cdot \operatorname{grad} \rho\right)}_{=0} \tag{8}$$

Using this manipulation the momentum equation (5) can alternatively be rewritten as:

$$\rho \left(\frac{\partial v}{\partial t} + \operatorname{div}(v \otimes v)\right) = -\operatorname{grad} p + \operatorname{div}2\mu\mathbb{D} + \rho g \tag{9}$$

Here the momentum equation (9) is written in the divergence (conservative) form. It can be rewritten using the divergence-free constraint into the convective (non-conservative) form using the expansion

$$\operatorname{div}(v \otimes v) = (v \cdot \operatorname{grad})v + v \underbrace{\operatorname{div}v}_{=0} \tag{10}$$

which leads to the convective form of the momentum equation (9)

$$\rho \left(\frac{\partial v}{\partial t} + v \cdot \operatorname{grad} v\right) = -\operatorname{grad} p + \operatorname{div}2\mu\mathbb{D} + \rho g \tag{11}$$

The governing systems (4)-(5), resp. (7), (9), represent the full incompressible, viscous (laminar), variable density model. This model is sometimes called the *non-homogeneous Navier-Stokes equations*. This is the system that we use as a starting point to develop the so called Boussinesq approximation.

---

[3]Here we assume the case of laminar flow with constant viscosity. For turbulent flow with variable (eddy) viscosity the model will require some changes.

2.2 Boussinesq approximation

Now we will assume that the pressure and density fields are perturbation of hydrostatic equilibrium state, i.e.:

$$\rho(\boldsymbol{x}, t) = \rho_0(\boldsymbol{x}) + \rho'(\boldsymbol{x}, t) \quad \text{i.e.} \quad \rho(x, y, z, t) = \rho_0(z) + \rho'(x, y, z, t) \tag{12}$$

$$p(\boldsymbol{x}, t) = p_0(\boldsymbol{x}) + p'(\boldsymbol{x}, t) \quad \text{i.e.} \quad p(x, y, z, t) = p_0(z) + p'(x, y, z, t) \tag{13}$$

where the background density and pressure fields are linked by the hydrostatic relation:

$$\operatorname{grad} p_0 = \rho_0 \boldsymbol{g} \quad \text{i.e.} \quad \frac{\partial p_0}{\partial z} = \rho_0 g \quad . \tag{14}$$

Using this decomposition of density where $\rho = \rho_0 + \rho'$, the continuity equation (7) can be expanded to

$$\frac{\partial \rho}{\partial t} + \boldsymbol{v} \cdot \operatorname{grad} \rho = \underbrace{\frac{\partial \rho_0}{\partial t}}_{=0} + \frac{\partial \rho'}{\partial t} + \underbrace{\boldsymbol{v} \cdot \operatorname{grad} \rho_0}_{\gamma} + \boldsymbol{v} \cdot \operatorname{grad} \rho' \tag{15}$$

where the background (hydrostatic) pressure gradient was denoted by $\boldsymbol{\gamma} = (0, 0, \gamma)$, which leads to

$$\frac{\partial \rho'}{\partial t} + \boldsymbol{v} \cdot \operatorname{grad} \rho' = -\boldsymbol{v} \cdot \boldsymbol{\gamma} \quad i.e. \quad \frac{\partial \rho'}{\partial t} + \boldsymbol{v} \cdot \operatorname{grad} \rho' = -w\gamma \tag{16}$$

This new version of the continuity equation is equivalent to the original (7), resp. (4).

The momentum equations (9) can be transformed in a similar way by withdrawing the background, hydrostatic pressure gradient force. This leads to a rearranged equation

$$\rho \left(\frac{\partial \boldsymbol{v}}{\partial t} + \operatorname{div}(\boldsymbol{v} \otimes \boldsymbol{v}) \right) = -\operatorname{grad} p' + \operatorname{div} 2\mu \mathbb{D} + \rho' \boldsymbol{g} \quad . \tag{17}$$

It is good to note here, that so far only decompositions and rearrangements were applied to the governing system. No approximations were made and thus the momentum equation (17) is still fully equivalent to the original (9), resp. (5).

The *Boussinesq approximation* is obtained from the full model by replacing the complete density $\rho(\boldsymbol{x}, t)$ on the right hand side of momentum equation (17) by a suitable fixed (in space and time) characteristic density ρ^*. This immediately leads to the approximate set of governing equations, the so called Boussinesq approximation:

$$\frac{\partial \rho'}{\partial t} + \boldsymbol{v} \cdot \operatorname{grad} \rho' = -w\gamma \tag{18}$$

$$\rho^* \left(\frac{\partial \boldsymbol{v}}{\partial t} + \operatorname{div}(\boldsymbol{v} \otimes \boldsymbol{v}) \right) = -\operatorname{grad} p' + \operatorname{div} 2\mu \mathbb{D} + \rho' \boldsymbol{g} \quad . \tag{19}$$

Here the system was written in terms of the density perturbation $\rho' = (\rho - \rho_0)$, however it can also be written in terms of the complete density

$$\frac{\partial \rho}{\partial t} + \boldsymbol{v} \cdot \operatorname{grad} \rho = 0 \tag{20}$$

$$\rho^* \left(\frac{\partial \boldsymbol{v}}{\partial t} + \operatorname{div}(\boldsymbol{v} \otimes \boldsymbol{v}) \right) = -\operatorname{grad} p' + \operatorname{div} 2\mu \mathbb{D} + (\rho - \rho_0) \boldsymbol{g} \quad . \tag{21}$$

This is the system that was used in the numerical simulations presented in this paper.

The only difference between the full system of non-homogeneous Navier-Stokes equations and the Boussinesq approximation is in the scaling of certain terms in the momentum equation by the constant characteristic density ρ^* instead of the complete $\rho(\boldsymbol{x}, t)$. Thus the validity of Boussinesq approximation depends on the difference between the ρ^* and $\rho(\boldsymbol{x}, t)$ for the considered case.

The characteristic density ρ^* is usually chosen as a kind of a mean density defined from the background density ρ_0. Instead of using an average, we have chosen the characteristic density to be equal to the background density at a pre-defined characteristic height h^*, i.e. $\rho^* = \rho_0(h^*)$ and thus $\rho_0(z) = \rho^* + \gamma \cdot (z - h^*)$. This choice allows to keep the ρ^* (i.e. the Reynolds number) independent of the computational domain size (height).

3   Numerical Solver

The numerical solution of stably stratified flows is a very specific discipline. The typical resulting solution includes all of the features of neutrally stratified cases (i.e. boundary layers, recirculation zones, stagnation points, wakes, etc.), but in addition, the stable stratification allows the existence of gravity waves in the computational field. These gravity waves usually have rather small amplitude, their wavelength can vary according to the flow conditions, but more importantly, their spatial extent is enormous, compared to the size of the geometrical feature (obstacle), that initially generated the perturbation.

This specific character of the solution of stably stratified flows makes them quite distinct from the classical neutral cases. The numerical solution of stratified flows requires specific treatment starting from grid generation, through numerical discretization and stabilization, up to the implementation of specific boundary conditions that should be non-reflective for the internal waves.

The numerical solver presented hereafter is designed as a modular tool, where the spatial and temporal discretizations are separated, and so is the numerical stabilization. Therefore a semi-discretization is applied, i.e. first a discretization in space is applied, resulting in a system of ordinary differential equations for temporal evolution of the variables in grid points. These ODEs are integrated in time by a suitable method (*Runge-Kutta multistage method* was adopted here). The central in space discretizations are intentionally used (*compact finite-difference schemes* in this case), because they are free of embedded upwinding and numerical diffusion.

Primary focus is on steady flows, so stationary solution is sought. Thus the *artificial compressibility method* was adopted (adding a pseudo time-derivative of pressure to the divergence-free constraint). The *time-marching procedure* is further applied, i.e. the stationary solution is obtained as a limit for $t \longrightarrow \infty$ from solving an unsteady system of governing equations with steady boundary conditions. In the limit, the time-derivatives will vanish (including the non-physical added time-derivative of pressure) and the steady solution is recovered (satisfying the divergence-free condition).

3.1   Discretization in space

In order to resolve the low-amplitude and possibly high-(spatial) frequency gravity waves, a high resolution numerical discretization is required. The compact finite-difference schemes seem to be a natural choice, because they not only have a high formal order of accuracy, but they also have well documented numerical dispersion/diffusion behavior.

This type of discretization was chosen because it offers high resolution while retaining well defined dispersion/diffusion characteristics. This is a rare among the modern high resolution methods that often employ complicated non-linear reconstruction and stabilization techniques. The family of compact (in the sense of narrow computational stencil) schemes in its current form was introduced in [18] and is successfully used e.g. in computational aeroacoustics (see e.g. [11], [42]). Its superior resolution and low numerical diffusion/dispersion makes it suitable for capturing various wave phenomena, including those in stratified flows.

The basic concept of the compact finite-difference schemes naturally extends and generalizes the construction of the classical (sometimes called explicit) finite difference approximations. In the classical approach the central approximation of first derivative $\phi'(x)$ of a (sufficiently smooth) function $\phi(x)$ can be obtained as a (symmetric) linear combination of neighboring grid values ϕ_i (resp. their divided differences).

$$\phi'_i \approx \alpha_1 \frac{\phi_{i+1} - \phi_{i-1}}{2h} + \alpha_2 \frac{\phi_{i+2} - \phi_{i-2}}{4h} + \ldots + \alpha_\ell \frac{\phi_{i+\ell} - \phi_{i-\ell}}{2\ell h} \tag{22}$$

The coefficients α_m; $m = 0, \ldots, \ell$ are obtained by matching the above expression to Taylor expansion of $\phi(x_i \pm mh)$. So the classical central finite-difference approximations take the following form.

$$\phi'_i \approx \sum_{m=1}^{m=\ell} \alpha_m \frac{\phi_{i+m} - \phi_{i-m}}{2mh} \tag{23}$$

The compact approximations can reduce the computational stencil (needed for required order of accuracy) and in some cases also improve the resolution of the method. The main idea of compact finite

differencing is to instead of looking for an (explicit) formula approximating the value of ϕ_i', an approximate (symmetric) linear combination of neighboring derivatives $(\ldots, \phi_{i-1}', \phi_i', \phi_{i+1}', \ldots)$ is sought.

$$a_q\phi_{i-q}' + \ldots + a_2\phi_{i-2}' + a_1\phi_{i-1}' + \phi_i' + a_1\phi_{i+1}' + a_2\phi_{i+2}' + \ldots + a_q\phi_{i+q}' \approx \qquad (24)$$

$$\approx \alpha_1\frac{\phi_{i+1} - \phi_{i-1}}{2h} + \alpha_2\frac{\phi_{i+2} - \phi_{i-2}}{4h} + \ldots + \alpha_\ell\frac{\phi_{i+\ell} - \phi_{i-\ell}}{2\ell h} \qquad (25)$$

The approximation (24) could be understood as an implicit relation between the function values ϕ_i and the approximate derivatives ϕ_i'. This approach generalizes the classical finite-differencing, which now becomes just a special case of the compact approach.

Using the compact differencing, the approximation formula becomes more complicated.

$$\phi_i' + \sum_{n=1}^{n=q} a_n(\phi_{i-n}' + \phi_{i+n}') \approx \sum_{m=1}^{m=\ell} \alpha_m\frac{\phi_{i+m} - \phi_{i-m}}{2mh} \qquad (26)$$

In this paper the compact schemes with at maximum tri-diagonal system of equations and five-point discretization stencil are used. These could be written in the form:

$$a_1\phi_{i-1}' + \phi_i' + a_1\phi_{i+1}' = \alpha_1\frac{\phi_{i+1} - \phi_{i-1}}{2h} + \alpha_2\frac{\phi_{i+2} - \phi_{i-2}}{4h} \qquad . \qquad (27)$$

To get the approximation formula of desired order, it is necessary to match the general formula with Taylor series expansions. The first non-matching coefficient determines the leading order of the truncation error. The following conditions on the coefficients should be satisfied to attain certain order of accuracy.

Second order	$\alpha_1 + \alpha_2 = 1 + 2a_1$
Fourth order	$\alpha_1 + 2^2\alpha_2 = 2\frac{3!}{2!}a_1$
Sixth order	$\alpha_1 + 2^4\alpha_2 = 2\frac{5!}{4!}a_1$

Table 1: Order conditions for compact approximations

It is obvious that for the approximations of the order lower than six, there are more unknown parameters than equations from the which these parameters can be computed. This means that the coefficients for the lower order schemes are not unique. This offers a possibility to choose a-priori some of the coefficients (usually to make the solution easier). For example we may get the classical (explicit) difference schemes for $a_1 = 0$. In the same way the discretization stencil width can be reduced by choosing e.g. $\alpha_2 = 0$. This is shown in the table 2 where the coefficients of the compact finite difference schemes with tri-diagonal matrix and up to five point stencil are summarized.

Scheme	a_1	α_1	α_2	Diagonals	Points	Order
A	a	$\frac{2}{3}(a+2)$	$\frac{1}{3}(4a-1)$	3	5	4
B	$a = \frac{1}{3}$	$\frac{14}{9}$	$\frac{1}{9}$	3	5	6
C	$a = \frac{1}{4}$	$\frac{3}{2}$	0	3	3	4

Table 2: Parameters for tri-diagonal schemes

Without further constrains, this setup leads to a one-parametric family of schemes of the type denoted A in the Table 2. Various specific choices of the free parameter a may further lead to either increase of the order of accuracy of the scheme (as for $a = 1/3$ leading to, highest in this class, 6th order of accuracy) or reduction of the size of the computational stencil (as for $a = 1/4$ leading to three-point stencil rather than five-point stencil necessary for classical explicit approximation of the same 4th order of accuracy).

The 6th order compact scheme with $a = 1/3$ was used for the simulations presented in this paper.

3.2 Discretization in time

Due to a modularity of the numerical solver (and semi-discretization approach) a relative freedom is kept in the choice of the method for numerical integration in time. Here we have opted for the explicit Runge-Kutta multistage schemes, more specifically for the Strong Stability Preserving family of Runge-Kutta (SSP-RK) schemes. This choice is motivated by the aim to retain simplicity, flexibility and guaranteed non-oscillatory behavior of discretization. The choice of explicit scheme leads to a very simple implementation, at the expense of the lower computational efficiency (compared to implicit schemes), especially in the steady case. The Runge-Kutta family of schemes allows for high flexibility of the solver, because several specific methods can be tested just by switching the coefficients of the RK method. The SSP-RK schemes were chosen to guarantee that no non-physical oscillations will be introduced by the temporal discretization, which is of key importance in resolving any wave phenomena.

As it was already mentioned in the previous sections, the concept of semi-discretization of evolutionary PDE's, allows to transform problems involving both space- and time- derivatives into problems containing only the derivatives with respect to time. A typical example of such approach could be the discretization of hyperbolic conservation laws. Written in one space dimension, the conservation of scalar quantity $\mathtt{w}(\boldsymbol{x}, t)$ can be expressed in differential form as[4]:

$$\mathtt{w}_t + f(\mathtt{w})_x = 0 . \tag{28}$$

Assuming now that the equation (28) was discretized in space, e.g. using one of the suitable FV or FD discretizations, it is transformed into the system of ODE's of the form:

$$\mathsf{W}_t = \widetilde{\mathcal{L}}(t, \mathsf{W}(t)) , \tag{29}$$

where $\mathsf{W} = \mathsf{W}(t)$ is the vector of discretized variable, i.e. $[\mathsf{W}(t)]_i = \mathsf{W}_i(t) = \mathtt{w}(x_i, t)$, and $\widetilde{\mathcal{L}}$ is a discrete version of the differentiation in space operator $\mathcal{L} = -f(\mathtt{w}(x_i, t))_x$.

The system (29) describes the evolution in time of the discrete grid values of unknown function $\mathtt{w}$. In order to solve the initial value problem based on this system of ODE's, virtually any of the methods originally developed for ODE's could be used.

The family of explicit SSP Runge-Kutta schemes is usually written in the form introduced in [26]:

$$\begin{aligned}
\mathsf{W}^{(0)} &= \mathsf{W}^n \\
\mathsf{W}^{(r)} &= \sum_{p=0}^{r-1} \left(\alpha_{rp} \mathsf{W}^{(p)} + \beta_{rp} \Delta t \widetilde{\mathcal{L}}(\mathsf{W}^{(p)}) \right) \qquad r = 1, \dots, s \\
\mathsf{W}^{n+1} &= \mathsf{W}^{(s)}
\end{aligned} \tag{30}$$

It is not difficult to see that in the case the coefficients β_{rp} are positive, the method (30) is nothing but a convex combination of Euler stages with fractional time-steps of the length $\frac{\beta_{rp}}{\alpha_{rp}} \Delta t$. Here we just shortly present some of the optimal, in the sense of accuracy versus stability, three-stage SSP-RK methods, originally studied in [33]. Hereafter the SSP(s,o) denotes the Runge-Kutta method which consists of s stages and has order of accuracy o. The above described three-stage SSP-RK methods were used to obtain the results in this paper. From the Table 3 follows that for given number of stages there is always a balance between the accuracy of the method and the maximum CFL number, where higher accuracy leads to lower CFL. The actual choice of the method only requires the use of different coefficients, without any additional re-programming of the code. The specific choice thus depends on the solved case and required time-accuracy. The data in the Table 3 suggest that the choice of the first order method with larger CFL (i.e. allowable time-step) should be preferable for seeking the steady case solution using the time-marching technique as a limit for $t \longrightarrow \infty$.

3.3 Numerical stabilization

Because a central discretization of spatial derivatives is used, a suitable stabilization method is required to remove the non-physical oscillations in the computational field.

---

[4]The subscripts are used to denote partial derivatives.

Method	α_{rp}			β_{rp}			CFL
	1			$\frac{1}{3}$			
SSP(3,1)	0	1		0	$\frac{1}{3}$		3
	0	0	1	0	0	$\frac{1}{3}$	
	1			$\frac{1}{2}$			
SSP(3,2)	0	1		0	$\frac{1}{2}$		2
	$\frac{1}{3}$	0	$\frac{2}{3}$	0	0	$\frac{1}{3}$	
	1			1			
SSP(3,3)	$\frac{3}{4}$	$\frac{1}{4}$		0	$\frac{1}{4}$		1
	$\frac{1}{3}$	0	$\frac{2}{3}$	0	0	$\frac{2}{3}$	

Table 3: Three stage SSP-RK methods

The main idea of filtering comes from the area of signal processing, where so called low-pass filters are used to suppress high frequencies in various signals. The amplitudes of high frequency modes are reduced, while low-frequencies remain unchanged. The filtering is in some sense very close to the classical artificial viscosity approach used for the stabilization of the numerical solution of hyperbolic PDEs. The filtering however is a little bit more general concept because it can also be used for other than hyperbolic problems.

An important subclass of low-pass filters is formed by the compact filters. A specific compact approximation functions are constructed in a similar fashion as the compact finite-difference schemes. This approach was proposed in [18] and applied and analyzed in [11] and [42]. According to [18] a typical compact filter could be written in the following form [5] :

$$b\hat{\phi}_{i-1} + \hat{\phi}_i + b\hat{\phi}_{i+1} = \sum_{n=0}^{N} \frac{\beta_n}{2}(\phi_{i-n} + \phi_{i+n}) \tag{31}$$

The coefficients β_i can be chosen to obtain filters of various orders. The single remaining parameter b takes the values $-0.5 \leqq b \leqq 0.5$. From the table 4, summarizing the coefficients of compact filters, follows that the filter of order P can be obtained using the stencil of the width $2Ph$, i.e. using $2P + 1$ points. The effect of a certain filter could be characterized by its *transfer function*[6]. When both the original

Filter	β_0	β_1	β_2	β_3	β_4
F2	$\frac{1+2b}{2}$	$\frac{1+2b}{2}$	0	0	0
F4	$\frac{5+6b}{8}$	$\frac{1+2b}{2}$	$\frac{2b-1}{8}$	0	0
F6	$\frac{11+10b}{16}$	$\frac{15+34b}{32}$	$\frac{3(2b-1)}{16}$	$\frac{1-2b}{32}$	0
F8	$\frac{93+70b}{128}$	$\frac{7+18b}{16}$	$\frac{7(2b-1)}{32}$	$\frac{1-2b}{16}$	$\frac{2b-1}{128}$

Table 4: Coefficients of the tri-diagonal family of compact filters.

and filtered "signal" is represented in Fourier space by its wave number and corresponding amplitude, the value of transfer function $T(w)$ is obtained as the ratio of the amplitudes of filtered and non-filtered

---

[5]In the context of the compact finite-difference schemes introduced in the table 2 it is natural to focus the attention on the compact filters leading to the solution of tri-diagonal system of equations.

[6]Sometimes called spectral function or spectral response (see e.g. [42] for more details)

signal for a given wave number w. According to [18] the transfer function of the tri-diagonal compact filter family is given by

$$T(\mathsf{w}) = \frac{\sum_{n=0}^{N} \beta_n \cos(n\mathsf{w})}{1 + 2b\cos(\mathsf{w})} \tag{32}$$

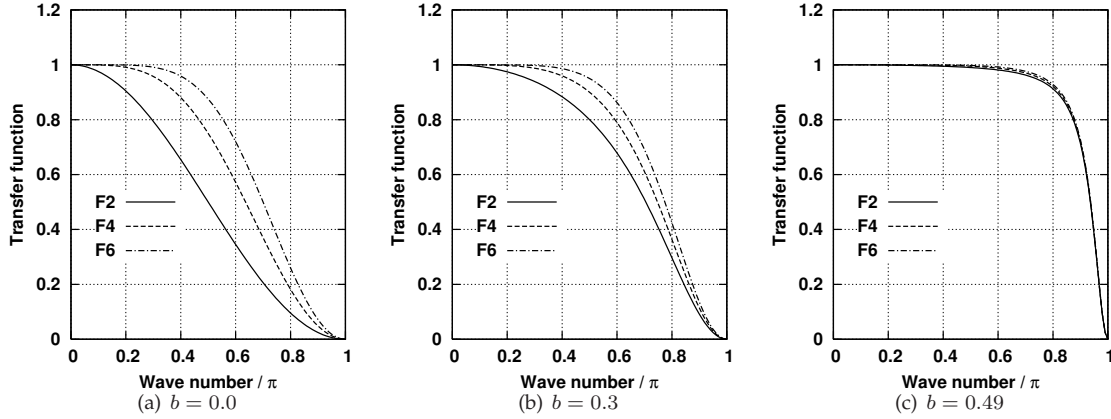The effect of filter order could be judged from the Figure 1.

Figure 1: Transfer functions of compact filters for different values of b.

From the above figures it is evident that the damping effect of all the filters is stronger with lower values of parameter b. Lowering the parameter b forces also lower frequencies being damped. The opposite effect is achieved by choosing the parameter b close to 0.5, when only the highest wave number (corresponding to grid frequency, point-to-point oscillations) components are damped. In the limit case of $b = 0.5$ the filter relation (31) reduces to identity, i.e. $\hat{\phi} = \phi$, and no damping occurs at all.

The eight order filter was used in this paper along with the sixth order spatial discretization.

3.4   Curvilinear coordinate transformation

The governing equations are expressed in physical Cartesian coordinate system (x, y, z) in which, the corresponding computational grid would be highly non-orthogonal, stretched and distorted. Such setup is not suitable for performing the above described finite-difference discretization. Therefore a new, regularly spaced orthogonal grid is associated with a coordinate system (ξ, η, ζ).
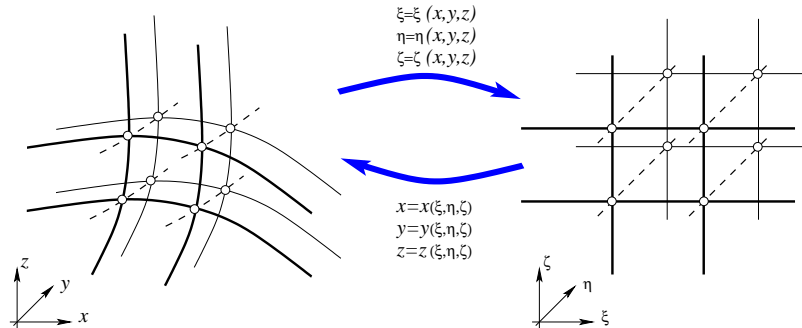

Figure 2: Curvilinear coordinate transformation

The coordinate transformation between physical space (x, y, z) and computational space (ξ, η, ζ) is

formally defined by the following relations:

$$
\left.
\begin{aligned}
x &= x(\xi, \eta, \zeta) \\
y &= y(\xi, \eta, \zeta) \\
z &= z(\xi, \eta, \zeta)
\end{aligned}
\right\}
\quad \boldsymbol{x} = \boldsymbol{x}(\boldsymbol{\xi})
\tag{33}
$$

The gradient of a scalar function $\phi(x, y, z)$ with respect to physical coordinates (x, y, z), i.e. $\nabla_x \phi$, can be expanded using the chain rule of differentiation as:

$$
\left.
\begin{aligned}
\frac{\partial \phi}{\partial x} &= \frac{\partial \phi}{\partial \xi}\frac{\partial \xi}{\partial x} + \frac{\partial \phi}{\partial \eta}\frac{\partial \eta}{\partial x} + \frac{\partial \phi}{\partial \zeta}\frac{\partial \zeta}{\partial x} \\
\frac{\partial \phi}{\partial y} &= \frac{\partial \phi}{\partial \xi}\frac{\partial \xi}{\partial y} + \frac{\partial \phi}{\partial \eta}\frac{\partial \eta}{\partial y} + \frac{\partial \phi}{\partial \zeta}\frac{\partial \zeta}{\partial y} \\
\frac{\partial \phi}{\partial z} &= \frac{\partial \phi}{\partial \xi}\frac{\partial \xi}{\partial z} + \frac{\partial \phi}{\partial \eta}\frac{\partial \eta}{\partial z} + \frac{\partial \phi}{\partial \zeta}\frac{\partial \zeta}{\partial z}
\end{aligned}
\right\}
\quad \nabla_x \phi = \boldsymbol{J}_\xi \, \nabla_\xi \phi
\tag{34}
$$

The Jacobi matrix $\boldsymbol{J}_\xi$ comes from the inverse transformation

$$
\boldsymbol{J}_\xi = \frac{\partial(\xi, \eta, \zeta)}{\partial(x, y, z)} =
\begin{pmatrix}
\frac{\partial \xi}{\partial x} & \frac{\partial \eta}{\partial x} & \frac{\partial \zeta}{\partial x} \\
\frac{\partial \xi}{\partial y} & \frac{\partial \eta}{\partial y} & \frac{\partial \zeta}{\partial y} \\
\frac{\partial \xi}{\partial z} & \frac{\partial \eta}{\partial z} & \frac{\partial \zeta}{\partial z}
\end{pmatrix}
=
\begin{pmatrix}
\xi_x & \eta_x & \zeta_x \\
\xi_y & \eta_y & \zeta_y \\
\xi_z & \eta_z & \zeta_z
\end{pmatrix}
\tag{35}
$$

This matrix is not computed directly, but using the Jacobi matrix $\boldsymbol{J}_x$, which arises in the expansion of the gradient of $\phi(\xi, \eta, \zeta)$ with respect to computational coordinates (ξ, η, ζ).

$$
\left.
\begin{aligned}
\frac{\partial \phi}{\partial \xi} &= \frac{\partial \phi}{\partial x}\frac{\partial x}{\partial \xi} + \frac{\partial \phi}{\partial y}\frac{\partial y}{\partial \xi} + \frac{\partial \phi}{\partial z}\frac{\partial z}{\partial \xi} \\
\frac{\partial \phi}{\partial \eta} &= \frac{\partial \phi}{\partial x}\frac{\partial x}{\partial \eta} + \frac{\partial \phi}{\partial y}\frac{\partial y}{\partial \eta} + \frac{\partial \phi}{\partial z}\frac{\partial z}{\partial \eta} \\
\frac{\partial \phi}{\partial \zeta} &= \frac{\partial \phi}{\partial x}\frac{\partial x}{\partial \zeta} + \frac{\partial \phi}{\partial y}\frac{\partial y}{\partial \zeta} + \frac{\partial \phi}{\partial z}\frac{\partial z}{\partial \zeta}
\end{aligned}
\right\}
\quad \nabla_\xi \phi = \boldsymbol{J}_x \, \nabla_x \phi
\tag{36}
$$

Here the transformation Jacobi matrix $\boldsymbol{J}_x$ is defined by:

$$
\boldsymbol{J}_x = \frac{\partial(x, y, z)}{\partial(\xi, \eta, \zeta)} =
\begin{pmatrix}
\frac{\partial x}{\partial \xi} & \frac{\partial y}{\partial \xi} & \frac{\partial z}{\partial \xi} \\
\frac{\partial x}{\partial \eta} & \frac{\partial y}{\partial \eta} & \frac{\partial z}{\partial \eta} \\
\frac{\partial x}{\partial \zeta} & \frac{\partial y}{\partial \zeta} & \frac{\partial z}{\partial \zeta}
\end{pmatrix}
=
\begin{pmatrix}
x_\xi & y_\xi & z_\xi \\
x_\eta & y_\eta & z_\eta \\
x_\zeta & y_\zeta & z_\zeta
\end{pmatrix}
\tag{37}
$$

From the expansion of gradients (34) and (36) follows that

$$
\left.
\begin{aligned}
\nabla_x \phi = \boldsymbol{J}_\xi \, \nabla_\xi \phi &\implies \nabla_\xi \phi = \boldsymbol{J}_\xi^{-1} \, \nabla_x \phi \\
\nabla_\xi \phi = \boldsymbol{J}_x \, \nabla_x \phi &\implies \nabla_x \phi = \boldsymbol{J}_x^{-1} \, \nabla_\xi \phi
\end{aligned}
\right\}
\implies
\left\{
\begin{aligned}
\boldsymbol{J}_\xi^{-1} &= \boldsymbol{J}_x \\
\boldsymbol{J}_x^{-1} &= \boldsymbol{J}_\xi
\end{aligned}
\right.
\tag{38}
$$

This means, that

$$
\nabla_x \phi = \boldsymbol{J}_\xi \, \nabla_\xi \phi = \boldsymbol{J}_x^{-1} \, \nabla_\xi \phi
\tag{39}
$$

where

$$
\boldsymbol{J}_\xi = \boldsymbol{J}_x^{-1} =
\begin{pmatrix}
x_\xi & y_\xi & z_\xi \\
x_\eta & y_\eta & z_\eta \\
x_\zeta & y_\zeta & z_\zeta
\end{pmatrix}^{-1}
= \frac{1}{\det \boldsymbol{J}_x}
\begin{pmatrix}
y_\eta z_\zeta - z_\eta y_\zeta & y_\zeta z_\xi - z_\zeta y_\xi & y_\xi z_\eta - z_\xi y_\eta \\
z_\eta x_\zeta - x_\eta z_\zeta & z_\zeta x_\xi - x_\zeta z_\xi & z_\xi x_\eta - x_\xi z_\eta \\
x_\eta y_\zeta - y_\eta x_\zeta & x_\zeta y_\xi - y_\zeta x_\xi & x_\xi y_\eta - y_\xi x_\eta
\end{pmatrix}
\tag{40}
$$

This matrix can be computed directly for given transformation $\boldsymbol{x} = \boldsymbol{x}(\boldsymbol{\xi})$. It allows to evaluate the physical space gradients $\nabla_x \phi$ by only computing those in computational space, i.e. $\nabla_\xi \phi$ and transforming them using the Jacobi matrix $\boldsymbol{J}_\xi$ according to (39).

For given curvilinear grid the Jacobi matrix can be computed point wise using suitable discretization of spatial derivatives. In the numerical solver used to obtain the results presented in this paper, the same compact finite-difference discretization scheme was used to evaluate Jacobi matrices as well as to discretize the governing equations.

4 Numerical Simulations

The numerical simulations presented in this paper are motivated by atmospheric boundary layer flows in complex terrain under stable stratification. The aim of this initial study is to identify critical issues in performing high-resolution three-dimensional simulations of stratified flows. Thus the computational setup is kept simple, to be able to separate different flow features and identify their causes. The influence of time/space discretization, numerical stabilization, boundary conditions and computational grid is studied and discussed in detail.

4.1 Computational setup

The computational setup used in this study is motivated by the towing tank laboratory experiments described in [15] and numerical simulations from [7]. This is however just a starting point and the actual configuration of our numerical test cases differs substantially in several aspects from the above mentioned papers.

4.1.1 Computational domain

A three-dimensional computational domain is chosen as a bounded part of a half-space, with a rotationally symmetric hill placed on a wall. The 3D computational block has a size $L_x \times L_y \times L_z$, with the z coordinate pointing in vertical direction (against the gravity acceleration) and the x coordinate pointing in the free stream direction. The hill shape is the same as in [15], resp. [7], i.e. the surface elevation $z_s(r)$ is given by an inverse of a fourth order polynomial in terms of a distance r from the hill symmetry axis.

$$z_s(r) = \frac{h}{1 + (r/h)^4} \tag{41}$$

The parameter (length scale) h represents the maximum hill height, as well as the hill half width[7]. The domain dimensions, in terms of this parameter, are $L_x = 30h$, $L_y = 10h$, $L_z = 5h$. The hill is placed (together with the origin of the coordinate system) at the center of this domain, i.e. at the position $L_x/2 = 15h$ from the inlet, at the plane of symmetry.
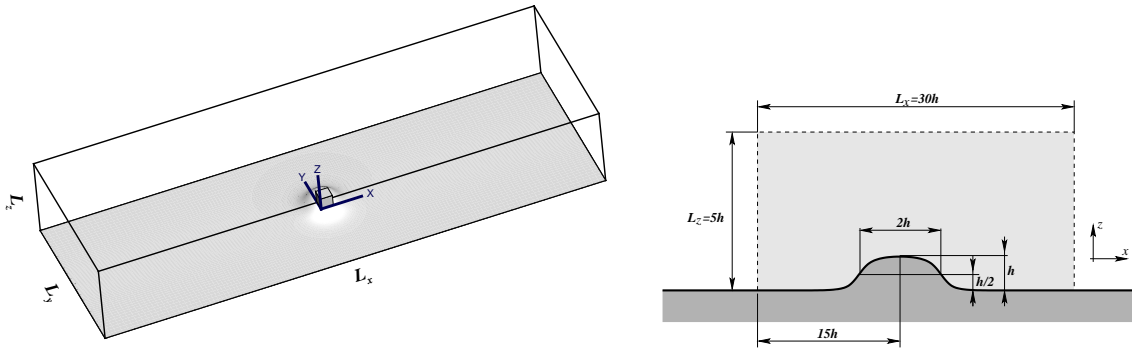

Figure 3: Computational domain configuration

4.1.2 Boundary conditions

Besides of physical relevance, the choice of boundary conditions is essential in obtaining well posed mathematical problem that will be numerically solvable. In the case considered here, it should be kept in mind that except the solid wall, all the other boundaries of the domain are artificial and so are most of

---

[7]The width of the hill at the height of $z = h/2$ is $2h$.

the boundary conditions. Our choice of the boundary conditions is motivated by physics and adjusted to the character of governing equations of the mathematical model.

- **Inlet** ... The velocity profile $\boldsymbol{v} = (u(z), 0, 0)$ is prescribed. The horizontal velocity component u is given by the Pohlhausen-Kármán profile $u(z) = U_*(2\tilde{z} - 2\tilde{z}^3 + \tilde{z}^4)$, where non-dimensional height $\tilde{z}$ is defined using the boundary layer thickness H as $\tilde{z} = z/H$. Here we have chosen the boundary layer thickness to be equal to the hill height, i.e. $H = h$ Density perturbation ρ' is set to zero, while homogeneous Neumann condition is used for pressure.

- **Outlet** ... Homogeneous Neumann condition is prescribed for all velocity components, as well as for the pressure and density perturbations.

- **Wall** ... No-slip conditions are used on the wall, i.e. the velocity vector is set to $\boldsymbol{v} = (0, 0, 0)$. Homogeneous Neumann condition is used for pressure and density perturbations.

- **Top (Free stream)** ... Homogeneous Neumann condition is used for all quantities including pressure and density perturbations. Free stream is emulated rather than a free-slip condition used in many other studies. This is essential for allowing the evolution of the boundary layer as well as the vertical extension of the gravity wave field.

- **Sides** ... Homogeneous Neumann condition is used for all quantities including pressure and density perturbations.

See the Section 4.2 for the remaining parameters.

4.1.3 Computational grid

The numerical simulations were performed on a structured, non-orthogonal wall-fitted grid shown in the figure 4. The grid is refined close to the hill and near the wall.
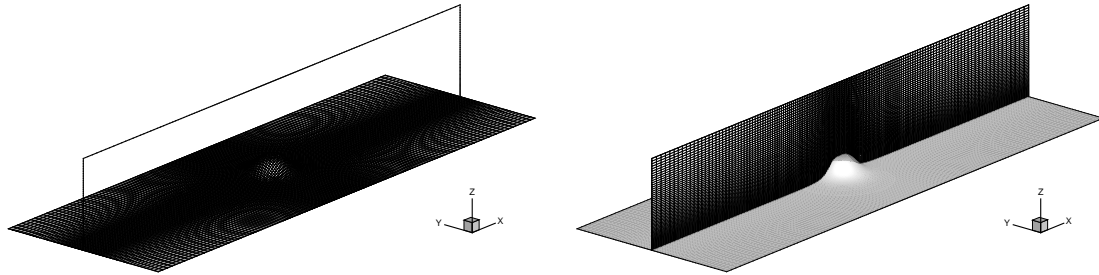

Figure 4: Computational grid structure

The grid has $156 \times 66 \times 56$ cells with the minimum cell size $\Delta x_{min} = h/10$, $\Delta y_{min} = h/10$, $\Delta z_{min} = h/20$. The cell size growth is limited to 5% in the horizontal and 2% in the vertical direction. I.e. the ratio of the sizes of two consecutive cells is 1.05 and 1.02 respectively.

4.2 Simulation parameters

In the simulations shown below, the fluid and flow parameters are chosen close to those used in [15, 7]. The fluid is characterized by density $\rho^* = 1000 kg \cdot m^{-3}$ and dynamical viscosity $\mu = 10^{-3} kg \cdot m^{-1} \cdot s^{-1}$. The linear background density profile is defined by $\rho_0(z) = \rho^* + \gamma \cdot (z - h)$. The gravity acceleration acts against the z coordinate, so $g = -10 m \cdot s^{-2}$. The hill height $h = 2cm = 0.02\,m$ was chosen as the characteristic length scale for both, the Reynolds number (where h represents the boundary layer thickness) as well as for the Froude number (where h represents the vertical displacement scale).
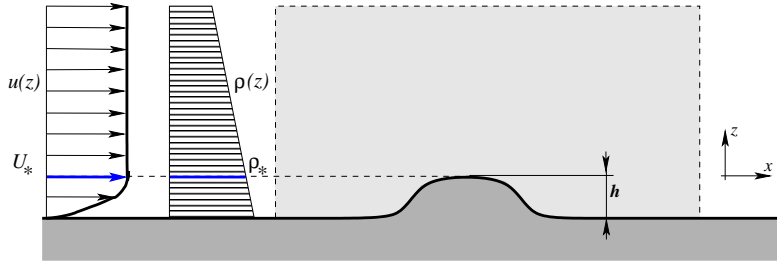
Figure 5: Characteristic values choice.

The two physical quantities that are being varied in simulations are the characteristic (free stream) velocity $U_\infty [m \cdot s^{-1}]$ and the background density gradient $\gamma = \frac{\partial \rho_0}{\partial z} [kg \cdot m^{-4}]$. The buoyancy frequency N, Reynolds number Re can be then expressed in terms of these two free parameters as

$$N = \sqrt{\frac{g}{\rho^*}\gamma} = \sqrt{\frac{-10}{10^3}\gamma} = 0.1\sqrt{|\gamma|} \tag{42}$$

$$Re = \frac{\rho^* h U_\infty}{\mu} = \frac{10^3 \cdot 0.02 \cdot U_\infty}{10^{-3}} = 2 \cdot 10^4 U_\infty \qquad . \tag{43}$$

The Froude number is then given by

$$F = \frac{U_\infty}{Nh} = \frac{U_\infty}{0.1\sqrt{|\gamma|} \cdot 0.02} = 500\frac{U_\infty}{\sqrt{|\gamma|}} = \frac{1}{400}\frac{Re}{N} \tag{44}$$

The parameters for all solved cases are summarized in the table 5.

	$\gamma = 0$ $N = 0$	$\gamma = -25$ $N = 1/2$	$\gamma = -100$ $N = 1$	$\gamma = -400$ $N = 2$	$\gamma = -1600$ $N = 4$
$U_\infty = 0.01$ $Re = 200$	∞	1	1/2	1/4	1/8
$U_\infty = 0.02$ $Re = 400$	∞	2	1	1/2	1/4
$U_\infty = 0.04$ $Re = 800$	∞	4	2	1	1/2

Table 5: Froude number as a function of simulation parameters

4.3   Numerical results

The basic set of numerical simulations consists of 15 cases, whose parameters are described in the Table 5. The computational grid, boundary conditions and other simulation settings were kept exactly the same for these simulations. In this series of simulations the aims were twofold:

1. *Physical* – Typically the Froude number is considered to be the key parameter in the investigation of the stratified flow over hills. Here we were testing the model predictions sensitivity with respect to variation of free-stream velocity U_∞ (i.e. the Reynolds number) and background density gradient γ (i.e. the Brunt–Väisälä frequency).

2. *Numerical* – The boundary of the computational domain (except the solid wall) is arbitrarily chosen and the artificial boundary conditions are imposed. Our aim was to identify, describe and understand some of the boundary issues that might affect the results.

The basic description of results is presented in this section, while some more detailed discussion is kept for the Section 5. Some additional results (with different grid, boundary conditions, etc.) are presented at the end of this section to demonstrate some specific features.

First of all let's note that in the non-stratified case at the low speed $U_\infty = 0.01 m/s$ the flow field is steady and symmetric. By increasing the speed to $U_\infty = 0.02 m/s$, the wake behind the hill becomes unsteady[8], time-periodic but still symmetric, while at even higher speed $U_\infty = 0.04 m/s$, the wake starts to become non-symmetric. If the stratification is introduced for these cases, the flow retains its steadiness and symmetry. So evidently the stable stratification contributes to the stabilization of the flow.

In the stratified flows the flow field has a very specific wavy structure. While the amplitude of the waves depends mainly on the height of the hill, the wavelength is dictated by the stratification parameter γ and the flow speed U_∞. This is clearly demonstrated in the Figure 6, showing the vertical velocity contours (isosurfaces) for all the basic considered cases. It is easy to see that increase in U_∞ leads to longer waves, while increasing the stratification parameter γ shortens the wavelength. It's important to note that e.g. reducing the velocity U_∞ to one half has a similar effect as increasing the stratification γ four times. So the wavelength depends on the ratio $U_\infty/\sqrt{\gamma}$. This similarity is hidden in the Froude number F, which is confirmed e.g. by the relation (44). Comparing in the Figure 6 the flow patterns for cases with the same Froude number clearly shows very similar shapes of the isosurfaces, for the considered range of Reynolds numbers $Re = 200 - 800$. So the Froude number is really the key parameter determining the flow pattern in strongly stratified flows.

The global character of results for the cases with same F seems to be quite similar. There are however significant differences that, at least locally distinguish, the separate influence of U_∞ and γ. The differences are clearly visible in the Figure 7 and 8, showing the streamlines in horizontal cuts of the domain.

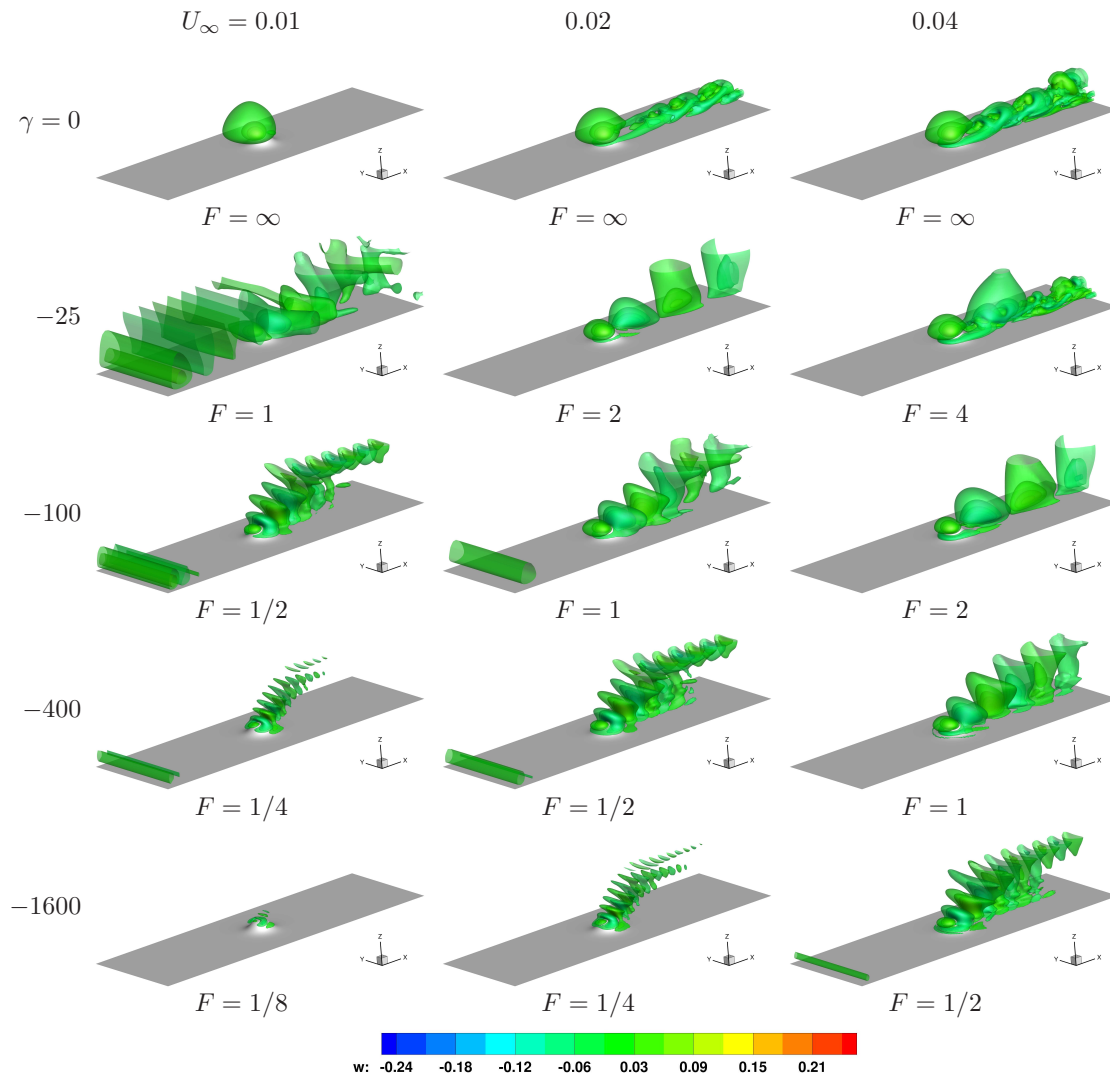[8]Only a snapshot is shown for selected time.

Figure 6: Isosurfaces of the (nondimensional) vertical velocity $\widetilde{w} = w/U_\infty$.

The recirculation zone on the lee side of the hill changes (increases) in size with both the higher flow speed U_∞ and stratification γ. The effect of γ is weaker at lower speeds, leading to similar length of the recirculation zone. For higher speeds however the length of recirculating region increases with γ. This is due to buoyancy force acting against the vertical motion. As a consequence, at the highest stratification, the recirculation zone is very flat, allowing only quasi two-dimensional horizontal recirculation in the near wall region. The fluid parcels in the boundary layer simply don't have enough kinetic energy to raise to higher levels against the buoyancy force and are thus obliged to only move horizontally.
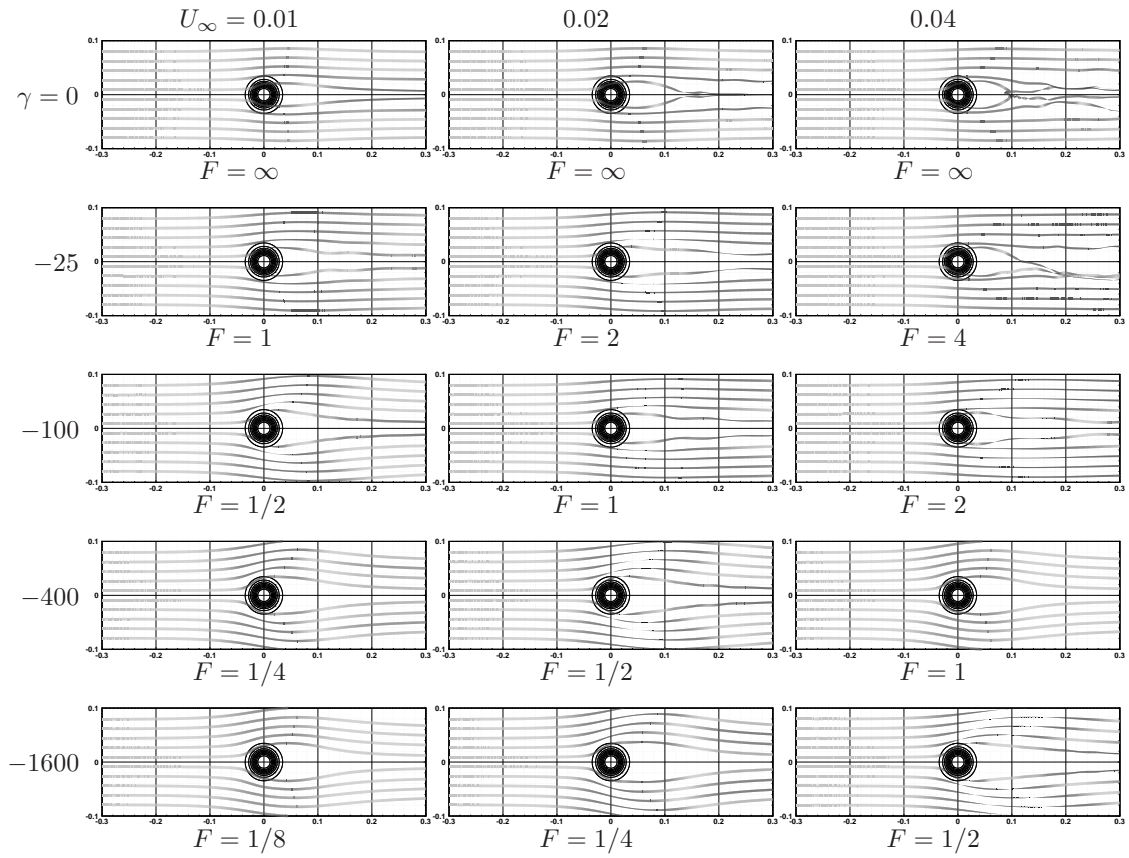
Figure 7: Streamlines released at the height $h/2$.
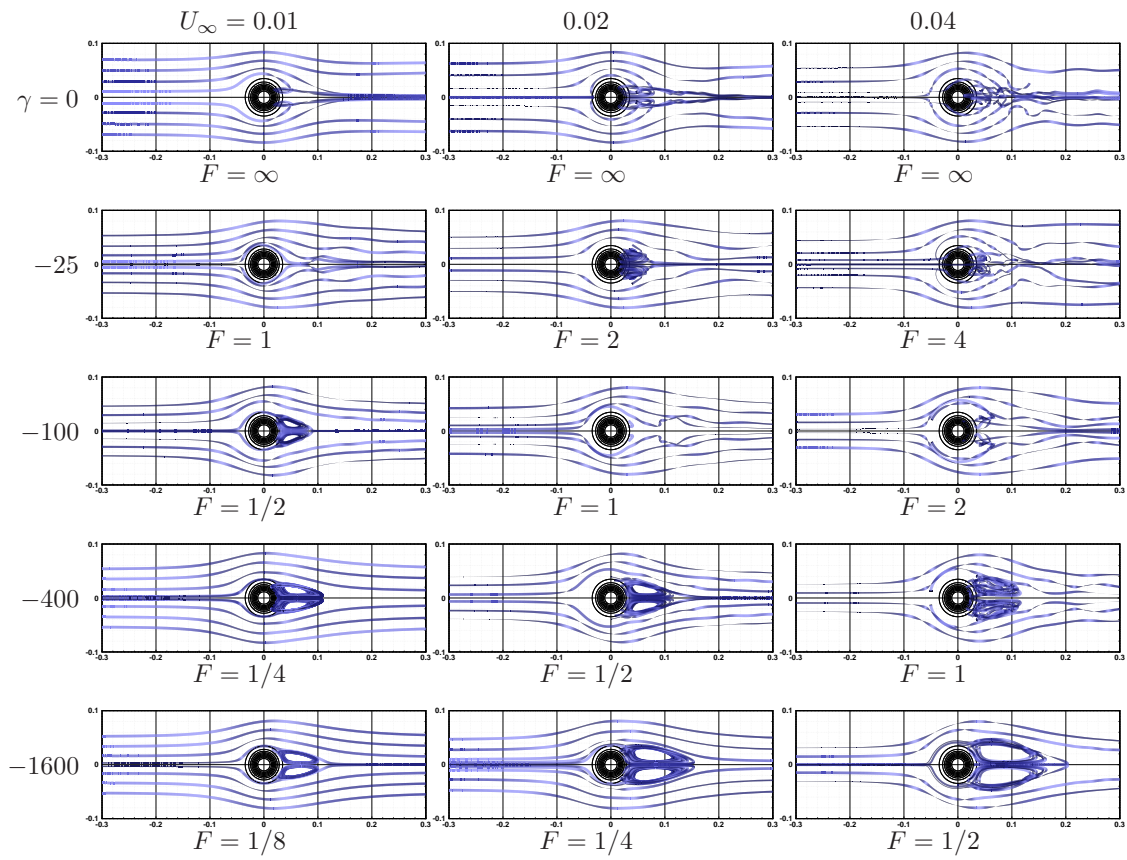
Figure 8: Streamlines released at the height $h/10$ behind the hill.
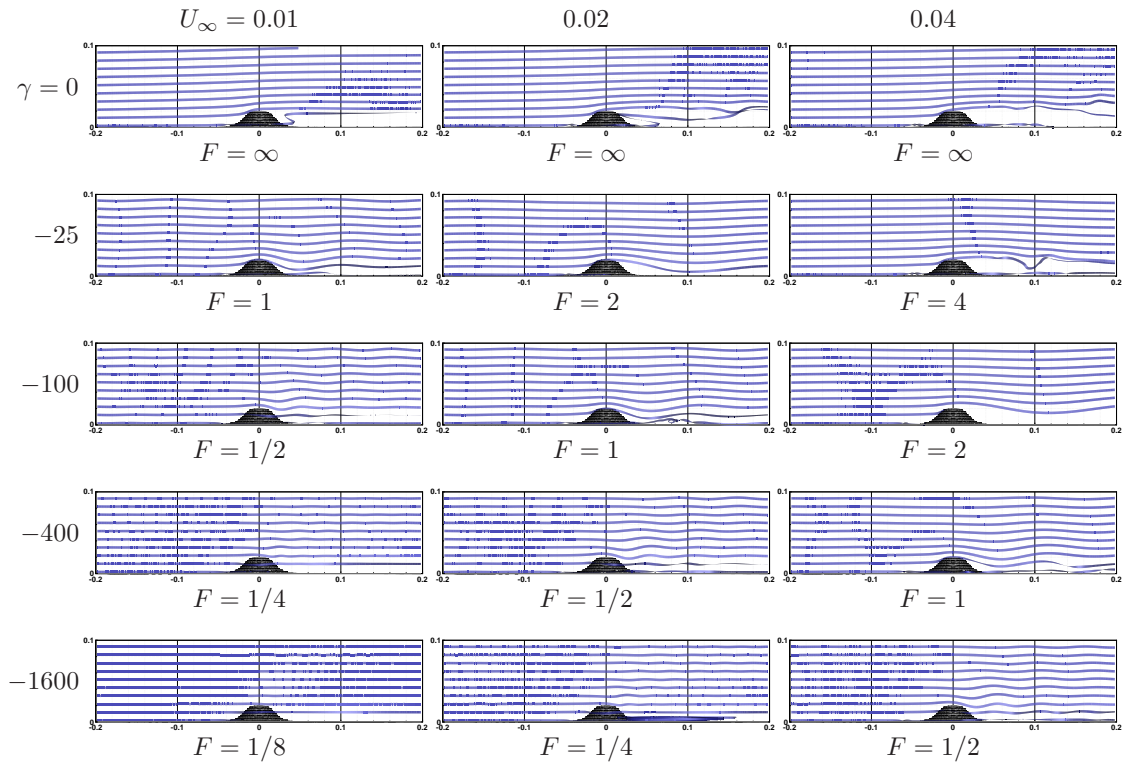
Figure 9: Streamlines released along the xz symmetry plane with the offset of $h/10$.

5　Conclusions and Remarks

5.1　Physical effects

The series of simulations clearly showed that the Froude number is the key parameter here. The cases with the same Froude lead to a qualitatively very similar results. Nevertheless, the role of the advection velocity is also extremely important.

- First, it should be understood, that although the changes in velocity consequently change the Reynolds number, we are referring here to velocity induced effects only, because the viscosity variation (to achieve the same Reynolds number) will have a completely different influence.

- The increase in the flow speed could lead to the loss of the flow stationarity, stability and symmetry. The stronger stratification can help to stabilize the flow, however the velocity effect will be still visible, potentially leading to turbulence.

- The kinetic energy of a fluid parcels depends on its velocity much stronger than the potential energy does[9]. The balance between the kinetic and potential energy is the determining factor for stratified flows.

- While reducing the flow speed, we are moving away from the class of "advection dominated flows". This has deep consequences in the physical nature of the flow. Rather than being governed by the inlet conditions (due to advection), the flow becomes more and more dominated by the hill induced perturbations (due to buoyancy source terms).

Velocity (Reynolds number) is very important in many different ways for the stratified flow over hills. As for the non-stratified case, the vortex pattern behind the hill is steady and symmetric for low speed, becoming first unsteady at higher speeds, later non-symmetric but periodic in time, and finally asymmetric in space and aperiodic in time for highest speeds. The stratification plays a stabilizing role in this game, postponing the symmetry and periodicity breakdown to higher velocities for larger (absolute) values of the stratification (parameter γ).

Another velocity effect in the stratified flows is associated with the no-slip condition on the wall, leading to very low-speed boundary layer, in which the fluid parcels have a very low kinetic energy, that can be transformed to potential energy (due to gravity and stratification) in vertical motion. Therefore the vertical motion is very restricted for fluid parcels within the boundary layer. The thickness of such "horizontal-only motion" layer becomes larger as the characteristic velocity reduces.

5.2　Numerical issues

The numerical simulations revealed certain problems. Some of them are related to the chosen numerical solver, while some are rather specific to strongly stratified flows.

5.2.1　Discretization

In general, the whole numerical solver performed very well in the simulations. The compact finite difference discretization has proved its high resolving power in situations where the low amplitude waves are essential. The compact filters seem to be a good choice, because they allow to damp the point-to-point numerical oscillations without visibly affecting the longer wavelength physical features in the flow. The sixth-order compact scheme with five point stencil and three-diagonal matrix (i.e. $a = 1/3$) was used together with the eight order filter $F8$ (with coefficient $b = 0.49$). This combination was chosen after many tests, considering its superior resolution capabilities and low level of damping of physical waves (with longer wavelengths). Also the sixth order scheme seemed to be a marginally more robust than the other schemes in this family.

---

[9]The potential energy is rather proportional to the hill height, just weakly depending on velocity and corresponding fluid parcel vertical elevation.

The choice of time-discretization seems to have only a very little impact on the numerical results. The differences were mostly due to different stability requirements and thus different maximum achievable time-steps associated with the chosen method. Although the accuracy (in time) was not of a primary interest in this steady state simulations, the more accurate methods proved to be also more robust for the studied problem. This is why the $SSP(3,3)$ method was used for our numerical simulations, despite of the fact that the lower order three-stage methods were expected to have larger available CFL number. The higher practical robustness of the higher order discretization can probably be attributed to the non-linearity of the solved problem, where some transitional (in time) effects are better captured by the higher order discretization without the need to reduce the time-step. Nevertheless, the final (steady) results are not affected by the choice of the time-discretization. In this case it only affects the efficiency (i.e. computational cost) of the solver.

5.2.2   Boundary conditions

As previously noted, most of the computational domain boundaries are artificial, and so are the boundary conditions. These conditions should be chosen "soft", in the sense that they should not significantly affect the physical behavior of the flow, especially in the regions of the primary interest. They should also respect the mathematical nature of the governing system, as well as the specific needs of numerical discretization.

First observations showed that the boundary conditions setup, that worked very well for the homogeneous and non-stratified case, leads to certain problems in stratified case. The typical example is the problem appearing in the near-wall region at the inlet boundary. As it can be seen in the Figure 6, some waves are generated in that corner (edge) of the computational domain. These spurious waves are becoming more pronounced with lower velocity and stronger stratification (parameter γ).

This kind of boundary issues is treated in different ways in the earlier studies of various authors. For example only small part of the computational domain is shown (far from boundary), simulation is stopped at finite time (before the spurious wave problem develops), artificial sponge regions are used close to far-field boundaries (to damp all waves caused by boundary conditions), free-slip condition is used instead of no-slip (to avoid inaccurate/inexact inlet boundary conditions), etc.. This kind of numerical tricks can certainly be used, but it limits the validity of the numerical results, without truly understanding and resolving the boundary issues at artificial boundaries.

The problems come from the inconsistencies between the behavior of flow field obtained from discrete solution of governing equations confronted with artificial (and approximate) boundary conditions. For example any inaccuracy (with respect to the exact solution with far-field values prescribed at infinite distance) in prescribing e.g. velocity profile, generates a vertical perturbation to the flow field. This perturbation (in the same way as e.g. hill) leads to a large spurious wave fields that may interfere with the physical flow features deep inside of the computational domain. This spurious wave phenomena is evidently connected with buoyancy and stratification.

Further investigation in this area is needed to fully fix the problem and to prescribe a meaningful, problem-free boundary conditions.

5.2.3   Domain size

In order to verify the influence of the artificial boundaries (and associated boundary conditions) on the structure of the flow-field, a series of additional simulations was performed on enlarged computational domain. The size of the domain was doubled in each direction, while the distance of the hill from the inlet was kept the same[10]. The grid spacing was kept the same as for the original domain, being smoothly coarsened towards the outer boundaries.

The results obtained for the cases with $\gamma = -400$ and $U_\infty = 0.01, 0.02, 0.04~m/s$ are shown in the Figure 10. The results are shown for the complete original domain, while the double-sized domain results are cut off to the original size. The results of simulations on the double sized domain do not exhibit any significant differences in the near-hill flow structure. There are however some visible differences

---

[10]To assure the same boundary layer thickness.

close to the artificial boundaries. This just confirms, that a special care must be taken concerning the artificial boundary conditions on these ad-hoc chosen boundaries.
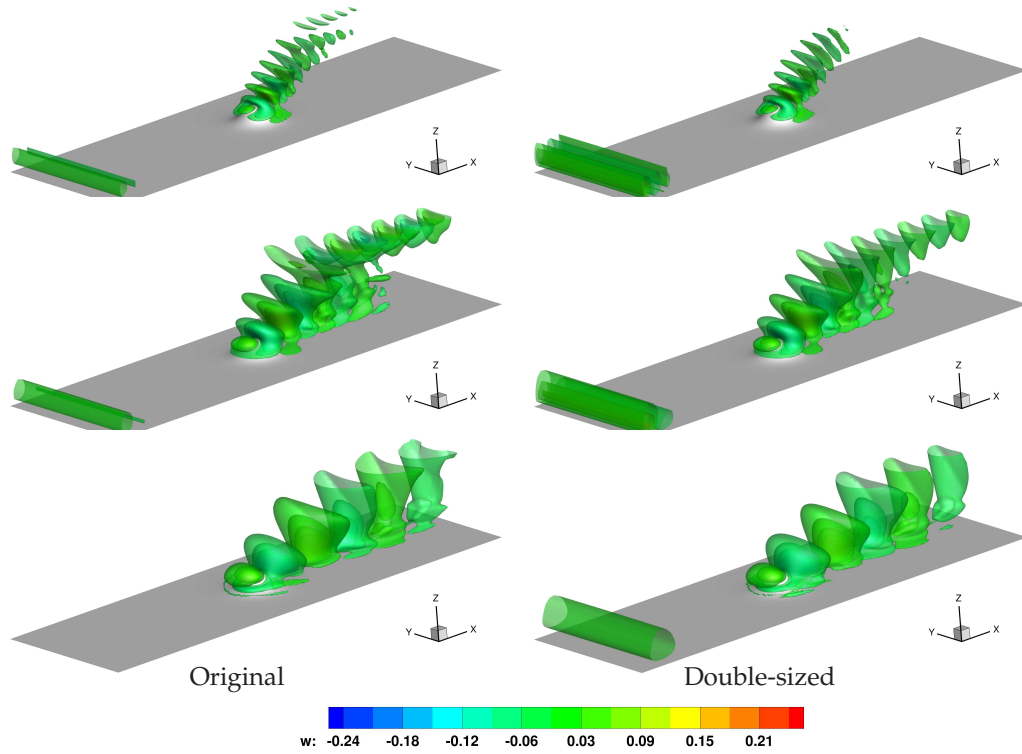

Original   Double-sized

w: -0.24 -0.18 -0.12 -0.06 0.03 0.09 0.15 0.21

Figure 10: Isosurfaces of the (nondimensional) vertical velocity $\widetilde{w} = w/U_\infty$.

It is also worth noting that the non-physical disturbance in the lower inlet corner of the boundary becomes more pronounced on the double-sized domain. This can be attributed to the longer distance of the outflow boundary, where the "non-disturbed" flow is assumed with prescribed constant pressure. As it was mentioned above, this phenomena deserves a further investigation and detailed explanation.

5.2.4 Grid resolution

The stratified flows exhibit massive wave fields that have to be resolved by numerical simulation. The results demonstrate the physically justified behavior when the wavelength of gravity waves decreases with lower flow speeds (i.e. lower Reynolds number). In fact, the Froude number is the key parameter as the characteristic wavelength is the same for the cases with equal Froude number. This behavior is expected from the physical point of view, however from the numerical simulation point of view, it's a little bit counter intuitive. This is due to the fact that for lower speed (Reynolds number) the grid resolution should be increased (i.e. grid cell size decreased) in order to resolve the shorter wavelengths in the gravity wave field.

In the numerical simulations of homogeneous (non-stratified) wall bounded flows the grid resolution is dictated by the Reynolds number dependent boundary layer thickness. This affects namely the wall-normal grid cell thickness, that should decrease as the Reynolds number increases. Typically the $\Delta z \propto Re^{-1/2}$ as a consequence of the boundary layer thickness estimate. This limitation should primarily apply in the wall-normal direction, i.e. across the boundary layer.

The second grid size limitation arises due to buoyancy induced waves and thus can be related to Froude number. The grid cell size should be proportional to the Froude number (resp. to velocity or

Reynolds number), i.e. $\Delta x \propto F^1$. This grid cell size limitation should apply along the flow, in the direction of the wave propagation.

These limitations should be respected in the regions where physical flow features (boundary layers, gravity wave fields) need to be resolved. On the other hand, the grid coarsening towards the far-field (artificial) boundaries can be used to smoothly fade out the waves and to avoid their reflections from artificial boundaries. Then however it should be kept in mind, that such flow field smoothing is non-physical and so are the results in this coarse grid regions.

5.3 Conclusions

In the summary, it's possible to say that the newly developed high resolution numerical code is able to deliver very detailed information about the three-dimensional structure of the flow field in the case of stably stratified flow over hills. The obtained results have brought a deeper insight into the effects of different physical parameters to the qualitative as well as quantitative properties of the flow over a range of Froude and Reynolds numbers.

The simulations however also brought and opened several questions that remain unanswered so far. To name at least some of them, let's mention the problems concerning a suitable mathematical model, computational setup and boundary conditions. It was found, that the simulation results are very (much more than in the homogeneous, non-stratified case) sensitive to computational setup. While the higher grid resolution requirements can be met relatively easily, the choice of artificial boundaries of the computational domain, including the prescription of meaningful and non-intrusive boundary conditions seems to require more attention in the future. This is supposed to be the aim of our future studies.

References

[1] M. H. P. Ambaum and D. P. Marshall. The effects of stratification on flow separation. *Journal of the Atmospheric Sciences*, 62(7 II):2618–2625, July 2005.

[2] M. H. Bauer, G. J. Mayr, I. Vergeiner, and H. Pichler. Strongly nonlinear flow over and around a three-dimensional mountain as a function of the horizontal aspect ratio. *Journal of the Atmospheric Sciences*, 57:3971–3991, 2000.

[3] I. P. Castro. A note on lee wave structures in stratified flow over three–dimensional obstacles. *Tellus*, 39A:72–81, 1987.

[4] I. P. Castro, W. H. Snyder, and G. L. Marsh. Stratified flow over three–dimensional ridges. *Journal of Fluid Mechanics*, 135:261–282, 1983.

[5] R. E. Davis. The two–dimensional flow of a stratified fluid over an obstacle. *Journal of Fluid Mechanics*, 36(1):127–143, 1969.

[6] L. Ding and R. L. Street. Numerical study of the wake structure behind a three-dimensional hill. *Journal of the Atmospheric Sciences*, 60(1679–1690), 2003.

[7] L. Ding, R. J. Calhoun, and R. L. Street. Numerical simulation of strongly stratified flow over a three-dimensional hill. *Boundary-Layer Meteorology*, 107(1):81–114, April 2003.

[8] C. C. Epifanio. *Encyclopedia of the Atmospheric Sciences*, chapter Lee Vortices, pages 1150–1160. Cambridge University Press, 2003.

[9] C. C. Epifanio and D. R. Durran. Lee–vortex formation in free-slip stratified flow over ridges. Part I: Comparison of weakly nonlinear inviscid theory and fully nonlinear viscous simulations. *Journal of the Atmospheric Sciences*, 59(7):1153–1165, April 2002.

[10] R. Ford. A nonhydrostatic finite–element model for three-dimensional stratified oceanic flows. part ii: Model validation. *Monthly Weather Review*, 2004.

[11] D. V. Gaitonde, J. S. Shang, and J. L. Young. Practical aspects of higher-order numerical schemes for wave propagation phenomena. *International Journal for Numerical Methods in Engineering*, 45: 1849–1869, 1999.

[12] C. Gatti-Bono and P. Colella. An anelastic allspeed projection method for gravitationally stratified flows. *Journal of Computational Physics*, 216:589–615, 2006.

[13] B. Gyüre and I. M. Jánosi. Stratified flow over asymmetric and double bell–shaped obstacles. *Dynamics of Atmospheres and Oceans*, 35:155–170, 2003.

[14] H. Hanazaki. On the three–dimensional internal waves excited by topography in the flow of a stratified fluid. *Journal of Fluid Mechanics*, 263:293–318, 1994.

[15] J. C. R. Hunt and W. H. Snyder. Experiments on stably and neutrally stratified flow over a model three-dimensional hill. *Journal of Fluid Mechanics*, 96(4):671–704, 1980.

[16] J. C. R. Hunt, G. G. Vilenski, and E. R. Johnson. Stratified separated flow around a mountain with an inversion layer below the mountain top. *Journal of Fluid Mechanics*, pages 105–119, 2006.

[17] Y. Kadri, P. Bonneton, J.M. Chomaz, and M. Perrier. Stratified flow over three–dimensional topography. *Dynamics of Atmospheres and Oceans*, 23:321–334, 1996.

[18] S. K. Lele. Compact finite difference schemes with spectral-like resolution. *Journal of Computational Physics*, 103:16–42, 1992.

[19] L. S. Leo, M. Y. Thompson, S. Di Sabatino, and H. J. S. Fernando. Stratified flow past a hill: Dividing streamline concept revisited. *Boundary-Layer Meteorology*, pages 1–24, 2015.

[20] Y.-L. Ling and T.-A. Wang. Flow regimes and transient dynamics of two–dimensional stratified flow over an isolated mountain ridge. *Journal of Atmospheric Sciences*, 53(1):139–158, 1996.

[21] W. R. Peltier and T. L. Clark. Nonlinear mountain waves in two and three spatial dimensions. *Quarterly Journal of the Royal Meteorological Society*, 109:527–548, 1983.

[22] A. N. Ross and S. B. Vosper. Numerical simulations of stably stratified flow through a mountain pass. *Quarterly Journal of the Royal Meteorological Society*, 129:97–115, 2003.

[23] A. N. Ross, S. Arnold, S. B. Vosper, S. D. Mobbs, N. Dixon, and A. G. Robins. A comparison of wind–tunnel experiments and numerical simulations of neutral and stratified flow over a hill. *Boundary Layer Meteorology*, 113:427–459, 2004.

[24] R. Rotunno, V. Grubišić, and P. K. Smolarkiewicz. Vorticity and potential vorticity in mountain wakes. *Journal of the Atmospheric Sciences*, 56:2796–2810, 1999.

[25] J. Sachsperger, S. Serafina, and Vanda Grubišić. Dynamics of rotor formation in uniformly stratified two–dimensional flow over a mountain. *Quarterly Journal of the Royal Meteorological Society*, 142: 1201–1212, April 2016.

[26] C. W. Shu and S. Osher. Efficient implementation of essentially non-oscillatory shock-capturing schemes. *Journal of Computational Physics*, 77:439–471, 1988.

[27] R. B. Smith. The influence of mountains on the atmosphere. *Advances in Geophysics*, 21:87–230, 1979.

[28] R. B. Smith. Linear theory of stratified hydrostatic flow past an isolated mountain. *Tellus*, 32:348–364, 1980.

[29] R. B. Smith. Linear theory of stratified flow past an isolated mountain in isosteric coordinates. *Journal of the Atmospheric Sciences*, 45(24):3889–3896, 1988.

[30] R. B. Smith. Mountain–induced stagnation points in hydrostatic flow. *Tellus*, 41A:270–274, 1989.

[31] R. B. Smith. Hydrostatic airflow over mountains. *Advances in Geophysics*, 31:1–41, 1989.

[32] P. K. Smolarkiewicz and R. Rotunno. Low froude number flow past three-dimensional obstacles. Part I.: Baroclinically generated lee vortices. *Journal of the Atmospheric Sciences*, 46(8):1154–1164, 1988.

[33] R. J. Spiteri and S. J. Ruuth. A new class of optimal high-order strong-stability-preserving time discretization methods. *SIAM Journal on Numerical Analysis*, 40(2):469–491, 2002.

[34] B. R. Sutherland and D. A. Aguilar. Stratified flow over topography: wave generation and boundary layer separation. In *Advances in Fluid Mechanics VI*, volume 52 of *WIT Transactions on Engineering Sciences*, pages 317–326. WIT Press.

[35] M. Suzuki and K. Kuwahara. Stratified flow past a bell–shaped hill. *Fluid Dynamics Research*, 9: 1–18, 1992.

[36] J. Szmelter, Z. Zhang, and P. K. Smolarkiewicz. An unstructured–mesh atmospheric model for nonhydrostatic dynamics: Towards optimal mesh resolution. *Journal of Computational Physics*, 294: 363–381, 2015.

[37] T. Takahashi, S. Kato, S. Murakami, R. Ooka, M. F. Yassin, and R. Kono. Wind tunnel tests of effects of atmospheric stability on turbulent flow over a three–dimensional hill. *Journal of Wind Engineering and Industrial Aerodynamics*, 93:155–169, 2005.

[38] R. S. Thompson, M. S. Shipman, and J. W. Rottman. Moderately stable flow over a three–dimensional hill. A comparison of linear theory with laboratory measurements. *Tellus*, 43A:49–63, 1991.

[39] C. R. Torres and J. E. Castillo. Stratified rotating flow over complex terrain. *Applied Numerical Mathematics 47 (2003) 531541*, 47:531–541, 2003.

[40] T. Uchida and Y. Ohya. A numerical study of stably stratified flows over a two–dimensional hill – Part I. Free–slip condition on the ground. *Journal of Wind Engineering and Industrial Aerodynamics*, 67 & 68:493–506, 1997.

[41] T. Uchida and Y. Ohya. Three–dimensional numerical simulation of stably stratified flows over a two–dimensional hill: Effect of stratification on the non-periodic separation and reattachment of the flow. Reports of Research Institute for Applied Mechanics 139, Kyushu University, September 2010.

[42] M. R. Visbal and D. V. Gaitonde. On the use of higher-order finite-difference schemes on curvilinear and deforming meshes. *Journal of Computational Physics*, 181:155–185, 2002.

[43] S. B. Vosper, I. P. Castro, W. H. Snyder, and S. D. Mobbs. Experimental studies of strongly stratified flow past three–dimensional orography. *Journal of Fluid Mechanics*, 390:223–249, 1999.

[44] F. Wan and F. Porté-Agel. Large–eddy simulation of stably–stratified flow over a steep hill. *Boundary–Layer Meteorology*, 138:367–384, 2011.

[45] W. Weng. Stably stratified boundary-layer flow over low hills: A comparison of model results and field data. *Boundary–Layer Meteorology*, 85:223–241, 1997.

[46] G. L. Wooldridge, D. G. Fox, and R. W. Furman. Airflow patterns over and around a large three–dimensional hill. *Meteorology and Atmospheric Physics*, 37:259–270, 1987.

Chapter B

Biomedical Applications

Contents

The biomedical applications are represented here by the flow of blood. Due to the complicated microstructure of blood, its rheological properties can no longer be captured by the constitutive relation of Newtonian fluid (N.4). The main problem is that due to the complex rheological behavior of blood, there is no single generally accepted model that can be used for all hemodynamic simulations. The following sections are showing some of the models that have been used for blood flow simulations presented in the full length papers listed further in this chapter.

Rheological Constitutive Laws for Blood

From the point of view of fluid mechanics, blood is a very complex liquid. The major part is formed by plasma. Blood plasma alone can be considered as a Newtonian liquid. It however transports the other blood constituents as red blood cells, white blood cells, platelets and various proteins and chemicals. The complete list of blood constituents can be very long (see e.g. [B.7], [B.4]). The particulate matter dispersed in plasma is responsible for the non-Newtonian behavior of blood.

Generalized Newtonian models

This is the simplest class of non-Newtonian models as it differs from the Newtonian fluid model just by variable viscosity. It means that the (viscous, or deviatoric) stress tensor is still proportional to strain rate tensor $\mathbf{D}$ and can be expressed as $\mathbf{T} = 2\mu(\cdot)\mathbf{D}$. The apparent viscosity $\mu(\cdot)$ can be a function of flow variables[1]. The corresponding governing system (N.27),(N.30) is

---

[1] e.g. temperature, shear rate, pressure, concentration of chemicals, etc.

then called *generalized Navier-Stokes equations*.

The generalized Newtonian models can account for the most distinct rheological property of blood, which is its *shear-thinning* character. The red blood cells are one of the most important components of blood. These small, disc-like elastic cells are mainly responsible for oxygen transport. At rest, or at low shear rates, the red blood cells can aggregate and form a larger structures called *rouleaux*. These larger structures are responsible for the increase of the apparent viscosity of blood. Under higher shear rates however, these aggregates start to break into individual cells. This mechanism (together with some others) leads to decrease of the viscosity of blood with growing shear rate. Liquids exhibiting a decrease of viscosity in response to the shear rate growth, are called *shear-thinning*.
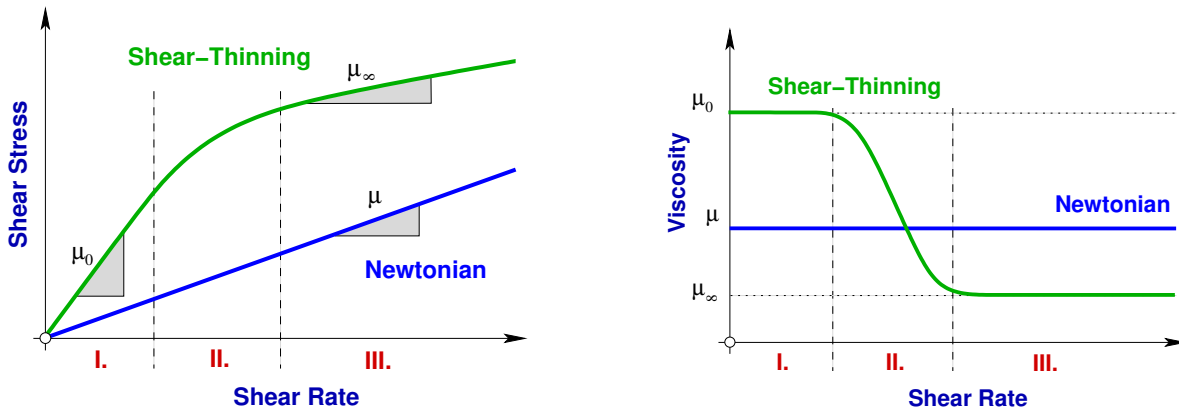
Figure B.1: Generalized Newtonian shear-thinning fluid and Newtonian fluid behavior.

In order to account for the shear-thinning behavior of blood, the constant viscosity coefficient μ is replaced by a shear rate dependent viscosity function $\mu(\dot{\gamma})$ where *shear rate* is defined by $\dot{\gamma} = 2\sqrt{\mathbf{D} : \mathbf{D}}$. This function can be written in the following general form

$$\mu(\dot{\gamma}) = \mu_\infty + (\mu_0 - \mu_\infty)F(\dot{\gamma}) \qquad . \tag{B.1}$$

Here μ_0 and μ_∞ are the asymptotic viscosity values at zero and infinite shear rates. The appropriate transition between these values is assured by the shear rate dependent function $F(\dot{\gamma})$, which satisfies the limit conditions:

$$\lim_{\dot{\gamma}\to 0^+} F(\dot{\gamma}) = 1 \qquad \text{and} \qquad \lim_{\dot{\gamma}\to\infty} F(\dot{\gamma}) = 0.$$

The class of generalized Newtonian models is from the mathematical modeling point of view very similar to turbulent models using Boussinesq assumption on turbulent viscosity. In this context, the above described simple non-Newtonian model looks like an algebraic turbulence model.

> *This shear-thinning model has been used in all the papers shown in the Sections B.1–B.4 as well as in many other publications (e.g. [B.9]), solving the blood flow problems. These are listed in the author's full bibliography in the Appendix A, page 205.*

Viscoelastic models

Blood cells are essentially elastic membranes filled by a fluid. Thus it seems reasonable, at least under certain flow conditions, to expect that blood behaves like a viscoelastic fluid. At low shear rates, erythrocytes aggregate and store elastic energy that accounts for the memory effects in blood. Thurston [B.12] was among the earliest to recognize the viscoelastic nature of blood. He also found out that the viscoelastic behavior is less prominent with increasing shear rate.

There exist many models describing viscoelastic fluids. The *Oldroyd-B model* can be considered as one of the elementary models within this class. The stress tensor in the momentum equations (N.30) is in this case governed by the following constitutive law:

$$\mathbf{T} + \lambda_1 \frac{\delta \mathbf{T}}{\delta t} = 2\mu \left(\mathbf{D} + \lambda_2 \frac{\delta \mathbf{D}}{\delta t} \right), \tag{B.2}$$

where λ_1 and λ_2 have dimension of time and represent the relaxation, resp. retardation time scales. Symbol $\delta \cdot / \delta t$ denotes in this case the upper convected time-derivative. This is a kind of a prototype model that is often used as a reference model in simulations of polymeric liquids. It can be shown, that this model can further be decomposed into more elementary constitutive laws for *Newtonian* and *Maxwell* fluids. This decomposition can be expressed using the following simple mechanical analog for the Oldroyd type model[2]:
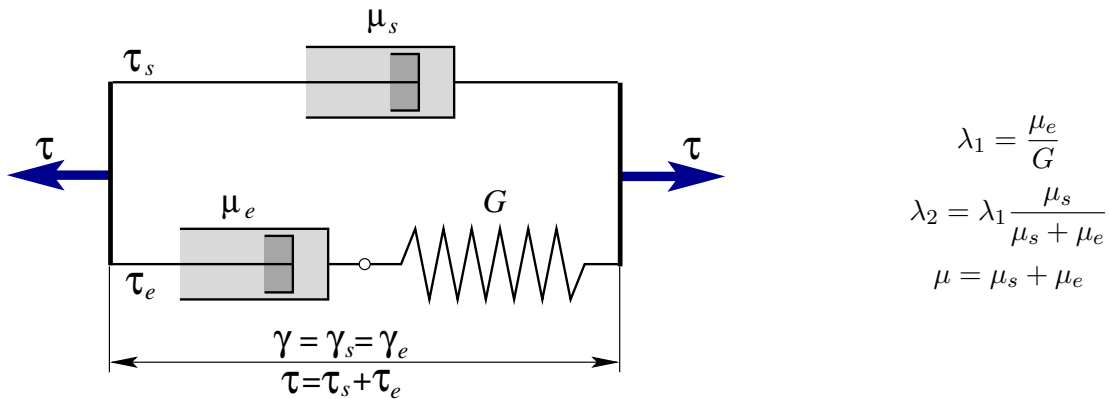

Figure B.2: Mechanical analog of an Oldroyd-type model

The extra stress tensor $\mathbf{T}$ in equation (B.2) can be decomposed into its Newtonian (solvent) part $\mathbf{T}_s$ and its elastic part $\mathbf{T}_e$. It means that the whole Oldroyd-B model (including the momentum equations) can be written in the following form:

$$\frac{\partial \boldsymbol{v}}{\partial t} + (\boldsymbol{v} \cdot \boldsymbol{\nabla})\boldsymbol{v} = -\frac{\boldsymbol{\nabla} p}{\rho} + \frac{1}{\rho} \operatorname{div}\left[\mathbf{T}_s + \mathbf{T}_e \right] \tag{B.3}$$

$$\mathbf{T}_s = 2\mu_s \mathbf{D} \tag{B.4}$$

$$\frac{\partial \mathbf{T}_e}{\partial t} + (\boldsymbol{v} \cdot \boldsymbol{\nabla}) \mathbf{T}_e = \frac{2\mu_e}{\lambda_1} \mathbf{D} - \frac{1}{\lambda_1} \mathbf{T}_e + (\mathbf{W}\mathbf{T}_e - \mathbf{T}_e\mathbf{W}) + (\mathbf{D}\mathbf{T}_e + \mathbf{T}_e\mathbf{W}) \tag{B.5}$$

---

[2]See the author's paper [B.8] for details and references

In the above equation (B.5) the **D** resp. **W** stands for the symmetric, resp. skew-symmetric part of the velocity gradient. It is good to note, that this governing system only differs from the standard incompressible Navier-Stokes equations by the additional term $\text{div}\mathbf{T}_e$. The evolution of the viscoelastic extra stress tensor $\mathbf{T}_e$ is governed by the tensorial equation (B.5). It means that in 3D case 6 additional equations[3] have to be solved together with the original governing system (of 4 equations).

This model captures some of the viscoelastic effects, however for the purpose of blood flow simulations it has to be extended by adding the shear-thinning effects into it. The easiest way how to do that is to assume that the viscosity μ_s is shear dependent. This means that the $\mathbf{T}_s = \mu_s(\dot{\gamma})\mathbf{D}$, where the viscosity function $\mu_s(\dot{\gamma})$ is obtained from suitable experimental data. Such variable-viscosity model is then referred to as the *generalized Oldroyd-B model*[4].

The empirical three constant generalized Oldroyd-B model studied in [B.13] belongs to this class. It has been obtained by fitting experimental data in one dimensional flows and generalizing such curve fits to three dimensions. This model captures the shear-thinning behavior of blood over a large range of shear rates but it has its limitations, given that the relaxation times do not depend on the shear rate, which does not agree with experimental observations. The model developed by Anand and Rajagopal [B.1] in the general thermodynamic framework stated in [B.10] includes relaxation times depending on the shear rate and gives good agreement with experimental data in steady Poiseuille and oscillatory flow.

This model follows quite different terminology and notation than the standard viscoelastic models, it can however be transformed into a form that can directly be compared with the above described Oldroyd-B model (see the full paper in Section B.3). The elastic stress is expressed using the tensor $\mathbf{B}_{\kappa_p(t)}$, which is the left Cauchy-Green elastic stretch tensor with respect to reference natural configuration $\kappa_p(t)$. This tensor is governed by the following constitutive law:

$$\frac{\partial \mathbf{B}_{\kappa_p(t)}}{\partial t} + (\boldsymbol{v} \cdot \boldsymbol{\nabla}) \, \mathbf{B}_{\kappa_p(t)} = \frac{\omega}{\lambda}\mathbf{I} - \frac{1}{\lambda}\mathbf{B}_{\kappa_p(t)} + \left[\mathbf{L}\mathbf{B}_{\kappa_p(t)} + \mathbf{B}_{\kappa_p(t)}\mathbf{L}^T\right] \tag{B.6}$$

with $\mathbf{D} = (\mathbf{L} + \mathbf{L}^T)/2$ denoting the symmetric part of the velocity gradient tensor $\mathbf{L} = \boldsymbol{\nabla v}$. It should be noted that the coefficients ω and λ are scalar functions of the tensor $\mathbf{B}_{\kappa_p(t)}$, respectively it's invariants. The classical (constant coefficients) Oldroyd-B (resp. Upper-convected Maxwell) model takes the same form:

$$\frac{\partial \mathbf{T}_e}{\partial t} + (\boldsymbol{v} \cdot \boldsymbol{\nabla}) \, \mathbf{T}_e = \frac{2\mu_e}{\lambda}\mathbf{D} - \frac{1}{\lambda}\mathbf{T}_e + \left[\mathbf{L}\mathbf{T}_e + \mathbf{T}_e\mathbf{L}^T\right] \tag{B.7}$$

These models are formally similar, however the coefficients (or rather parameter functions $\lambda = \lambda(\mathbf{B}_{\kappa_p(t)})$ and $\omega = \omega(\mathbf{B}_{\kappa_p(t)})$) in (B.6) are stress-dependent and thus can be chosen to capture the specific shear-thinning behavior of blood. This model was for the first time used in the author's paper [B.6] (shown in the Section B.3), where it is compared with the classical models for blood flow in simple geometry.

These viscoelastic models have been used in the papers shown in the Sections B.2 resp. B.3 as well as in many other publications, solving some of the blood flows problems. These papers are listed in the author's full bibliography in the Appendix A, page 205.

---

[3]Only 6 components, because of the symmetry of the tensor $\mathbf{T}_e$.
[4]For more detailed discussion of the behavior of this model see e.g. the paper [B.9].

Blood Coagulation Model

Blood coagulation is a very complex process that can not be simply (shortly) described here. It will only serve as another example of incompressible flow with variable material properties. In this specific case, the viscosity of fluid (blood) will locally depend not only on the shear-rate $\dot{\gamma}$, but also on the concentration of certain chemical.

For the purpose of this introduction, the whole blood coagulation process can be seen as a cascade of biochemical reactions that leads to the production of *fibrin*. This is a polymer that is present in blood clots (thrombi) at large concentration. It can be thus used as an indicator of the presence of blood clots. The clot itself behaves like a very viscous (maybe viscoelastic) liquid. Therefore one possible approach to clot-flow interaction modeling is to assume that the blood viscosity is just variable, depending on the concentration of fibrin, and the whole blood-clot two phase problem can be treated as a single liquid flow.

The model includes not only rheological factors but also biochemical indicators that are essential to describe the coagulation and fibrinolysis (fibrin dissolution) dynamics and consequently the formation, growth and dissolution of clots. It is based on the model introduced in [B.3] and further developed and refined in [B.2]. A set of 23 coupled advection-diffusion-reaction equations describing the evolution in time and space of various chemicals involved in the extrinsic pathway of the blood coagulation process , takes the following form:

$$\frac{\partial \mathsf{C}_i}{\partial t} + \mathrm{div}\,(\mathsf{C}_i\,\boldsymbol{v}) = \mathrm{div}\,(\mathsf{D}_i \nabla \mathsf{C}_i) + \mathsf{R}_i \qquad i = 1, \ldots, 23 \tag{B.8}$$

In these equations C_i stands for the concentration of $i-$th reactant, D_i denotes the corresponding diffusion coefficient (which could be a function of the shear rate). R_i are the nonlinear reaction terms that represent the production or depletion of C_i due to the enzymatic cascade of reactions. Equations (B.8) are complemented with appropriate initial and flux boundary conditions, involving the concentration of various species at an injured site of the vascular wall.

This model was for the first time implemented in the paper shown in the Section B.1. It has been coupled with generalized Navier-Stokes equations where viscosity was a function of local shear-rate and fibrin concentration. The model suggest a linear growth of viscosity (resp. the factor $\tilde{\mu}(C)$) with concentration up to certain saturation level.
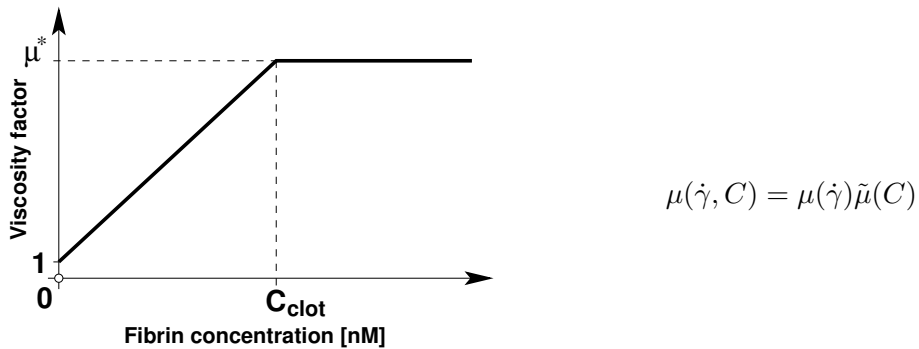

$$\mu(\dot{\gamma}, C) = \mu(\dot{\gamma})\tilde{\mu}(C)$$

Figure B.3: Clot viscosity behavior

References - B

[B.1] ANAND, M., AND RAJAGOPAL, K. A shear-thinning viscoelastic fluid model for describing the flow of blood. *Intern. Journal of Cardiovasc. Medicine and Sci. 4*, 2 (2004), 59–68.

[B.2] ANAND, M., RAJAGOPAL, K., AND RAJAGOPAL, K. A model for the formation, growth and lysis of clots in quiescent plasma. A comparison between the effects of antithrombin III deficiency and protein C deficiency. *Journal of Theoretical Biology 253* (2008), 725–738.

[B.3] ANAND, M., RAJAGOPAL, K., AND RAJAGOPAL, K. R. A model incorporating some of the mechanical and biochemical factors underlying clot formation and dissolution in flowing blood. *Journal of Theoretical Medicine 5*, 3–4 (September–December 2003), 183–218.

[B.4] BODNÁR, T., FASANO, A., AND SEQUEIRA, A. *Fluid-Structure Interaction and Biomedical Applications*. Birkhäuser Basel, 2014, ch. Mathematical Models for Blood Coagulation.

[B.5] BODNÁR, T., GALDI, G., AND Š. NEČASOVÁ, Eds. *Fluid-Structure Interaction and Biomedical Applications*, vol. XII. of *Advances in Mathematical Fluid Mechanics*. Birkhäuser Basel, 2014.

[B.6] BODNÁR, T., RAJAGOPAL, K., AND SEQUEIRA, A. Simulation of the three-dimensional flow of blood using a shear-thinning viscoelastic fluid model. *Mathematical Modelling of Natural Phenomena 6*, 5 (2011), 1–24.

[B.7] BODNÁR, T., AND SEQUEIRA, A. Numerical simulation of the coagulation dynamics of blood. *Computational and Mathematical Methods in Medicine 9*, 2 (2008), 83–104.

[B.8] BODNÁR, T., AND SEQUEIRA, A. Numerical study of the significance of the non-newtonian nature of blood in steady flow through a stenosed vessel. In *Advances in Mathematical Fluid Mechanics*, R. Rannacher and A. Sequeira, Eds. Springer - Verlag, 2009. in press.

[B.9] BODNÁR, T., AND SEQUEIRA, A. Numerical study of the significance of the non-Newtonian nature of blood in steady flow through a stenosed vessel. In *Advances in Mathematical Fluid Mechanics*, R. Rannacher and A. Sequeira, Eds. Springer Verlag, 2010, pp. 83–104.

[B.10] RAJAGOPAL, K., AND SRINIVASA, A. A thermodynamic frame work for rate type fluid models. *Journal of Non-Newtonian Fluid Mechanics 80* (2000), 207–227.

[B.11] SEQUEIRA, A., SANTOS, R. F., AND BODNÁR, T. Blood coagulation dynamics: Mathematical modeling and stability results. *Mathematical Biosciences and Engineering 8*, 2 (2011), 425–443.

[B.12] THURSTON, G. B. Viscoelasticity of human blood. *Biophysical Journal 12* (1972), 1205–1217.

[B.13] YELESWARAPU, K., KAMENEVA, M., RAJAGOPAL, K., AND ANTAKI, J. The flow of blood in tubes: theory and experiments. *Mechanics Research Communications 25*, 3 (1998), 257–262.

B.1 Numerical Simulation of the Coagulation Dynamics of Blood

BODNÁR T., SEQUEIRA A.

In this paper the complex coagulation model developed by prof. Rajagopal in [B.3] and [B.2] was for the fist time used for 3D simulations. It was coupled with flow equations based on generalized Navier-Stokes equations. Several difficulties had to be overcome in order to successfully implement this completely new model. This experience also led prof. Rajagopal to the release of a new, improved version of the biochemistry model. Due to high computational cost of this model the advection-diffusion optimized Runge-Kutta method was implemented, which saved a large part of the computational time. Also because of the very small diffusion coefficients in the advection-diffusion-reaction equations, the non-linear TVD filtering was adopted instead of the classical artificial viscosity, to minimize non-physical diffusive effects.

T. Bodnár has implemented the blood flow and coagulation model and performed all the simulations presented in this paper.

Numerical simulation of the coagulation dynamics of blood

T. Bodnár[a] and A. Sequeira[b]*

aDepartment of Technical Mathematics, Faculty of Mechanical Engineering, Czech Technical University, Karlovo Náměstí 13, 121 35 Prague 2, Czech Republic; bDepartment of Mathematics – CEMAT, Instituto Superior Técnico, Av. Rovisco Pais, 1049-001 Lisbon, Portugal

The process of platelet activation and blood coagulation is quite complex and not yet completely understood. Recently, a phenomenological meaningful model of blood coagulation and clot formation in flowing blood that extends existing models to integrate biochemical, physiological and rheological factors, has been developed. The aim of this paper is to present results from a computational study of a simplified version of this coupled fluid-biochemistry model. A generalized Newtonian model with shear-thinning viscosity has been adopted to describe the flow of blood. To simulate the biochemical changes and transport of various enzymes, proteins and platelets involved in the coagulation process, a set of coupled advection–diffusion–reaction equations is used. Three-dimensional numerical simulations are carried out for the whole model in a straight vessel with circular cross-section, using a finite volume semi-discretization in space, on structured grids, and a multistage scheme for time integration. Clot formation and growth are investigated in the vicinity of an injured region of the vessel wall. These are preliminary results aimed at showing the validation of the model and of the numerical code.

Keywords: blood coagulation; clot; fibrin; finite-volume; Runge–Kutta

AMS Subject Classification: 35M20; 65L06; 76M12; 92C35; 76Z05; 92C40; 92C50

1. Introduction

Haemostasis is a complex physiological process involving an interaction between blood vessels, platelets, coagulation factors, coagulation inhibitors and fibrinolytic proteins. When blood coagulates in a blood vessel during life, the process is called thrombosis. Haemostasis keeps blood flowing while allowing solid clot formation, or thrombosis, to prevent blood loss from sites of vascular damage. The haemostatic system preserves intravascular integrity by achieving a balance between haemorrhage and thrombosis.

Blood platelets participate in both haemostasis and thrombosis. The first stage of thrombogenesis is platelets activation, followed by platelets aggregation, adhesion and blood coagulation, with the formation of clots. Blood platelets can be activated by prolonged exposure to high or rapid increase in shear stress that lead to erythrocytes and platelets damage [10,15]. This is due to mechanical vascular injuries or endothelial disturbance, alterations in the blood composition, fissuring of atherosclerotic plaques as well as to the contact of blood with the surfaces of medical devices. Numerous experimental studies recognize that clot formation rarely occurs in regions of parallel flow,

---

but primarily in regions of stagnation point flows, within blood vessel bifurcations, branching and curvatures.

Following endothelial disruption, there is an immediate reaction that promotes vasoconstriction, minimizing vessel diameter and diminishing blood loss. Vasoconstriction slows blood flow, enhancing platelet adhesion and activation. During activation, platelets undergo intrinsic and extrinsic mechanisms leading to a series of chemical and morphological changes. Organelles contained in the platelet cytoplasm bind to collagen (exposed by arterial damage), release their contents of cytoplasmic granules containing serotonin, adenosine diphosphate (ADP) and platelet-activating factors and platelets become spheroids in shape. Additional platelets attracted by ADP are activated, interact with plasma proteins like fibrinogen and fibrin and promote platelet aggregation and adhesion to sub-endothelial tissue. This results in the formation of haemostatic plugs and concludes the primary step in haemostasis. However, when the concentration of activators exceeds a threshold value, platelet aggregates that are formed by this process can break up, damaging the platelets and causing aggregation at locations other than at the site of damage.

The final haemostatic mechanism or secondary haemostasis is coagulation (clot formation) which involves a very complex cascade of enzymatic reactions (Figure 1). Thrombin is the bottom enzyme of the coagulation cascade. Prothrombin activator converts prothrombin to thrombin. Thrombin activates platelets that release ADP which
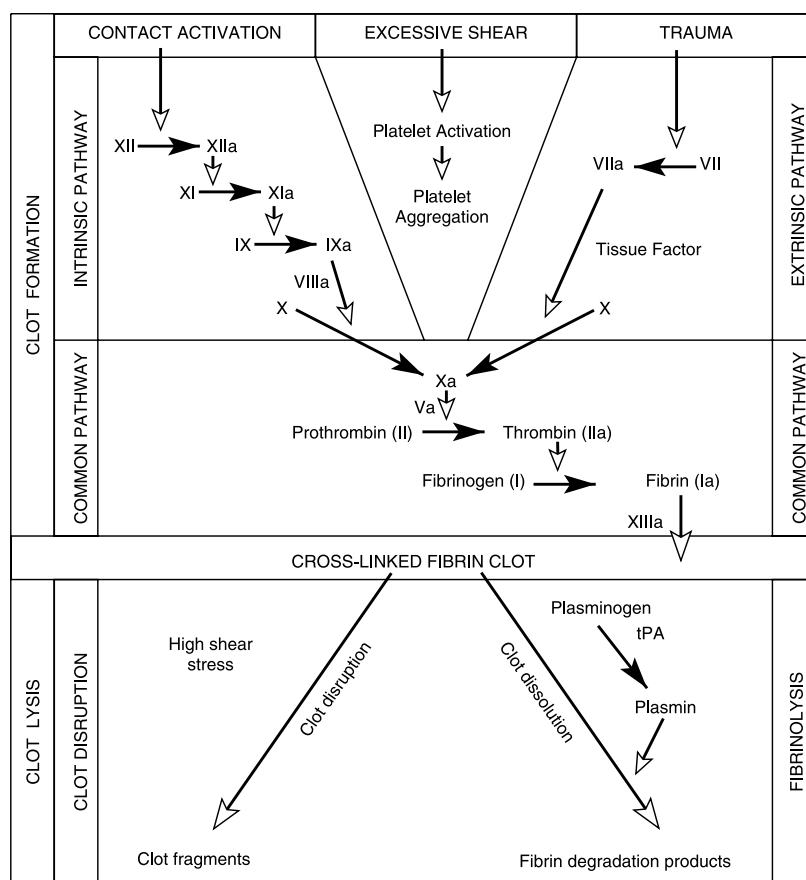

Figure 1. Schematic of the cascade of events during clot formation and lysis.

lead in turn to the activation of other platelets. The primary role of thrombin is to convert fibrinogen, a blood protein, into polymerized fibrin, stabilizing the adhered platelets and forming a viscoelastic blood clot (or thrombus) (e.g. [21,24]).

The clot attracts and stimulates the growth of fibroplasts and smooth muscle cells within the vessel wall, and begins the repair process which ultimately results in fibrinolysis and in the dissolution of the clot (clot lysis). Clot dissolution can also occur due to mechanical factors such as high shear stress. In practice, a blood clot can be continuously formed and dissolved. Generally, many factors affect its structure, including the concentration of fibrinogen, thrombin, albumin, platelets and red bloodcells, and other not specified factors which determine cross-linked structure of the fibrin network. At the end of the haemostatic process, normal blood flow conditions are restored. However, some abnormal haemodynamic and biochemical conditions of flowing blood, related to inadequate levels or dysfunction of the haemostatic system, can lead to pathologies like thromboembolic or bleeding disorders which are of great clinical importance. The mechanism of platelet activation and blood coagulation is quite complex. Recent reviews detailing the structure of the blood coagulation system are available for example in Refs. [3,24].

Whole blood is a concentrated suspension of formed cellular elements that includes red blood cells (RBCs) or erythrocytes, white blood cells or leukocytes and platelets or thrombocytes, representing approximately 45% of the volume in human blood. These cellular elements are suspended in plasma, an aqueous ionic solution of low viscosity. Plasma behaves as a Newtonian fluid but whole blood has non-Newtonian properties. In the large vessels where shear rates are high enough, it is also reasonable to assume that blood has a constant viscosity and a Newtonian behaviour. However, in smaller vessels, or in some disease conditions, the presence of the cells induces low shear rate and whole blood exhibits remarkable non-Newtonian characteristics, like shear-thinning viscosity, thixotropy, viscoelasticity and possibly a yield stress. This is largely due to erythrocytes behaviour, namely their ability to aggregate into microstructures (*rouleaux*) at low shear rates, their deformability into an infinite variety of shapes without changing volume and their tendency to align with the flow field at high shear rates [8,25].

The most well-known non-Newtonian characteristic of blood is its shear-thinning behaviour [7,9]: at low shear rates, blood seems to have a high apparent viscosity (due to RBCs aggregation) while at high shear rates there is a reduction in the blood's viscosity (due to RBCs deformability). Stress relaxation properties of blood arise from its ability to store and release elastic energy from RBC networks and are mainly related to the viscoelastic nature of the RBC membrane. The viscoelastic behaviour of blood is less important at higher shear rates [27]. An understanding of the coupling between the blood composition and its physical properties is essential for developing suitable constitutive models to describe blood behaviour (see the recent reviews [22,23]).

While there has been a considerable research effort in blood rheology, the constitutive models have thus far focused on the aggregation and deformability of the RBCs, ignoring the role of platelets in the flow characteristics. However, platelets, which are much smaller than erythrocytes (approximately $6 \, \mu m^3$ in size as compared to $90 \, \mu m^3$) and form a small fraction of the particulate matter in human blood (around 3% in volume) are among the most sensitive of all the components of blood to chemical and physical agents and play an important role in coagulation, as already discussed. In the last two decades, mathematical modelling and computer simulation research have emerged as useful tools, supplementing experimental data and analysis and giving new insights in the studies of the regulation of the coagulation cascade in clinical applications and device design. Reliable

phenomenological models that can predict regions of platelet activation and deposition (either in artificial devices or in arteries) have the potential to help optimize design of such devices and also identify regions of the arterial tree susceptible to the formation of thrombotic plaques and possible rupture in stenosed arteries. Most of the models that are currently in use neglect some of the biochemical or mechanical aspects involved in the complex phenomena of blood coagulation and must be considered as first approaches to address this oversight, see, for example [5,6,12,16,18,29,31,32]. Other relevant biochemistry related references can be found in the recent review paper by Rajagopal and Lawson [20]. Anand *et al.* [2–4] recently developed a phenomenological comprehensive model for clot formation and lysis in flowing blood that extends existing models to integrate biochemical, physiological and rheological factors. In what follows, we present some preliminary computational results for a simplified version of this model where the viscoelasticity of blood is not considered. Section 2 is devoted to a description of the coupled blood flow-biochemistry mathematical model. The numerical methods and adopted stabilization techniques are briefly outlined in Section 3. Preliminary results of the three-dimensional simulations predicted by the simpler model are presented in Section 4. Finally, some comments on the limitations and extensions of the model are also included.

2. Mathematical model

2.1 Blood flow equations

An incompressible generalized Newtonian model with shear-thinning viscosity has been adopted to describe the flow of blood. We denote by $\mathbf{u}(x, t)$ and $p(x, t)$ the blood velocity and pressure defined in the domain Ω, the vascular lumen, with $t \geq 0$. The application of the physical principles of momentum and mass conservation leads to the equations defined in Ω

$$\rho\left(\frac{\partial \mathbf{u}}{\partial t} + \mathbf{u} \cdot \nabla \mathbf{u}\right) = -\nabla p + \operatorname{div} \tau(\mathbf{u}) \qquad \operatorname{div} \mathbf{u} = 0, \tag{1}$$

completed with appropriate initial and boundary conditions. Here, ρ is the fluid density and $\tau(\mathbf{u})$ is the deviatoric stress tensor, proportional to the symmetric part of the velocity gradient, given by

$$\tau(\mathbf{u}) = 2\mu(\dot{\gamma})\mathsf{D}, \tag{2}$$

where $\mathsf{D} = (\nabla \mathbf{u} + \nabla \mathbf{u}^{\mathsf{T}})/2$ is the stretching tensor, $\dot{\gamma} = 2\sqrt{\mathsf{D} : \mathsf{D}}$ is the shear rate (a measure of the rate of shear deformation) and $\mu(\dot{\gamma})$ is the shear dependent viscosity function which decreases with increasing shear rate and can be written in the following general form

$$\mu(\dot{\gamma}) = \mu_\infty + (\mu_0 - \mu_\infty)F(\dot{\gamma}), \tag{3}$$

or, in non-dimensional form as

$$\frac{\mu(\dot{\gamma}) - \mu_\infty}{\mu_0 - \mu_\infty} = F(\dot{\gamma}).$$

Here, $\mu_0 = \lim_{\dot{\gamma}\to 0}\mu(\dot{\gamma})$ and $\mu_\infty = \lim_{\dot{\gamma}\to\infty}\mu(\dot{\gamma})$ are the asymptotic viscosity values at low and high shear rates and $F(\dot{\gamma})$ is a shear dependent function satisfying the following natural limit conditions $\lim_{\dot{\gamma}\to 0}F(\dot{\gamma}) = 1$ and $\lim_{\dot{\gamma}\to\infty}F(\dot{\gamma}) = 0$. The generalized Cross model has

frequently been used for blood and has been adopted here. The corresponding viscosity function is written as

$$\frac{\mu(\dot{\gamma}) - \mu_\infty}{\mu_0 - \mu_\infty} = \frac{1}{(1 + (\lambda \dot{\gamma})^b)^a}. \tag{4}$$

Using nonlinear regression analysis, it is possible to fit viscosity functions against blood viscosity experimental data and obtain the corresponding parameters λ, a and b. However, blood viscosity is quite sensitive to a number of factors including haematocrit, temperature, plasma viscosity, age of RBCs, exercise level, gender or disease state, and care must be taken in selecting blood parameters for blood flow simulations. Here, we have adopted the following values of the material constants (see Ref. [17]):

$$\mu_0 = 1.6 \cdot 10^{-1}\,\text{Pa} \cdot \text{s} \quad \mu_\infty = 3.6 \cdot 10^{-3}\,\text{Pa} \cdot \text{s} \quad a = 1.23 \quad b = 0.64 \quad \lambda = 8.2\,\text{s}. \tag{5}$$

The viscosity function (4) with these values is represented in Figure 2.

2.2 Equations governing the cascade of biochemical reactions

The model includes not only rheological factors but also biochemical indicators that are essential to describe coagulation and fibrinolysis dynamics and consequently the formation, growth and dissolution of clots. It is based on the model introduced in Ref. [3] and further developed and refined in Ref. [2]. A set of twenty-three coupled advection–diffusion–reaction equations, describing the evolution in time and space of various enzymes and zymogenes, proteins, inhibitors, tissue plasminogen activator and fibrin/fibrinogen (Table 1) involved in the extrinsic pathway of the blood coagulation process and fibrinolysis in quiescent plasma, takes the following form

$$\frac{\partial C_i}{\partial t} + \text{div}(C_i \mathbf{u}) = \text{div}(D_i \nabla C_i) + R_i \quad i = 1, \ldots, 23. \tag{6}$$

In these equations, C_i stands for the concentration of ith reactant, D_i denotes the corresponding diffusion coefficient (which could be a function of the shear rate) and $\mathbf{u}$ is the velocity field. R_i are the nonlinear reaction terms that represent the production or depletion of C_i due to the enzymatic cascade of reactions. The specific form of the reaction terms, the diffusion coefficients and corresponding parameters for each of the 23-model
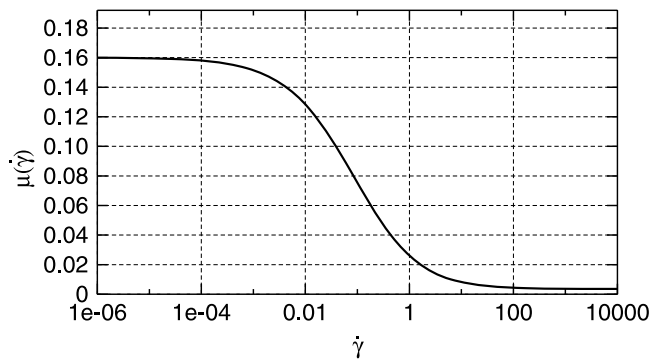

Figure 2.   Variation of the apparent viscosity of blood as a function of the shear rate for the generalized Cross model with physiological parameters given by (5).

Table 1.   Constituents involved in the coagulation cascade and fibrinolysis.

Species	Names
IXa	?Enzym?
IX	Zymogen IX
VIIIa	Enzym VIIIa
VIII	Zymogen VIII
Va	Enzym Va
V	Zymogen V
Xa	Enzym Xa
X	Zymogen X
IIa	Thrombin
II	Prothrombin
Ia	Fibrin
I	Fibrinogen
XIa	Enzym XIa
XI	Zymogen XI
ATIII	AntiThrombin-III
TFPI	Tissue factor pathway inhibitor
APC	Active protein C
PC	Protein C
L1AT	α_1-AntiTrypsin
tPA	Tissue plasminogen activator
PLA	Plasmin
PLS	Plasminogen
L2AP	α_2-AntiPlasmin
Z	Tenase
W	Prothrombinase

Equations (6) is shown in Tables 2 and 3. In order to keep the model readable, symbol [·] is used to denote the concentration of a reactant and to distinguish it from its name (e.g. [*ATIII*] denotes the concentration of AntiThrombin III (*ATIII*)).

Equations (6) are complemented with appropriate initial and flux boundary conditions involving the concentration of various species at an injured site of the vascular wall (see Section 4.1.2). A schematic representation of these reactions, including boundary conditions is given in Figure 3. This figure also includes interactions with two other chemical species *Z* (tenase) and *W* (prothrombinase), see Table 6. Separate convection–diffusion reactions are not written for the corresponding concentrations, since they are embedded in the equations for *VIIIa*, *IXa*, *Va* and *Xa*. Their values can be obtained through the relations $[Z] = [VIIIa][IXa]/K_{dZ}$, $[W] = [Va][Xa]/K_{dW}$ [2], respectively.

2.3   Clot modeling

Under normal conditions, no clot exists and we assume that the presence of all these constituents does not affect the velocity of the bulk flow. Clot formation occurs when an activation threshold in the flux boundary conditions, related to the concentration of *tissue factor* (*TF−VIIa* complex released from sub-endothelium) is exceeded and the clotting cascade is initiated, which results in the increase of fibrin concentration [*Ia*] in the clotting area (see Section 4.1.2). Clot growth is determined by tracking in time the extent of the flow region where fibrin concentration C_F equals or exceeds a specific critical value C_{Clot}. The clot region can thus be defined as a region where the fibrin concentration is higher than in the normal blood. The main features of the modelling approach are schematically shown in Figure 4.

Table 2.　Reaction terms and diffusion coefficients.

Species	Reaction terms (R_i)	Diffusion coefficients D_i (cm^2/s)
IXa	$(k_9[XIa][IX])/(K_{9M} + [IX]) - h_9[IXa][ATIII]$	6.27×10^{-7}
IX	$-(k_9[XIa][IX])/(K_{9M} + [IX])$	5.63×10^{-7}
VIIIa	$(k_8[IIa][VIII])/(K_{8M} + [VIII]) - h_8[VIIIa]$ $-(h_{C8}[APC][VIIIa])/(H_{C8} + [VIIIa])$	3.92×10^{-7}
VIII	$-(k_8[IIa][VIII])/(K_{8M} + [VIII])$	3.12×10^{-7}
Va	$(k_5[IIa][V])/(K_{5M} + [V]) - h_5[Va]$ $-(h_{C5}[APC][Va])/(H_{C5M} + [Va])$	3.82×10^{-7}
V	$-(k_5[IIa][V])/(K_{5M} + [V])$	5.63×10^{-7}
Xa	$(k_{10}[Z][X])/(K_{10M} + [X]) - h_{10}[Xa][ATIII] - h_{TFPI}[TFPI][Xa]$	7.37×10^{-7}
X	$-(k_{10}[Z][X])/(K_{10M} + [X])$	5.63×10^{-7}
IIa	$(k_2[W][II])/(K_{2M} + [II]) - h_2[IIa][ATIII]$	6.47×10^{-7}
II	$-(k_2[W][II])/(K_{2M} + [II])$	5.21×10^{-7}
Ia	$(k_1[IIa][I])/(K_{1M} + [I]) - (h_1[PLA][Ia])/(H_{1M} + [Ia])$	2.47×10^{-7}
I	$-(k_1[IIa][I])/(K_{1M} + [I])$	3.10×10^{-7}
XIa	$(k_{11}[IIa][XI])/(K_{11M} + [XI]) - h_{11}^{A3}[XIa][ATIII] - h_{11}^{L1}[XIa][L1AT]$	5.00×10^{-7}
XI	$-(k_{11}[IIa][XI])/(K_{11M} + [XI])$	3.97×10^{-7}
ATIII	$-(h_9[IXa] + h_{10}[Xa] + h_2[IIa] + h_{11}^{A3}[XIa])[ATIII]$	5.57×10^{-7}
TFPI	$-h_{TFPI}[TFPI][Xa]$	6.30×10^{-7}
APC	$(k_{PC}[IIa][PC])/(K_{PCM} + [PC]) - h_{PC}[APC][L1AT]$	5.50×10^{-7}
PC	$-(k_{PC}[IIa][PC])/(K_{PCM} + [PC])$	5.44×10^{-7}
L1AT	$-h_{PC}[APC][L1AT] - h_{11}^{L1}[XIa][L1AT]$	5.82×10^{-7}
tPA	0	5.28×10^{-7}
PLA	$(k_{PLA}[tPA][PLS])/(K_{PLAM} + [PLS]) - h_{PLA}[PLA][L2AP]$	4.93×10^{-7}
PLS	$-(k_{PLA}[tPA][PLS])/(K_{PLAM} + [PLS])$	4.81×10^{-7}
L2AP	$-h_{PLA}[PLA][L2AP]$	5.25×10^{-7}

An important assumption of the coupling strategy for blood and clot is to assume that the corresponding constitutive models are similar, but their viscosities have different values. This can be done introducing a viscosity factor related to the fibrin concentration around the injured vessel wall region. More precisely, when fibrin concentration is close to zero, the local viscosity is equal to the viscosity of blood (thus the viscosity factor is equal to 1). As the fibrin concentration grows, the viscosity increases linearly up to a certain threshold C_{Clot} and the viscosity factor is equal to μ^* (Figure 5). The parameters μ^* and C_{Clot} should be chosen to mimic the clot properties. In our study, we have used $\mu^* = 100$ and $C_{Clot} = 1000$ nM corresponding to a viscosity of the clot region 100 times higher than that of the blood.

This model function of the viscosity factor based on fibrin concentration as well as the values used to simulate the clot growth look reasonable, but can easily been improved if experimental data are available.

3.　Numerical methods

The numerical solution of the coupled fluid-biochemistry model given by Equations (1)–(2)–(6) is obtained using a three-dimensional code based on a finite-volume semi-discretization in space, on structured grids, where both inviscid and viscous flux integrals are evaluated using centred cell numerical fluxes. An explicit multistage Runge–Kutta scheme is used for time integration. The same method is applied for both the flow and the biochemical solutions of the coupled model. The coupling is carried out by means of an iterative process at each time step. The flow field is first computed using Equations (1)–(2)

Table 3. Reaction kinetics parameters.

Parameters	Values	Units
k_9	11.0	min^{-1}
K_{9M}	160	nM
h_9^{A3}	0.0162	$nM^{-1} min^{-1}$
k_8	194.4	min^{-1}
K_{8M}	112,000	nM
h_8	0.222	min^{-1}
h_{C8}	10.2	min^{-1}
H_{C8M}	14.6	nM
k_5	27.0	min^{-1}
K_{5M}	140.5	nM
h_5	0.17	min^{-1}
h_{C5}	10.5	min^{-1}
H_{C5M}	14.6	nM
k_{10}	2391	min^{-1}
K_{10M}	160.0	nM
h_{10}	0.347	$nM^{-1} min^{-1}$
h_{TFPI}	0.48	$nM^{-1} min^{-1}$
k_2	1344.0	min^{-1}
K_{2M}	1060.0	nM
h_2	0.714	$nM^{-1} min^{-1}$
k_1	3540	min^{-1}
K_{1M}	3160	nM
h_1	1500	min^{-1}
H_{1M}	250,000	nM
k_{11}	0.0078	min^{-1}
K_{11M}	50.0	nM
h_{11}^{A3}	1.6×10^{-3}	$nM^{-1} min^{-1}$
h_{11}^{L1}	1.3×10^{-5}	$nM^{-1} min^{-1}$
k_{PC}	39.0	min^{-1}
K_{PCM}	3190.0	nM
h_{PC}	6.6×10^{-7}	$nM^{-1} min^{-1}$
k_{PLA}	12.0	min^{-1}
K_{PLAM}	18.0	nM
h_{PLA}	0.096	$nM^{-1} min^{-1}$
k_{AP}^{AP}	18.0	$nM^{-1} min^{-1}$
h_{AP}^{IIa}	30.0	min^{-1}
K_{dZ}	0.56	nM
K_{dW}	0.1	nM

with a given viscosity, and next inserted into (6) to obtain the concentrations (including that of fibrin). The local viscosity is updated by a factor which depends on the calculated fibrin concentration in the clotting area and the flow field is recomputed in the next time step using the updated viscosity.

An artificial compressibility formulation (see, e.g. [28]) is used to calculate the pressure and to enforce the divergence-free constraint. Continuity Equation $(1)_2$ is modified by adding the time-derivative of pressure properly scaled by the artificial speed of sound $\mathfrak{c}$, as follows:

$$\frac{1}{\mathfrak{c}^2} \frac{\partial p}{\partial t} + \text{div } \mathbf{u} = 0. \tag{7}$$

Figure 3. Schematic of the selected reactions involved in the extrinsic pathway of the blood coagulation process.

This non-physical modification of the continuity equation is often used in steady flow simulations. In the present case, the sub-iterative procedure based on the artificial compressibility method is only used to enforce the divergence-free constraint before simulating the biochemical concentrations. This could be justified by the quasi-steady nature of the flow, due to the slow evolution in time of the local viscosity. Thus, it looks acceptable to assume the flow to be described by a steady generalized Newtonian system at each time step.

Figure 4. Clot modeling.

Figure 5.   Clot viscosity behaviour.

3.1   Space discretization

The computational mesh is structured and consists of hexahedral primary control volumes. To evaluate the viscous fluxes also, dual finite volumes are needed. They have octahedral shape and are centred around the corresponding primary cell faces. Figure 6 shows a schematic representation of this configuration. The same grid is used for the calculation of both flow field and biochemical concentrations. Thus, it is natural to use the same method for solving both problems simultaneously. The algorithm described below for the flow variables W, can thus be directly applied to the calculation of the concentrations C_i.

The system of generalized NS Equations (1)–(2) can be rewritten in the vector form. Here, we use W to denote the vector of unknowns (including pressure). Vectors F, G and H denote the inviscid fluxes in x, y, z directions, while R, S and T stand for their viscous counterparts. Using this notation, the spatial finite-volume semi-discretization in the computational cell $D \equiv D_{i,j,k}$ can be written in the following form:

$$\frac{\partial \mathsf{W}}{\partial t} = \frac{-1}{|D|} \oint_{\partial D} [(\mathsf{F} - \mathsf{R}), (\mathsf{G} - \mathsf{S}), (\mathsf{H} - \mathsf{T})] \cdot \hat{\boldsymbol{v}} \, \mathrm{d}S. \tag{8}$$

Here, $\hat{\boldsymbol{v}}$ denotes the outer unit normal vector of the cell boundary and $\mathrm{d}S$ is the surface element of this boundary. Equation (8) can be rewritten in operator form:

$$\frac{\partial \mathsf{W}_{ijk}}{\partial t} = -\mathcal{L}\mathsf{W}_{i,j,k}, \tag{9}$$
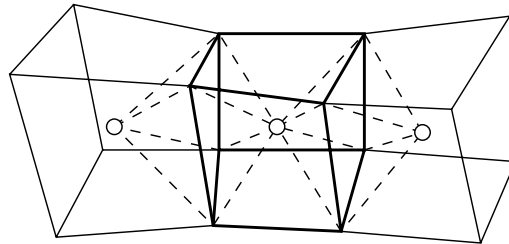
Figure 6.   Finite-volume grid in 3D.

where $\mathcal{L}$ stands for the finite-volume discretization operator. This operator is still exact at this stage and must be properly discretized.

The inviscid flux integral can be approximated using centred cell fluxes, e.g. the value of the flux F on the cell face with index $\ell = 1$ is computed as the average of cell-centred values from both sides of this face:

$$\mathsf{F}_1^n = \frac{1}{2}\left[\mathsf{F}\left(\mathsf{W}_{i,j,k}^n\right) + \mathsf{F}\left(\mathsf{W}_{i+1,j,k}^n\right)\right]. \tag{10}$$

The contribution of inviscid fluxes is finally summed up over the cell faces $\ell = 1,\ldots,6$. In this way, we can write the inviscid flux approximation:

$$\oint_{\partial D} \mathsf{F}\nu^x \mathrm{d}y\,\mathrm{d}z \approx \sum_{\ell=1}^{6} \mathsf{F}_\ell \nu_\ell^x S_\ell. \tag{11}$$

The discretization of viscous fluxes is more complicated since vectors R, S, T involve the derivatives of the velocity components that need to be approximated at cell faces. This can be done using a dual finite-volume grid, with octahedral cells, centred around the corresponding faces (Figure 7). The evaluation of the velocity gradient components is then replaced by the evaluation of the surface integral over the dual volume boundary. Finally, this surface integral is approximated by a discrete sum over the dual cell faces (with indices $m = 1,\ldots,8$). For example, if we want to evaluate the first component of the viscous flux R_1 (i.e. to approximate u_x) at the cell face $l = 1$, we must proceed in the following way:

$$u_x \approx \oint_{\partial \tilde{D}} u\nu^x \mathrm{d}y\,\mathrm{d}z \approx \sum_{m=1}^{8} u_m \nu_m^x S_m. \tag{12}$$

The outer normal to the dual cell faces must be properly approximated $\nu^x \approx \nu_m^x$. The values of the velocity components in the middle nodes of these faces are taken as an average of the values in the corresponding vertices.

3.2 Time integration

After space discretization, the problem is now in the semi-discrete form:

$$\frac{\mathrm{d}\mathsf{W}_{ijk}}{\mathrm{d}t} = -\mathcal{L}\mathsf{W}_{i,j,k}, \tag{13}$$

where $\mathcal{L}$ is the approximate space discretization operator.
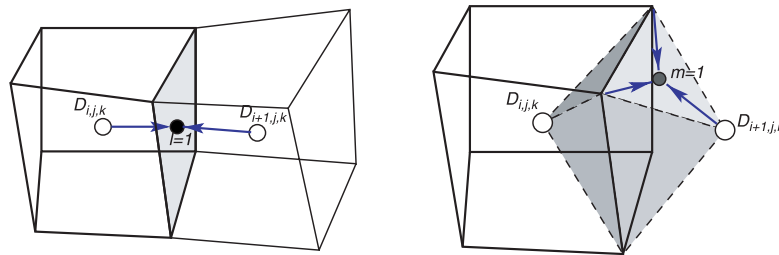
Figure 7.   Inviscid flux (left) and viscous flux (right) discretizations.

This system of ordinary differential equations for W (or concentration C_i) can be solved, e.g. by the Runge–Kutta multistage method. For simplicity, we use the same time integration method for both, flow field and concentrations. One of the simplest Runge–Kutta methods can be written in the form:

$$\mathsf{W}^{(0)}_{i,j,k} = \mathsf{W}^n_{i,j,k}$$

$$\mathsf{W}^{(r+1)}_{i,j,k} = \mathsf{W}^{(0)}_{i,j,k} - \alpha_{(r)}\Delta t \mathcal{L}\mathsf{W}^{(r)}_{i,j,k} \tag{14}$$

$$\mathsf{W}^{n+1}_{i,j,k} = \mathsf{W}^{(m)}_{i,j,k}.$$

Here, $r = 1, \ldots, m$ is related to the m-stage method. The three-stage explicit RK scheme has coefficients: $\alpha_{(1)} = 1/2$, $\alpha_{(2)} = 1/2$ and $\alpha_{(3)} = 1$. This method is useful and efficient with minimum requirements on the storage space associated with intermediate stages.

The efficiency and robustness of the method could be further increased modifying the above algoritm. The modification used in the numerical simulations presented in this paper follows the Runge–Kutta time integration procedures outlined in Ref. [14] and further refined in Ref. [13]. The idea behind this modified approach lies in splitting the space discretization operator into its inviscid and viscous parts. The inviscid operator is evaluated at each Runge–Kutta stage, while the viscous operator is evaluated in just a few more stages. This corresponds to the use of different Runge–Kutta coefficients for time integration of inviscid and viscous fluxes. The modified algorithm can thus be written in the form:

$$\mathsf{W}^{(0)}_{i,j,k} = \mathsf{W}^n_{i,j,k}$$

$$\mathsf{W}^{(r+1)}_{i,j,k} = \mathsf{W}^{(0)}_{i,j,k} - \alpha_{(r)}\Delta t(\mathcal{Q}^{(r)} + \mathcal{D}^{(r)}) \tag{15}$$

$$\mathsf{W}^{n+1}_{i,j,k} = \mathsf{W}^{(m)}_{i,j,k}.$$

Here, the space discretization operator at stage (r) is split as:

$$\mathcal{L}\mathsf{W}^{(r)}_{i,j,k} = \mathcal{Q}^{(r)} + \mathcal{D}^{(r)}. \tag{16}$$

The inviscid flux $\mathcal{Q}$ is evaluated in the usual way at each stage

$$\mathcal{Q}^{(r)} = \mathcal{Q}\mathsf{W}^{(r)}_{i,j,k} \quad \text{with} \quad \mathcal{Q}^{(0)} = \mathcal{Q}\mathsf{W}^n_{i,j,k}. \tag{17}$$

The viscous flux $\mathcal{D}$ uses a blended value from the previous and the actual stages according to the following rule:

$$\mathcal{D}^{(r)} = \beta_{(r)}\mathcal{D}\mathsf{W}^{(r)}_{i,j,k} + (1 - \beta_{(r)})\mathcal{D}^{(r-1)} \quad \text{with} \quad \mathcal{D}^{(0)} = \mathcal{D}\mathsf{W}^n_{i,j,k}. \tag{18}$$

The coefficients $\alpha_{(r)}$ and $\beta_{(r)}$ are chosen to guarantee a large enough stability region for the Runge–Kutta method. The following set of coefficients was used in this study:

$$
\begin{aligned}
\alpha_{(1)} &= 1/3 & \beta_{(1)} &= 1 \\
\alpha_{(2)} &= 4/15 & \beta_{(2)} &= 1/2 \\
\alpha_{(3)} &= 5/9 & \beta_{(3)} &= 0 \\
\alpha_{(4)} &= 1 & \beta_{(4)} &= 0
\end{aligned}
$$

We realize that only two evaluations of the dissipative terms are needed when this four-stage method is used. This characteristic of the method significantly saves the amount of calculations while retaining the advantage of a large stability region. Further admissible sets of coefficients together with comments on the increase of the efficiency and robustness of the corresponding methods can be found in Refs. [13,14] and the references therein.

3.3 Numerical stabilization

A well-known property of central schemes is that, in the presence of strong gradients, non-physical oscillations appear in the solution. Procedures aiming at stabilizing the discrete solution and to avoid spurious pressure modes can be accomplished according to several criteria.

In the present simulations, we use a pressure stabilization method that consists in adding a pressure dissipation term (Laplacian) on the right-hand side of the modified continuity Equation (7). This term takes the form:

$$
Q_{i,j,k} = \frac{1}{|D_{i,j,k}|} \sum_{\ell=1}^{2N} \frac{p_\ell - p_{i,j,k}}{b_\ell} S_\ell. \tag{19}
$$

Here, ℓ denotes the control volume cell face index, p_ℓ is the pressure in the corresponding neighbouring cell and S_ℓ is the cell face area. The value b_ℓ has the dimension of velocity and represents the maximal convective velocity in the domain and local diffusive velocity.

$$
b_\ell = \max\left(\sqrt{u_1^2 + u_2^2 + u_3^2} \right) + \frac{2\nu}{L_\ell}. \tag{20}
$$

Symbol L_ℓ corresponds to a distance between the current and the neighbouring cell centres.

It is possible to show that on the uniform cartesian mesh with cells of size δx, this term is given by:

$$
Q = \frac{\delta x}{2b} \Delta p. \tag{21}
$$

This stabilization method has some advantages over the classical artificial diffusion applied to the velocity components. The artificial effects induced by the pressure dissipation term do not interfere with the physical shear dependent viscosity. Moreover, this stabilization term contains only second derivatives of the pressure and will vanish if pressure is a linear function of space coordinates. See also Ref. [19] for other stabilization approaches.

Finally, it is important to observe that since the diffusion coefficients in the advection–diffusion–reaction equations of the biochemistry model are extremely small, the use of a central space-discretization, with no internal numerical diffusion, seems to be a natural

choice. To prevent the appearance of numerical oscillations typically associated to central schemes, a special non-linear filter was also used at each iteration to postprocess the concentration fields. This filtering technique described in Ref. [11] was further studied in Ref. [26].

4. Numerical simulations and preliminary results

The computational domain consists of a segment of a rigid-walled cylindrical vessel with diameter $D = 2R = 6.2\,$mm and length $L = 10R = 31\,$mm. The whole domain is discretized using a structured multiblock mesh with hexahedral cells as shown in Figure 8. The grid is fitted to the vessel wall in order to capture the near-wall gradients of the velocity and concentration fields. The grid has $10 \times 10 \times 60$ cells in the core block, while there are $40 \times 20 \times 60$ cells in the outer, near-wall block.

4.1 Boundary and initial conditions

4.1.1 Velocity and pressure

A fully developed velocity profile, with mean velocity $U = 3.1\,$cm/s (related to the vessel length by $U = L/s = 10R/s$), is prescribed at the inlet (Dirichlet condition) and, at the outlet, homogeneous Neumann conditions for the velocity components, are imposed. Pressure is fixed only at the outlet and is extrapolated at the other boundaries. On the vessel wall, no-slip Dirichlet conditions for the velocity field are prescribed. Since at time $t = 0$ no clot exists, an undisturbed fully developed non-Newtonian flow is conveniently computed and imposed as initial condition. This undisturbed flow is also used as initial condition for the biochemistry simulations.

4.1.2 Concentrations

The vessel wall is impermeable and the boundary conditions for the concentrations of all the twenty-three chemical species, at the healthy vessel wall, are homogeneous of Neumann type (i.e. no-flux). In the injured wall region, no-flux boundary conditions are prescribed for all constituents except for seven selected chemical species which are directly involved in the initiation of the coagulation cascade [2–4]. Figure 9 represents this configuration.

The simulated vessel wall injury is considered to be a region which is the intersection of the outer surface of the vessel with a sphere of radius R, centered on the vessel wall
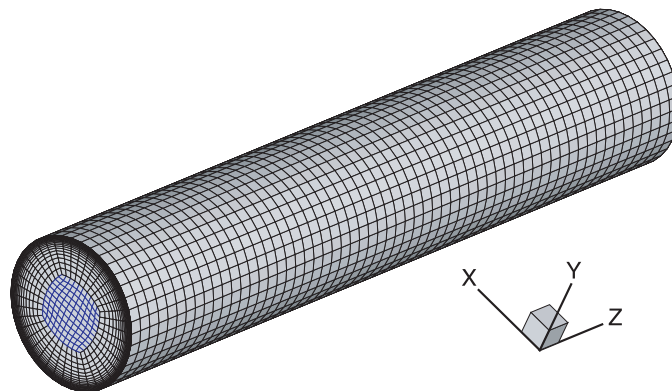
Figure 8.   Computational geometry and grid.

at one third of the length of the vessel segment. This means the clotting surface on the vessel wall is elliptical-shaped. In this region, non-homogeneous boundary conditions of the Neumann type $\partial C_i/\partial \mathbf{n} = B_i$ are prescribed for the following seven chemicals: *IXa*, *IX*, *Xa*, *X*, *XIa*, *XI* and *tPa*. These flux terms are summarized in Table 4, where $[C]^w$ denotes the value of C on the wall.

Diffusion coefficients D have already been listed in Table 2. The length scale L is chosen to be equal to the vessel radius R. The other parameters appearing in the formulation of boundary fluxes are summarized in Table 5.

Along with these constant type parameters, another three free parameters describing the level of the blood vessel wall injury appear and should be specified. These values are the *TF−VIIa* complex concentration ($[TF−VIIa]$), the number of intact endothelial cells per unit area $[ENDO]$, and the *XIIa* enzyme concentration ($[XIIa]$). These values should be prescribed separately for injured and healthy vessel wall as shown in Figure 10 (using ??? and ??, respectively).

In addition, we require normal human physiological values as initial conditions for the concentrations of all chemical species (see Refs. [2−4]). These values are listed in Table 6. To avoid instabilities in the numerical simulations here, we assume that the initial concentrations of the enzymes originally set to zero (*IXa*, *VIIIa*, *Va*, *Xa*, *IIa* and *Ia*) are replaced by suitable very small (but non-zero) values, set to be 0.1% of the initial values for the corresponding zymogens (*IX*, *VIII*, *V*, *X*, *II* and *I*). These free parameters are chosen to be equal to zero on the healthy part of the vessel wall, while on the injured area their prescribed values are shown in Table 7.

4.2   *Numerical results*

In this section, we present some of the results obtained with the three-dimensional numerical simulations of the coupled fluid-biochemistry model described above for the prediction of clot formation and growth around an injured vessel wall region, under physiological conditions. As already mentioned (Section 2.3), the initiation of the clotting cascade is associated to the extent of injury in the vessel wall, reflected in a threshold concentration of the *TF−VIIa* complex (*tissue factor*) imposed in the flux boundary conditions. The clot is formed when fibrin concentration $[Ia]$ equals or exceeds a specific value (1000 nM in our case) and clot growth is determined by tracking in time the evolution of fibrin concentration in the clot region.

All the twenty-three chemical species involved in the advection−reaction−diffusion Equations (6) play an important role in the clotting process. Their concentrations are computed pointwise in the whole computational domain and can be visualized during
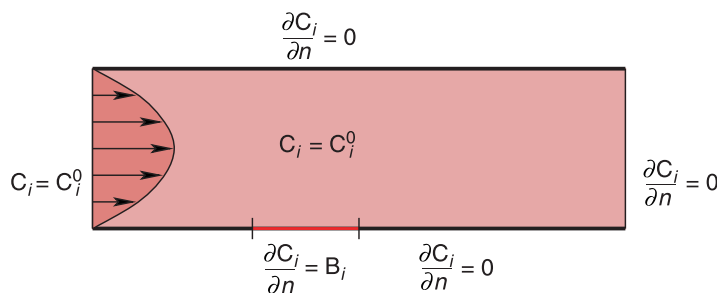
Figure 9.   Concentration boundary conditions.

Table 4.   Flux boundary conditions at the injured vessel wall region.

Species	Expressions of the boundary flux terms B_i
IXa	$((k_{7,9}[IX]^w[TF-VIIa]^w)/(K_{7,9M}+[IX]^w))(L/\mathsf{D}_{IXa})$
IX	$-((k_{7,9}[IX]^w[TF-VIIa]^w)/(K_{7,9M}+[IX]^w))(L/\mathsf{D}_{IX})$
Xa	$((k_{7,10}[X]^w[TF-VIIa]^w)/(K_{7,10M}+[X]^w))(L/\mathsf{D}_{Xa})$
X	$-((k_{7,10}[X]^w[TF-VIIa]^w)/(K_{7,10M}+[X]^w))(L/\mathsf{D}_X)$
XIa	$((\phi_{11}[XI]^w[XIIa]^w/(\Phi_{11M}+[XI]^w))(L/\mathsf{D}_{XIa})$
XI	$-((\phi_{11}[XI]^w[XIIa]^w)/(\Phi_{11M}+[XI]^w))(L/\mathsf{D}_{XI})$
tPa	$((k_{tPA}^C+k_{tPA}^{IIa}[IIa]^w+k_{tPA}^{Ia}[Ia]^w)[ENDO]^w)(L/\mathsf{D}_{tPa})$

Table 5.   Boundary flux parameters.

Parameters	Values	Units
ϕ_{11}	0.034	min^{-1}
Φ_{11M}	2000	nM
$k_{7,9}$	32.4	nM
$K_{7,9M}$	24	nM
$k_{7,10}$	103	$\text{min}^{-1}\,\text{m}$
$K_{7,10M}$	240	nM
k_{tPA}^C	6.52×10^{-13}	$\text{nM}\,\text{m}^2\,\text{min}^{-1}$
k_{tPA}^{IIa}	$9.27 \times 10^{-12}\mathrm{e}^{-134.8(t-t_0)}$	$\text{m}^2\,\text{min}^{-1}$
k_{tPA}^{Ia}	5.059×10^{-18}	$\text{m}^2\,\text{min}^{-1}$

aselected simulation time. Figure 11 illustrates the evolution in time (300 s) of the concentrations of the six most important species involved in the blood coagulation, namely [*IIa*] (Thrombin), [*Ia*] (Fibrin), [*ATIII*] (Anti-Thrombin III), [*APC*] (Active Protein C), [*tPA*] (Tissue Plasminogen Activator) and [*PLA*] (Plasmin). The concentrations versus time history are shown at the centre of the simulated vessel wall injured region.

During the simulation time period of 300 s the concentrations of these chemicals undergo a profound evolution. The most relevant is the jump in all concentrations that occurs approximately 20 s after the initiation of the clotting cascade. At this time, the system response becomes stronger and the concentration of fibrin increases rapidly and reaches its maximum value at approximately 120 s, remaining relatively stable after that time, Figure 11(b). Observing the different graphs shown in Figure 11, we also conclude that the time evolution is not similar for the various chemical species.
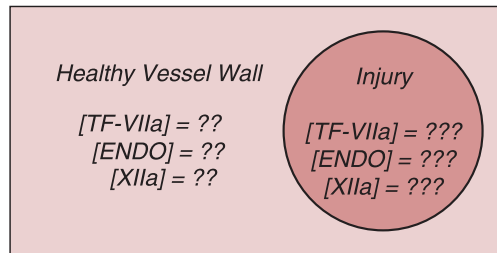
Figure 10.   Free parameters in flux boundary conditions.

Table 6.   Initial concentrations.

Species	Initial values (nM)
IXa	0.0*
IX	90.0
VIIIa	0.0*
VIII	0.7
Va	0.0*
V	20.0
Xa	0.0*
X	170.0
IIa	0.0*
II	1400.0
Ia	0.0*
I	7000.0
XIa	0.0*
XI	30.0
ATIII	2410.0
TFPI	2.5
APC	0.0*
PC	60.0
L1AT	45000.0
tPA	0.08
PLA	0.0*
PLS	2180.0
L2AP	105.0

Clot growth can be better observed in Figure 12, which shows the contours of fibrin concentration on the vessel wall after 60 s. The simulations suggest that fibrin concentration has significantly increased in the clotting area. Moreover, due to advection, fibrin is transported downstream in the injured vessel wall region, as expected and the clot's shape changes its form during the clotting process.

These phenomena become more evident in Figure 13, where the variations of surface fibrin concentration contours during the initial 60 s of clotting are displayed. The length scales of both axes correspond to the axial and tangential coordinates, normalized by the vessel cross-section radius R. The blood flow direction is from left to right. In the first 20 s, simulations do not show any change in the fibrin concentration and therefore only results for the time period 30–60 s are shown in Figure 13. Due to advection, fibrin is transported downstream in the injured vessel wall region, as already referred, and the clot's shape changes its form during the clotting process.

Advection effects are better captured with a longer simulation time of clot growth. This is shown in Figure 14 for the time period 0–300 s. It is clear that the clot evolution process is not yet finished, as the clot shape is still changing. Also, clot dissolution that

Table 7.   Free parameters in boundary fluxes.

Concentrations	Values
[*TF−VIIa*]	0.25 nM
[*ENDO*]	2.0×10^9 cells/m^2
[*XIIa*]	375 nM
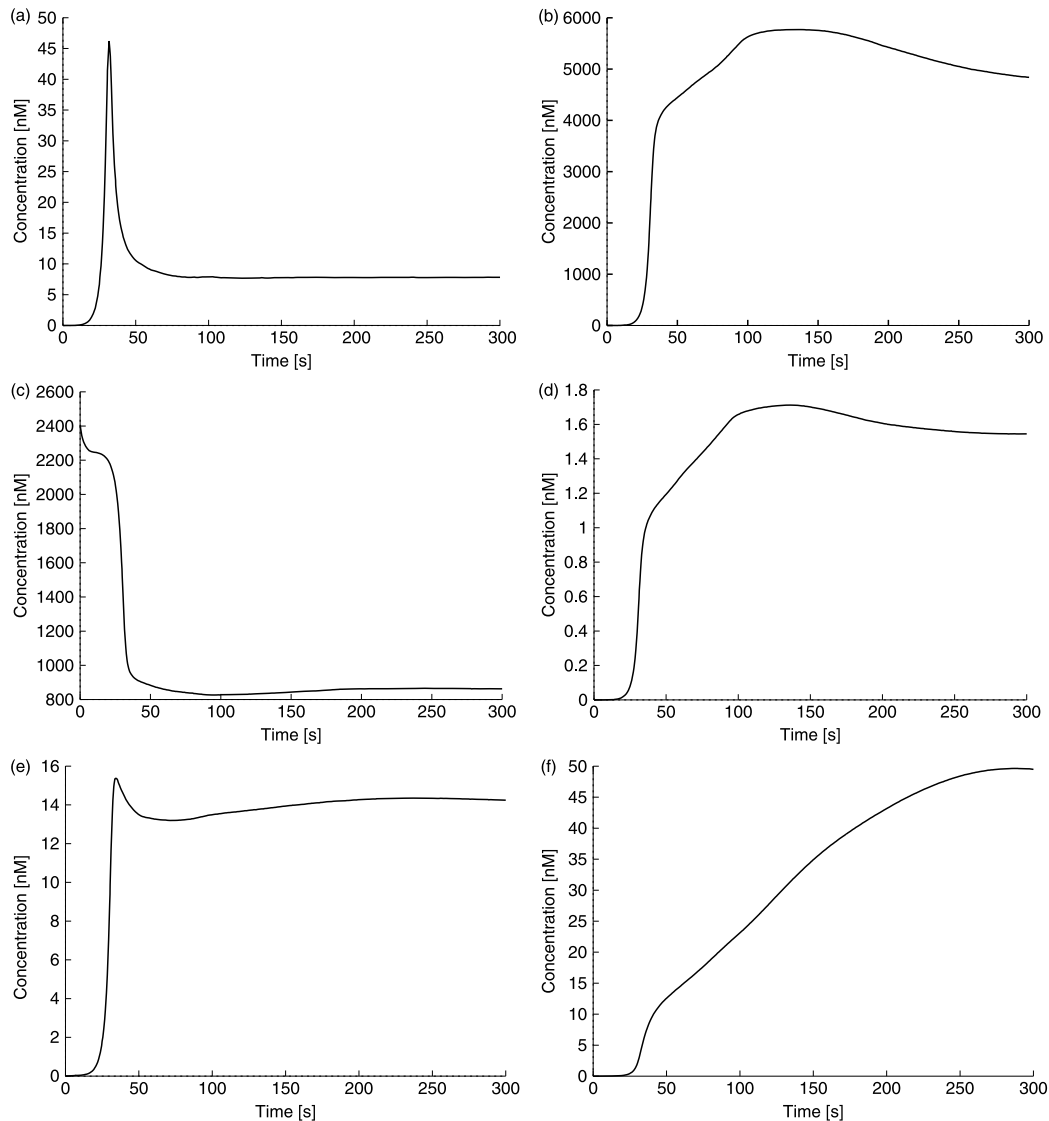
Figure 11. Time evolution of the concentrations of selected chemical species in the centre of the clotting surface. (a) Thrombin [IIa]; (b) Fibrin [Ia]; (c) Anti-Thrombin III [ATIII]; (d) Active Protein C [APC]; (e) Tissue Plasminogen [tPA]; (f) Plasmin [PLA].

occurs in regions where fibrin concentration drops below C_{Clot}, after initially exceeding it, or when the shear stress exceeds a critical value forcing the clot's rupture, has not been captured in the present simulations. A longer time clot growth and dissolution needs more computational time and is beyond the purpose of the preliminary numerical simulations performed in this study.

5. Conclusion and remarks

Preliminary numerical results of three-dimensional simulations for a simplified version of an advanced comprehensive model of clot growth and lysis, introduced and discussed in Refs. [2−4], have been presented here to emphasize its effectiveness.
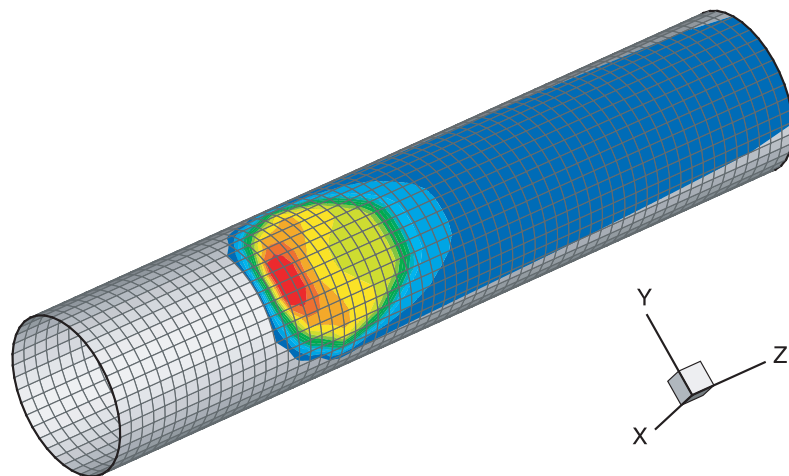
Figure 12.   Fibrin concentration on the vessel surface after 60 s.

The blood flow model used in the simulations only captures its shear-thinning viscosity and could be improved with more complex rheological models including viscoelasticity, as studied by Yeleswarapu [30], or the thermodynamically based model derived by Anand and Rajagopal [1] (with deformation dependent relaxation times) and used in Refs. [2–4]. Moreover, it would be interesting to incorporate in the solvers additional chemical constituents and their interactions, as in those involved in platelets activation and aggregation, to obtain numerical results for a more realistic coagulation model that fits physiological experimental data and may be used in clinical applications. Results can also
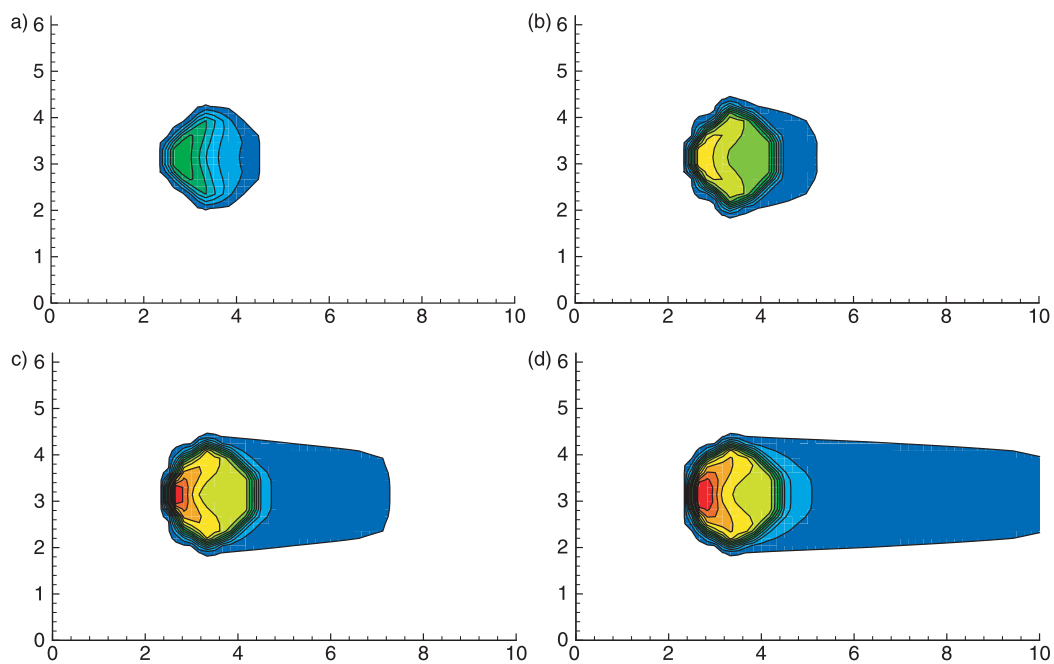
Figure 13.   Evolution of fibrin concentrations on the vessel wall during the first minute of clotting. (a) 30 s; (b) 40 s; (c) 50 s; (d) 60 s.
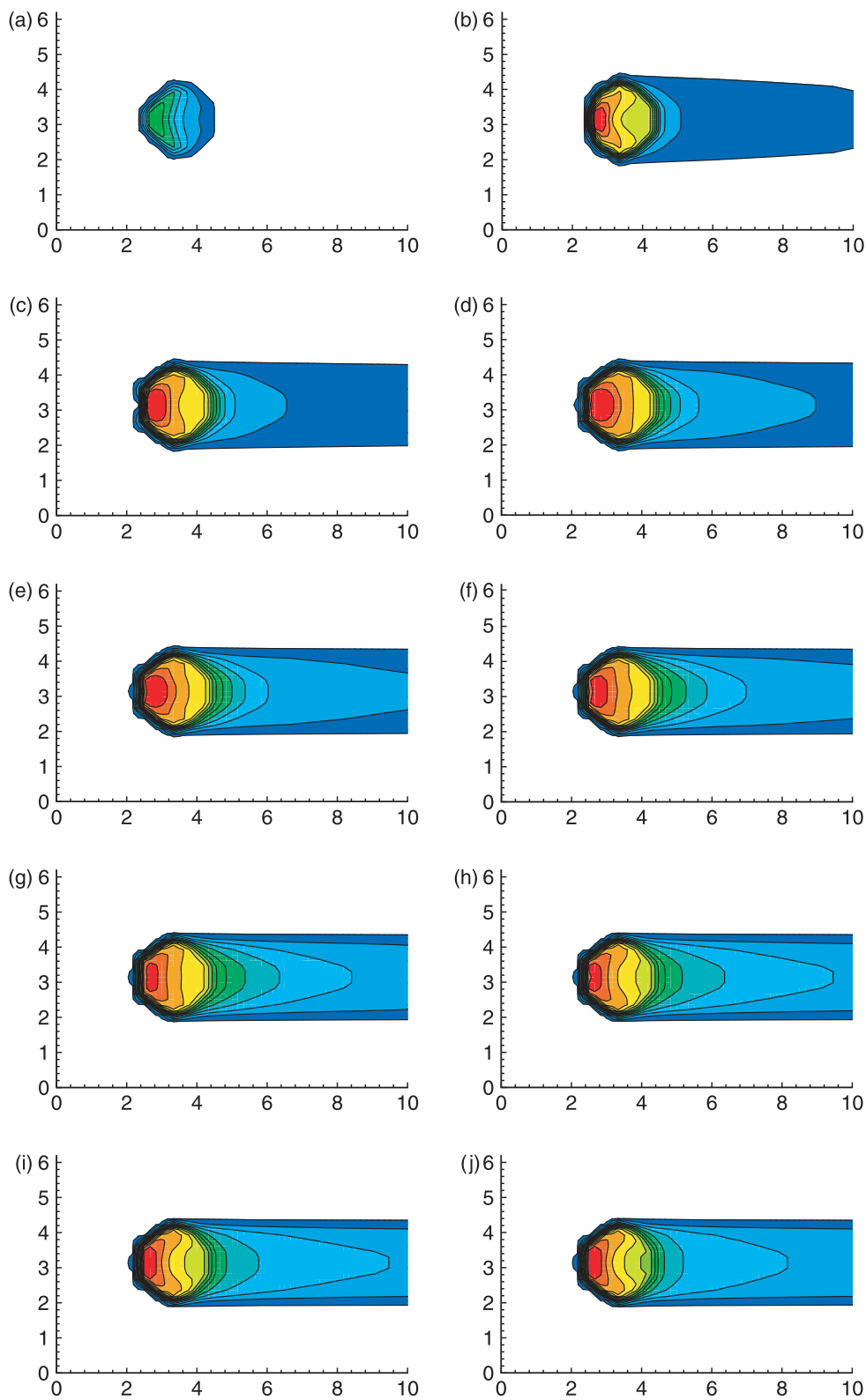
Figure 14. Evolution of fibrin concentrations on the vessel wall during the first 5 min of clotting. (a) 30 s; (b) 60 s; (c) 90 s; (d) 120 s; (e) 150 s; (f) 180 s; (g) 210 s; (h) 240 s; (i) 270 s; (j) 300 s.

be improved using more efficient and robust space and time semi-discretization solvers that allow for the simulation of clot growth and dissolution with affordable computational costs. This is the object of our current research.

Acknowledgements

References

[1] M. Anand and K.R. Rajagopal, *A shear-thinning viscoelastic fluid model for describing the flow of blood*, Int. J. Cardiovas. Med. Sci. 4(2) (2004), pp. 59–68.

[2] M. Anand and K.R. Rajagopal, *A model for the formation and lysis of clots in quiescent plasma. A comparison between the effects of antithrombin III deficiency and protein C deficiency*, submitted (2007).

[3] M. Anand, K. Rajagopal, and K.R. Rajagopal, *A model incorporating some of the mechanical and biochemical factors underlying clot formation and dissolution in flowing blood*, J. Theor. Med. 5(3–4) (2003), pp. 183–218.

[4] M. Anand, K. Rajagopal, and K.R. Rajagopal, *A model for the formation and lysis of blood clots*, Pathophysiol. Haemost. Thromb. 34 (2005), pp. 109–120.

[5] F. Ataullakhanov, V. Zarnitsina, A. Pokhilko, A. Lobanov, and O. Morozova, *Spatio-temporal dynamics of blood coagulation and pattern formation. A theoretical approach*, Int. J. Bifur. Chaos 12(9) (2002), pp. 1985–2002.

[6] S. Butenas and K.G. Mann, *Blood coagulation*, Biochemistry (Moscow) 67(1) (2002), pp. 3–12 (translated from Biokhimiya, Vol. 67, No. 1, 2002, pp. 5–15.).

[7] S.E. Charm, and G.S. Kurland, *Viscometry of human blood for shear rates of 0–100,000 sec^{-1}*, Nature 206 (1965), pp. 617–618.

[8] S. Chien, S. Usami, H.M. Taylor, J.L. Lundberg, and M.I. Gregersen, *Effect of hematocrit and plasma proteins on human blood rheology at low shear rates*, J. Appl. Physiol. 21 (1966), pp. 81–87.

[9] S. Chien, S. Usami, R. Dellenback, and M. Gregersen, *Shear-dependent deformation of erythrocytes in rheology of human blood*, Am. J. Physiol. 219 (1970), pp. 136–142.

[10] G. Colantuoni, J. Hellums, J. Moake, and C. Alfre, *The response of human platelets to shear stress at short exposure times*, Trans. Amer. Soc. Artificial Int. Organs 23 (1977), pp. 626–631.

[11] B. Engquist, P. Lötstedt, and B. Sjögreen, *Nonlinear filters for efficient shock computation*, Math. Comput. 52(186) (1989), pp. 509–537.

[12] A.L. Fogelson, *Continuum models of platelet aggregation: Formulation and mechanical properties*, SIAM J. Appl. Math. 52 (1992), pp. 1089–1110.

[13] A. Jameson, *Time dependent calculations using multigrid, with applications to unsteady flows past airfoils and wings*, in *Proceedings of the AIAA 10th Computational Fluid Dynamics Conference, Honolulu*. 1991, June (aIAA Paper 91–1596).

[14] A. Jameson, W. Schmidt, and E. Turkel, *Numerical solutions of the Euler equations by finite volume methods using Runge–Kutta time-stepping Schemes*, in *Proceedings of the AIAA 14th Fluid and Plasma Dynamic Conference, Palo Alto, CA*. 1981, June (aIAA paper 81–1259).

[15] H. Kroll, J. Hellums, L. McIntire, A.I. Schafer, and J. Moake, *Platelets and shear stress*, Blood 88 (1996), pp. 1525–1541.

[16] A.L. Kuharsky and A.L. Fogelson, *Surface-mediated control of blood coagulation: The role of binding site densities and platelet deposition*, Biophys. J. 80 (2001), pp. 1050–1074.

[17] A. Leuprecht and K. Perktold, *Computer simulation of non-Newtonian effects of blood flow in large arteries*, Comput. Meth. Biomech. Biomech. Eng. 4 (2001), pp. 149–163.

[18] K. Mann, K. Brummel-Ziedins, T. Orfeo, and S. Butenas, *Models of blood coagulation*, Blood Cells, Mol. Dis. 36 (2006), pp. 108–117.

[19] S. Nägele and G. Wittum, *On the influence of different stabilisation methods for the incompressible Navier–Stokes equations*, J. Comp. Phys. 224 (2007), pp. 100–116.

[20] K. Rajagopal and J. Lawson, *Regulation of hemostatic system function by biochemical and mechanical factors*, in *Modeling of Biological Materials*. Birkhäuser, Boston, 2007, pp. 179–210.

[21] P. Riha, X. Wang, R. Liao, and J. Stoltz, *Elasticity and fracture strain of blood clots*, Clin. Hemorheol. Microcirc. 21(1) (1999), pp. 45–49.

104 *T. Bodnár and A. Sequeira*

[22] A. Robertson, A. Sequeira, and M. Kameneva, *Hemorheology*, in *Hemodynamical Flows: Modelling, Analysis and Simulation*. Oberwolfach Seminars Series. Birkhäuser, Boston, 2008.

[23] A. Robertson, A. Sequeira, and R. Owens, *Rheological models for blood*, in *Cardiovascular Mathematics*. Springer, Berlin (to appear) 2008.

[24] M. Schenone and B. Furie *The blood coagulation cascade*, Curr. Opin. Hematol. 11 (2004), pp. 272–277.

[25] H. Schmid-Schönbein and R. Wells, *Fluid drop-like transition of erythrocytes under shear*, Science 165 (1969), pp. 288–291.

[26] W. Shyy, M.H. Chen, R. Mittal, and H.S. Udaykumar, *On the suppression of numerical oscillations using a non-linear filter*, J. Comput. Phys. 102 (1992), pp. 49–62.

[27] G.B. Thurston, *Frequency and shear rate dependence of viscoelasticity of human blood*, Biorheology 10 (1973), pp. 375–381.

[28] J. Vierendeels, K. Riemslagh, and E. Dick, *A multigrid semi-implicit line-method for viscous incompressible and low-Mach-number flows on high aspect ratio grids*, J. Comput. Phys. 154 (1999), pp. 310–344.

[29] N. Wang and A.L. Fogelson, *Computational methods for continuum models of platelet aggregation*, J. Comput. Phys. 151 (1999), pp. 649–675.

[30] K. Yeleswarapu, M. Kameneva, K. Rajagopal, and J. Antaki, *The flow of blood in tubes: Theory and experiments*, Mech. Res. Commun. 25(3) (1998), pp. 257–262.

[31] V.I. Zarnitsina, A.V. Pokhilko, and F.I. Ataullakhanov, *A mathematical model for the spatio-temporal dynamics of intrinsic pathway of blood coagulation – I. The model description*, Thromb. Res. 84(4) (1996a), pp. 225–236.

[32] V.I. Zarnitsina, A.V. Pokhilko, and F.I. Ataullakhanov, *A mathematical model for the spatio-temporal dynamics of intrinsic pathway of blood coagulation – II. Results*, Thromb. Res. 84(5) (1996b), pp. 333–344.

B.2   On the Shear–Thinning and Viscoelastic Effects of Blood Flow under Various Flow Rates

The shear-thinning viscosity model suggests that the fluid behaves quite differently depending on the actual shear- resp. flow- rate. This study presents an overview of results obtained for flows in a stenosed vessel under different flow-rates. The solutions are compared, including such parameters like local wall-shear-stress or pressure drop. The generalized Newtonian model was also implemented (in collaboration with M. Prosi) into an open source finite-element code LifeV, that was used to simulate the blood flow in a segment of real blood vessel.

T. Bodnár performed all simulations for the idealized blood vessel using his own finite-volume based code. The flow in the realistic vessel was solved by Martin Prosi, using the modified LifeV finite-element code.

On the shear-thinning and viscoelastic effects of blood flow under various flow rates

T. Bodnár [a,b,*], A. Sequeira [c], M. Prosi [d]

[a] Department of Technical Mathematics, Faculty of Mechanical Engineering, Czech Technical University, Karlovo Náměstí 13, 121 35 Prague 2, Czech Republic
[b] Institute of Thermomechanics, Academy of Sciences of Czech Republic, Dolejškova 5, 182 00 Prague 8, Czech Republic
[c] Department of Mathematics and CEMAT, Instituto Superior Técnico, Av. Rovisco Pais, 1049-001 Lisbon, Portugal
[d] MOX, Modeling and Scientific Computing, Dipartimento di Matematica "F. Brioschi", Politecnico di Milano, Via Bonardi 9, I-20133 Milano, Italy

ARTICLE INFO

ABSTRACT

The aim of this paper is to describe and discuss the results of numerical comparative study performed in order to demonstrate and quantify some of the most relevant non-Newtonian characteristics of blood flow in medium-sized blood vessels, namely its shear-thinning and viscoelastic behavior.

The models studied in this work are the classical Newtonian and Oldroyd-B models, as well as their generalized (shear-thinning) modifications. Numerical tests are performed on three-dimensional geometries, namely an idealized axisymmetric stenosis and a realistic stenosed carotid bifurcation reconstructed from medical images. The numerical solution of the system of governing equations is obtained by a finite-volume method on a structured grid. Model sensitivity tests are achieved with respect to the characteristic flow rate to evaluate its impact on the observed non-Newtonian effects.

© 2010 Elsevier Inc. All rights reserved.

1. Introduction

There is strong evidence that hemodynamical factors such as flow separation, flow recirculation, low and oscillatory wall shear stress, as well as changes in the rheological properties of blood and its components, play a major role in the development and progression of atherosclerotic plaques and other arterial lesions (see e.g. [1–3]). However, their specific role is not completely understood. The mathematical and numerical study of meaningful constitutive models, that can accurately capture the rheological response of blood over a range of physiological flow conditions, is recognized as an invaluable tool for the interpretation and analysis of the circulatory system functionality, in both physiological and pathological situations [4].

Whole blood is a concentrated suspension of formed cellular elements that includes red blood cells (RBCs) or erythrocytes, white blood cells (WBCs) or leukocytes and platelets or thrombocytes. These cellular elements are suspended in an aqueous polymer solution, the plasma, containing electrolytes and organic molecules such as metabolites, hormones, enzymes, antibodies and other proteins [2]. Erythrocytes have been shown to exert the most significant influence on the mechanical properties of blood, mainly due to their presence in very high concentration compared to the other formed elements (approximately $4–6 \times 10^6$ RBC/mm^3), comprising about 40–45% of its volume in healthy individuals (hematocrit).

While plasma is nearly a Newtonian fluid, whole blood exhibits marked non-Newtonian characteristics, in particular at low shear rates, like shear-thinning viscosity, thixotropy, viscoelasticity, and possibly a yield stress. The non-Newtonian behavior of blood is mainly explained by three phenomena: the tendency of erythrocytes to form three-dimensional micro-

---

* Corresponding author at: Department of Technical Mathematics, Faculty of Mechanical Engineering, Czech Technical University, Karlovo Náměstí 13, 121 35 Prague 2, Czech Republic.
E-mail address: rjb@vt.edu (T. Bodnár).

structures (*rouleaux*) at low shear rates, their deformability (or breakup) and their tendency to align with the flow field at high shear rates. When blood is at rest or at low shear rates (below 1 s^{-1}) it seems to have a high apparent viscosity, while at high shear rates there is a reduction in the blood's viscosity. Attempts to recognize the shear-thinning nature of blood were initiated by Chien et al. [5,6] in the 1960s. Empirical models like the power-law, Cross, Carreau or W-S generalized Newtonian fluid models (see [7,8]) have been obtained by fitting experimental data in one dimensional flows. More recently, Vlastos et al. [9] proposed a modified Carreau equation to capture the shear dependence of blood viscosity.

None of the previous homogenized models can predict the viscoelastic response of blood. Blood cells are essentially elastic membranes filled with a fluid and it seems reasonable, at least under certain flow conditions, to expect blood to behave like a viscoelastic fluid. At low shear rates, erythrocytes aggregate and store elastic energy that accounts for the memory effects in blood. At high shear rates, they disaggregate forming smaller rouleaux, and later individual cells, that are characterized by distinct relaxation times. They lose their ability to store elastic energy and the dissipation is primarily due to the internal friction. Thurston [10] was among the earliest to recognize the viscoelastic nature of blood and that the viscoelastic behavior is less prominent with increasing shear rate. Thurston's work (e.g. [11]) was suggested to be more applicable to venous or low shear unhealthy blood flow than to arterial flows. Other viscoelastic constitutive models for describing blood rheology have been proposed in the recent literature. The empirical three constant generalized Oldroyd-B model studied in [12] belongs to this class. It has been obtained by fitting experimental data in one dimensional flows and generalizing such curve fits to three dimensions. This model captures the shear-thinning behavior of blood over a large range of shear rates but it has its limitations, given that the relaxation times do not depend on the shear rate, which does not agree with experimental observations. The model developed by Anand and Rajagopal [13] in the general thermodynamic framework stated in [14] includes relaxation times depending on the shear rate and gives good agreement with experimental data in steady Poiseuille and oscillatory flow.

Non-Newtonian homogeneous continuum models are very significant in hemodynamics and hemorheology. However, it should be emphasized that blood flow is Newtonian in most parts of the arterial system and attention should be drawn to flow regimes and clinical situations where non-Newtonian effects of blood can probably be observed. These include, for normal blood, regions of stable recirculation like in the venous system and parts of the arterial vasculature where geometry has been altered and RBC aggregates become more stable, like downstream a stenosis, inside a saccular aneurysm or in some cerebral anastomoses. In addition, several pathologies are accompanied by significant changes in the mechanical properties of blood and this results in alterations in blood viscosity and viscoelastic properties, as reported in the recent review articles [15,16].

Our purpose in this paper is to present a comparative numerical study of non-Newtonian fluid models capturing shear-thinning and viscoelastic effects of blood flow in idealized and realistic stenosed vessels. Important contributions to this subject have been given by several authors. Among them we cite, for example,[17–19]. The work presented here follows and significantly extends the preliminary results obtained in [20].

2. Mathematical models

As a first step towards the macroscopic modelling of blood flow in 3D regions of the vascular system, we recall the momentum and mass balance laws for incompressible isothermal viscous flows

$$\rho \frac{d\boldsymbol{u}}{dt} = \text{div}\mathbf{T} - \boldsymbol{\nabla} p, \tag{1}$$

$$\text{div}\,\boldsymbol{u} = 0. \tag{2}$$

Here $\boldsymbol{u}$ denotes the velocity field, p is the pressure, ρ is the density and $d(\cdot)/dt = \partial(\cdot)/\partial t + \boldsymbol{u} \cdot \boldsymbol{\nabla}(\cdot)$ denotes the material time derivative. To close the system a constitutive equation relating the extra stress tensor $\mathbf{T}$ with the kinematic variables, velocity and pressure, must be provided. In the case of a Newtonian fluid $\mathbf{T}$ is proportional to the symmetric part of the velocity gradient $\mathbf{D} = (\boldsymbol{\nabla}\boldsymbol{u} + \boldsymbol{\nabla}\boldsymbol{u}^T)/2$, i.e. $\mathbf{T} = 2\mu\mathbf{D}$, where μ is the constant viscosity. Substitution of the value of $\mathbf{T}$ into the Eq. (1) leads to the well-known Navier–Stokes equations (NS) for an incompressible viscous fluid.

2.1. Shear-thinning and viscoelastic models

In order to account for the shear-thinning behavior of blood, the constant viscosity coefficient μ is replaced by a shear rate dependent viscosity function $\mu(\dot{\gamma})$ where *shear rate* is defined by $\dot{\gamma} = 2\sqrt{\mathbf{D} : \mathbf{D}}$. This function can be written in the following general form

$$\mu(\dot{\gamma}) = \mu_\infty + (\mu_0 - \mu_\infty)F(\dot{\gamma}) \tag{3}$$

or, in non-dimensional form as

$$\frac{\mu(\dot{\gamma}) - \mu_\infty}{\mu_0 - \mu_\infty} = F(\dot{\gamma}). \tag{4}$$

Here μ_0 and μ_∞ are the asymptotic viscosity values at zero and infinite shear rates. The appropriate transition between these values is carried out by the shear rate dependent function $F(\dot{\gamma})$ which satisfies the limit conditions

$$\lim_{\dot{\gamma}\to 0^+} F(\dot{\gamma}) = 1 \quad \text{and} \quad \lim_{\dot{\gamma}\to\infty} F(\dot{\gamma}) = 0.$$

There are many possible choices for such a function $F(\dot{\gamma})$. One of the most frequently used shear-thinning models for blood is the generalized *Cross* model given by

$$\mu(\dot{\gamma}) = \mu_\infty + \frac{\mu_0 - \mu_\infty}{\left(1 + (\lambda\dot{\gamma})^b\right)^a}. \tag{5}$$

Blood viscosity is quite sensitive to several factors including hematocrit, temperature, plasma viscosity, age of RBCs, gender, healthy or disease state, which have a remarkable influence in the choice of parameters in the selected constitutive model, obtained by calibration against suitable experimental data. The following parameters found in [21] have been used for the blood flow simulations presented in this paper:

$$\mu_0 = 1.6 \cdot 10^{-1}\,\text{Pa}\cdot\text{s} \quad \mu_\infty = 3.6 \cdot 10^{-3}\,\text{Pa}\cdot\text{s},$$
$$a = 1.23, \quad b = 0.64 \quad \lambda = 8.2\,\text{s}.$$

The viscosity function $F(\dot{\gamma})$ is represented in Fig. 1.

It is important to remark the huge difference between the viscosity values μ_0 and μ_∞. The ratio $\mu_0/\mu_\infty \approx 50$ (see Section 5.1 for further details).

To account for the viscoelasticity of blood we consider the equations for the conservation of linear momentum (1) and mass (2) where the extra stress tensor **T** is decomposed into its Newtonian part $\mathbf{T}_s$ and its elastic part $\mathbf{T}_e$, $\mathbf{T} = \mathbf{T}_s + \mathbf{T}_e$, such that

$$\mathbf{T}_s = 2\mu_s(\dot{\gamma})\mathbf{D} \tag{6}$$

and $\mathbf{T}_e$ satisfies a constitutive equation of Oldroyd-B type, namely

$$\frac{\partial \mathbf{T}_e}{\partial t} + (\boldsymbol{u}\cdot\nabla)\mathbf{T}_e = \frac{2\mu_e}{\lambda_1}\mathbf{D} - \frac{1}{\lambda_1}\mathbf{T}_e + (\mathbf{W}\mathbf{T}_e - \mathbf{T}_e\mathbf{W}) + (\mathbf{D}\mathbf{T}_e + \mathbf{T}_e\mathbf{D}). \tag{7}$$

Here **D** and **W** denote the symmetric and antisymmetric parts of the velocity gradient related to local shear, resp. vorticity (see e.g. [22]). The μ_e denotes the elastic viscosity coefficient and λ_1 is the relaxation time. We consider $\mu_e = 4.0 \cdot 10^{-4}\,\text{Pa}\cdot\text{s}$ and $\lambda_1 = 0.06\,\text{s}$ (according to [21]). For the more detailed description of the models and their parameters see e.g. [20]. The following four special parameters settings related to four specific models will be used in our numerical simulations:

Newtonian (NS) $\mu_s(\dot{\gamma}) = \mu_\infty$ $\mathbf{T}_e \equiv 0$,
Generalized Newtonian (GNS) $\mu_s(\dot{\gamma})$ $\mathbf{T}_e \equiv 0$,
Oldroyd-B (OB) $\mu_s(\dot{\gamma}) = \mu_\infty$ $\mathbf{T}_e$,
Generalized Oldroyd-B (GOB) $\mu_s(\dot{\gamma})$ $\mathbf{T}_e$.

These equations are solved for the variables velocity, pressure and shear stress, provided the viscosity function, flow parameters and appropriate boundary conditions are given.

With respect to boundary conditions for the Navier–Stokes and generalized Navier–Stokes equations, it is necessary to prescribe either the velocity or the surface traction force (Dirichlet or Neumann boundary conditions, respectively) at the inflow boundary. Usually, physiological data are not available and a fully developed Poiseuille velocity profile (or the Womersley solution, in the unsteady case) can be prescribed. This is an acceptable idealization of the inflow condition in relatively long straight vessel segments. At the outflow boundary, a condition prescribing surface traction force can be applied and at the vessel wall, the no-slip condition is appropriate.
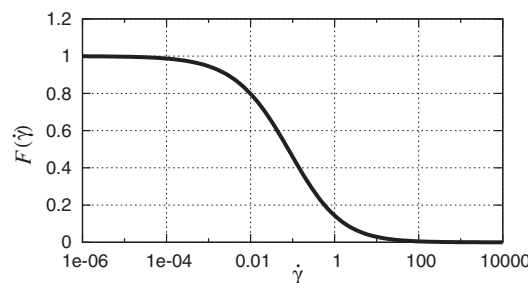

Fig. 1. Viscosity function.

The Oldroyd-B and generalized Oldroyd-B models are of mixed elliptic-hyperbolic type (or parabolic–hyperbolic, in the unsteady case). The extra stresses behave hyperbolic, which means that they are only determined by past time. For these models the boundary conditions are the same as for the Navier–Stokes and generalized Navier–Stokes equations. The stress prescribed at the inflow is in this case only determined by the processes upwind from the inlet and thus represents in some sens the fluid memory [22,35,36].

3. Numerical methods

The numerical solutions of the governing systems of PDEs are based on a finite-volume space discretization on structured grids, and an explicit Runge–Kutta time integration scheme. Numerical fluxes are evaluated in a centered way for both inviscid and viscous parts. To avoid numerical oscillations a pressure stabilization technique proposed in [23] has been implemented. We look for steady solutions by a time-marching approach, i.e. the unsteady governing systems are solved with steady boundary conditions and stationary solutions are recovered when $t \to \infty$. Details on the space and time discretization procedures are described in [24–26,20,27].

Assuming that the system of governing equations has been discretized in space, e.g. using the above mentioned finite-volume method, we obtain a system of ODE's of the form

$$W_t = \mathcal{L}(t, W(t)), \tag{8}$$

where $W = W(t)$ is the vector of discretized variables, and $\mathcal{L}$ stands for the space differentiation operator.

System (8) describes the evolution in time of the discrete grid values of the unknown flow variables. In order to solve the initial value problem based on this system of ODE's, virtually any of the methods originaly developed for ODE's could be used. There is an enormous amount of specialized literature dealing with various aspects of the numerical solution of ODE's. Among others we mention e.g. [28,29] and references cited therein.

In this study the time integration is carried out by an explicit Runge–Kutta method. From the definition of the multistage Runge–Kutta methods it is obvious that these methods require multiple evaluations of the operator $\mathcal{L}$ within a single time-step. In the case discussed here, $\mathcal{L}$ is a space discretization operator which is based on the original system of PDE's and the selected discretization method. The construction of this operator is often quite complicated and the amount of computational work increases rapidly with the number of stages of the applied RK method. This disadvantage is usualy compensated by the higher accuracy or higher stability of multistage methods. However, in specific cases, it is possible to reduce the amount of computational work per RK stage and, at the same time, improve the stability of the method. The approach presented here is designed for the numerical solution of advection–diffusion equations. The main idea behind this specific modification of RK methods is that the discrete advection–diffusion operator $\mathcal{L}$ could be splitted into its advection and diffusion parts and, instead of evaluating the full operator $\mathcal{L}(W^{(r)})$ at each stage of RK method, only a part of $\mathcal{L}$ is updated at each stage (e.g. the advection part for advection dominated problems), while the value of the remaining (diffusion) part of $\mathcal{L}$ is kept frozen from the previous RK stage.

$$
\begin{aligned}
W^{(0)} &= W^n, \\
W^{(r+1)} &= W^{(0)} - \alpha_{(r)} \Delta t \left(\mathcal{Q}^{(r-1)} + \mathcal{D}^{(r-1)} \right) \quad r = 1, \ldots, s, \\
W^{n+1} &= W^{(s)}.
\end{aligned}
\tag{9}
$$

Here the space discretization operator at stage (r) is split as follows:

$$\mathcal{L}W^{(r)} = \mathcal{Q}^{(r)} + \mathcal{D}^{(r)}. \tag{10}$$

The inviscid (advection) flux $\mathcal{Q}$ is evaluated in the usual way at each stage

$$\mathcal{Q}^{(r)} = \mathcal{Q}W^{(r)}. \tag{11}$$

The viscous (diffusive) flux $\mathcal{D}$ uses a blended value from the previous stage and the actual stage according to the rule

$$\mathcal{D}^{(r)} = \beta_{(r)} \mathcal{D}W^{(r)} + (1 - \beta_{(r)}) \mathcal{D}^{(r-1)} \quad \text{with } \mathcal{D}^{(0)} = \mathcal{D}W^n. \tag{12}$$

The coefficients $\alpha_{(r)}$ and $\beta_{(r)}$ are chosen to guarantee a large enough stability region for the Runge–Kutta method. The following set of coefficients was used in this study:ing set of coefficients was used in this study:

$$
\begin{aligned}
\alpha_{(1)} &= 1/3 & \beta_{(1)} &= 1, \\
\alpha_{(2)} &= 4/15 & \beta_{(2)} &= 1/2, \\
\alpha_{(3)} &= 5/9 & \beta_{(3)} &= 0, \\
\alpha_{(4)} &= 1 & \beta_{(4)} &= 0.
\end{aligned}
$$

It is easy to see that for this four-stage method only two evaluations of the dissipative terms are needed, which saves a significant amount of calculations while retaining the advantage of a large stability region. Further admissible sets of

coefficients can be used to improve the stability of the method. Comments on the efficiency and robustness of these methods can be found in the original papers [30,31] and the references therein.

4. Numerical simulations

4.1. Test geometry

Numerical tests have been performed in an idealized stenosed vessel and applied in a realistic stenosed carotid bifurcation reconstructed from medical images (Section 5.3). The stenosed vessel is assumed to be three-dimensional with circular cross-section (see Figs. 2 and 3). The nominal vessel diameter is $D = 2R = 6.2$ mm which reduces smoothly to one half in the stenosed region. The stenosis cross-sectional area ratio is 4:1 and thus a significant local acceleration of the flow is expected.

4.2. Computational grid

The computational domain is discretized using a structured, wall fitted mesh with hexahedral cells and uniform axial cell spacing. Multiblock mesh structure was adopted to avoid high distortion of cells, see Fig. 3.

The outer mesh block has $40 \times 16 \times 80$ cells, while the central mesh block has $10 \times 10 \times 80$ control volumes.

4.3. Model parameters

Numerical simulations have been obtained under physiological conditions, using the values already introduced in Section 2.1 for the Cross model, as well as the following parameters used for blood flow in a carotid artery (see [21]):

$$\mu_e = 4.0 \cdot 10^{-4} \text{ Pa} \cdot \text{s} \quad \mu_s = 3.6 \cdot 10^{-3} \text{ Pa} \cdot \text{s},$$
$$\mu_0 = \mu = \mu_s + \mu_e \quad \mu_\infty = \mu_s,$$
$$\lambda_1 = 0.06 \text{ s} \quad \rho = 1050 \text{ kg} \cdot \text{m}^{-3}.$$

Using these data, fully developed Poiseuille velocity profile (for Newtonian fluid) is prescribed at the inlet (Dirichlet condition). The flow rates are set to three different values $Q = 0.5, 1.0, 2.0$ cm^3/s. At the outlet homogeneous Neumann conditions for the velocity components and a constant pressure are prescribed. On the vessel walls no-slip homogeneous Dirichlet conditions are prescribed for the velocity field. In the case of the Oldroyd-B and generalized Oldroyd-B models, homogeneous Neumann conditions are imposed for the components of the extra stress tensor at all boundaries.

5. Numerical results

We use the models described in Section 2.1 to investigate the influence of the shear-thinning and viscoelastic effects on the behavior of blood in different flow situations. To highlight these non-Newtonian effects, the solution of the NS equations, obtained under the same conditions as the solutions of the non-Newtonian equations, is used as a reference for direct flow field comparison. The only change is the viscosity which was kept constant (equal to μ_∞) and the extra stress $\mathbf{T}_e = 0$. Numerical simulations were performed and compared for all four models, i.e. for the Newtonian (NS) and generalized Newtonian (GNS) models, and for the Oldroyd-B (OB) and generalized Oldroyd-B (GOB) models.

5.1. Viscosity distribution

In order to get more insight into the nature of non-Newtonian shear-thinning effects it is necessary to evaluate the influence of variable viscosity in the flow situations of practical interest.

The non-Newtonian behavior originates from the changes in local viscosity which depend on shear rate, as discussed in Section 2.1. The characteristic shear rate varies depending on flow rate. For a given geometry, higher flow rates lead to higher
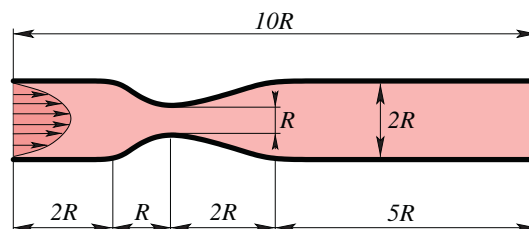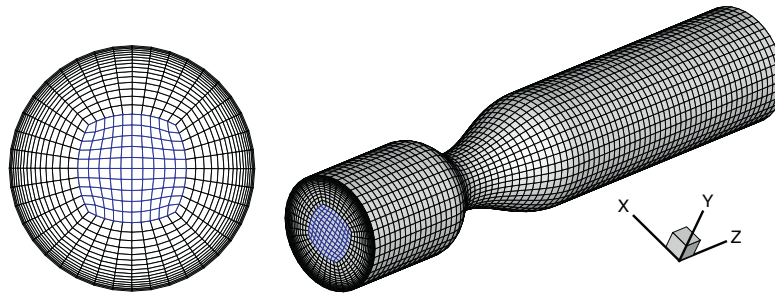

Fig. 2. Stenosis.

Fig. 3. Computational grid structure.

shear rates. It is easy to see that in the case of Poiseuille flow (fully developed steady flow in a straight tube) the viscosity attains its maxima μ_0 at the centerline, while the minimum value is reached at the wall.

Fig. 4 shows the variation of the apparent viscosity of blood as a function of the shear rate, for the generalized Cross model (5) with the physiological parameters given in Section 2.1.

Defining the relative non-Newtonian extra viscosity $\bar{\mu} = (\mu(\dot{\gamma}) - \mu_\infty)/\mu_\infty$, which measures the deviation of the local shear-thinning viscosity from the Newtonian one, we can observe three distinct ranges of values for the apparent viscosity, marked with a color scale and separated by two important viscosity values. The value $\bar{\mu} = 1$ refers to the regions where the actual viscosity is the double of the original Newtonian value μ_∞. While moving away from $\dot{\gamma} = 0$ the viscosity changes quickly, and this can be characterized, for example, by the value where $\bar{\mu} = 10$. The maximum value of the viscosity is, in our case, $\bar{\mu} = (\mu_0 - \mu_\infty)/\mu_\infty \doteq 45$. These two characteristic viscosity values split the whole viscosity range into three regions with different characteristics:

(i) $0 \leqslant \bar{\mu} \leqslant 1$ Low-viscosity region which can be described as "pseudo-Newtonian" region with characteristic viscosity μ_∞.
(ii) $1 \leqslant \bar{\mu} \leqslant 10$ Higher non-Newtonian viscosity region (with viscosity $\mu(\dot{\gamma})$) having strong shear rate dependency.
(iii) $10 \leqslant \bar{\mu} \leqslant 45$ High-viscosity region which can be characterized by low shear rate viscosity μ_0.

Based on the above viscosity field classification we can explore a wider range of shear rates, varying the flow rate. The original value is $Q_0 = 1$ cm^3/s and simulations have been performed for the flow rates corresponding to $Q = 2, 1, 0.5$ cm^3/s.

At this point it is good to mention here the fact that in the case of Poiseuille flow (i.e. fully developed steady flow in a straight tube), the shear rate $\dot{\gamma} = 0$ at the axis of the pipe, while it's maxima is achieved at the wall, where the shear is most apparent due to the no-slip condition. Thus in undisturbed pipe flow, the shear-thinning viscosity theoreticaly reaches it's maxima μ_0 at the center axis of the pipe, while the apparent viscosity reduces towards the wall, where it's minima (depending on the actual flow rate) is reached. This situation is however significantly modified when considering more complicated geometry as in the case discussed here.

Axial contours of the $\bar{\mu}$ viscosity in the idealized axisymmetric stenosis are shown in Fig. 5 as a result of the generalized Newtonian (GNS) model simulation. It is evident that with decreasing flow rate the non-Newtonian shear-thinning effects become more pronounced. On the other hand in the basic case with flow rate $Q/Q_0 = 1$ the only non-Newtonian effects could be observed close to the entry (due to the prescribed "Newtonian" inlet velocity profile), in the center of the vessel just behind the stenosis and at the boundary of reversal flow region within the recirculation zone. Increasing shear-thinning and viscoelastic effects for decreasing flow rate values could also be observed in Figs. 10–12.
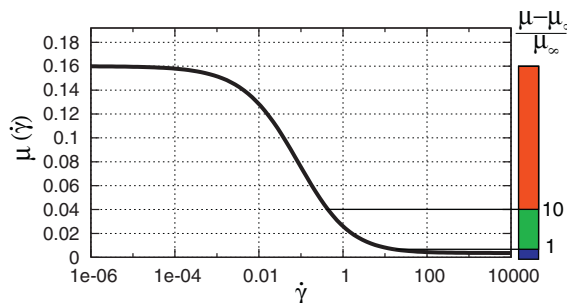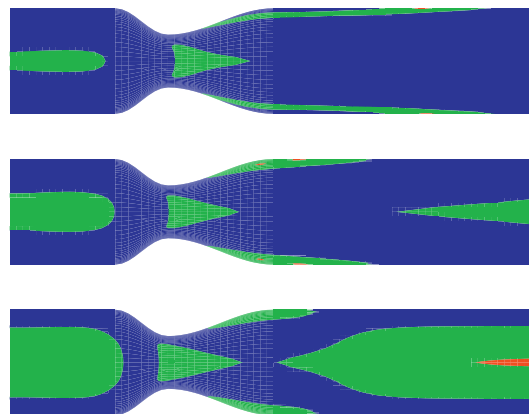

Fig. 4. Viscosity distribution.

Fig. 5. Contours of the renormalized viscosity $\tilde{\mu}$ in the symmetry plane for flow rates (from top) Q = 2.0, 1.0, 0.5 cm³/s.

5.2. Flow field (idealized vessel)

Figs. 6–9 present a comparison of the axial velocity contours corresponding to the four models, with the flow rate Q = 1.0 cm³/s. To emphasize the flow separation behind the stenosis the regions of reversal flow (with respect to axial direction) are marked with white color.

These results clearly show that for shear-thinning flows the recirculation zone becomes shorter. This is easy to understand, because the characteristic viscosity in the Newtonian case is the μ_∞ and thus a shear-thinning viscosity of the form (5), leads to the increase of the local viscosity in the low shear regions. Other choices of the characteristic viscosity for the Newtonian model may give significantly different results.

The combined shear-thinning and viscoelastic effects can be depicted by observing the difference between the generalized Oldroyd-B (GOB) and the Navier–Stokes (NS) solutions. Figs. 10–12 present the contours of the normalized difference between these two solutions at various flow rates. The quantity plotted is $(u_{GOB} - u_{NS})/U_0$, where U_0 is the maximum inlet velocity (negative isolines are drawn by a dashed line).
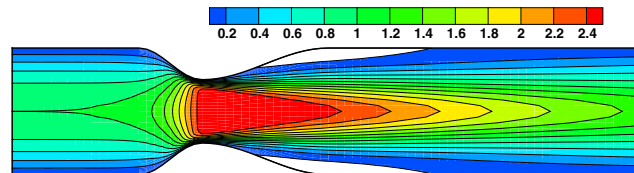
Fig. 6. Axial velocity contours for the Newtonian (NS) fluid with constant viscosity μ_∞ and flow rate Q = 1.0 cm³/s.
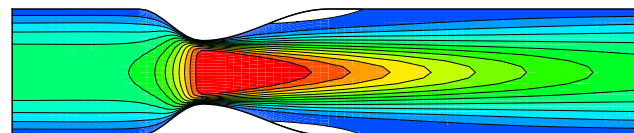
Fig. 7. Axial velocity contours for the generalized Newtonian (GNS) fluid with variable (shear-thinning) viscosity and flow rate Q = 1.0 cm³/s.
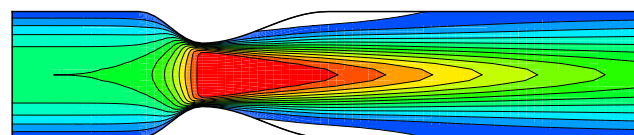
Fig. 8. Axial velocity contours for the (viscoelastic) Oldroyd-B (OB) fluid with constant viscosity μ_∞ and flow rate Q = 1.0 cm³/s.
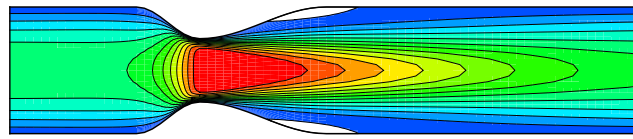
Fig. 9. Axial velocity contours for the generalized Oldroyd-B (GOB) fluid with variable (shear-thinning) viscosity and flow rate $Q = 1.0 \text{ cm}^3/\text{s}$.
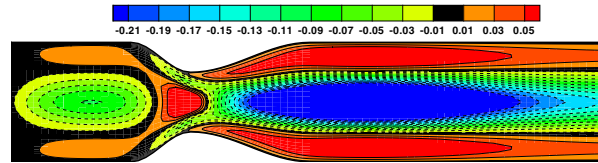
Fig. 10. Normalized difference between the solutions of GOB and NS models with flow rate $Q = 0.5 \text{ cm}^3/\text{s}$.
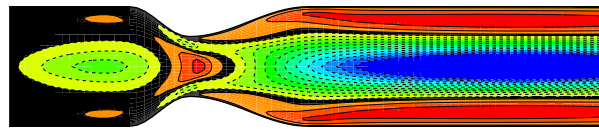
Fig. 11. Normalized difference between the solutions of GOB and NS models with flow rate $Q = 1.0 \text{ cm}^3/\text{s}$.
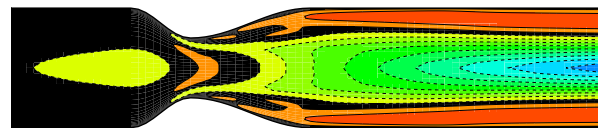

Fig. 12. Normalized difference between the solutions of GOB and NS models with flow rate $Q = 2.0 \text{ cm}^3/\text{s}$.

This comparison again shows the significant increase of the non-Newtonian shear-thinning effects as the flow rate (and thus the characteristic shear rate) decreases. As it was already mentioned, this is related to the choice of the characteristic viscosity in the Newtonian case. At higher flow rates the viscosity is close to μ_∞ (see Section 5.1 and Fig. 5) and thus the results obtained with a shear-thinning model are close to the Newtonian model solution.

In blood flow experiments blood pressure can easily be measured, in particular the pressure drop (i.e. the inlet–outlet pressure difference) needed to achieve a prescribed flow rate. The axial pressure profiles for all four models at various flow rates are shown in Fig. 13. By simple observation we conclude that the main effect of the blood shear-thinning behavior is visible mainly in the recirculation zone, where the local viscosity (and thus the resistance to flow) increases significantly. The effects of viscoelasticity are about one order of magnitude lower in this case. This conclusion however has just a limited validity for the given test case. For other cases, i.e. for pulsatile flow or other flow rates or geometries, the viscoelastic effects may become more important. Similar conclusions could be drawn from the observation of the axial velocity profiles depicted in Fig. 14.

Another important parameter in blood flow simulations is the wall shear stress (WSS). It represents the tangential component of the surface force at the vessel wall, acting against the fluid flow.

$$\text{WSS} := -(\mathbf{T} \cdot \hat{n}) \cdot \hat{t}. \tag{13}$$

Here $\hat{n}$ is the local wall-normal unit vector (pointing towards the fluid) and $\hat{t}$ is the corresponding unit tangential vector. The wall shear stress profiles for all the models at various flow rates are shown in Fig. 15. The negative values of the WSS can be found in regions of reversal flow and also in regions where the flow speeds up significantly.

5.3. Realistic stenosed bifurcation model

This test case has been selected to show the presence of non-Newtonian effects on blood flow behavior in a realistic geometry reconstructed fom medical images. The computational domain corresponds to a human carotid bifurcation artery
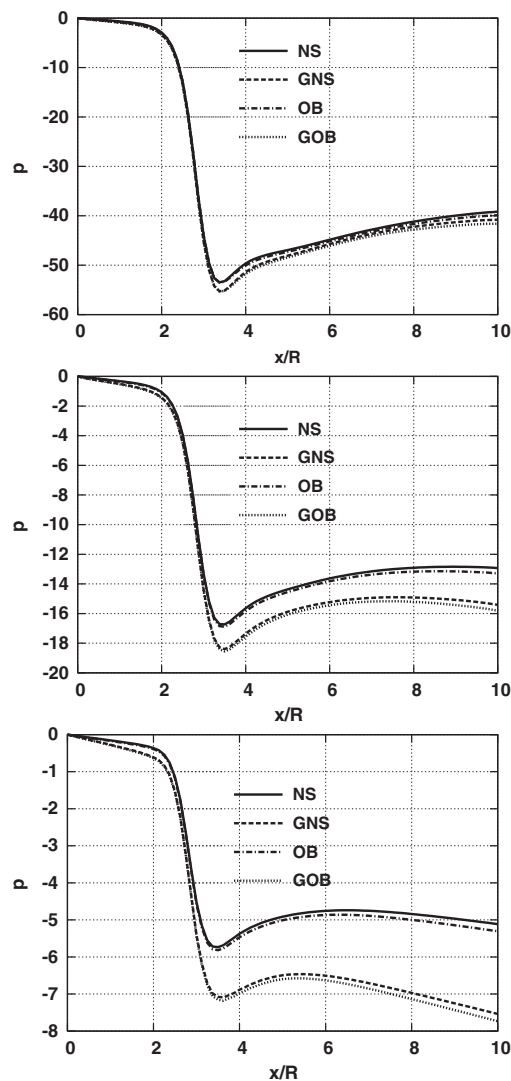
Fig. 13. Pressure distribution along the axis of the vessel for the flow rates (from top) $Q = 2.0, 1.0, 0.5$ cm^3/s.

with a stenosis, as shown in Fig. 16. The geometrical model of the healthy bifurcation (without stenosis) has been developed by Perktold (TU Graz) based on a digitalized experimental cast (Liepsch and Munich). For details of the geometry see [32]. A stenosis of 75% has been generated in the internal carotid artery near the bifurcation region where stenotic obstructions related to atherosclerosis usually occur. For the discretization of the geometrical model we use tetrahedral elements. The numerical solution of the Navier–Stokes equations is based on a velocity pressure splitting scheme with algebraic factorization implemented in the open source finite element library LifeV (http://www.lifev.org). A detailed description of the numerical method can be found in [33] or [34].

The main goal is to investigate shear-thinning effects in steady flow simulations, using the Newtonian and generalized Cross models (Section 2.1). The shear-thinning viscosity parameters we use in this study are the physiological values used in the previous test case (Section 2.1). The flow rate of 5.5 cm^3/s imposed at the commmon carotid artery corresponds to the mean physiologic flow rate. Together with the mean inflow diameter of 0.62 cm this results in a Reynolds number of $Re = 300$ in the Newtonian case. The difference between Newtonian and non-Newtonian solution in these simulations can be observed comparing the wall shear stress distributions in the stenosed region, depicted in Figs. 17 and 18.

The same color scale is used in both figures, showing that the higher wall shear stress values are in the stenosed region predicted by the generalized Navier–Stokes model. Also in the curved part of the upper branch the wall shear stress seems to
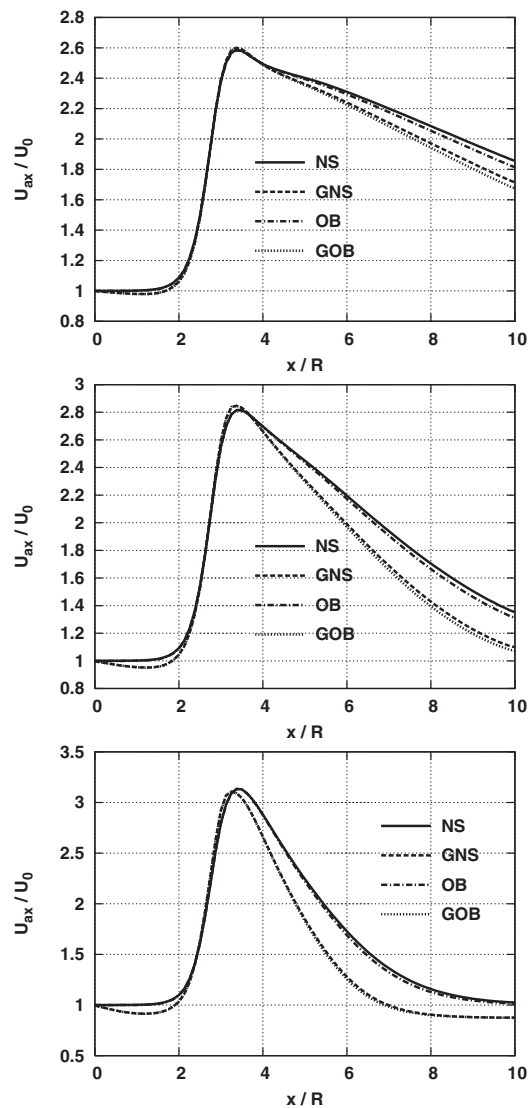
Fig. 14. Normalized velocity distribution along the axis of the vessel for the flow rates (from top) $Q = 2.0, 1.0, 0.5$ cm^3/s.

be higher in the shear-thinning case. The reason for this can clearly be confirmed by the results of the viscosity distribution shown in Fig. 19. We conclude that the non-uniform viscosity distribution leads to important discrepancies between Newtonian and generalized Newtonian model predictions. Therefore, in complex flow situations, it is of major importance to better understand the influence of the viscosity distribution in complex flow situations.

6. Conclusions and final remarks

Classical Newtonian and Oldroyd-B models, as well as their generalized (shear-thinning) modifications have been considered to model blood flow in an idealized axisymmetric stenosis and in a realistic stenosed carotid bifurcation vessel, to investigate shear-thinning and viscoelastic effects in steady flow simulations.

Based on the above computation results we conclude that shear-thinning effects related to the flow variables (velocity and pressure) and to WSS are more pronounced than the viscoelastic ones and they are predominant in the recirculation zone downstream the stenosis, increasing as the flow rate (and consequently the shear rate) decreases. This could be explained by the specific choice of the characteristic viscosity μ_∞ for the reference Newtonian and (non-generalized)
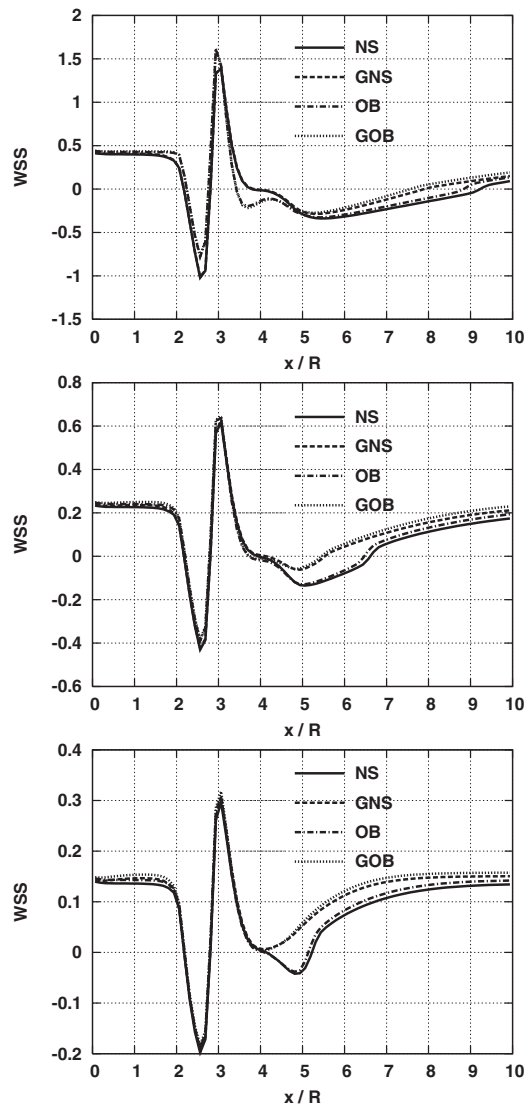
Fig. 15. Wall shear stress (WSS) distribution along the axis of the vessel for the flow rates (from top) $Q = 2.0, 1.0, 0.5$ cm^3/s.
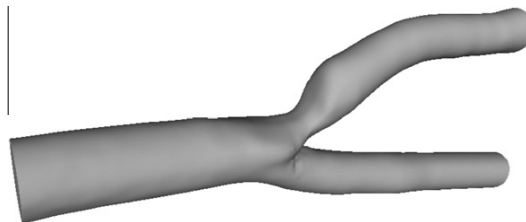
Fig. 16. Stenosed carotid bifurcation geometry.

Oldroyd-B solution. For low shear rates the apparent viscosity is in the large part of the vessel close to the value μ_0 and thus the differences from the Newtonian solution (obtained for the viscosity μ_∞) are larger than in the case of high flow rate.
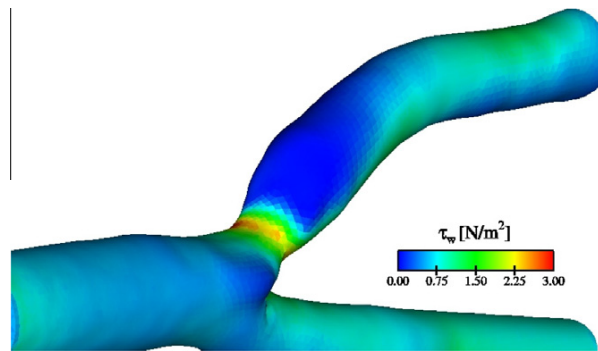
Fig. 17. Wall shear stress magnitude distribution in the Newtonian case.
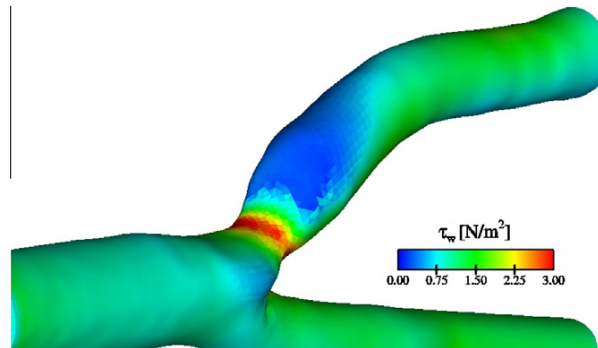
Fig. 18. Wall shear stress magnitude distribution in the generalized Newtonian case.
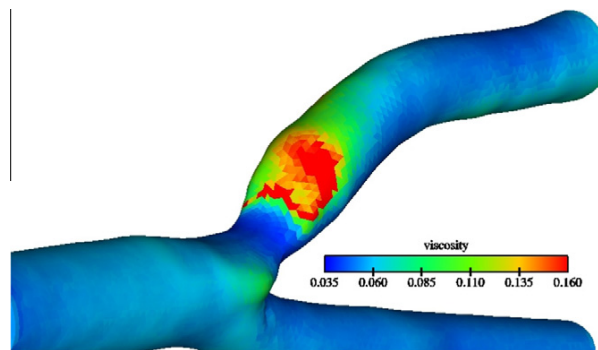
Fig. 19. Shear-thinning viscosity contours at the bifurcation surface.

The numerical method used to solve the governing equations seems to be sufficiently robust and efficient for the appropriate resolution of the given class of problems.

Future work will be devoted to an extension of this numerical study to unsteady blood flow and fluid-structure interaction simulations in stenotic vessels, to provide a deeper understanding of the significance of the non-Newtonian characteristics of blood and its correlation with the atherosclerosis.

Acknowledgements

References

[1] S.A. Berger, L.D. Jou, Flows in stenotic vessels, Annual Review of Fluid Mechanics 32 (2000) 347–382.
[2] C.G. Caro, T.J. Pedley, R.C. Schroter, W.A. Seed, The Mechanics of the Circulation, Oxford University Press, 1978.
[3] C. Verdier, Rheological properties of living materials from cells to tissues, Journal of Theoretical Medicine 5 (2) (2003) 67–91.
[4] D. Lowe, Clinical Blood Rheology, vol. I, II, CRC Press, Boca Raton, Florida, 1998.
[5] S. Chien, S. Usami, R.J. Dellenback, M.I. Gregersen, Blood viscosity: influence of erythrocyte aggregation, Science 157 (3790) (1967) 829–831.
[6] S. Chien, S. Usami, R.J. Dellenback, M.I. Gregersen, Blood viscosity: influence of erythrocyte deformation, Science 157 (3790) (1967) 827–829.
[7] R.B. Bird, R.C. Armstrong, O. Hassager, Dynamics of Polymeric Liquids, vol. 1, second ed., John Willey & Sons, 1987.
[8] F.J. Walburn, D.J. Schneck, A constitutive equation for whole human blood, Biorheology 13 (1976) 201–210.
[9] G. Vlastos, D. Lerche, B. Koch, The superposition of steady on oscillatory shear and its effect on the viscoelasticity of human blood and a blood-like model fluid, Biorheology 34 (1997) 19–36.
[10] G.B. Thurston, Viscoelasticity of human blood, Biophysical Journal 12 (1972) 1205–1217.
[11] G.B. Thurston, Non-Newtonian viscosity of human blood: flow induced changes in microstructure, Biorheology 31 (2) (1994) 179–192.
[12] K.K. Yeleswarapu, M.V. Kameneva, K.R. Rajagopal, J.F. Antaki, The flow of blood in tubes: theory and experiment, Mechanics Research Communications 25 (1998) 257–262.
[13] M. Anand, K.R. Rajagopal, A shear-thinning viscoelastic fluid model for describing the flow of blood, International Journal of Cardiovascular Medicine and Science 4 (2) (2004) 59–68.
[14] K. Rajagopal, A. Srinivasa, A thermodynamic frame work for rate type fluid models, Journal of Non-Newtonian Fluid Mechanics 80 (2000) 207–227.
[15] A.M. Robertson, A. Sequeira, M.V. Kameneva, Hemorheology, in: G. Galdi, R. Rannacher, A.M. Robertson, S. Turek (Eds.), Hemodynamical Flows: Modeling Analysis and Simulation, Oberwolfach Seminars, vol. 37, Birkhäuser Verlag, 2008, pp. 63–120.
[16] A.M. Robertson, A. Sequeira, R.G. Owens, Rheological models for blood, in: L. Formaggia, A. Quarteroni, A. Veneziani (Eds.), Cardiovascular Mathematics: Modeling and Simulation of the Circulatory System, MS & A, Modeling, Simulations & Applications, vol. 1, Springer-Verlag, 2009, pp. 211–241.
[17] F. Gijsen, F. van de Vosse, J. Janssen, The influence of the non-Newtonian properties of blood on the flow in large arteries: steady flow in a carotid bifurcation model, Journal of Biomechanics 32 (1999) 601–608.
[18] P.D. Bailyk, D.A. Steinman, C.R. Ethier, Simulation of non-Newtonian blood flow in an end-to-side anastomosis, Biorheology 31 (5) (1994) 565–586.
[19] J. Chen, X. Lu, Numerical investigation of the non-Newtonian pulsatile blood flow in a bifurcation model with a non-planar branch, Journal of Biomechanics 39 (2006) 818–832.
[20] T. Bodnár, A. Sequeira, Numerical study of the significance of the non-newtonian nature of blood in steady flow through a stenosed vessel, in: R. Rannacher, A. Sequeira (Eds.), Advances in Mathematical Fluid Mechanics, Springer-Verlag, 2010, pp. 83–104.
[21] A. Leuprecht, K. Perktold, Computer simulation of non-Newtonian effects of blood flow in large arteries, Computer Methods in Biomechanics and Biomechanical Engineering 4 (2001) 149–163.
[22] D.D. Joseph, Fluid Dynamics of Viscoelasic Liquids, Applied Mathematical Sciences, vol. 84, Springer-Verlag, 1990.
[23] J. Vierendeels, K. Riemslagh, E. Dick, A multigrid semi-implicit line-method for viscous incompressible and low-mach-number flows on high aspect ratio grids, Journal of Computational Physics 154 (1999) 310–344.
[24] T. Bodnár, A. Sequeira, Shear-thinning effects of blood flow past a formed clot, WSEAS Transactions on Fluid Mechanics 1 (3) (2006) 207–214.
[25] T. Bodnár, J. Příhoda, Numerical simulation of turbulent free-surface flow in curved channel, Journal of Flow, Turbulence and Combustion 76 (4) (2006) 429–442.
[26] T. Bodnár, A. Sequeira, Numerical simulation of the coagulation dynamics of blood, Computational and Mathematical Methods in Medicine 9 (2) (2008) 83–104.
[27] L. Beneš, K. Kozel, I. Sládek, Numerical simulation of influence of various types obstacles on dustiness of coal depot, Engineering Mechanics 13 (2) (2006) 201–212.
[28] J.C. Butcher, Numerical Methods for Ordinary Differential Equations, John Wiley & Sons, 2003.
[29] J.C. Dormand, Numerical Methods for Differential Equations – A Computational Approach, JRC Press, 1996.
[30] A. Jameson, W. Schmidt, E. Turkel, Numerical solutions of the Euler equations by finite volume methods using Runge-Kutta time-stepping schemes, in: AIAA 14th Fluid and Plasma Dynamic Conference, Palo Alto, 1981, aIAA paper 81-1259.
[31] A. Jameson, Time dependent calculations using multigrid, with applications to unsteady flows past airfoils and wings, in: AIAA 10th Computational Fluid Dynamics Conference, Honolulu, 1991, aIAA Paper 91-1596.
[32] G. Karner, K. Perktold, M. Hofer, D. Liepsch, Flow characteristic in anatomically realistic complian carotid artery bifurcation model, Computer Methods in Biomechanics and Biomechanical Engineering 2 (1999) 171–185.
[33] A. Quarteroni, F. Saleri, A. Veneziani, Factorization methods for the numerical approximation of the Navier–Stokes equations, Computer Methods in Applied Mechanics and Engineering 188 (2000) 505–526.
[34] A. Veneziani, Block factorized preconditioners for high-order accurate in time approximation of the Navier–Stokes equations, Numerical methods for Partial Differential Equations 19 (2003) 487–510.
[35] A.M. Grillet, A.C.B. Bogaerds, G.W.M. Peters, F.P. Baaijens, Stability analysis of constitutive equations for polymer melts in viscometric flows, Journal of Non-Newtonian Fluid Mechanics 103 (2002) 221–250.
[36] V. Bertola, E. Cafaro, Analogy between pipe flow of non-newtonian fluids and 2-d compressible flow, Journal of Non-Newtonian Fluid Mechanics 109 (2002) 1–12.

B.3   Simulation of the Three–Dimensional Flow of Blood Using a Shear–Thinning Viscoelastic Fluid Model

Bodnár T., Rajagopal K.R., Sequeira A.

This paper contains an overview of numerical results obtained using a new nonlinear viscoelastic model proposed recently by Anand and Rajagopal [B.1] based on the general thermodynamic framework postulated in [B.10]. This naturally shear-thinning model created especially for blood flow simulations is compared with the generalized Oldroyd-B model. This paper is a first attempt to use this new model for practical 3D simulations. A significant effort has been made to convert the model into a more standard notation that will allow for a detailed comparison with some other classical models. Some new techniques had to be developed to use this model. This part of the work still remains to be published in the near future.

In this paper T. Bodnár rewrote the new model (proposed by K.R. Rajagopal) into the standard form and performed all the presented numerical simulations using his own original finite-volume code.

Simulation of the Three-Dimensional Flow of Blood Using a Shear-Thinning Viscoelastic Fluid Model

T. Bodnár[1], K.R. Rajagopal [2] and A. Sequeira[3] *

[1] Department of Technical Mathematics, Faculty of Mechanical Engineering
Czech Technical University, Náměstí 13, 121 35 Prague 2, Czech Republic
[2] Department of Mechanical Engineering, Texas A & M University
College Station, TX 77843-3123, USA
[3] Department of Mathematics and CEMAT/IST, Instituto Superior Técnico
Technical University of Lisbon, Av. Rovisco Pais 1, 1049-001 Lisboa, Portugal

Abstract. This paper is concerned with the numerical simulation of a thermodynamically compatible viscoelastic shear-thinning fluid model, particularly well suited to describe the rheological response of blood, under physiological conditions. Numerical simulations are performed in two idealized three-dimensional geometries, a stenosis and a curved vessel, to investigate the combined effects of flow inertia, viscosity and viscoelasticity in these geometries. The aim of this work is to provide new insights into the modeling and simulation of homogeneous rheological models for blood and a basis for further developments in modeling and prediction.

Key words: blood rheology, viscoelasticity, stenosis, curved vessel, secondary flows
AMS subject classification: 76A10, 76M12, 76Z05

1.   Introduction

Blood is a complex mixture of several formed elements, red blood cells (RBCs or erythrocytes), white blood cells (WBCs or leukocytes) and platelets (thrombocytes), in an aqueous polymeric and ionic solution, the plasma, containing electrolytes, organic molecules and numerous proteins. Despite being such a complicated mixture, it can be modeled in sufficiently large blood vessels as

---

*Corresponding author. E-mail: adelia.sequeira@math.ist.utl.pt

a single constituent fluid and, depending on the size of the blood vessels and the flow behvior, it is approximated as a Navier-Stokes fluid or as a non-Newtonian fluid.

The presence of the formed elements in blood leads to some significant and fascinating changes in its rheological properties and more experiments need to be performed, at the scale of the red blood cells, to extend the existing models by including microstructural aspects of blood. Reliable measurements of velocity and shear stress, as well as interactions between the cellular components of blood and plasma are essential to develop these microstructural models, appropriate in smaller vessels in which the cell and lumen sizes are comparable.

This paper concerns the flow of blood in vessels where it needs to be described by a non-Newtonian fluid model. There is a large body of literature confirming that blood shear thins due to the aggregation of the red blood cells, and the formation of rouleau 3D microstructures at low shear rates and their deformability at high shear ([15, 16, 17, 18, 19]). There is also experimental evidence that supports the fact that blood is capable of stress relaxation, see e.g. Thurston [30], Quemada [27], Chien et al. [20]. Evans and Hochmuth [21] have found that the red blood cell membrane, which is a component of blood, exhibits stress relaxation. Moreover, the experimental results of Thurston [31] imply that the relaxation time depends on the shear rate. In view of the available experimental evidence, it is reasonable to develop a non-Newtonian fluid model for blood that is capable of shear-thinning and stress relaxation, with the relaxation time depending on the shear rate. To date, very little is known concerning the response of such fluids.

Rajagopal and Srinivasa [28] have developed a thermodynamic framework within which one could systematically develop rate type models to describe the viscoelastic response of fluids. The framework is general enough to develop models wherein the relaxation time depends on the shear rate. All that the thermodynamic framework requires is a knowledge of how the material stores energy and how it produces entropy. The models that are developed, automatically satisfy the second law of thermodynamics. In fact, the framework requires the rate of entropy production to be non-negative. Moreover, from amongst the class of admissible constitutive relations meeting the condition that the rate of entropy production is non-negative, this theory also requires that the model should maximize the rate of entropy production. Based on [28], Anand et al. [1] introduced a model that is suitable for describing the response characteristics of blood. This model contains the Oldroyd-B model as a special sub-class.

The theory developed by Rajagopal and Srinivasa [28] makes use of the fact that the natural configuration of the material changes as the body produces entropy, and also that one can unload from the current configuration of the body to its natural configuration through an instantaneous elastic response. As blood is modeled as a viscoelastic fluid capable of instantaneous elastic response, the framework developed in [28] is particularly well suited to develop a model for blood. This framework needs the specification of how the body stores and dissipates energy. The way in which the body stores energy is usually provided by associating a specific Helmholtz potential with the body, and how the body dissipates energy is given by a rate of dissipation function. However, as shown recently in [29], not all viscoelastic fluids can be described within that earlier framework. In fact, there are (rate type) viscoelastic fluids that cannot have a specific Helmholtz potential associated with them. For certain viscoelastic fluids one cannot associate a specific Helmholtz potential but only a Gibbs potential. Rate type fluids stemming from a Gibbs potential approach might be

useful in describing the response of blood. In this paper we shall not pursue such models but restrict our attention to the model developed by Anand et al. [1] that has proven to be successful in describing the response of blood.

Anand et al. [2], [3], [4] have also studied the problem of the formation and lysis of blood clots, and more recently the problem of ATIII and protein C deficiency [5] within the context of the above model. Due to the complexity of the model, their studies are based on simple geometries and flow assumptions so that the problem under consideration can be reduced to a simple system of equations in one spatial dimension. However, if the model is to be used to study realistic problems with relevance to biomedicine, it is necessary to consider blood flow in more complex geometries than those studied in the above referenced papers, and to perform three-dimensional simulations. We address this issue in the present work. We consider the model described in [1] and perform a numerical investigation of the combined effects of inertia, viscosity and viscoelasticity of the fluid in two idealized three-dimensional geometries, a stenosis and a curved vessel. These combined effects are observed by comparing the results of the axial velocity, radial velocity and pressure contours for the new model with those obtained for classical blood flow models, namely the Newtonian and the generalized (shear-thinning) Oldroyd-B models, as previously done in [10, 13, 14] (see also e.g. [24, 26, 23, 8]).

2. The mathematical model

2.1. Kinematics

In this section we provide the minimum kinematical definitions that will make this paper self-contained. In order to understand the model that is being used in this work, it is necessary to define some kinematical quantities. The notation introduced in Rajagopal and Srinivasa [28] is used here. Let $\boldsymbol{X} \in \kappa_R$ denote a material point in the reference configuration κ_R of the body $\mathcal{B}$ (see Fig. 1), and let $\boldsymbol{x} \in \kappa_t$ denote the same material point in the current configuration κ_t at time t. Let $\kappa_{p(t)}$ denote the natural configuration that can be accessed by instantaneously unloading the body which is at the current configuration. As the body deforms, the underlying natural configuration $\kappa_{p(t)}$ changes. By the motion of a body we mean a one to one mapping $\chi(\boldsymbol{X}, t)$, that assigns to each point $\boldsymbol{X} \in \kappa_R$ a point $\boldsymbol{x} \in \kappa_t$, for each t, i. e.,

$$\chi : \kappa_R \times \mathbb{R} \to \mathcal{E}, \qquad \boldsymbol{x} := \chi(\boldsymbol{X}, t).$$

We will assume that the motion is invertible and sufficiently smooth, in such a way that all derivatives that are taken make sense.

The deformation gradient $\boldsymbol{F}_{\kappa_R}$ is defined through

$$\boldsymbol{F}_{\kappa_R} := \frac{\partial \chi}{\partial \boldsymbol{X}}$$

and the left and right Cauchy-Green stretch tensors $\boldsymbol{B}_{\kappa_R}$ and $\boldsymbol{C}_{\kappa_R}$ are defined through

$$\boldsymbol{B}_{\kappa_R} := \boldsymbol{F}_{\kappa_R} \boldsymbol{F}_{\kappa_R}^T, \qquad \boldsymbol{C}_{\kappa_R} := \boldsymbol{F}_{\kappa_R}^T \boldsymbol{F}_{\kappa_R},$$
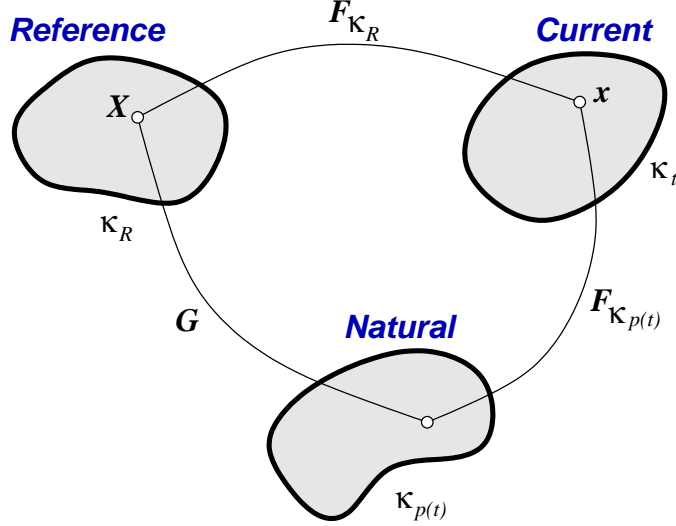
Figure 1: Schematic of the natural configurations of a body $\mathcal{B}$ at time t.

where the superscript T denotes transpose. The deformation gradient and the Cauchy-Green stretch tensors, with respect to the natural configuration, are defined by (see Fig. 1)

$$\boldsymbol{F}_{\kappa_{p(t)}} := \frac{\partial \chi}{\partial \boldsymbol{X}_{\kappa_{p(t)}}}$$

and

$$\boldsymbol{B}_{\kappa_{p(t)}} := \boldsymbol{F}_{\kappa_{p(t)}} \boldsymbol{F}_{\kappa_{p(t)}}^{T}, \qquad \boldsymbol{C}_{\kappa_{p(t)}} := \boldsymbol{F}_{\kappa_{p(t)}}^{T} \boldsymbol{F}_{\kappa_{p(t)}},$$

respectively. The principal invariants of $\boldsymbol{B}_{\kappa_{p(t)}}$ are given by

$$\boldsymbol{I}_{\boldsymbol{B}_{\kappa_{p(t)}}} := \operatorname{tr}\boldsymbol{B}_{\kappa_{p(t)}}, \quad \boldsymbol{II}_{\boldsymbol{B}_{\kappa_{p(t)}}} := \frac{1}{2}\left[(\operatorname{tr}\boldsymbol{B}_{\kappa_{p(t)}})^2 - \operatorname{tr}\boldsymbol{B}_{\kappa_{p(t)}}^2\right], \quad \boldsymbol{III}_{\boldsymbol{B}_{\kappa_{p(t)}}} := \det\boldsymbol{B}_{\kappa_{p(t)}}.$$

The mapping $\boldsymbol{G}$, that is a mapping from the reference configuration to the current natural configuration is defined through

$$\boldsymbol{G} := \boldsymbol{F}_{\kappa_{p(t)}}^{-1} \boldsymbol{F}_{\kappa_R}.$$

The velocity gradients $\boldsymbol{L}$ and $\boldsymbol{L}_{\kappa_{p(t)}}$, and their respective symmetric parts $\boldsymbol{D}$ and $\boldsymbol{D}_{\kappa_{p(t)}}$, are defined through

$$\boldsymbol{L} := \frac{d}{dt}(\boldsymbol{F}_{\kappa_R})\boldsymbol{F}_{\kappa_R}^{-1}, \qquad \boldsymbol{L}_{\kappa_{p(t)}} := \frac{d\boldsymbol{G}}{dt}\boldsymbol{G}^{-1},$$

$$\boldsymbol{D} =: \frac{1}{2}(\boldsymbol{L} + \boldsymbol{L}^T), \qquad \boldsymbol{D}_{\kappa_{p(t)}} =: \frac{1}{2}(\boldsymbol{L}_{\kappa_{p(t)}} + \boldsymbol{L}_{\kappa_{p(t)}}^T).$$

where $\frac{d}{dt}$ denotes the usual material time derivative.

The upper–convected Oldroyd derivative of a tensor $\boldsymbol{A}$ is defined by

$$\overset{\triangledown}{\boldsymbol{A}} =: \frac{d\boldsymbol{A}}{dt} - \boldsymbol{L}\boldsymbol{A} - \boldsymbol{A}\boldsymbol{L}^T. \tag{2.1}$$

It then follows that

$$\overset{\triangledown}{\boldsymbol{B}}_{\kappa_{p(t)}} = \frac{d\boldsymbol{B}_{\kappa_{p(t)}}}{dt} - \boldsymbol{L}\boldsymbol{B}_{\kappa_{p(t)}} - \boldsymbol{B}_{\kappa_{p(t)}}\boldsymbol{L}^T = -2\boldsymbol{F}_{\kappa_{p(t)}}\boldsymbol{D}_{\kappa_{p(t)}}\boldsymbol{F}_{\kappa_{p(t)}}^T. \tag{2.2}$$

Since we shall model blood as an incompressible viscoelastic shear-thinning fluid, we shall require that

$$\mathrm{tr}\boldsymbol{D} = 0, \qquad \mathrm{tr}\boldsymbol{D}_{\kappa_{p(t)}} = 0.$$

The above kinematic conditions suffice for our purpose.

2.2. A shear-thinning viscoelastic rate type fluid model for blood

For details of the development of rate type viscoelastic fluid models capable of instantaneous elastic response, within the context of a specific Helmholtz potential and rate of dissipation, we refer the reader to [28]. The theory requires the specification of a Helmholtz potential ψ and a rate of dissipation ξ that satisfies

$$\xi = \boldsymbol{T}.\boldsymbol{D} - \rho\frac{d\psi}{dt} \tag{2.3}$$

where ρ denotes the fluid density and $\boldsymbol{T}$ is the stress tensor. The model is assumed to meet the requirement that amongst all processes that are accessible to the body it chooses that which maximizes the rate of dissipation (in general, the rate of entropy production). In this study we are assuming that the processes undergone by blood are isothermal, otherwise we will have to modify equation (2.3).

We shall assume that the specific Helmholtz potential is given by

$$\psi = \frac{\mu}{2}\left(\boldsymbol{I}_{\boldsymbol{B}_{\kappa_{p(t)}}} - 3\right). \tag{2.4}$$

Thus, we are assuming that the fluid (blood) stores energy like a neo-Hookean solid. The constant μ that appears in the above equation is the shear modulus and it is non-negative (in fact, positive) based on physical considerations.

Next, we assume that the rate of dissipation function is given by

$$\xi = \alpha\left(\boldsymbol{D}_{\kappa_{p(t)}}.\boldsymbol{B}_{\kappa_{p(t)}}\boldsymbol{D}_{\kappa_{p(t)}}\right)^{\gamma} + \eta_1\boldsymbol{D}.\boldsymbol{D}. \tag{2.5}$$

T. Bodnár et al.   **Simulation of the three-dimensional flow of blood**

where α, γ and η_1 are material parameters. When $\gamma = 0$, the above model corresponds to the rate of dissipation in a generalized Oldroyd-B fluid (see [28]) and when $\gamma = 1$ and $\eta_1 = 0$, the rate of dissipation corresponds to that of a generalized Maxwell fluid. On the basis of physical considerations, we shall assume that α and η_1 are non-negative.

A lengthy but straightforward procedure based on the maximization of the rate of dissipation leads to (see Anand et al. [3])

$$\boldsymbol{T} = -p\boldsymbol{1} + \boldsymbol{S} \tag{2.6}$$

$$\boldsymbol{S} = \mu \boldsymbol{B}_{\kappa_{p(t)}} + \eta_1 \boldsymbol{D}, \tag{2.7}$$

$$\overset{\triangledown}{\boldsymbol{B}}_{\kappa_{p(t)}} = -2 \left(\frac{\mu}{\alpha}\right)^{1+2n} \left(\text{tr}(\boldsymbol{B}_{\kappa_{p(t)}}) - 3\lambda\right)^n \left[\boldsymbol{B}_{\kappa_{p(t)}} - \lambda\boldsymbol{1}\right], \tag{2.8}$$

$$\lambda = \frac{3}{\text{tr}\left(\boldsymbol{B}_{\kappa_{p(t)}}^{-1}\right)}, \tag{2.9}$$

$$n = \frac{\gamma - 1}{1 - 2\gamma} \tag{2.10}$$

In the above equations, $\overset{\triangledown}{\boldsymbol{B}}_{\kappa_{p(t)}}$ stands for the upper-convected Oldroyd derivative of tensor $\boldsymbol{B}_{\kappa_{p(t)}}$ defined by (2.2), $\boldsymbol{1}$ is the unit (identity) tensor, p denotes the Lagrange multiplier that is a consequence of the requirement of incompressibility and $\boldsymbol{S}$ is usually referred to as the extra stress tensor, or the constitutively determined part of the tensor $\boldsymbol{T}$.

2.2.1. Governing equations

Since blood is modeled as an incompressible fluid, all motions have to satisfy the balance of mass

$$\text{div } \boldsymbol{u} = 0, \tag{2.11}$$

and the balance of linear momentum

$$\rho \frac{d\boldsymbol{u}}{dt} = \text{div } \boldsymbol{T} \tag{2.12}$$

where $\boldsymbol{u}$ is the velocity field and ρ denotes the density of blood. These equations have to be solved simultaneously with the constitutive relations (2.6) - (2.10) wherein the expression for the stress is substituted into (2.12) to obtain the governing equation for the velocity field $\boldsymbol{u}$.

The following parameters obtained from human blood [1] will be used in the numerical simulations of this model:

$$\eta_1 = 0.01 \ Pa \cdot s; \quad \mu = 0.1611 \ N/m^2; \quad n = 0.5859; \quad K = \left(\frac{\mu}{\alpha}\right)^{1+2n} = 58.0725 \ s^{-1} \tag{2.13}$$

(n is positive to ensure shear-thinning behavior).

Equation (2.8) can be rewritten in a more conventional form in terms of the material time-derivative. Let us denote by

$$\frac{1}{\tau(\boldsymbol{B}_{\kappa_{p(t)}})} = 2K \left(\text{tr}(\boldsymbol{B}_{\kappa_{p(t)}}) - 3\lambda \right)^n$$

where $\tau = \tau(\boldsymbol{B}_{\kappa_{p(t)}})$ has the dimension of time and plays a role similar to the relaxation time in the classical Oldroyd-B (Maxwell) model [10]. Using this expression, equation (2.8) for the tensor $\boldsymbol{B}_{\kappa_{p(t)}}$ can be rewritten in the following way

$$\overset{\triangledown}{\boldsymbol{B}}_{\kappa_{p(t)}} = -\frac{1}{\tau(\boldsymbol{B}_{\kappa_{p(t)}})} \left[\boldsymbol{B}_{\kappa_{p(t)}} - \lambda \boldsymbol{1} \right] \tag{2.14}$$

Using the definition of the upper-convected time derivative (2.1), the left-hand side takes the form

$$\frac{d\boldsymbol{B}_{\kappa_{p(t)}}}{dt} - \left[\boldsymbol{L}\boldsymbol{B}_{\kappa_{p(t)}} + \boldsymbol{B}_{\kappa_{p(t)}} \boldsymbol{L}^T \right] = -\frac{1}{\tau(\boldsymbol{B}_{\kappa_{p(t)}})} \left[\boldsymbol{B}_{\kappa_{p(t)}} - \lambda \boldsymbol{1} \right] \tag{2.15}$$

Finally, expanding the material time-derivative on the left-hand side we end up with

$$\frac{\partial \boldsymbol{B}_{\kappa_{p(t)}}}{\partial t} + (\boldsymbol{u} \cdot \boldsymbol{\nabla}) \, \boldsymbol{B}_{\kappa_{p(t)}} = -\frac{1}{\tau} \left[\boldsymbol{B}_{\kappa_{p(t)}} - \lambda \boldsymbol{1} \right] + \left[\boldsymbol{L}\boldsymbol{B}_{\kappa_{p(t)}} + \boldsymbol{B}_{\kappa_{p(t)}} \boldsymbol{L}^T \right] \tag{2.16}$$

where the coefficients λ and τ are scalar functions of the tensor $\boldsymbol{B}_{\kappa_{p(t)}}$ and its invariants. It is interesting to observe that the classical Oldroyd-B (upper-convected Maxwell) model takes a similar form

$$\frac{\partial \boldsymbol{T}_e}{\partial t} + (\boldsymbol{u} \cdot \boldsymbol{\nabla}) \, \boldsymbol{T}_e = \frac{2\eta_e}{\tau} \boldsymbol{D} - \frac{1}{\tau} \boldsymbol{T}_e + \left[\boldsymbol{L}\boldsymbol{T}_e + \boldsymbol{T}_e \boldsymbol{L}^T \right] \tag{2.17}$$

$\boldsymbol{T}_e$ being the extra stress, η_e the elastic viscosity coefficient and τ the (constant) relaxation time.

3. Numerical simulations

Some numerical experiments have been performed in order to check the functionality of the above described shear-thinning viscoelastic fluid model for blood flow (further denoted as $bNOB$) and compare its predictions with the classical Newtonian (NS) and generalized Oldroyd-B (GOB) fluid models, under different flow conditions. The GOB model used here is obtained from the Oldroyd-B model (2.17) (see [10] for details) replacing the total (constant) viscosity by the shear dependent viscosity given by the generalized Cross function

$$\frac{\eta(\dot{\gamma}) - \eta_\infty}{\eta_0 - \eta_\infty} = \frac{1}{(1 + (\alpha\dot{\gamma})^b)^a} \tag{3.1}$$

where η_0 and η_∞ are the asymptotic viscosities at low and high shear rates and parameters α, a and b are estimated by curve fitting of experimental data. These parameters of the GOB model have

been taken from [10] (see also [26]), except for the asymptotic viscosities η_0 and η_∞, that have been adjusted to fit the $bNOB$'s model parameters, namely $\eta_0 = 0.0736 \; Pa \cdot s$ and $\eta_\infty = 0.005 \; Pa \cdot s$.

The main goal is to evaluate the hemodynamic and rheological characteristics of this new $bNOB$ model in two simple idealized three-dimensional geometries, based on previous works dealing with similar test cases for simpler models as the generalized Newtonian or the classical and generalized Oldroyd-B models [10, 13, 14].

3.1. Numerical method

The numerical method used to solve the governing equations is based on a spatial finite-volume discretization on structured grids and an explicit Runge-Kutta time-stepping scheme, namely a robust modified Runge-Kutta four-stage method [25]. The computational mesh is structured and consists of hexahedral primary control volumes. To evaluate the viscous numerical fluxes also dual finite volumes with octahedral shape and centered around the primary cell faces are used.

We look for steady solutions by a time-marching approach, which means that the unsteady governing equations are solved with steady boundary conditions and steady solutions are recovered when $t \to \infty$. An artificial compressibility formulation [33], often used in steady flow simulations, is applied to obtain the pressure and to enforce the divergence-free constraint. The continuity equation (2.11) is modified by adding the pressure time-derivative, properly scaled by the artificial speed of sound $\mathbf{c}$ (equal to 1, for simplicity), as follows:

$$\frac{1}{\mathbf{c}^2}\frac{\partial p}{\partial t} + \operatorname{div} \boldsymbol{u} = 0, \tag{3.2}$$

A pressure stabilization technique has been used in the present simulations (see e. g. [33]) to avoid numerical oscillations in the pressure mainly due to the presence of strong gradients. This technique consists in adding a pressure dissipation term (Laplacian) into the right hand side of the modified continuity equation (3.2) such that

$$\frac{\partial p}{\partial t} + \mathbf{c}^2 \operatorname{div} \boldsymbol{u} = \epsilon \Delta p, \tag{3.3}$$

which, in particular, vanishes if the pressure is a linear function of the space coordinates.

The Reynolds number used in the simulations was quite low (of the order of 10^2) and thus no additional stabilization was needed for the flow variables. The details of this approach can be found in earlier papers [11, 12] and the references therein.

Numerical tests have been performed in two different geometries. The first computational domain represents a non-symmetric (with respect to the bulk flow direction) cosine-shaped vessel *stenosis* shown in Fig. 2. The stenosed vessel is three-dimensional, rotationally symmetric, with diameter $D = 2R = 6.2mm$ which reduces to its one half in the stenosed region. This leads to a $4 : 1$ cross-sectional area reduction and thus to a significant local flow acceleration.

The second computational domain, is a curved $90°$ *elbow* shaped vessel with constant curvature, as shown in Fig. 3. The curved vessel is three-dimensional with circular cross-section of the same size as the above described stenosis. The length of the inflow and outflow straight sections are $L_{in} = L_{out} = 10R$.
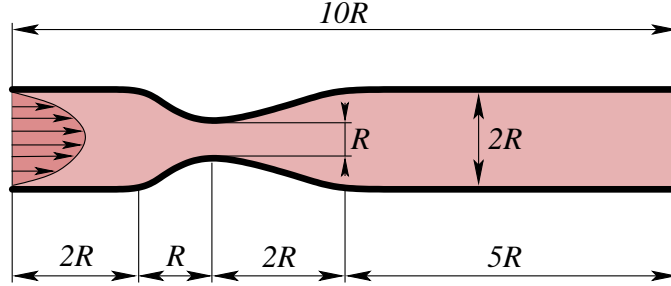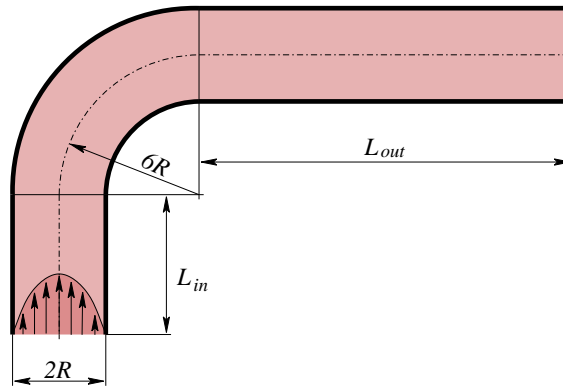
Figure 2: Stenosed vessel

Figure 3: Curved vessel (elbow)

3.1.1. Computational grid

The computational domain is discretized using a structured, wall fitted mesh with hexahedral cells and non-uniform axial cell spacing. A multiblock mesh structure was adopted to avoid high distortion of cells, see Fig. 4. The outer mesh block has $64 \times 16 \times 100$ cells, while the central mesh block has $16 \times 16 \times 100$ control volumes. A similar grid structure was used in both test case geometries.

3.1.2. Boundary conditions

A parabolic velocity profile with given flow-rate Q is prescribed at the inlet of each domain, for $bNOB$, GOB and NS models. Homogeneous Neumann conditions for the velocity components are imposed at the outlet and no-slip conditions are prescribed at the wall. Pressure is fixed at the outlet and extrapolated at the other boundaries. Moreover, homogeneous Neumann boundary conditions are prescribed at all boundaries for the components of tensor $\boldsymbol{B}_{\kappa_p(t)}$. As an alternative, some simulations have been performed using a Dirichlet type boundary condition $\boldsymbol{B}_{\kappa_p(t)} = \boldsymbol{1}$ prescribed at the inlet, but no significant impact on the solution has been found.
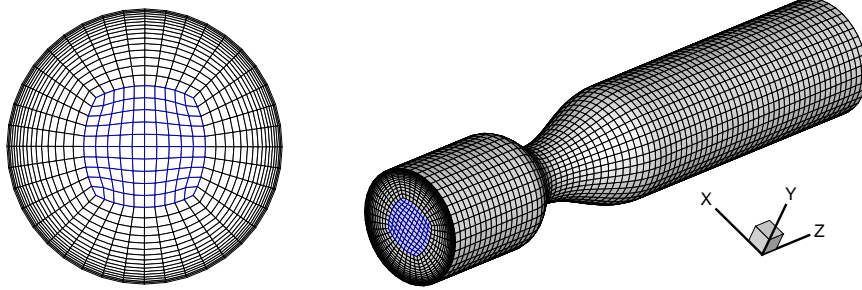
Figure 4: Computational grid structure

3.2. Numerical Results

3.2.1. Stenosed vessel

The stenosed vessel has been chosen as a test case to study the behavior of the new blood model $bNOB$ in the presence of a high shear region. The sudden (but smooth) reduction of the cross-sectional area generates jet-like flow patterns with significant recirculation zones downstream of the stenosis. The sizes of the recirculation zones depend, for a given geometry, mainly on the flow rate and the rheological model. Therefore, three different flow rates $Q = 2.0,\ 1.0$ and $0.5\,cm^3/s$ were investigated in the simulations for the three considered models, using for the $bNOB$ model the blood flow parameters given by (2.13).

Flow field.   The influence of the shear-thinning and viscoelastic effects on the qualitative behavior of the flow field can be observed by comparing the results of the axial velocity, radial velocity and pressure contours for both the Newtonian (NS) model (with viscosity $\eta_1 = 2\eta_\infty = 0.01\ Pa\cdot s$) and the shear-thinning viscoelastic fluid model $bNOB$. Figures 5 and 6 show the axial velocity, radial velocity and pressure contours [†] for the NS and $bNOB$ models, with the flow rates $Q = 2.0\,cm^3/s$ and $Q = 0.5\,cm^3/s$, respectively.

As expected (see previous results in [10] and [14]) there are essentially two main differences between the Newtonian (NS) model solution and the blood model ($bNOB$) solution.

  i) The velocity profile obtained using the $bNOB$ model is flatter in the central part of the vessel, which corresponds to a reduced value of the maximum velocity. As a consequence, the near wall flow is accelerated and thus the recirculation zones become shorter.

  ii) The pressure drop is higher[‡] for the $bNOB$ flow model, due to the local increase of the viscosity (with respect to the Newtonian flow reference viscosity $\eta_\infty = \eta_1/2$) in the low

---

[†]The color scale, with units in m/s (shown below in Fig. 7), is the same in both figures, to allow for a direct comparison. Regions with negative axial velocity (i.e. reversal flow) are plotted in grey color.

[‡]The pressure is fixed at the outlet, with the same value for both cases. The resulting higher pressure at the inlet indicates a higher pressure drop.

shear regions, which leads to a higher pressure loss.

Both of these effects can be attributed to the combined shear-thinning and viscoelastic behavior captured by the $bNOB$ model. A better comparison can be done by directly observing figures (7 - 10) displaying the axial velocity and radial velocity contours for the NS, GOB and $bNOB$ models and both flow rates $Q = 2.0\,cm^3/s$ and $Q = 0.5\,cm^3/s$.
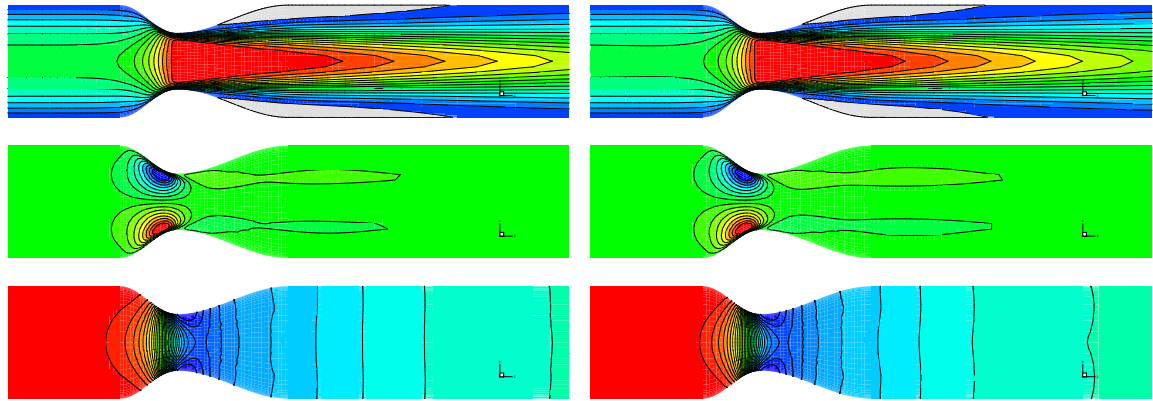
Figure 5: Axial velocity (top), radial velocity (middle) and pressure (bottom) contours, with flow rate $Q = 2.0\,cm^3/s$, for the NS fluid (left) and $bNOB$ fluid (right).
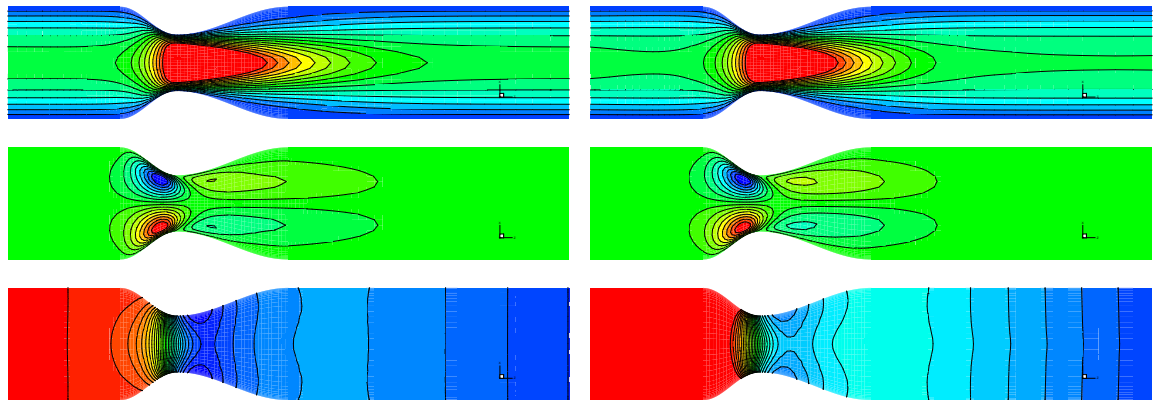
Figure 6: Axial velocity (top), radial velocity (middle) and pressure (bottom) contours, with flow rate $Q = 0.5\,cm^3/s$, for the NS fluid (left) and $bNOB$ fluid (right).

A more detailed study of the rheological effects of the $bNOB$ blood model on the axial velocity contours can be done by directly computing the differences between the NS and the $bNOB$ solutions or between the GOB and $bNOB$ solutions. Figure 11 shows the normalized difference between the NS and the $bNOB$ solutions for different flow rates $Q = 2.0,\ 1.0$ and $0.5\,cm^3/s$. It is obvious that the velocity predicted by the $bNOB$ blood model is lower in the central part of the
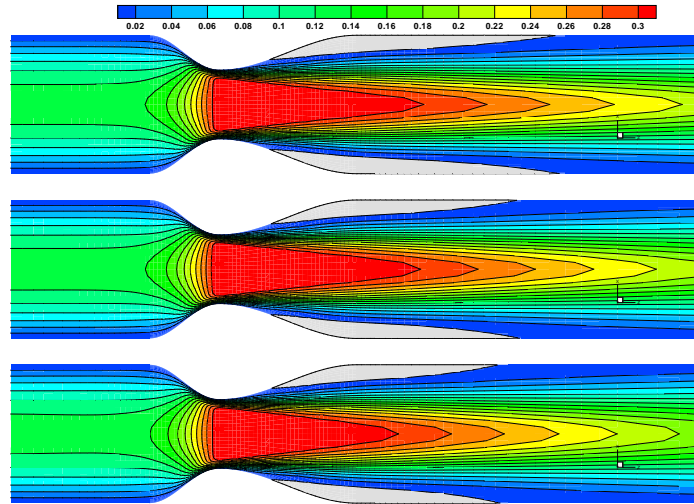
Figure 7: Comparison of the axial velocity contours for $Q = 2.0\,cm^3/s$: NS fluid (top), GOB model (middle) and $bNOB$ blood model (bottom).
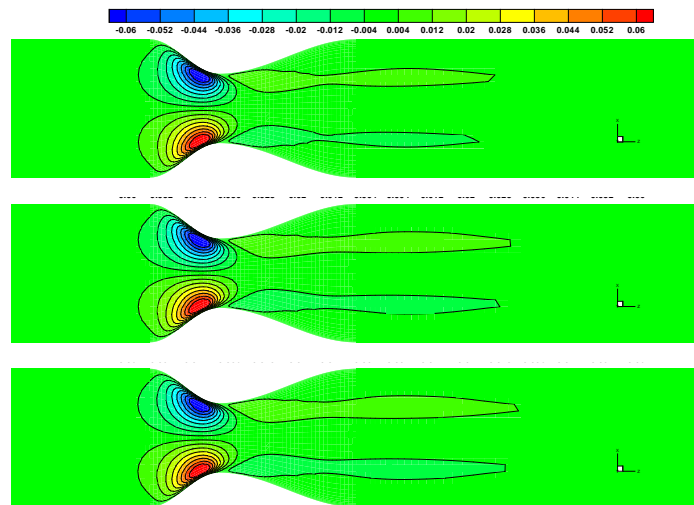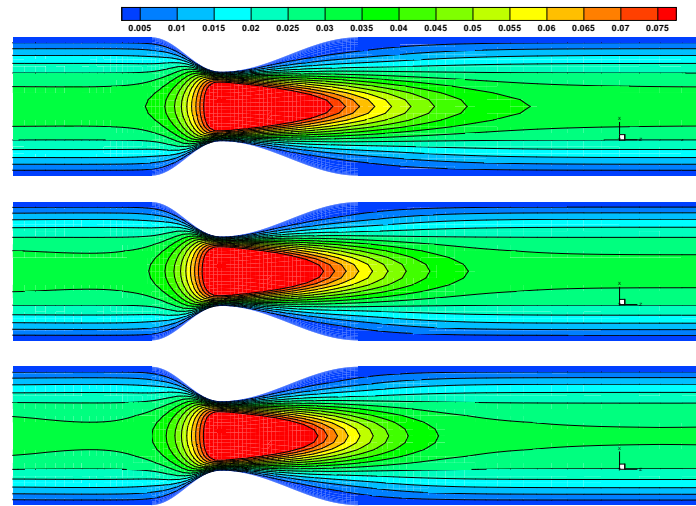

Figure 8: Comparison of the radial velocity contours for $Q = 2.0\,cm^3/s$: NS fluid (top), GOB model (middle) and $bNOB$ blood model (bottom).

vessel than the one predicted by NS. This is compensated by a faster flow in the near-wall region. This marked flattening of the velocity profile is a typical shear-thinning characteristic, not related to the fluid viscoelasticity.

It is also interesting to observe that the magnitude of the axial velocity difference increases with the reduction of the flow rate. This is a natural result, since the Newtonian (NS) solution is computed using a lower viscosity η_∞ and thus when the flow rate is reduced and, consequently, the

Figure 9: Comparison of the axial velocity contours for $Q = 0.5\,cm^3/s$: NS fluid (top), GOB model (middle) and $bNOB$ blood model (bottom).
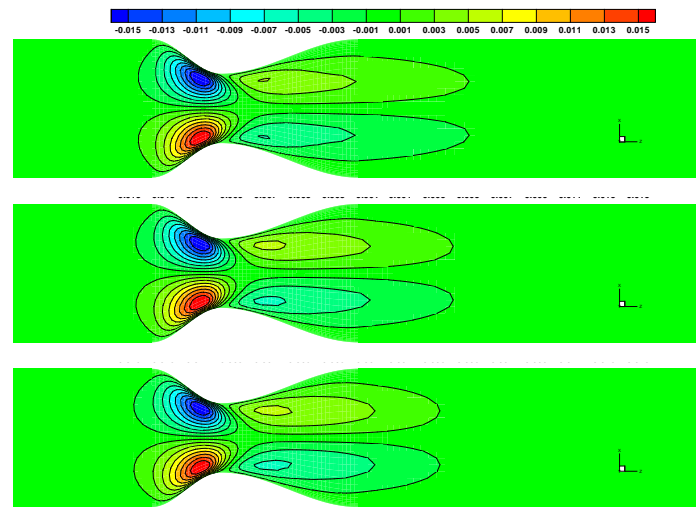
Figure 10: Comparison of the radial velocity contours for $Q = 0.5\,cm^3/s$: NS fluid (top), GOB model (middle) and $bNOB$ blood model (bottom).

local shear-rate reduces as well, this leads to an increase of the local apparent viscosity. Therefore the magnitude of the axial velocity differences is higher in this case. It is obvious that a different choice of the reference viscosity for the NS model could lead to different results.

The normalized difference between the $bNOB$ and GOB axial velocities, corresponding to the three flow rates $Q = 2.0,\ 1.0$ and $0.5\,cm^3/s$ is shown in Figure 12. As expected, the impact of the viscoelasticity on the flow behavior predicted by the $bNOB$ blood model is less significant than

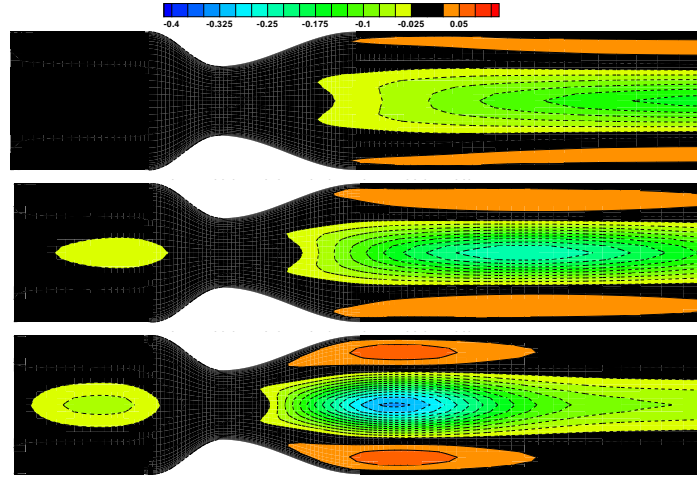13

the shear-thinning one shown in Figure 11.

Figure 11: Relative difference of axial velocity $(u_{bNOB} - u_{NS})/U_0$ for flow rates $Q = 2.0,\ 1.0$ and $0.5\,cm^3/s$ (from top to bottom).
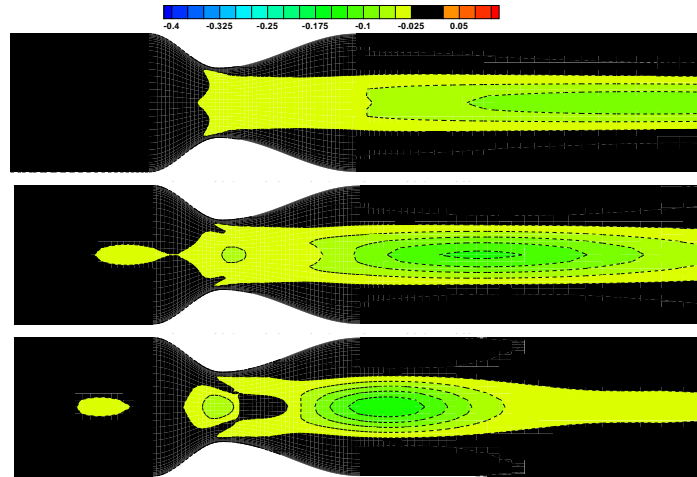

Figure 12: Relative difference of axial velocity $(u_{bNOB} - u_{GOB})/U_0$ for flow rates $Q = 2.0,\ 1.0$ and $0.5\,cm^3/s$ (from top to bottom).

Forcing effects. The effects of the extra stress can be expressed in terms of the divergence of the tensor $\boldsymbol{B}_{\kappa_{p(t)}}$ The term div $\boldsymbol{B}_{\kappa_{p(t)}}$ represents an additional force in the balance of linear momentum

14

(2.12) related to the viscoelastic behavior predicted by the $bNOB$ blood model. In the present test case the most important component of this force is the axial one. Figure 13 shows the contours of the axial component of div $\boldsymbol{B}_{\kappa_{p(t)}}$. The blue color represents a force acting against the main flow and causing its deceleration, whose maximum value is attained at the axis of symmetry. This is also a typical behavior captured by shear-thinning models, which has been previously observed in [10] and [14] where the generalized (i.e. shear-thinning) Newtonian and generalized Oldroyd-B models were compared with the classical Newtonian and Oldroyd-B models. Figure 14 shows
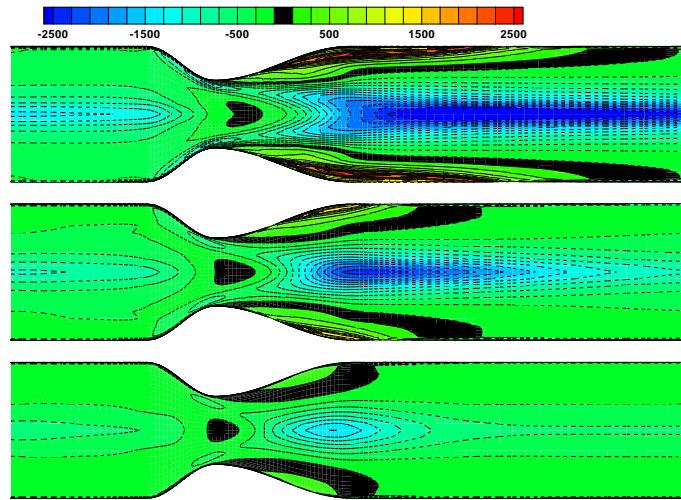

Figure 13: Axial component of the divergence of the tensor $\boldsymbol{B}_{\kappa_{p(t)}}$ for flow rates $Q = 2.0,\ 1.0$ and $0.5\,cm^3/s$ (from top to bottom).

the contours of the six components of the extra stress tensor $\boldsymbol{B}_{\kappa_{p(t)}}$ in the $x - z$ plane, in some cross-sections of the flow domain, for a flow rate $Q = 2.0\,cm^3/s$. The components b_i of the tensor $\boldsymbol{B}_{\kappa_{p(t)}}$ are numbered according to the following scheme

$$\boldsymbol{B}_{\kappa_{p(t)}} = \begin{pmatrix} b_1 & b_2 & b_3 \\ b_2 & b_4 & b_5 \\ b_3 & b_5 & b_6 \end{pmatrix}$$

The contour color scale is the same for all these plots. It is clear that the diagonal components of the tensor $\boldsymbol{B}_{\kappa_{p(t)}}$ are dominant (in magnitude), so the whole tensor is a kind of perturbation of the identity tensor $\boldsymbol{1}$. The same has been observed for the lower flow rates.

3.3. Curved vessel

Flows in curved vessels are very challenging and considerably more complex than flows in straight vessels. For inertial Newtonian flows it is well known that a slight curvature of the vessel axis
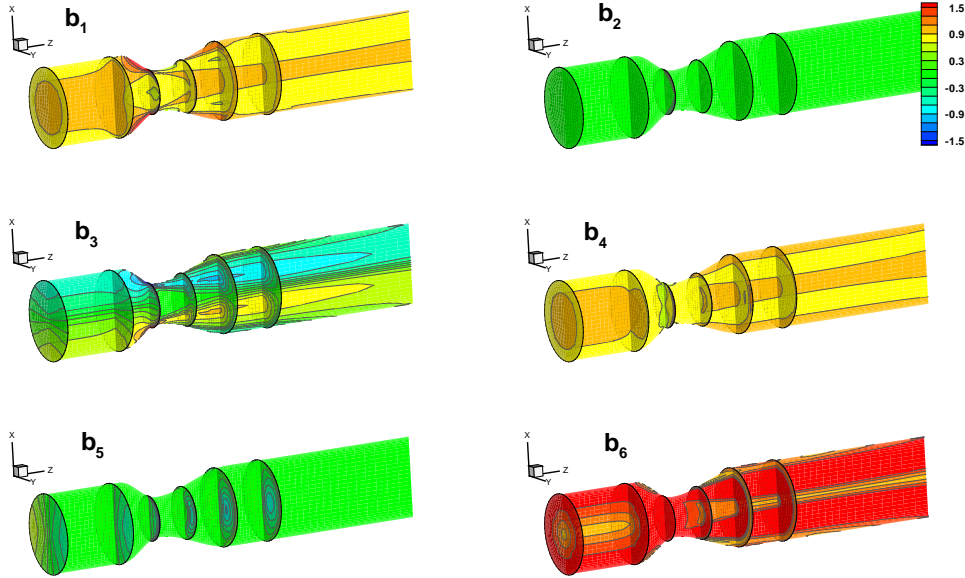
T. Bodnár et al.   **Simulation of the three-dimensional flow of blood**

Figure 14: Contours of the components of tensor $\boldsymbol{B}_{\kappa_{p(t)}}$ for the flow rate $Q = 2.0\,cm^3/s$.

induces centrifugal forces on the fluid and, in addition to the primary initial flow, a secondary motion appears, sending fluid outward along the symmetry axis and returning along the upper and lower curved surfaces. This secondary motion is induced by an imbalance between the cross-stream pressure gradient and the centrifugal forces developed at the curvature sites, and consists of a pair of symmetrical counter-rotating vortices that is superposed to the axial Poiseuille flow. This results in asymmetrical wall stresses with high shear and low pressure regions (see e.g. [9, 22, 6, 7]).

A $90°$ curved vessel (Fig. 3) has been chosen as a second test case to study the behavior of the new blood model $bNOB$ in the presence of high streamline curvature and non-negligible secondary flows. Since the secondary flow pattern is more pronounced at higher flow rates, only the flow rate $Q = 2.0\,cm^3/s$ has been considered for the simulations in this geometry.

One of the important features of the flow predicted by the new blood model $bNOB$ is related to the axial velocity profile. This can clearly be observed in Fig. 15 showing, for the NS, GOB and $bNOB$ models, the plots of the axial velocity in three different sections placed at $30°$, $60°$ and $90°$ in the curved part of the vessel. In the case of the $bNOB$ and GOB models flatter axial velocity profiles are obtained when compared to the NS model. As in the case of the flow in the stenosed vessel, this effect can be attributed to the shear-thinning behavior predicted by the $bNOB$ and GOB models where the low shear rates around the centerline of the vessel lead to a local increase of the apparent viscosity. In this case, it is apparent that viscoelasticity of both flows does not play a significant impact in their behavior, however other numerical experiments should be done to prove this ansatz. Curvature effects can be observed in the contours of the axial

velocity, which are shifted away from the central axis as the curvature of the vessel increases. This is visible in Fig. 16 and, with more details in Fig. 17. Secondary flow streamlines have a similar qualitative behavior for the NS, GOB and $bNOB$ models, as shown in Fig. 16. More details and differences are visible in the comparison of axial and radial velocity contours shown in figures 17 and 18, where the magnitude of the secondary flow velocities is clearly lower for the GOB and $bNOB$ models due to a higher apparent viscosity.

Figures 19 and 20 show the normalized solution differences between the new $bNOB$ and the classical NS and shear-thinning GOB models. The differences on the axial velocity between the $bNOB$ and the Newtonian model (Fig. 19, left) show the expected slow-down of the core flow (caused by the shear-thinning behavior) in the straight inlet part of the vessel. This is compensated by a faster near-wall flow. As soon as the flow reaches the bended part of the curved vessel, the slow core of the flow is pushed towards the outer wall (see Fig. 20 for a more detailed view), while close to the inner radius of the bend, the flow becomes faster. A similar (although weaker) tendency of the flow behavior can also be seen for the difference between the $bNOB$ and GOB models (Fig. 19, right and Fig. 21). This is mainly due to the fact that both models have a shear-thinning viscosity. In the $bNOB$ model shear-thinning effects seem to be slightly more pronounced than in the GOB model. This behavior needs further investigation in a future work.

4.   Conclusions and remarks

Blood is a very complex multiconstituent material that, in intermediate sized vessels, can be modeled as a single homogeneized continuum which exhibits non-Newtonian behavior. Such response can be captured by the phenomenological shear-thinning viscoelastic constitutive model of Anand and Rajagopal [1]. The present work was devoted to the numerical simulation of this model in two idealized three-dimensional geometries, a stenosis and a curved vessel, to investigate the combined rheological effects of inertia, shear-thinning viscosity and viscoelasticity, for steady flows.

Solutions for the new shear-thinning viscoelastic model ($bNOB$) have been compared to the classical Navier-Stokes (NS) and generalized Oldroyd-B (GOB) solutions showing, as expected, that the shear-thinning effects are dominant with respect to the viscoelastic ones in both geometries [10, 13, 14]. In the case of the stenosed vessel, the shear-thinning effects are predominant in the recirculation zone downstream the stenosis, increasing as the flow rate (and consequently the shear rate) decreases. In the curved vessel we observed in particular that the axial velocity profile is flatter for the $bNOB$ and GOB models than for the NS model. In summary, we can also conclude that results obtained with the new $bNOB$ model are very similar to those obtained with the classical GOB model, showing in particular that the $bNOB$ model has been properly adjusted and implemented. In addition, this blood rheological model has been created within the novel thermodynamical framework developed by Rajagopal and Srinivasa [28] and the simulations presented here are one of the first making use of that promising approach.

Future work will be devoted to an extension of this numerical study to unsteady flows in geometries like stenosed vessels with different degrees of contraction and curved vessels with different curvatures, to provide a deeper understanding of the significance of the non-Newtonian character-
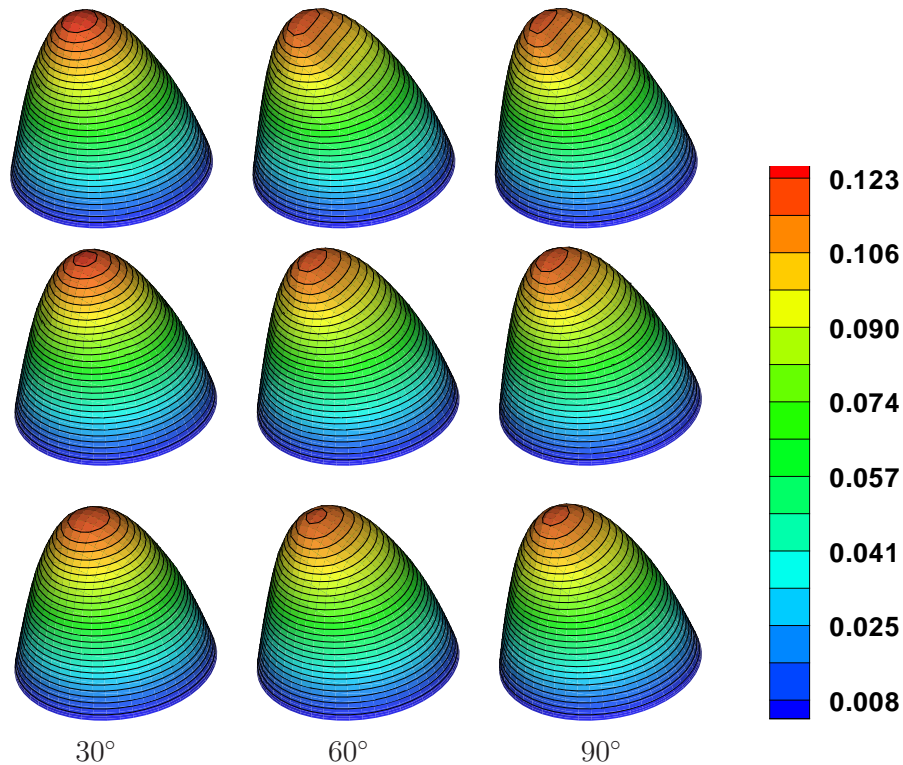
Figure 15: Axial velocity profiles for NS flows (top row), GOB flows (middle row) and $bNOB$ flows (bottom row) in the curved vessel.

istics of blood captured by the $bNOB$ model and their correlation with arterial diseases.

Acknowledgements

References

[1] M. Anand, K.R. Rajagopal. *A shear-thinning viscoelastic fluid model for describing the flow of blood*. Int. J. of Cardiovascular Medicine and Science, 4, 2 (2004), 59–68.
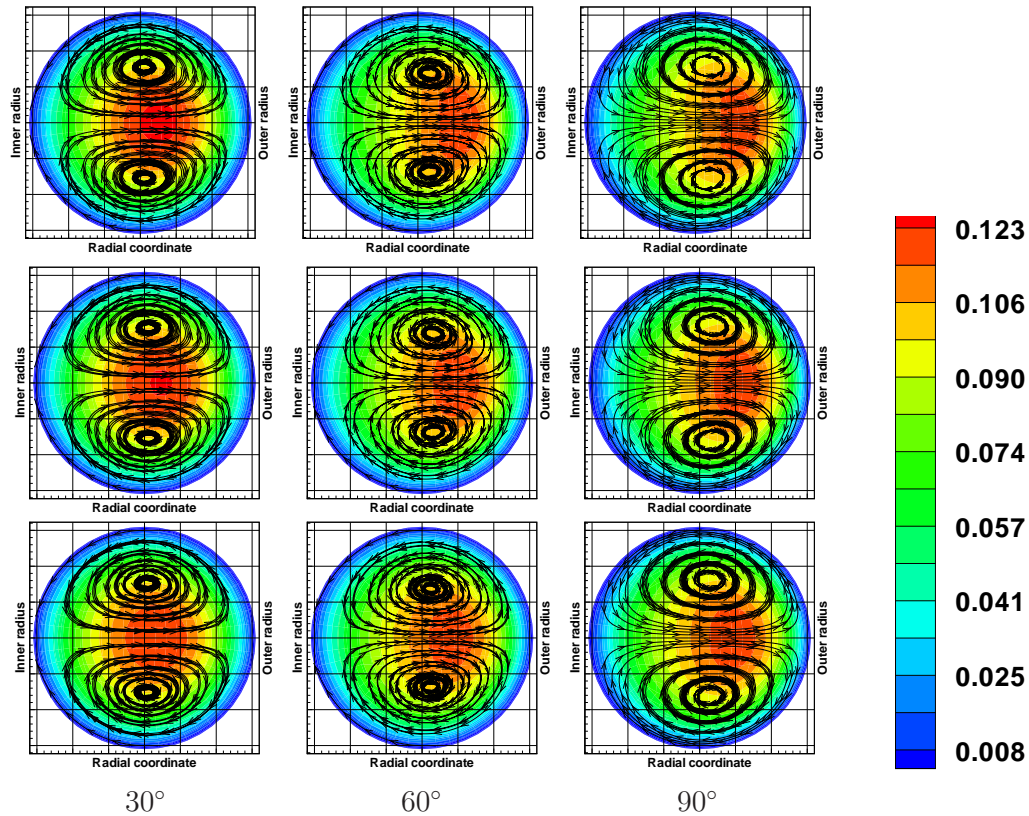
T. Bodnár et al. **Simulation of the three-dimensional flow of blood**

Figure 16: Axial velocity contours and secondary flow streamlines for the NS (top row), GOB flows (middle row) and the $bNOB$ models (bottom row).

[2] M. Anand, K.R. Rajagopal. *A mathematical model to describe the change in the constitutive character of blood due to platelet activation*. C. R. Méchanique, 330 (2002), 557–562.

[3] M. Anand, K. Rajagopal, K.R. Rajagopal. *A model incorporating some of the mechanical and biochemical factors underlying clot formation and dissolution in flowing blood*. J. of Theoretical Medicine, 5, 3–4 (2003), 183–218.

[4] M. Anand, K. Rajagopal, K.R. Rajagopal. *A model for the formation and lysis of blood clots*. Pathophysiology Haemostasis Thrombosis, 34 (2005), 109-120.

[5] M. Anand, K. Rajagopal, K.R. Rajagopal. *A model for the formation, growth, and lysis of clots in quiescent plasma. A comparison between the effects of antithrombin III deficiency and protein C deficiency*. J. of Theoretical Biology, 253 (2008), 725–738.
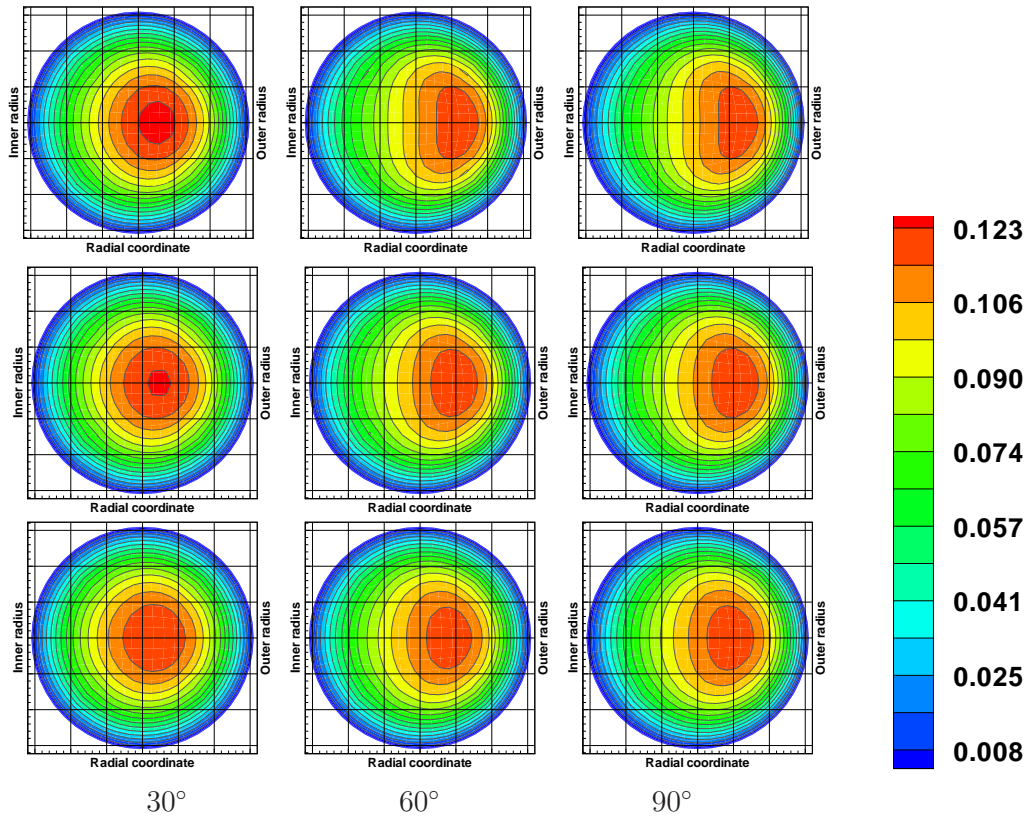
Figure 17: Axial velocity contours for the NS (top row), GOB flows (middle row) and the $bNOB$ models (bottom row).

[6] N. Arada, M. Pires, A. Sequeira. *Viscosity effects on flows of generalized Newtonian fluids through curved pipes*. Computers and Mathematics with Applications, 53 (2007), pp. 625-646.

[7] N. Arada, M. Pires, A. Sequeira. *Numerical simulations of shear-thinning Oldroyd-B fluids in curved pipes*. IASME Transactions, Issue 6, 2 (2005), pp. 948-959.

[8] P.D. Bailyk, D.A. Steinman, C.R. Ethier. *Simulation of non-Newtonian blood flow in an end-to-side anastomosis*. Biorheology, 31 (5) (1994) 565-586.

[9] A.A. Berger, L. Talbot, L.-S. Yao. *Flow in curved pipes*. Annu. Rev. Fluid Mech., 15 (1983) 461512.

[10] T. Bodnár, A. Sequeira. *Numerical Study of the Significance of the Non-Newtonian Nature of Blood in Steady Flow Through a Stenosed Vessel*. In: Advances in Mathematical Fluid Mechanics (edited by R. Rannacher & A. Sequeira), pp. 83–104. Springer Verlag (2010).
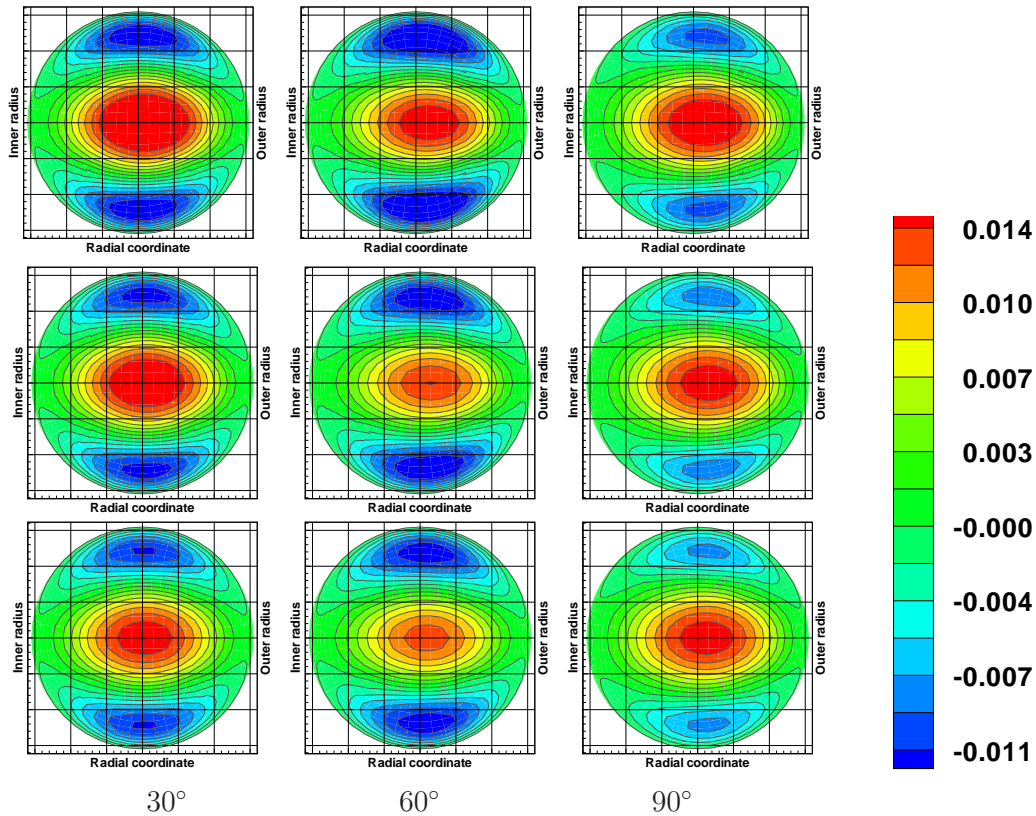
Figure 18: Radial velocity contours for the NS (top row), GOB flows (middle row) and the $bNOB$ models (bottom row).

[11] T. Bodnár, J. Příhoda. *Numerical simulation of turbulent free-surface flow in curved channel*. Journal of Flow, Turbulence and Combustion, 76 (4) (2006) 429–442.

[12] T. Bodnár, A. Sequeira. *Numerical simulation of the coagulation dynamics of blood*. Computational and Mathematical Methods in Medicine, 9 (2) (2008) 83–104.

[13] T. Bodnár, A. Sequeira, L. Pirkl. *Numerical Simulations of Blood Flow in a Stenosed Vessel under Different Flow Rates using a Generalized Oldroyd - B Model* In: Numerical Analysis and Applied Mathematics, Vols 1 and 2. Melville, New York: American Institute of Physics, (2009), vol. 2, pp. 645–648.

[14] T. Bodnár, A. Sequeira, M. Prosi. *On the Shear-Thinning and Viscoelastic Effects of Blood Flow under Various Flow Rates*. Applied Mathematics and Computation, 217 (2011), 5055–5067.
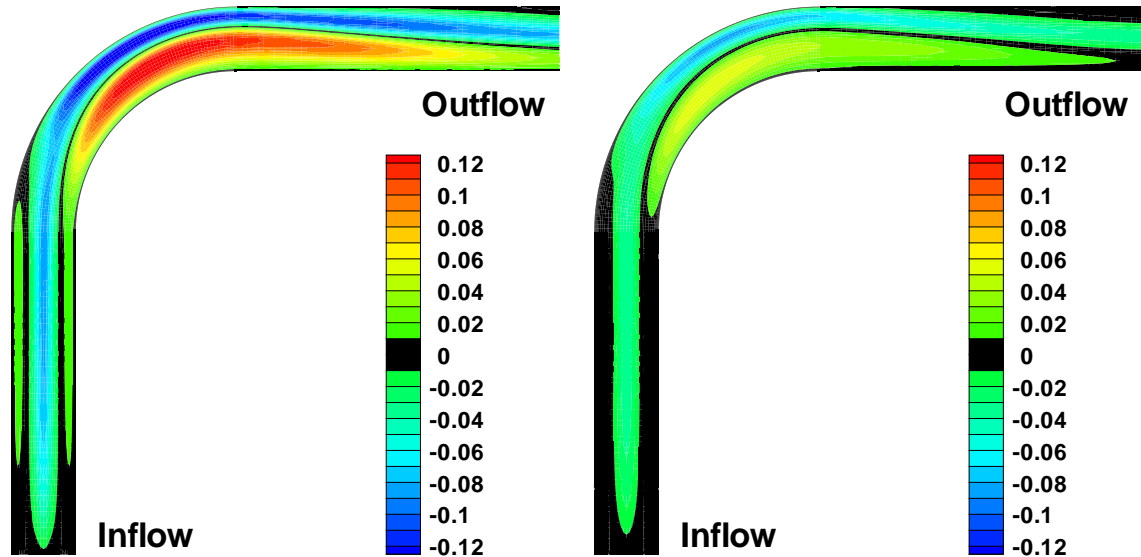
Figure 19: Relative difference of axial velocity $(u_{bNOB} - u_{NS})/U_0$ (left) and $(u_{bNOB} - u_{GOB})/U_0$ (right).
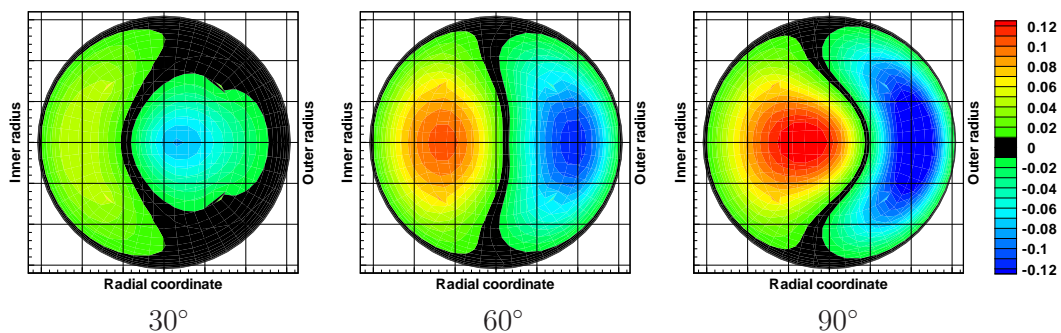

Figure 20: Relative difference of axial velocity $(u_{bNOB} - u_{NS})/U_0$.

[15] S.E. Charm, G.S. Kurland. *Viscometry of human blood for shear rates of 0-100,000 sec⁻¹*. Nature, 206 (1965), 617–618.

[16] S. Chien, S. Usami, H.M. Taylor, J.L. Lundberg, M.I. Gregersen. *Effect of hematocrit and plasma proteins on human blood rheology at low shear rates*. Journal of Applied Physiology, 21, 1 (1966), 81–87.

[17] S. Chien, S. Usami, R.J. Dellenback, M.I. Gregersen. *Blood viscosity: Influence of erythrocyte aggregation*. Science, 157, 3790 (1967), 829–831.
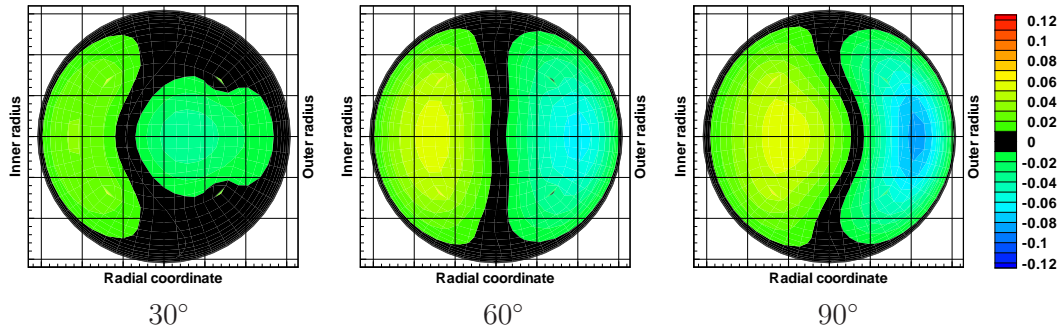
30°   60°   90°

Figure 21: Relative difference of axial velocity $(u_{bNOB} - u_{GOB})/U_0$.

[18] S. Chien, S. Usami, R.J. Dellenback, M.I. Gregersen. *Blood viscosity: Influence of erythrocyte deformation*. Science, 157, 3790 (1967), 827–829.

[19] S. Chien, S. Usami, R. J. Dellenback, M.I. Gregersen. *Shear-dependent deformation of erythrocytes in rheology of human blood*. American Journal of Physiology, 219 (1970), 136–142.

[20] S. Chien, K.L.P. Sung, R. Skalak, S. Usami, A.L. Tozeren. *Theoretical and experimental studies on viscoelastic properties of erythrocyte membrane*. Biophysical Journal, 24, 2 (1978), 463–487.

[21] E.A. Evans, R.M. Hochmuth. *Membrane viscoelasticity*. Biophysical Journal, 16, 1 (1976), 1–11.

[22] Y. Fan, R.I. Tanner, N. Phan-Thien. *Fully developed viscous and viscoelastic flows in curved pipes*. J. Fluid Mech., 440 (2001), 327-357.

[23] F. Gijsen, F. van de Vosse, J. Janssen. *The influence of the non-Newtonian properties of blood on the flow in large arteries: steady flow in a carotid bifurcation model*. Journal of Biomechanics, 32 (1999), 601-608.

[24] J. Hron, J. Málek, S. Turek. *A numerical investigation of flows of shear-thinning fluids with applications to blood rheology*. Int. J. Numer. Meth., Fluids, 32 (2000), 863-879.

[25] A. Jameson, W. Schmidt, E. Turkel. *Numerical solutions of the Euler equations by finite volume methods using Runge-Kutta time-stepping scheme*. In:AIAA 14th Fluid and Plasma Dynamics Conference, Palo Alto (1981), AIAA paper 81 - 1259.

[26] A. Leuprecht, K. Perktold. *Computer simulation of non-Newtonian effects of blood flow in large arteries*. Comp. Methods in Biomech. and Biomech. Eng., 4 (2001), 149–163.

[27] D. Quemada. *Rheology of concentrated disperse systems III. General features of the proposed non-Newtonian model. Comparison with experimental data*. Rheol. Acta, 17 (1978), 643–653.

[28] K.R. Rajagopal, A.R. Srinivasa. *A thermodynamic frame work for rate type fluid models*. Journal of Non-Newtonian Fluid Mechanics, 80 (2000), 207–227.

[29] K.R. Rajagopal, A.R. Srinivasa. *A Gibbs-potential-based formulation for obtaining the response functions for a class of viscoelastic materials*. Proc. R. Soc. A, 467 (2011), 39–58.

[30] G.B. Thurston. *Viscoelasticity of human blood*. Biophysical Journal, 12 (1972), 1205–1217.

[31] G.B. Thurston. *Frequency and shear rate dependence of viscoelasticity of blood*. Biorheology, 10, 3 (1973), 375–381.

[32] G.B. Thurston. *Non-Newtonian viscosity of human blood: Flow induced changes in microstructure*. Biorheology, 31(2), (1994), 179–192.

[33] J. Vierendeels, K. Riemslagh, E. Dick. *A multi-grid semi-implicit line-method for viscous incompressible and low-Mach-number flows on high aspect ratio grids*. J. Comput. Phys., 154 (1999), 310–344.

B.4 Blood Coagulation Simulations Using a Viscoelastic Model

SEQUEIRA A., BODNÁR T.

In this paper the non-linear viscoelastic model proposed by Anand and Rajagopal in [B.1] (and solved by T. Bodnár in [B.6]) is for the first time adopted in blood coagulation simulations. This paper is a natural extension and continuation of the author's previous papers shown in the sections B.1 and B.3. The main aim was to prove the useabilty of the numerical solver and adopted flow-biochemistry coupling strategy.

The computational test case was proposed and solved by T. Bodnár using his own original finite-volume based code.

Blood Coagulation Simulations
using a Viscoelastic Model

A. Sequeira[1] *, T. Bodnár[2]

[1] Department of Mathematics and CEMAT/IST, Instituto Superior Técnico, University of Lisbon
Av. Rovisco Pais 1, 1049-001 Lisboa, Portugal

[2] Faculty of Mechanical Engineering, Czech Technical University in Prague
Karlovo Náměstí 13, 121 35 Prague 2, Czech Republic

Abstract. This paper presents numerical results based on a macroscopic blood coagulation model coupled with a non-linear viscoelastic model for blood flow. The system of governing equations is solved using a central finite-volume scheme for space discretization and an explicit Runge-Kutta time-integration. An artificial compressibility method is used to resolve pressure and a non-linear TVD filter is applied for stabilization. A simple test case of flowing blood over a clotting surface in a straight 3D vessel is solved. This work presents a significant extension of the previous studies [10] and [9].

Keywords and phrases: blood coagulation, clot, viscoelastic model, numerical simulations

Mathematics Subject Classification: 76Z05, 76V05, 80A32, 92C35, 74F25, 80A30, 92C45, 92C40

1. Introduction

Mathematical and numerical modeling of blood flow and related phenomena are very challenging problems. The flow of blood is difficult to model mainly due to its complex rheological behavior which can be highly non-Newtonian in certain regimes in healthy and unhealthy blood flow conditions [17, 29, 30]. Rheological characteristics like shear-thinning viscosity, thixotropy, viscoelasticity or yield stress can be observed. A variety of models have been developed for blood flow including some of these features and, nowadays, it is still not possible to accept a single model to capture the most important mechanical properties of blood. The modeling approach is usually based on the blood flow conditions in view of predicting its behavior. The work presented here follows previous studies [11–13] describing the shear-thinning and viscoelastic behavior of blood in simple geometries. Even if blood flow is considered as purely mechanical, its mathematical modeling and numerical simulations present serious challenges as shown e.g. in [18, 21] or [26].

The complex mechanical properties of blood flow are highly affected by the behavior of blood cellular elements (red blood cells, white blood cells and platelets), in particular by the aggregation of red blood cells into 3D microstructures at low shear rates and their disaggregation at high shear rates. Moreover,

---

*Corresponding author. E-mail: `adelia.sequeira@math.ist.utl.pt`

in flowing blood an enormous amount of biochemical reactions are associated to the complex process of blood coagulation and hemostasis.

Blood coagulation is an extremely complex biological process following a wound or a spontaneous internal injury, in which blood forms clots to prevent bleeding. The process involves platelets activation, the subsequent release of multiple factors from their cytoplasmatic granules, their interaction with the endothelial wall, with a huge impact of the flowing blood and on the thrombus growth regularization. The clot formation is followed by its dissolution repairing the injured wall, which is due to mechanical factors such as high shear stress (see e.g. [16,28]). The process of platelets activation and blood coagulation is not yet well understood. Numerous experimental studies have been performed and recent reviews detailing this complex process are available in the literature (as in e.g. [16] and references cited therein). A large number of sound phenomenological models for clot formation and lysis, based on different strategies, have been developed [6, 14, 25, 33] or [1, 24]. One of the major problems is the high complexity of the chemical system which crucially depends on the supply of chemicals by the flowing blood. This leads to an important dependence of the coagulation process on the blood flow. On the other hand the blood flow characteristics are determined by the size of the clot, forming an obstacle to the flow.

Any reliable model of blood coagulation should integrate a large number of biochemical, physiologic and rheological factors and be validated by experimental data. The aim of this paper is to present a successful way of coupling two of the most complex macroscopic continuum based models of blood flow and biochemistry proposed in [1,3]. The work presented herein merges and significantly extends our previous studies [10] and [9]. We refer the reader to those papers for details concerning the model development and implementation, since they are essential to fully understand the present work.

The main added features introduced in this new paper are related to the extension of the coupled coagulation model presented in [10] by switching from the simple generalized Newtonian model to a new non-linear viscoelastic model that was previously implemented and tested in [9]. In comparison with our previous papers, the clot evolution is simulated on a longer time-interval, giving a better picture of the long-term behavior of the clotting process. In addition, the mechanical effects of the clot formation on the perturbation of the surrounding blood flow is studied in more detail than in our previous works.

2. Mathematical Models

The mathematical model consists of a coupled system of nonlinear partial differential equations describing the flow of blood and a biochemical cascade of reactions leading to the clot formation.

2.1. Blood Flow Model

The flow is described by a nonlinear shear-thinning and viscoelastic fluid model following the thermodynamics framework established in [27] and extended for blood flow in [4]. The set of governing equations is based on the conservation of mass (reduced to a divergence-free constraint) and the conservation of linear momentum for an incompressible fluid

$$\boldsymbol{\nabla} \cdot \boldsymbol{u} = 0 \tag{2.1}$$

$$\rho \left(\frac{\partial \boldsymbol{u}}{\partial t} + \boldsymbol{u} \cdot \boldsymbol{\nabla} \boldsymbol{u} \right) = \boldsymbol{\nabla} \cdot \boldsymbol{T}. \tag{2.2}$$

The stress tensor $\boldsymbol{T}$ is split as follows:

$$\boldsymbol{T} = -p\boldsymbol{1} + \mu \, \boldsymbol{B}_{\kappa_p(t)} + \eta_1 \boldsymbol{D} \tag{2.3}$$

where $\boldsymbol{D} = (\boldsymbol{L} + \boldsymbol{L}^T)/2$ denotes the symmetric part of the velocity gradient tensor $\boldsymbol{L}$, $\boldsymbol{1}$ stands for the identity tensor and μ, η_1 are positive material parameters.

The upper-convected time-derivative[1] of the elastic stretch tensor $\boldsymbol{B}_{\kappa_p(t)}$ is given by[2]:

$$\overset{\triangledown}{\boldsymbol{B}}_{\kappa_p(t)} = -\frac{1}{\tau(\boldsymbol{B}_{\kappa_p(t)})}\left[\boldsymbol{B}_{\kappa_p(t)} - \lambda \boldsymbol{1}\right] \tag{2.5}$$

Here the $\tau = \tau(\boldsymbol{B}_{\kappa_p(t)})$ defined by equation (2.6) has the dimension of time and plays a role similar to the relaxation time in the classical Oldroyd-B (Maxwell) model [11].

$$\frac{1}{\tau(\boldsymbol{B}_{\kappa_p(t)})} = 2K\left(\text{tr}(\boldsymbol{B}_{\kappa_p(t)}) - 3\lambda\right)^n \tag{2.6}$$

The coefficient λ depends on the trace of the inverse of the tensor $\boldsymbol{B}_{\kappa_p(t)}$ according to

$$\lambda = \frac{3}{\text{tr}\left(\boldsymbol{B}_{\kappa_p(t)}^{-1}\right)} \qquad . \tag{2.7}$$

The remaining model coefficients for blood are taken from [4]:

$$\eta_1 = 0.01 \ Pa \cdot s; \quad \mu = 0.1611 \ N/m^2; \quad n = 0.5859; \quad K = \left(\frac{\mu}{\alpha}\right)^{1+2n} = 58.0725 \ s^{-1}$$

Using the definition of the upper-convected time derivative (2.4), the left-hand side can be rewritten in a more conventional form in terms of the material time-derivative:

$$\frac{d\boldsymbol{B}_{\kappa_p(t)}}{dt} - \left[\boldsymbol{L}\boldsymbol{B}_{\kappa_p(t)} + \boldsymbol{B}_{\kappa_p(t)}\boldsymbol{L}^T\right] = -\frac{1}{\tau(\boldsymbol{B}_{\kappa_p(t)})}\left[\boldsymbol{B}_{\kappa_p(t)} - \lambda\boldsymbol{1}\right] \tag{2.8}$$

Finally, expanding the material time-derivative on the left-hand side we end up with

$$\frac{\partial \boldsymbol{B}_{\kappa_p(t)}}{\partial t} + (\boldsymbol{u}\cdot\boldsymbol{\nabla})\,\boldsymbol{B}_{\kappa_p(t)} = -\frac{1}{\tau}\left[\boldsymbol{B}_{\kappa_p(t)} - \lambda\boldsymbol{1}\right] + \left[\boldsymbol{L}\boldsymbol{B}_{\kappa_p(t)} + \boldsymbol{B}_{\kappa_p(t)}\boldsymbol{L}^T\right] \tag{2.9}$$

where the coefficients λ and τ are scalar functions of the tensor $\boldsymbol{B}_{\kappa_p(t)}$ and its invariants. More details related to this model and its implementation can be found e.g. in [9].

2.2. Biochemistry Model

The biochemistry model is based on a coupled set of non-linear advection-diffusion-reaction (ADR) equations. It has been originally developed in [1] and further extended in [3]. It describes the spatio-temporal evolution of concentrations $[C_i]$ of 23 chemical constituents (enzymes, zymogens, proteins, etc.) that can be written as

$$\frac{\partial [C_i]}{\partial t} + \boldsymbol{u}\cdot\boldsymbol{\nabla}[C_i] = \boldsymbol{\nabla}\cdot(D_i\boldsymbol{\nabla}[C_i]) + R_i \tag{2.10}$$

The non-linear chemical reaction terms R_i are mainly based on first order, second order or Michaelis-Menten kinetics. As an example we mention the reaction term R_{Ia} in the equation for fibrin production[3]:

$$R_{Ia} = \frac{k_1[IIa][I]}{K_{1M} + [I]} - \frac{h_1[PLA][Ia]}{H_{1M} + [Ia]} \tag{2.11}$$

---

[1]The upper–convected Oldroyd derivative of a tensor $\boldsymbol{A}$ is defined by

$$\overset{\triangledown}{\boldsymbol{A}} =: \frac{d\boldsymbol{A}}{dt} - \boldsymbol{L}\boldsymbol{A} - \boldsymbol{A}\boldsymbol{L}^T. \tag{2.4}$$

[2]The subscript $\kappa_p(t)$ is used to emphasize that the stretch is expressed with respect to the natural (time dependent) configuration $\kappa_p(t)$. This notation has been used in [4,27] and [9] where the model has been introduced and used.

[3]The subscript Ia refers to the chemical notation for factor Ia, an activated protein named fibrin.

The concentrations of *thrombin* (denoted by $[IIa]$), *fibrinogen* (denoted by $[I]$), *fibrin* (denoted by $[Ia]$) and *plasminogen* (denoted by $[PLA]$) are used to evaluate the reaction term R_{Ia}. The chemical kinetics rates k_1, h_1 and the constants K_{1M}, H_{1M} are known in the literature (taken from [3]). The values of the diffusion parameters D_i and the exact form of the reaction terms R_i are given in [10], where the model has been implemented for the first time and used in 3D simulations.

2.3. Coupling Strategy

The clot is a gel like structure consisting of a polymer (*fibrin* network), entrapping various blood components [16] and thus fibrin concentration can be used as an indicator of the clot formation. The main idea is to make the material properties of blood/clot dependent on fibrin concentration. For low fibrin concentration the fluid behaves like flowing blood, while for high fibrin concentration the fluid changes its behavior to a clot-like medium. In our model the fluid viscosity is multiplied by a factor $\tilde{\eta}_1$ that locally depends (linearly, up to a certain saturation value η^*) on the fibrin concentration $[Ia]$. The viscosity η_1 is multiplied by a non-dimensional factor $\tilde{\eta}_1$

$$\tilde{\eta}_1 = \min\left\{1 + \frac{\eta^* - 1}{C_{clot}}[Ia], \eta^*\right\} \tag{2.12}$$

In our study we have used $\eta^* = 100$ and $C_{clot} = 1000 \ nM$.

In this framework the clot is characterized as a highly viscous fluid. The region occupied by the simulated clot represents an obstacle to the flow field, with much lower viscosity. This effect is even significantly magnified due to the non-Newtonian shear-thinning behavior of blood, leading to a further increase of the fluid viscosity in regions of low shear.

Changes in the viscosity modify the local flow field which consequently affects the concentration field that leads to further changes in viscosity. In this way the interaction biochemistry-flow through this coupling strategy is enforced. More details can be found in [10] where this technique has been used for a generalized Newtonian model, i.e. neglecting the viscoelasticity. In the present study the technique has been extended to the new non-linear viscoelastic model as suggested in [2, 3, 5].

3. Numerical Methods

The system of governing equations is rather complex and highly non-linear. This is why the numerical discretization has been chosen to be as simple and predictable as possible. We do not claim this choice is optimal, it only serves as the first step allowing the evaluation of the underlying mathematical model and to test its applicability in simple configurations. A semi-discretization approach is adopted to first discretize the PDEs in space and then integrating the resulting system of ODEs in time, both for the blood flow and the biochemical model.

The *space discretization* is based on a simple central finite-volume discretization on a structured grid with hexahedral cells. A multiblock grid topology with wall-fitted cells is used. The viscous fluxes are also discretized using a finite-volume method over a diamond-shaped cells adjoint to primary control volumes faces. This approach was used in our previous papers [8, 11, 13] or in [22, 23].

The *time integration* is performed using a Runge-Kutta (RK) multistage scheme. A specific advection-diffusion optimized RK method is used to reduce the computational cost. The basic idea behind this subclass of RK methods is to split the space-discretization operator into its inviscid and viscous parts. The inviscid part is evaluated in every stage of the RK method while the viscous fluxes are only evaluated in a few stages. This corresponds to an operator splitting technique with different RK methods (coefficients) used for the advection step and another for the diffusion step. This allows to save several (very expensive) evaluations of diffusive fluxes per time-step while retaining the rather large stability region of the RK method. For details see [19, 20] or [11, 13].

Along with these two basic components of the numerical solver a specific stabilization technique is used to avoid non-physical numerical oscillations due to the central discretization. The non-linear TVD filter [15, 32] was used to smooth the concentration fields, as recently reported in [7].
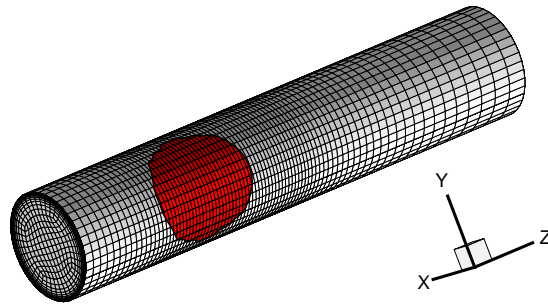
4. Numerical Results

FIGURE 1. Grid structure and clotting surface position.

(a) Thrombin

(b) Fibrin

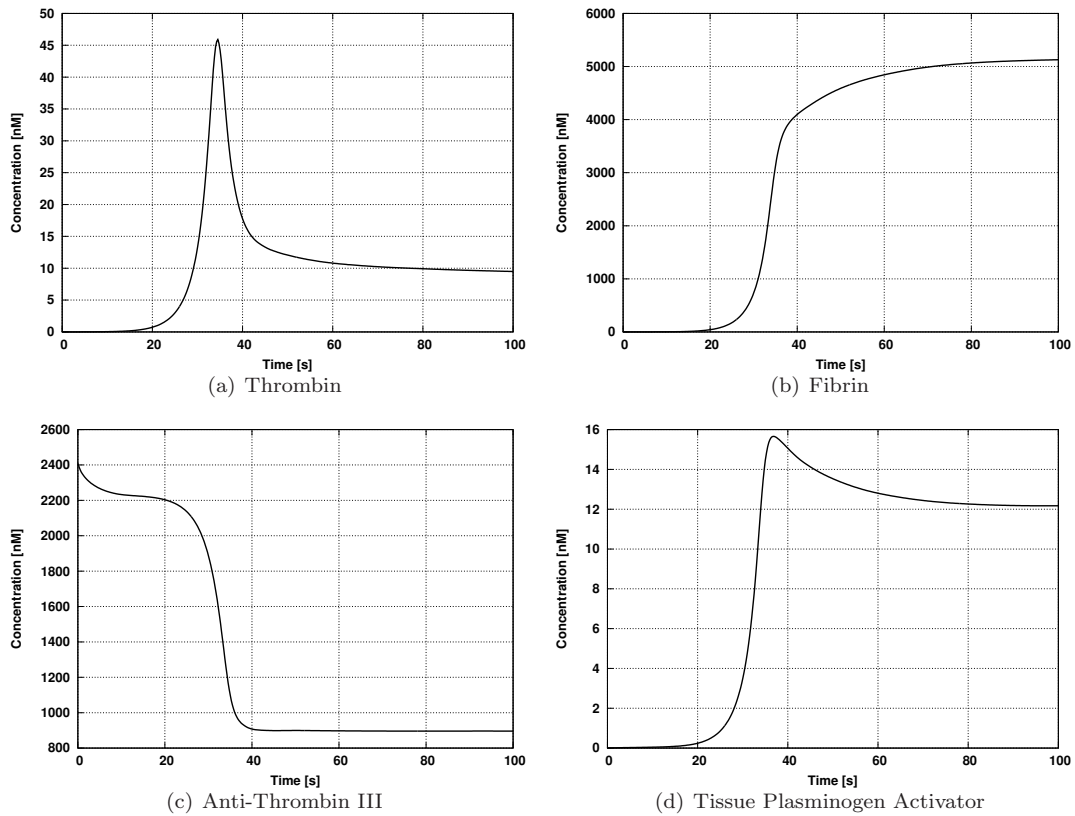(c) Anti-Thrombin III

(d) Tissue Plasminogen Activator

FIGURE 2. Time evolution of selected concentrations in the center of the clotting surface during the initial 100 seconds.
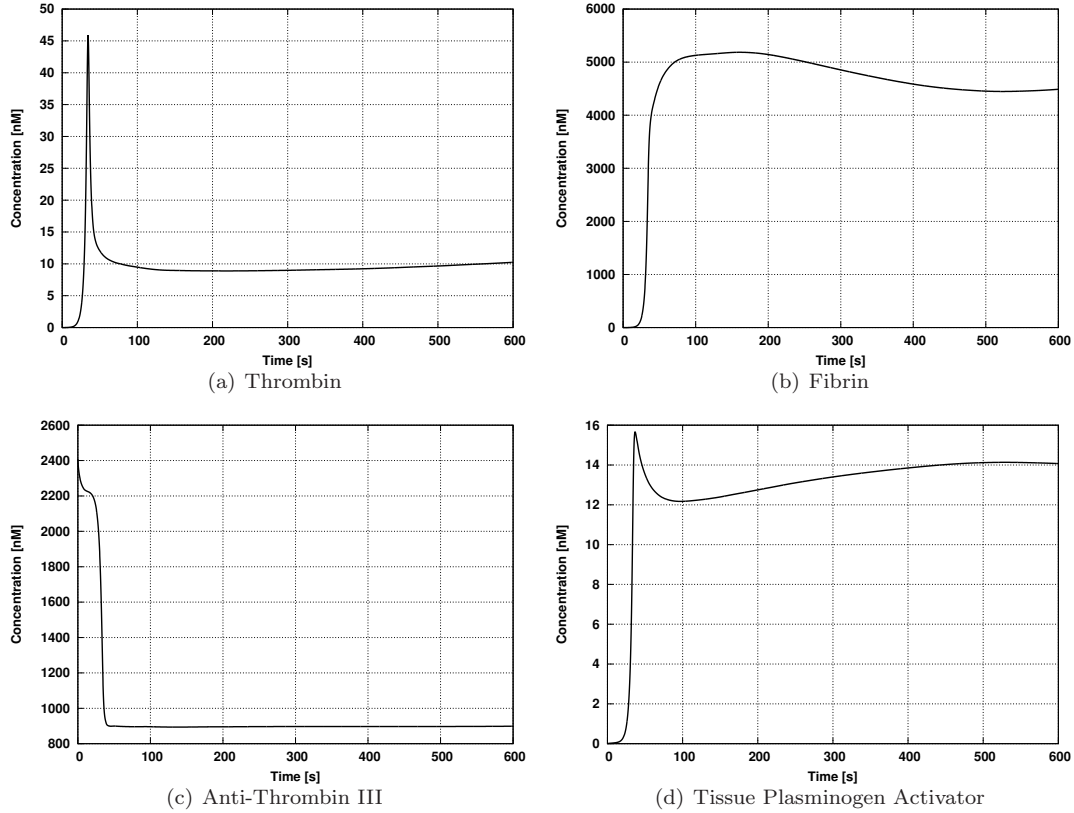
FIGURE 3. Time evolution of selected concentrations in the center of the clotting surface during the initial 10 minutes.

The numerical test case is similar to the one used in [10] and [9], where we refer the complete parameter set for this simulation. The geometry represents a straight section of a blood vessel with diameter $6.2\,mm$ and length $31\,mm$ with grid shown in Figure 1.

The clotting surface is simulated in a region that is formed by the intersection of a sphere (of radius $3.1\,mm$) with the blood vessel wall. The evolution in space and time of the clot is tracked down.

The model is very complex and thus the simulations generate large amounts of data to be visualized, analyzed, and understood. In this paper only a few snapshots of results are presented to demonstrate some of the most important model outputs.

The evolution in time of some of the coagulation factors can be observed in figures 2 and 3. The concentration is visualized in a single point located in the center of the clotting surface on the vessel wall. Only the initial 600 seconds of clotting are shown.

These graphs show the nature of the coagulation process, initially very fast, with rather slow long term evolution in the later phase.

The spatial extent of the clot can be shown using the fibrin concentration contours. Figure 4 shows those contours on the surface of the blood vessel.

The velocity field is affected by the clotting which results in flow deceleration and velocity magnitude reduction in the regions of high fibrin concentration. To quantify and visualize the local flow deceleration,
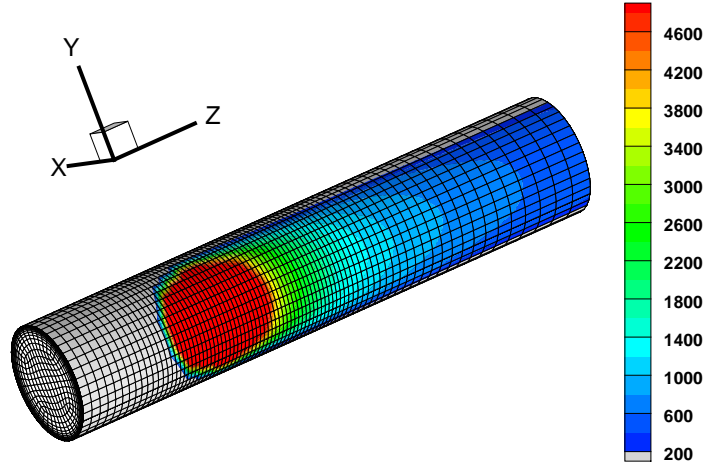
FIGURE 4. Fibrin concentration contours on the vessel wall at time $100\,s$.

the non-dimensional velocity reduction δ is defined as

$$\delta(\boldsymbol{x}, t) = \frac{q(\boldsymbol{x}, 0) - q(\boldsymbol{x}, t)}{q(\boldsymbol{x}, 0)} \quad . \tag{4.1}$$

Here $q(\boldsymbol{x}, t)$ is the local velocity magnitude $q = \sqrt{u^2 + v^2 + w^2}$. Since the no-slip condition is imposed on the vessel wall, the velocity reduction is evaluated in the first near-wall grid node.

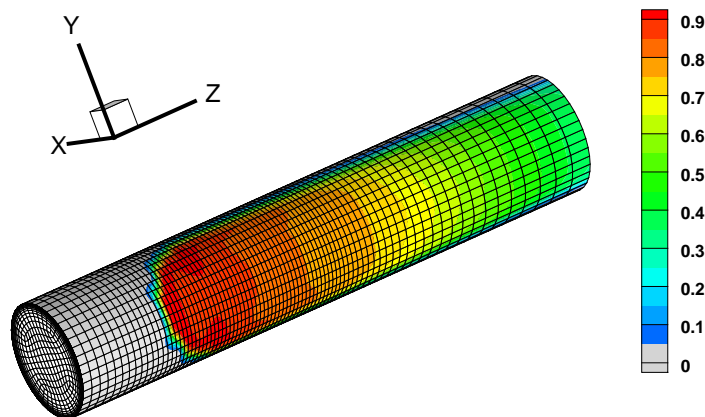A snapshot of flow velocity magnitude reduction δ is shown in Figure 5.

FIGURE 5. Near wall velocity magnitude reduction δ at time $100\,s$.

A. Sequeira, T. Bodnár   Blood coagulation simulations using a non-linear viscoelastic flow model

Time evolution of the clot growth and its effects on blood flow can be observed in Figure 6 showing the fibrin concentration and the velocity reduction δ on the deployed vessel surface[4].

(a) Fibrin concentration $[Ia]$ (b) Blood velocity reduction δ
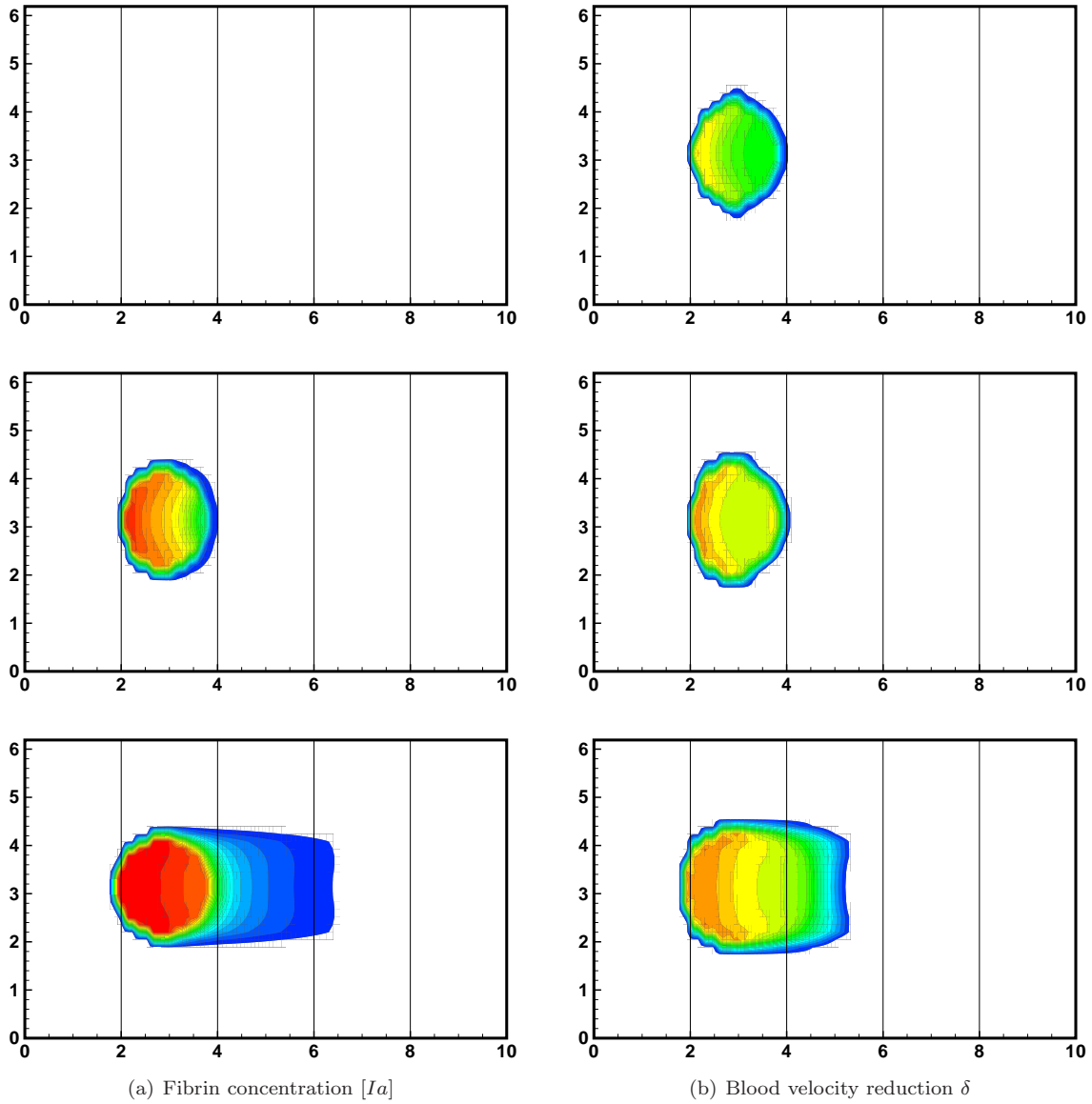
FIGURE 6. Clot evolution during the initial 60 seconds: snapshots at times $t = 20,\ 40,\ 60\,s$, from top to bottom.

---

[4]The spatial dimensions are normalized using the vessel radius (half-diameter) $R = 3.1mm$.

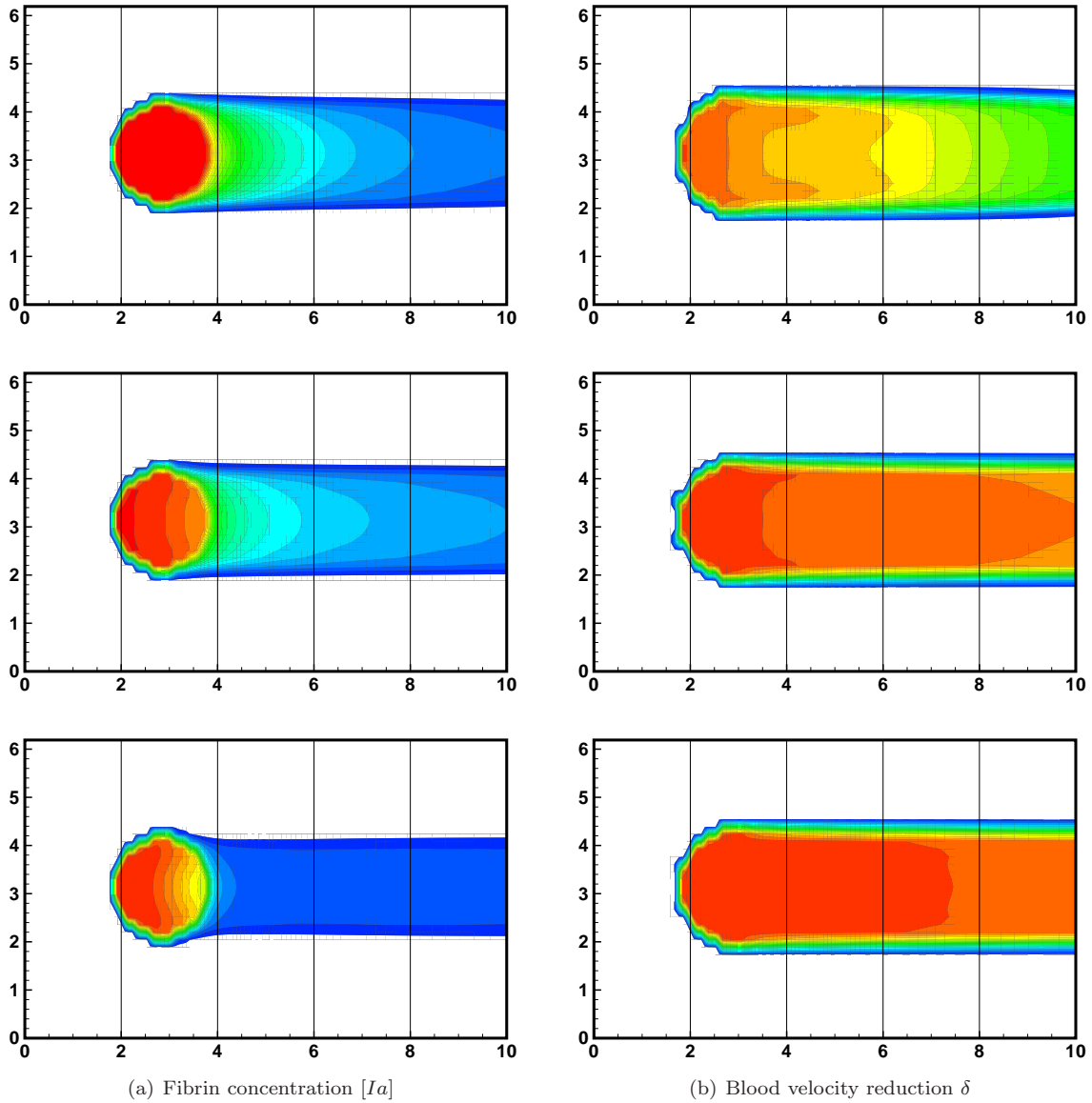The same kind of visualization, but for a longer period of 600 seconds was used in Figure 7.

(a) Fibrin concentration $[Ia]$ (b) Blood velocity reduction δ

FIGURE 7. Clot evolution during the initial 600 seconds: snapshots at times $t = 120,\ 360,\ 600\ s$, from top to bottom.

A better picture of the fibrin levels during the initial phase of clotting can be seen in Figure 8 showing the concentrations along a line segment passing through the center of the clotting surface. A longer time evolution of the clot during the initial $600\ s$ is visualized in the contour map in Figure 9. Resulting flow deceleration is depicted in Figure 10.
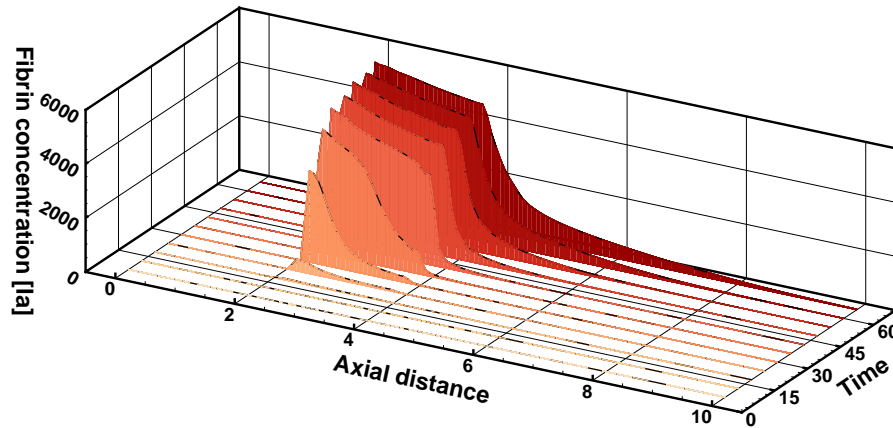
FIGURE 8. Fibrin concentration evolution along an axial surface line during the initial 60 seconds.

FIGURE 9. Fibrin concentration $[Ia]$ along the axial surface line.

5. Conclusions

The numerical study presented in this paper has demonstrated the successful implementation of the coupled blood flow and the biochemistry models. The blood flow model is now more complex in comparison with the one presented in our previous work for blood coagulation presented in [10]. The viscoelastic

FIGURE 10. Flow velocity reduction δ in the near-wall layer along the axial direction.
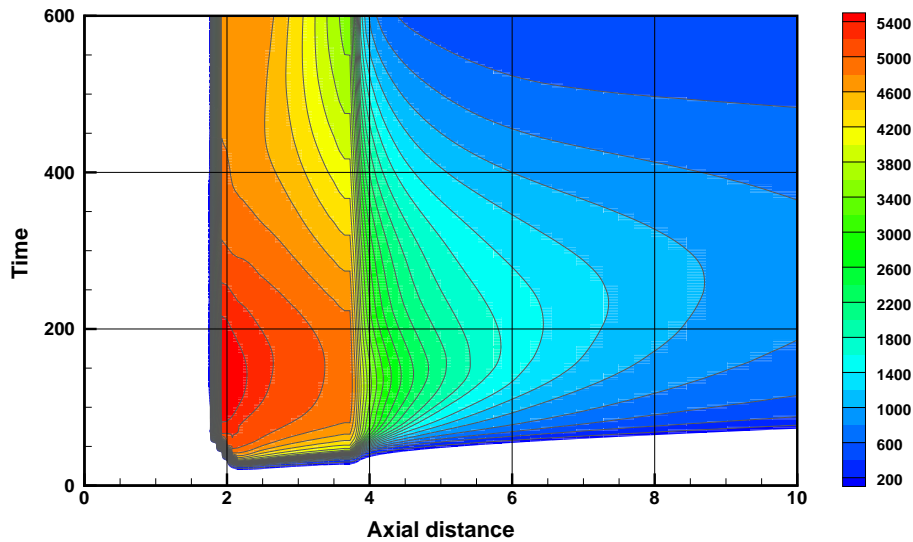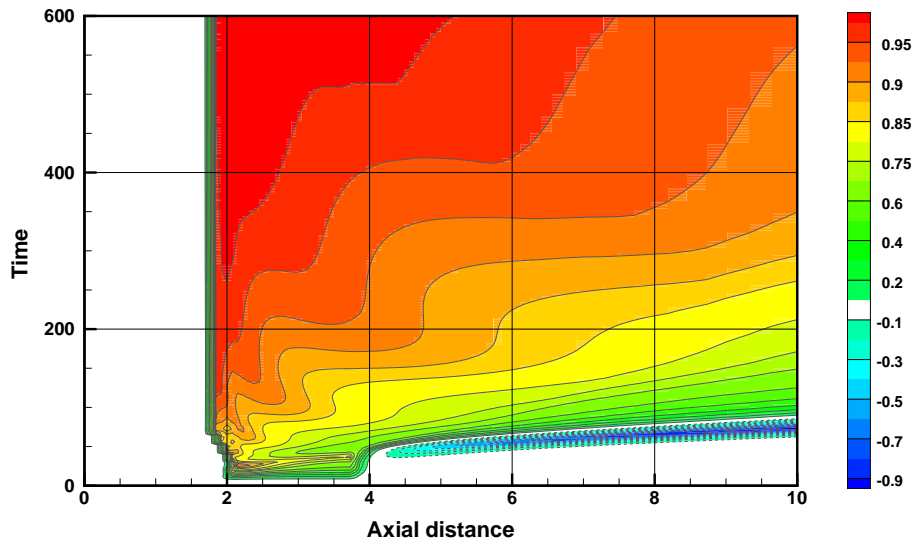
extension of the model should allow to extend the range of applicability of the model to critical flow regimes. However, the use of this non-linear viscoelastic model extension results in an important increase of the computational costs. The original, generalized Newtonian model with shear-thinning viscosity, contains $4 + 23 = 27$ PDEs to solve in 3D. The new model has 6 more equations for the components of the viscoelastic stress tensor. This means that we solved now $4 + 6 + 23 = 33$ equations for the coupled model accounting for the blood rheology and the biochemical processes.

Future research will focus on performance and robustness improvements of the model and numerical solvers. The stability issues raised in [31] should also be addressed in the context of the new modifications of the model. Both of these topics will be important in future applications of the model requiring long time simulations of the clot growth evolution.

References

[1] M. Anand, K. Rajagopal, K.R. Rajagopal. *A model incorporating some of the mechanical and biochemical factors underlying clot formation and dissolution in flowing blood.* J. of Theoretical Medicine, 5 (2003), no. 3–4, 183–218.

[2] M. Anand, K. Rajagopal, K.R. Rajagopal. *A model for the formation and lysis of blood clots.* Pathophysiology Haemostasis Thrombosis, 34 (2005), 109–120.

[3] M. Anand, K. Rajagopal, K.R. Rajagopal. *A model for the formation, growth, and lysis of clots in quiescent plasma. A comparison between the effects of antithrombin III deficiency and protein C deficiency.* J. of Theoretical Biology, 253 (2008), 725–738.

[4] M. Anand, K.R. Rajagopal. *A shear-thinning viscoelastic fluid model for describing the flow of blood.* Int. J. of Cardiovascular Medicine and Science, 4 (2004), no. 2, 59–68.

[5] M. Anand, K.R. Rajagopal. *A mathematical model to describe the change in the constitutive character of blood due to platelet activation.* C. R. Méchanique, 330 (2002), 557–562.

[6] F.I. Ataullakhanov, V.I. Zarnitsina, A.V. Pokhilko, A.I. Lobanov, O.L. Morozova. *A spatio-temporal dynamics of blood coagulation and pattern formation. A theoretical approach.* International Journal of Bifurcation and Chaos, 12 (2002), no. 9, 1985–2002.

[7] T. Bodnár. *On the use of non-linear TVD filters in finite-volume simulations.* In: Algoritmy 2012, Proceedings of Contributed Papers and Posters, Slovak University of Technology, Faculty of Civil Engineering, Bratislava (2012), 190–199.

[8] T. Bodnár, J. Příhoda. *Numerical simulation of turbulent free-surface flow in curved channel.* Journal of Flow, Turbulence and Combustion, 76 (2006), no. 4, 429–442.

[9] T. Bodnár, K.R. Rajagopal, A. Sequeira. *Simulation of the three-dimensional flow of blood using a shear-thinning viscoelastic fluid model.* Mathematical Modelling of Natural Phenomena, 6 (2011), no. 5, 1–24.

[10] T. Bodnár, A. Sequeira. *Numerical simulation of the coagulation dynamics of blood.* Computational and Mathematical Methods in Medicine, 9 (2008), no. 2, 83–104.

[11] T. Bodnár, A. Sequeira. *Numerical Study of the Significance of the Non-Newtonian Nature of Blood in Steady Flow Through a Stenosed Vessel.* In: Advances in Mathematical Fluid Mechanics. (edited by R. Rannacher & A. Sequeira), 83–104, Springer Verlag (2010).

[12] T. Bodnár, A. Sequeira, L. Pirkl. *Numerical Simulations of Blood Flow in a Stenosed Vessel under Different Flow Rates using a Generalized Oldroyd - B Model.* In: Numerical Analysis and Applied Mathematics, Vols 1 and 2. Melville, New York: American Institute of Physics, vol. 2 (2009), 645–648.

[13] T. Bodnár, A. Sequeira, M. Prosi. *On the Shear-Thinning and Viscoelastic Effects of Blood Flow under Various Flow Rates.* Applied Mathematics and Computation, 217 (2011), 5055–5067.

[14] S. Butenas, K. G. Mann. *Blood coagulation.* Biochemistry (Moscow), 67 (2002), no. 1, 3–12. Translated from Biokhimiya, 67 (2002), no. 1, 5–15.

[15] B. Engquist, P. Lötstedt, B. Sjögreen. *Nonlinear filters for efficient shock computation.* Mathematics of Computation, 52 (1989), no. 186, 509–537.

[16] A. Fasano, R.F. Santos, A. Sequeira. *Blood coagulation: a puzzle for biologists, a maze for mathematicians.* In D. Ambrosi, A. Quarteroni, and G. Rozza (Eds.) *Modeling of Physiological Flows.* vol. 5, Modeling, Simulation & Applications, ch. 3 (2012) 41–75, Springer.

[17] G.P. Galdi, R. Rannacher, A. M. Robertson, S. Turek (Eds.) *Hemodynamical Flows: Modeling, Analysis and Simulations.* (Oberwolfach Seminars), (2008) Birkhäuser Verlag.

[18] A.M. Gambaruto, J. Janela, A. Moura, A. Sequeira. *Sensitivity of hemodynamics in a patient specific cerebral aneurysm to vascular geometry and blood rheology.* Mathematical Biosciences and Engineering, 8 (2011), no. 2, 409–423.

[19] A. Jameson. *Time dependent calculations using multigrid, with applications to unsteady flows past airfoils and wings.* In AIAA 10th Computational Fluid Dynamics Conference, Honolulu (1991). AIAA Paper 91–1596.

[20] A. Jameson, W. Schmidt, E. Turkel. *Numerical solutions of the Euler equations by finite volume methods using Runge-Kutta time-stepping scheme.* In: AIAA 14th Fluid and Plasma Dynamics Conference, Palo Alto (1981), AIAA paper 81–1259.

[21] J. Janela, A. Moura, A. Sequeira. *Absorbing boundary conditions for a 3D non- Newtonian fluid-structure interaction model for blood flow in arteries.* International Journal of Engineering Science, 48 (2010), no. 11, 1332–1349.

[22] R. Keslerová. *Numerical study of effect of stress tensor for viscous and viscoelastic fluids flow.* In: A. Cangiani, R.L. Davidchack, E. Georgoulis, A.N. Gorban J. Levesley, and M.V. Tretyakov (Eds.) *Numerical Mathematics and Advanced Applications* (2013), 529– 538. Springer. Proceedings of ENUMATH 2011, the 9th European Conference on Numerical Mathematics and Advanced Applications, Leicester, September 2011.

[23] R. Keslerová, K. Kozel. *Numerical solution of laminar incompressible generalized newtonian fluids flow.* Applied Mathematics and Computation, 217 (2011), no. 11, 5125–5133.

[24] A.L. Kuharsky, A.L. Fogelson. *Surface-mediated control of blood coagulation: the role of binding site densities and platelet deposition.* Biophysical Journal, 80 (2001), 1050–1074.

[25] K.G. Mann, K. Brummel-Ziedins, T. Orfeo, S. Butenas. *Models of blood coagulation.* Blood Cells, Molecules, and Diseases, 36 (2006), 108–117.

[26] L. Pirkl, T. Bodnár, K. Tuma. *Viscoelastic fluid flows at moderate Weissenberg numbers using Oldroyd type model.* In: AIP Conference Proceedings, vol. 1389 (2011), 102–105, American Institute of Physics.

[27] K.R. Rajagopal, A.R. Srinivasa. *A thermodynamic frame work for rate type fluid models.* Journal of Non-Newtonian Fluid Mechanics, 80 (2000), 207–227.

[28] P. Riha, X. Wang, R. Liao, J.F. Stoltz. *Elasticity and fracture strain of blood clots.* Clinical Hemorheology and Microcirculation, 21 (1999), no. 1, 45–49.

[29] A.M. Robertson, A. Sequeira, M. Kameneva. *Hemorheology.* In: *Hemodynamical Flows: Modelling, Analysis and Simulation,* vol 37, (2008), 63–120, Birkhäuser .

[30] A.M. Robertson, A. Sequeira, R.G. Owens. *Rheological models for blood.* In:*Cardiovascular Mathematics. Modeling and Simulation of the Circulatory System* (MS&A) (2009), 211–241, Springer-Verlag .

[31] A. Sequeira, R.F. Santos, T. Bodnár. *Blood coagulation dynamics: Mathematical modeling and stability results.* Mathematical Biosciences and Engineering, 8 (2011), no. 2, 425–443.

[32] W. Shyy, M.-H. Chen, R. Mittal, H.S. Udaykumar. *On the suppression of numerical oscillations using a non-linear filter.* Journal of Computational Physics, 102 (1992), 49–62.

[33] V.I. Zarnitsina, A.V. Pokhilko, F. I. Ataullakhanov. *A mathematical model for the spatio-temporal dynamics of intrinsic pathway of blood coagulation - I. The model description.* Thrombosis Research, 84 (1996), no. 4, 225–236.

Chapter C

Concluding Remarks

The numerical methods and simulations presented in this work were focused on the solution of certain non-standard problems of incompressible fluids flows. Due to the variable density and non-trivial rheological behavior of the considered fluids, the original in-house built numerical codes were developed and used by the author of this work. The choice of mathematical models, numerical methods and discretization strategies was essentially motivated by the practical complex applications, although mainly simplified cases were solved at this stage.

The numerical simulations presented in the above selection of papers has shown that the adopted models and methods performed rather well in simulating specific physical phenomena. In most cases the development and testing of the used mathematical model was at least as important as the testing of numerical methods and their implementation. Thus the adopted numerical methods and test cases were kept often simple, which made their behavior easier to predict, distinguish and separate from the behavior of the considered mathematical model. In this context, it can be concluded, that the presented numerical simulations provided a useful insight into the development of new, non-standard numerical models of various physical phenomena arising in biomedical and environmental applications.

The presented work is currently being further developed and extended by the author. In the environmental applications branch, the variable density stratified flows are now studied in detail. Especially the problems related to well posedness of the mathematical formulations are addressed with special aim to employ mathematically consistent, computationally robust and physically meaningful boundary conditions. The biomedical applications oriented research led to a new series of works aimed to address the high Weissenberg number problem. The author's current work under progress in this field goes towards the application of the newly emerging log-conformation transformation methods in the for numerical simulation of viscoelastic fluids flows.

The wide range of problems presented in the above works has shown that the mathematical modeling and numerical simulation of incompressible fluids flows remains a challenging area of research. It has large potential of future development, to which the author of this work aims to further contribute.

<div align="right">

In Prague, July 30, 2017

Tomáš Bodnár

</div>

Chapter A

Appendix

Complete Bibliography of the Author

The bibliographic records are sorted chronologically in descending order, i.e. starting from the most recent ones. This list was taken from the official faculty database of publications. The records that appear in public databases *Web of Science* and *Scopus* are highlighted.

[1] **T. BODNÁR AND P. FRAUNIÉ. Numerical simulation of the wake structure behind three-dimensional hill under stable stratification. In *Topical problems of fluid mechanics 2016*, pages 17–22, Prague, CZ, 2016.**

[2] **T. BODNÁR AND P. FRAUNIÉ. Numerical study of stratification effects on local wind flow and pollution dispersion. In *Topical Problems of Fluid Mechanics 2015*, pages 11–16, Praha, CZ, 2015.**

[3] **T. BODNÁR. On the Eulerian formulation of a stress induced platelet activation function. *Mathematical Biosciences*, 257:91–95, November 2014.**

[4] T. BODNÁR, G.P. GALDI, AND Š. NEČASOVÁ, editors. *Fluid-Structure Interaction and Biomedical Applications*. Birkhäuser, 2014.

[5] T. BODNÁR, A. FASANO, AND A. SEQUEIRA. *Mathematical Models for Blood Coagulation*, pages 483–569. *Fluid-Structure Interaction and Biomedical Applications*. Birkhäuser, 2014.

[6] **T. BODNÁR, J. JANELA, AND M. PIRES. Blood flow simulation using traceless variant of Johnson-Segalman viscoelastic model. *Mathematical Modelling of Natural Phenomena*, 9(6):117–141, 2014.**

[7] T. BODNÁR, K. KOZEL, AND P. FRAUNIÉ. Simulation of the start-up of a turbulent free convection driven by wall heating and cooling. In *Conference Topical Problems of Fluid Mechanics 2014*, pages 21–24, Prague, CZ, 2014.

[8] **T. BODNÁR, L. MATEJÍČEK, Š. NOSEK, AND E. GULÍKOVÁ. Processing of environmental data for air dispersion numerical models and aerodynamic research in wind tunnels. In *Proceedings of the 7th International Congress on Environmental Modelling and Software*, San Diego, US, 2014.**

[9]   T. BODNÁR AND A. SEQUEIRA. **Blood coagulation simulations using a viscoelastic model.** *Mathematical Modelling of Natural Phenomena*, 9(6):34–45, 2014.

[10]   P. FRAUNIÉ, H. HOUCINE, A. GHARBI, T. BODNÁR, L. BENEŠ, AND Y. CHASHECHKIN. Numerical analysis of stratified wake flows. In *Conference Topical Problems of Fluid Mechanics 2014*, pages 29–30, Prague, CZ, 2014.

[11]   L. BENEŠ, T. BODNÁR, AND J. FÜRST. Numerical modeling of stably stratified fluid flow. In *Numerical Mathematics and Advanced Applications 2011*, pages 481–488, Heidelberg, DE, 2013.

[12]   T. BODNÁR AND K. KOZEL. Numerical simulation of atmospheric boundary layer flows at wind tunnel scale. In *Topical problems of Fluid Mechanics 2013*, pages 1–4, Praha, CZ, 2013.

[13]   T. BODNÁR AND A. SEQUEIRA. **On the implementation of a non-linear viscoelastic model into coupled blood flow-biochemistry model. In *SIMULTECH 2013*, pages 652–657, Porto, PT, 2013.**

[14]   L. BENEŠ, T. BODNÁR, AND K. KOZEL. **Numerical simulation of the neutrally stratified ABL flow over complex geometry. In *AIP conference proceedings International Conference of Computational Methods in Sciences and Engineering 2009*, pages 1043–1046, Melville, New York, US, 2012.**

[15]   L. BENEŠ AND T. BODNÁR. Numerical simulation of horizontal strip moving in stratified water. In *Conference Topical Problems of Fluid Mechanics 2012*, pages 9–12, Praha, CZ, 2012.

[16]   T. BODNÁR, L. BENEŠ, K. KOZEL, AND P. FRAUNIÉ. **Application of compact finite-difference schemes to simulations of stably stratified fluid flows. *Applied Mathematics and Computation*, 219(7):3336–3353, 2012.**

[17]   T. BODNÁR, L. BENEŠ, AND K. KOZEL. On a comparison of numerical simulations of atmospheric flow over complex terrain. In *Colloquium Fluid Dynamics 2012 Proceedings*, pages 1–2, Prague, CZ, 2012.

[18]   T. BODNÁR, L. BENEŠ, L. PIRKL, AND E. GULÍKOVÁ. **A numerical study of wind flow over a coal storage shelter. *Acta Polytechnica*, 52(6):116–123, 2012.**

[19]   T. BODNÁR. **On the use of non-linear TVD filters in finite–volume simulations. In *Algoritmy 2012 Proceedings of Contributed Papers and Posters*, pages 190–199, Bratislava, SK, 2012.**

[20]   T. BODNÁR AND L. BENEŠ. **On some high resolution schemes for stably stratified fluid flows. In *Finite Volumes for Complex Applications VI, Problems & Perspectives*, Springer Proceedings in Mathematics, pages 145–153, Berlin, DE, 2011.**

[21]   T. BODNÁR AND L. PIRKL. A remark on the deviatoric decomposition of Oldroyd type models. In *Colloquium Fluid Dynamics 2011*, pages 1–5, Prague, CZ, 2011.

[22]   T. BODNÁR, K.R. RAJAGOPAL, AND A. SEQUEIRA. **Simulation of the three–dimensional flow of blood using a shear–thinning viscoelastic fluid model. *Mathematical Modelling of Natural Phenomena*, 6(5):1–24, 2011.**

[23] T. BODNÁR, A. SEQUEIRA, AND M. PROSI. **On the shear–thinning and viscoelastic effects of blood flow under various flow rates.** *Applied Mathematics and Computation,* **217(11):5055–5067, 2011.**

[24] L. PIRKL AND T. BODNÁR. On the numerical simulation of blood coagulation in flowing blood. In *Topical Problems of Fluid Mechanics 2011*, pages 89–92, Prague, CZ, 2011.

[25] L. PIRKL, T. BODNÁR, AND K. TŮMA. **Viscoelastic fluid flows at moderate Weissenberg numbers using Oldroyd type model.** In *ICNAAM-2011 Proceedings of the International Conference on Numerical Analysis and Applied Mathematics 2011,* **AIP Conference Proceedings, pages 102–105, Melville, New York, US, 2011.**

[26] A. SEQUEIRA, R.F. SANTOS, AND T. BODNÁR. **Blood coagulation dynamics: Mathematical modeling and stability results.** *Mathematical Biosciences and Engineering,* **8(2):425–443, 2011.**

[27] T. BODNÁR, L. BENEŠ, I. SLÁDEK, AND K. KOZEL. Numerical models for complex atmospheric flows problems. In *Topical Problems of Fluid Mechanics 2010 Proceedings*, pages 19–22, Prague, CZ, 2010.

[28] T. BODNÁR, P. FRAUNIÉ, AND K. KOZEL. **Numerical simulations of stably stratified fluid flow using compact finite - difference schemes.** In *Numerical Analysis and Applied Mathematics, Vols I - III,* **AIP Conference Proceedings, pages 103–106, New York, US, 2010.**

[29] T. BODNÁR, P. FRAUNIÉ, AND K. KOZEL. On the use of high order compact schemes for the simulation of stably stratified fluid flow. In *Proceedings of the Fifth Conference on Computation Fluid Dynamics ECCOMAS CFD 2010*, Lisbon, PT, 2010.

[30] T. BODNÁR AND A. SEQUEIRA. **Numerical study of the significance of the non–Newtonian nature of blood in steady flow through a stenosed vessel.** In *Advances in Mathematical Fluid Mechanics: Dedicated to Giovanni Paolo Galdi on the Occasion of his 60th Birthday,* **pages 83–104, Berlin, DE, 2010.**

[31] L. PIRKL AND T. BODNÁR. The blood flow simulations using shear–thinning Oldroyd–B models. In *Topical Problems of Fluid Mechanics 2010 Proceedings*, pages 115–118, Prague, CZ, 2010.

[32] L. PIRKL AND T. BODNÁR. Numerical simulation of blood flow using generalized Oldroyd–B model. In *Proceedings of the Fifth Conference on Computation Fluid Dynamics ECCOMAS CFD 2010*, Lisbon, PT, 2010.

[33] T. BODNÁR, A. SEQUEIRA, AND L. PIRKL. **Numerical simulations of blood flow in a stenosed vessel under different flow rates using a generalized Oldroyd–B model.** In *Numerical Analysis and Applied Mathematics, Vols 1 and 2,* **AIP Conference Proceedings, pages 645–648, Melville, New York, US, 2009.**

[34] T. BODNÁR AND A. SEQUEIRA. On the blood flow simulations in axisymmetric aneurysm using generalized Oldroyd–B model. In *Topical Problems of Fluid Mechanics 2009*, pages 13–16, Prague, CZ, 2009.

[35] L. PIRKL AND T. BODNÁR. The blood flow simulations using generalized Newtonian models. In *Colloquium Fluid Dynamics 2009 Proceedings*, Prague, CZ, 2009.

[36] L. BENEŠ, T. BODNÁR, K. KOZEL, AND I. SLÁDEK. Two cases of the real ABL flow over complex orography. In *Finite Volumes for Complex Applications V*, pages 209–216, London, GB, 2008.

[37] T. BODNÁR, L. BENEŠ, AND K. KOZEL. Numerical simulation of flow and pollution dispersion in the area of opencast coal mine. In *Numerical Analysis and Applied Mathematics*, pages 100–103, Melville, New York, US, 2008.

[38] T. BODNÁR, L. BENEŠ, AND K. KOZEL. Numerical simulation of flow over barriers in complex terrain. *Nuovo Cimento Della Societa Italiana di Fisica C - Geophysics and Space Physics*, 31(5-6):619–632, 2008.

[39] T. BODNÁR AND K. KOZEL. Numerical simulation of turbulent free surface flow in an open channel. In *Topical Problems of Fluid Mechanics 2008*, pages 9–12, Praha, CZ, 2008.

[40] T. BODNÁR, K. KOZEL, AND J. PŘÍHODA. On the validation of numerical model for simulation of turbulent free - surface flows. In *Colloquium Fluid Dynamics 2008*, Prague, CZ, 2008.

[41] T. BODNÁR AND A. SEQUEIRA. Numerical simulation of the coagulation dynamics of blood. *Computational and Mathematical Methods in Medicine*, 9(2):83–104, 2008.

[42] L. MATĚJÍČEK, Z. JAŇOUR, L. BENEŠ, T. BODNÁR, AND E. GULÍKOVÁ. Spatio–temporal modelling of dust transport over surface mining areas and neighbouring residential zones. *Sensors*, 8(6):3830–3847, 2008.

[43] L. PIRKL AND T. BODNÁR. Numerical simulation of Newtonian and generalized Newtonian flows of human blood. In *Topical Problems of Fluid Mechanics 2008*, pages 81–84, Praha, CZ, 2008.

[44] L. BENEŠ, T. BODNÁR, K. KOZEL, AND I. SLÁDEK. Numerical study of atmospheric flow over open coal mine. In *Proceedings of the 9th ICDF Conference on Numerical Methods for Fluid Dynamics*, Reading, GB, 2007.

[45] T. BODNÁR AND K. KOZEL. Numerical simulation of free surface flow in a channel with ribbed bottom. In *Colloquium Fluid Dynamics 2007*, Praha, CZ, 2007.

[46] T. BODNÁR AND A. SEQUEIRA. Computational hemorheology: Progress in blood coagulation modelling. *Actas de Bioquímica*, -(9):31–41, 2007.

[47] T. BODNÁR AND A. SEQUEIRA. On the use of generalized Newtonian models for blood flow simulations. In *Topical Problems of Fluid Mechanics 2007*, pages 17–20, Praha, CZ, 2007.

[48] K. KOZEL, T. BODNÁR, E. GULÍKOVÁ, AND V. PÍŠA. Numerical simulation of flow and pollution dispersion over obstacles in complex terrain. In *Colloquium Fluid Dynamics 2007*, Praha, CZ, 2007.

[49] L. MATĚJÍČEK, T. BODNÁR, L. BENEŠ, AND E. GULÍKOVÁ. GIS based mapping for modelling of the flowfield above the surface of mining areas. In *Colloquium Fluid Dynamics 2007*, Praha, CZ, 2007.

[50] L. MATĚJÍČEK, T. BODNÁR, L. BENEŠ, AND E. GULÍKOVÁ. GIS based visualization for terrain measurements and dust deposition in the area of coal mines. In *Colloquium Fluid Dynamics 2007*, Praha, CZ, 2007.

[51] L. PIRKL AND T. BODNÁR. Numerical simulation of turbulent flows around sinusoidal hills. In *Colloquium Fluid Dynamics 2007*, Praha, CZ, 2007.

[52] I. SLÁDEK, T. BODNÁR, AND K. KOZEL.   On a numerical study of atmospheric 2D and 3D - flows over a complex topography with forest including pollution dispersion. *Journal of Wind Engineering and Industrial Aerodynamics*, 95(9-11):1424–1444, 2007.

[53] L. BENEŠ, T. BODNÁR, AND K. KOZEL. Matematické modely stratifikovaného proudění. In *Colloquium Fluid Dynamics 2006 Proceedings*, pages 5–8, Praha, CZ, 2006.

[54] T. BODNÁR AND K. KOZEL.   Numerical simulation of turbulent free surface flow over step roughness. In *Colloquium Fluid Dynamics 2006 Proceedings*, pages 17–20, Praha, CZ, 2006.

[55] T. BODNÁR AND L. PIRKL. Numerical simulation of non - Newtonian fluid flow using generalized Navier - stokes models. In *Colloquium Fluid Dynamics 2006 Proceedings*, pages 95–98, Praha, CZ, 2006.

[56] T. BODNÁR AND J. PŘÍHODA. Numerical simulation of turbulent free-surface flow in curved channel. *Flow, Turbulence and Combustion*, 76(4):429–442, 2006.

[57] T. BODNÁR AND A. SEQUEIRA. On the rheological modeling of blood flow around a clot. In *Proceedings of the 2006 WSEAS/IASME International Conference on Continuum Mechanics*, pages 73–78, Athens, GR, 2006.

[58] T. BODNÁR AND A. SEQUEIRA. Shear-thinning effects of blood flow past a formed clot. *WSEAS Transactions on Fluid Mechanics*, 1(3):207–214, 2006.

[59] T. BODNÁR AND A. SEQUEIRA.   Numerical simulation of blood flow around a clot in straight vessel. In *Topical Problem of Fluid Mechanics 2006*, pages 17–20, Praha, CZ, 2006.

[60] E. GULÍKOVÁ, T. BODNÁR, AND V. PÍŠA. Improvement of numerical models for solution of dust air pollution. In *Topical Problem of Fluid Mechanics 2006*, pages 63–66, Praha, CZ, 2006.

[61] I. SLÁDEK, L. BENEŠ, T. BODNÁR, AND K. KOZEL. A numerical study of atmospheric flow over a shelter-belt including pollution dispersion. In *Topical Problem of Fluid Mechanics 2006*, pages 151–154, Praha, CZ, 2006.

[62] T. BODNÁR, J. PŘÍHODA, AND K. KOZEL. Numerical simulation of 3D turbulent free surface flow in a curved channel. In *Topical Problems of Fluid Mechanics 2005*, pages 15–18, Praha, CZ, 2005.

[63] T. BODNÁR AND M. PROSI. Numerical simulation of 3D shear-thinning blood flow in axisymmetric vessel stenosis. In *Colloquium Fluid Dynamics 2005*, pages 17–20, Praha, CZ, 2005.

[64] I. SLÁDEK, L. BENEŠ, T. BODNÁR, AND K. KOZEL. On the numerical study of the atmospheric 3D-flow over a complex topography with a forest blocks. In *Colloquium Fluid Dynamics 2005*, pages 139–142, Praha, CZ, 2005.

[65] T. BODNÁR, K. KOZEL, I. SLÁDEK, AND P. FRAUNIÉ. Numerical simulation of complex atmospheric boundary layer flows problems. *ERCOFTAC Bulletin*, (60), pages 5–12, March 2004.

[66] L. BENEŠ, T. BODNÁR, AND K. KOZEL. Numerical modeling of two real-life cases of ABL flow. In *1st International Conference "From Scientific Computing to Computational Engineering"*, Athens, 2004.

[67] L. BENEŠ, T. BODNÁR, K. KOZEL, AND I. SLÁDEK. Numerical solution of some ABL problems. In *Colloquium Fluid Dynamics 2004*, pages 9–12, Praha, CZ, 2004.

[68] T. BODNÁR, L. BENEŠ, K. KOZEL, AND I. SLÁDEK. A mathematical study of the vegetation influence on the atmospheric flow over complex topography. In *Topical Problems in Fluid Mechanics 2004*, pages 9–12, Praha, CZ, 2004.

[69] T. BODNÁR, I. SLÁDEK, AND E. GULÍKOVÁ. Numerical simulation of wind flow in the vicinity of forest block. In *Advances in Computational & Experimental Engineering & Sciences*, pages 554–559, Forsyth, US, 2004.

[70] K. KOZEL, P. LOUDA, T. BODNÁR, L. BENEŠ, AND I. SLÁDEK. *Numerická simulace proudění II*. 1st edition, 2004.

[71] I. SLÁDEK, T. BODNÁR, L. BENEŠ, AND K. KOZEL. Numerical tests of flows in coal field. In *Colloquium Fluid Dynamics 2004*, pages 173–176, Praha, CZ, 2004.

[72] L. BENEŠ, T. BODNÁR, Z. JAŇOUR, K. KOZEL, AND I. SLÁDEK. Numerical solution of atmospheric boundary layer flows with 2D and 3D applications. In *Summer School "Geophysical Turbulence"*, pages 79–88, La Garde Cedex, FR, 2003.

[73] L. BENEŠ, T. BODNÁR, Z. JAŇOUR, K. KOZEL, AND I. SLÁDEK. On the complex atmospheric flow modelling including pollution. In *Wind Effects on Trees - Proceedings of the International Conference*, pages 183–188, Karlsruhe, DE, 2003.

[74] L. BENEŠ, T. BODNÁR, K. KOZEL, I. SLÁDEK, E. GULÍKOVÁ, AND V. PÍŠA. On the prediction of complex atmospheric flow including pollution dispersion over a coal depot. In *Topical Problems of Fluid Mechanics 2003*, pages 1–6, Praha, CZ, 2003.

[75] T. BODNÁR, Z. JAŇOUR, K. KOZEL, AND I. SLÁDEK. A real atmospheric boundary layer flow over the prague's agglomeration. In *Colloquium Fluid Dynamics 2003*, pages 129–132, Praha, CZ, 2003.

[76] T. BODNÁR, I. SLÁDEK, K. KOZEL, L. BENEŠ, AND Z. JAŇOUR. On the prediction of complex atmospheric flow. In *Proceedings of the International Conference Mathematical and Computer Modelling in Science and Engineering*, pages 53–57, Praha, CZ, 2003.

[77] **L. Beneš, T. Bodnár, P. Fraunié, and K. Kozel. Numerical modelling of pollution dispersion in 3D atmospheric boundary layer. In *Air Pollution Modelling and Simulation*, pages 69–78, Berlin, DE, 2002.**

[78] T. Bodnár, I. Sládek, K. Kozel, L. Beneš, J. Gulíková, and V. Píša. Studie vlivu ochranného valu na dispersi znečištění z uhelné skládky. In *Topical Problems of Fluid Mechanics 2002*, pages 13–16, Praha, CZ, 2002.

[79] T. Bodnár, I. Sládek, K. Kozel, L. Beneš, and Z. Jaňour. Application of numerical pollution dispersion models for complex terrain flows. In *Topical Problems of Fluid Mechanics 2002*, pages 9–12, Praha, CZ, 2002.

[80] T. Bodnár, I. Sládek, K. Kozel, L. Beneš, and Z. Jaňour. Mathematical modelling of atmospheric boundary layer flow over complex terrain including pollution dispersion. In *Colloquium Fluid Dynamics 2002*, pages 13–16, Praha, CZ, 2002.

[81] L. Beneš, T. Bodnár, P. Fraunié, and K. Kozel. Numerical simulation of 3D boundary layer of atmospheric flows. In *Discrete Modelling and Discrete Algorithms in Continuum Mechanics*, pages 27–36, Berlin, DE, 2001.

[82] L. Beneš, T. Bodnár, P. Fraunié, and K. Kozel. Mathematical modelling of the atmospheric boundary layer. In *Proceedings of Workshop 2001*, pages 516–517, Praha, CZ, 2001.

[83] L. Beneš, T. Bodnár, P. Fraunié, and K. Kozel. Numerical models for atmospheric boundary layer flows. In *Numerical Modelling in Continuum Mechanics*, pages 18–27, Praha, CZ, 2001.

[84] T. Bodnár, P. Fraunié, Z. Jaňour, and K. Kozel. Pollution dispersion in complex terrain. In *Proceedings of International Conference on Advanced Engineering Design*, pages 147–152, Glasgow, GB, 2001.

[85] **T. Bodnár, P. Fraunié, K. Kozel, and L. Beneš. Numerical modelling of pollution dispersion in complex terrain. In *Air Pollution IX*, pages 85–94, Southampton, GB, 2001.**

[86] **L. Beneš, T. Bodnár, P. Fraunié, K. Kozel, and I. Sládek. Numerical simulation of turbulent atmospheric boundary layer flows. In *Zeitschrift für Angewandte Mathematik und Mechanik*, 81: page S905–S906, DE, 2001.**

[87] T. Bodnár, K. Kozel, P. Fraunié, and Z. Jaňour. Numerical modelling of pollution dispersion in complex terrain. In *Proceedings of 4th Seminar Euler and Navier–Stokes Equations*, pages 15–18, Praha, CZ, 2001.

[88] T. Bodnár, K. Kozel, and P. Fraunié. On the Boussinesq approximation for atmospheric boundary layer flows. In *Topical Problems of Fluid Mechanics 2001*, pages 13–16, Praha, CZ, 2001.

[89] T. Bodnár, I. Sládek, K. Kozel, and L. Beneš. On the validation of numerical models for atmospheric boundary layer flows. In *Fluid Dynamics 2001*, pages 9–12, Praha, CZ, 2001.

[90] L. BENEŠ, T. BODNÁR, P. FRAUNIÉ, Z. JAŇOUR, AND K. KOZEL. Numerical models for atmospheric boundary layer flows. In *Dynamika tekutin 2000. Sborník příspěvků*, pages 5–8, Praha, CZ, 2000.

[91] L. BENEŠ, T. BODNÁR, P. FRAUNIÉ, Z. JAŇOUR, K. KOZEL, AND I. SLÁDEK. Computation of 3D boundary layer of atmospheric flows. In *Proceedings of Workshop 2000*, page 279, Praha, CZ, 2000.

[92] T. BODNÁR, P. FRAUNIÉ, Z. JAŇOUR, AND K. KOZEL. Atmospheric boundary layer modelling including the dispersion of pollutants. In *Topical Problems of Fluid Mechanics 2000*, pages 1–4, Praha, CZ, 2000.

[93] T. BODNÁR, K. KOZEL, P. FRAUNIÉ, AND Z. JAŇOUR. Numerical simulation of flow and pollution dispersion in 3D atmospheric boundary layer. *Computing and Visualization in Science*, 3(1-2):3–8, 5 2000.

[94] K. KOZEL, Z. JAŇOUR, P. FRAUNIÉ, AND T. BODNÁR. Numerical simulation of flow and pollution dispersion in 3D atmospheric boundary layer. In *ECCOMAS 2000*, Barcelona, ES, 2000.

[95] L. BENEŠ, T. BODNÁR, K. KOZEL, I. SLÁDEK, P. FRAUNIÉ, AND Z. JAŇOUR. Numerical solution of turbulent atmospheric boundary layer flows. In *First International Conference on Advanced Engineering Design*, pages 307–316, Praha, CZ, 1999.

[96] K. KOZEL, L. BENEŠ, T. BODNÁR, Z. JAŇOUR, AND I. SLÁDEK. Výpočet proudění v mezní vrstvě atmosféry s uvažováním pasivních příměsí. In *Transfer 99*, pages K3–K4, Brno, CZ, 1999.

[97] T. BODNÁR, Z. JAŇOUR, K. KOZEL, AND P. FRAUNIÉ. Numerical simulation of flow and pollution propagation in 3D atmospheric boundary layer. In *Euler and Navier-Stokes Equations*, pages 19–20, Praha, CZ, 1998.

[98] T. BODNÁR, Z. JAŇOUR, AND K. KOZEL. Výpočet 3D proudění v MVA s uvažováním transportních rovnic pro pasivní příměsi. In *Aktuální problémy mechaniky tekutin 98*, pages 5–6, Praha, CZ, 1998.

[99] T. BODNÁR, Z. JAŇOUR, K. KOZEL, AND I. SLÁDEK. Numerical solution of 3D atmospheric boundary layer flows models. In *Aktuální problémy mechaniky tekutin 97*, pages 1–2, Praha, CZ, 1997.

[100] T. BODNÁR, K. KOZEL, AND I. SLÁDEK. Matematické modelování a numerické řešení proudění v mezní vrstvě atmosféry. In *Aktuální problémy mechaniky tekutin 96*, pages 3–4, Praha, CZ, 1996.

[101] K. KOZEL, T. BODNÁR, AND Z. JAŇOUR. Numerické řešení modelu 3D proudění v mezní vrstvě atmosféry. In *Kolokvium Dynamika tekutin 96*, pages 7–8, Praha, CZ, 1996.